Use of Computational Fluid Dynamics to improve the layer thickness control of polyester based multilayered films

by

James Champion

A thesis submitted to the University of Birmingham

for the degree of Doctor of Engineering, EngD

School of Chemical Engineering

College of Engineering and Physical Sciences

University of Birmingham, Birmingham, UK

June 2015

UNIVERSITY OF
BIRMINGHAM

University of Birmingham Research Archive

e-theses repository

This unpublished thesis/dissertation is copyright of the author and/or third parties. The intellectual property rights of the author or third parties in respect of this work are as defined by The Copyright Designs and Patents Act 1988 or as modified by any successor legislation.

Any use made of information contained in this thesis/dissertation must be in accordance with that legislation and must be properly acknowledged. Further distribution or reproduction in any format is prohibited without the permission of the copyright holder.

Abstract

Polyester based multilayered films are a core part of DuPont Teijin Films' product portfolio. A *multilayered film* is a film consisting of several different polymer layers. The main application areas for multilayered films include digital displays, food packaging, reflector film and security cards. Such multilayered films are formed via coextrusion when separately extruded polymer melt streams come together for the first time in either an injector block linked to a die or a multi-manifold die. The formed melt curtain is then quenched into film using a cooled casting drum. As multilayered film structures increase in complexity it becomes more difficult to control the individual layer thicknesses. To improve the layer thickness control, STAR-CCM+ computational fluid dynamics software was used to model both coextrusion geometries and polymer melt flows (assuming Newtonian, inelastic behaviour) typical of DuPont Teijin Films' operations.

Initially, CD-adapco's STAR-CCM+ was used to model a pilot scale injector block linked to an end fed die. This was to test the capabilities and limitations of the software when simulating polyester coextrusion. The majority of results were found to be sufficiently accurate and representative of reality. The main numerical limitations were the unexpected presence of the secondary layer at the near edge of the die outlet and "noise" in the location of the interface between primary and secondary layers. The former was attributed to numerical diffusion errors in a sharp 90° transition within the end fed die and the latter to approximations of the exact polymer-polymer interface. The secondary layer thickness profile across the die outlet improved with the use of a finer mesh. For the total thickness profiles, these were shown to be both mesh and timestep independent.

The comparative ability of the injector block and multi-manifold die systems to handle

increasingly wide melt viscosity ratios was investigated numerically. It was found that the multi-manifold die was the better option when producing multilayered films with wide melt viscosity ratios. This is consistent with previous literature based findings. Furthermore, the limitations found when modelling the injector block and end fed die system did not occur when modelling the multi-manifold die.

Experimental validations using die plug analysis, chloroform washing to remove the outer layer, light microscopy and white light interferometry were conducted to test the accuracy and relevance to reality of the numerical results. At the data points considered, good agreement was generally found between both experimental and numerical data, showing the accuracy of the STAR-CCM+ results. The experimental work was conducted on two different films obtained during pilot scale trials. For the purpose of experimental validation, the maximum melt viscosity ratio between the different polymers was 2:1 and standard grade polyesters, co-polyester polymers and filled polyesters were investigated. The good agreement between experimental and numerical results shows that STAR-CCM+ can be used to predict the outcome of a trial prior to it occurring.

DuPont Teijin Films use die bolt heaters to improve the final film thickness profile via localised melt viscosity changes. Using computational fluid dynamics, a full set of die bolt heaters, spanning both pilot and production scale multi-manifold dies, was implemented. The individual heater powers were set to attempt to improve the film thickness profile at the edges. It was found that the edge heaters are located too far from the pilot scale geometry edges to fully ameliorate the film profile here. However, on a production scale multi-manifold die the film edges significantly improved. This confirmed that heat can be applied to improve the overall film thickness profile. Furthermore, it was shown that undesirable thermal non-uniformity of the geometry walls does not have a detrimental effect on the final film thickness.

In this thesis, both pilot and production scale film trials were successfully predicted using computational fluid dynamics. The numerical methods developed here will be used to reduce the need for pilot scale trials in the future, especially upon improvement of the limitations associated with modelling the injector block and end fed die approach.

Acknowledgements

I would like to express my sincere gratitude to Dr Kieran Looney and Professor Mark Simmons, my industrial and academic supervisors respectively, for their excellent guidance throughout the project and encouraging me to make the most of this opportunity. I want to thank Dr Richard Greenwood, my course manager and secondary supervisor, for accepting me onto the course, his scientific input and correcting my countless thesis drafts.

Thank you to the EPSRC, the University of Birmingham and DuPont Teijin Films for giving me a platform from which I could conduct this very interesting and rewarding research. I feel I have greatly developed both personally and professionally since commencing the EngD scheme. I hope the programme continues to thrive.

I would also like to thank my colleagues at DuPont Teijin Films for helping me settle quickly in Teesside, providing an excellent work atmosphere and their numerous contributions towards this thesis. I would particularly like to acknowledgement John Flett, John Holehouse, Duncan MacKerron, Karl Rakos, David Bell, Dmytro Stratiychuk-Dear and Richard Maltby.

I especially thank my girlfriend, Eilis, my mother, Cathy, and two brothers, Tommy and Freddy, for their constant encouragement and for the nice days out we had when I was back in London.

Thanks to my friends, both in London and those whom I met in Teesside, for their guidance and reminding me to play hard as well as work hard. Thanks also to the other EngD students for making the modules in Birmingham very enjoyable.

Contents

List of Figures

List of Tables

Nomenclature

Symbols

Symbol	Unit	Definition
A	m^2	Area
A	-	Pre-exponential constant
A'	m^2	Cross sectional area
a'_P	-	A coefficient when solving at a cell centre
a'_{nb}	-	A coefficient applied at neighbouring cells
B	m	The average plane gap
b'	-	A generalised source term
C	-	Courant number
Ca	-	Capillary number
CF	m	Additional flux
c_p	J kg^{-1} $^\circ C^{-1}$	Specific heat capacity
D	m	A length scale
De	-	Deborah number
E	J	Energy
$E(\dot{\gamma})$	J mol^{-1}	Activation energy at a constant shear rate
F	-	Volume fraction function
F_k	-	Volume fraction of Fluid k
F_A	-	Volume fraction of an acceptor cell

Symbols (continued)

Symbol	Unit	Definition
F_{D}	-	Volume fraction of a donor cell
F'	-	The result of a surface integral
F'_{e}	-	The surface integral at the east cell face
F_{flow}	N	Force in the flow direction
FF	-	Flow factor
f^{b}	N	Body force
f'	-	Convection or diffusion term
f'_{e}	-	Convection or diffusion term at the east cell
f'_{ne}	-	Convection or diffusion term at the north east cell
f'_{se}	-	Convection or diffusion term at the south east cell
G	Pa	Dynamic modulus
G^*	Pa	Complex modulus
G'	Pa	Storage modulus
G''	Pa	Loss modulus
g	$\mathrm{m^2\ s^{-1}}$	Gravity
g_i	$\mathrm{m^2\ s^{-1}}$	i^{th} component of the gravity vector
h	$\mathrm{W\ m^{-2}\ {}^{\circ}C^{-1}}$	Heat transfer coefficient
h'	m	Distance between two plates
$\underline{\underline{I}}$	-	The identity tensor
$\underline{i}$	-	Unit vector in the x direction
i_{D}	-	x component of a donor cell index
$\underline{j}$	-	Unit vector in the y direction
j_{D}	-	y component of a donor cell index
K	$\mathrm{Pa\ s}^n$	Consistency index
K'	Pa	Bulk modulus

Symbols (continued)

Symbol	Unit	Definition
k	-	An individual melt phase; $k = 1, 2, ..., \mathrm{N}$
$\underline{k}$	-	Unit vector in the z direction
L	m	Length
L_D	m	Development length for a parabolic velocity profile
M_n	g mol^{-1}	Molecular weight
MF	-	Multiplication factor
$\dot{m}$	kg hr^{-1}	Mass flow rate
N	-	A quantity
N_1	-	The primary normal stress difference
N_2	-	The secondary normal stress difference
n	-	Power-law index
$\underline{n}$	-	A normal vector
P	W	Heater power
p	Pa	Pressure
p_k	Pa	Pressure of Fluid k
p'	-	Pressure correction term
Q	m^3 s^{-1}	Volumetric flow rate
Q_h	W	Rate of heat transfer
Q'_h	W	Theoretical power supplied to the heaters
Q'_P	-	Volume integral at a cell centre
q	-	A source term
q_P	-	A source term at a cell centre
q_ϕ	-	Source term for an unknown scalar
R	m	Radius
R	J mol^{-1} $^\circ$C^{-1}	Universal gas constant (8.314)

Symbols (continued)

Symbol	Unit	Definition
Re	-	Reynolds number
R_{q}	nm	Surface roughness
R'	-	A residual
R'_{P}	-	A residual at a cell centre
R'_{Ω}	-	A normalised residual
r	m	Distance
S	-	A surface
S_{e}	-	The east face surface
$\underline{s}'$	-	A vector orthogonal to $\underline{n}$ and $\underline{t}$
T	°C	Temperature
T_k	°C	Temperature of Fluid k
T_{m}	°C	Melting temperature
T_{w}	°C	Wall temperature
$T_{\mathrm{w,\ 100\ \%}}$	°C	Wall temperature at 100 % heater power
$T_{\mathrm{w,\ }P\ \%}$	°C	Wall temperature at a desired heater power
$T_{\mathrm{w,\ max}}$	°C	Maximum wall temperature at 100 % heater power
t	s	Time
t_0	s	Initial time
t_{n+1}	s	Time after $n+1$ timesteps
t'	s	Viscoelastic relaxation time
$\underline{t}$	-	Tangential vector
$\bar{U}$	m s^{-1}	Superficial velocity
U_{x}	m s^{-1}	Velocity in the x direction
u	m s^{-1}	Velocity
$\underline{u}$	m s^{-1}	Velocity vector

Symbols (continued)

Symbol	Unit	Definition
$\underline{u}_k$	m s^{-1}	Velocity vector of Fluid k
u_i	m s^{-1}	i^{th} component of the velocity vector
u_j	m s^{-1}	j^{th} component of the velocity vector
u_{f}	m s^{-1}	Fluid velocity
u_{mesh}	m s^{-1}	Mesh velocity
$u_{i,j}$	m s^{-1}	Velocity in the (x, y) direction
V	m^3	Cell volume
V_{A}	m^3	Volume of Fluid A in a cell
v	m s^{-1}	Velocity component in the y direction
v^{n}	kg hr^{-1}	Flow rate variation
W	m	Plane length
We	-	Weissenberg number
w	m s^{-1}	Velocity component in the z direction
x	m	Distance in the x direction
x_i	m	i^{th} component of the distance vector
x_j	m	j^{th} component of the distance vector
x_{D}	-	x coordinate of a donor cell
$\bar{x}_{\text{flow}}$	m^2 s^{-1}	Mean total flow
y	m	Distance in the y direction
z	m	Distance in the z direction
z_0	m	Initial distance in the z direction
z_{h}	m	Die bolt heater position

Greek letters

Symbol	Unit	Definition
α	-	The ratio between the normal stress differences; $-2N_2/N_1$
β	-	Interfacial orientation
Γ	$m^2\ s^{-1}$	Fluid diffusivity
Γ'	-	Interfacial surface
γ	-	Strain
γ_0	-	Initial strain
$\dot{\gamma}$	s^{-1}	Shear rate
$\dot{\gamma}_0$	s^{-1}	Initial shear rate
$\dot{\gamma}_w$	s^{-1}	Wall shear rate
δ	radians	Phase angle
ζ	$N\ m^{-1}$	Interfacial tension
η	Pa s	Viscosity
η_k	Pa s	Viscosity of Fluid k
η_0	Pa s	Zero shear viscosity
η_∞	Pa s	Infinity shear viscosity
η_e	Pa s	Extensional viscosity
$[\eta]$	$dL\ g^{-1}$	Intrinsic viscosity
κ	$W\ m^{-1}\ ^\circ C^{-1}$	Thermal conductivity
κ_k	$W\ m^{-1}\ ^\circ C^{-1}$	Thermal conductivity of Fluid k
λ	nm	Wavelength of the sample light
λ_c	s	Time constant
$\underline{\Pi}$	Pa	Viscous stress tensor
$\underline{\Pi}_k$	Pa	Viscous stress tensor of Fluid k
$\underline{\Pi}_{ij,k}$	Pa	Individual components of the Fluid k viscous stress tensor
$\overset{\vee}{\underline{\Pi}}$	$Pa\ s^{-1}$	The upper convected time derivative of $\underline{\Pi}$

Greek letters (continued)

Symbol	Unit	Definition
π	-	Pi
ρ	kg m^{-3}	Density
ρ_k	kg m^{-3}	Density of Fluid k
σ	Pa	Normal stress
σ_x	Pa	Normal stress in the x direction
$\underline{\sigma}$	Pa	Total stress tensor
$\underline{\sigma}_k$	Pa	Total stress tensor of Fluid k
σ_{flow}	m^2 s^{-1}	Total flow standard deviation
τ	Pa	Shear stress
τ_{xy}	Pa	(x, y) shear stress component
Φ	-	Mapping matrix
ϕ	-	An unknown scalar
ϕ_{P}	-	Value of ϕ in the centre of the cell being solved for
ϕ_{E}	-	Value of ϕ in the centre of a cell adjacent east from P
ϕ_{EE}	-	Value of ϕ in the centre of a cell two east from P
ϕ_{W}	-	Value of ϕ in the centre of a cell adjacent west from P
ϕ_{nb}	-	Value of ϕ in the centre of neighbouring cells to P
ϕ_{e}	-	Value of ϕ at the wall east of P
ϕ_i	-	i^{th} position of ϕ on a grid; $i = \text{P}, \text{E}, ...,$
ϕ_{i+1}	-	$(i + 1)$ position of ϕ on a grid; $i = \text{P}, \text{E}, ...,$
ϕ_i^n	-	Value of ϕ_i after n timesteps
ϕ_i^{n+1}	-	Value of ϕ_i after $n + 1$ timesteps
φ	-	Level set scalar function
Ω	-	Volume
Ω'	rad s^{-1}	Angular velocity

Greek letters (continued)

Symbol	Unit	Definition
ω	rad s^{-1}	Angular frequency
Υ	-	Parabolic curvature function

Abbreviations

Abbreviation	Definition
2D	Two-dimensional
3D	Three-dimensional
AFM	Atomic force microscopy
AS	Air side
BC	Boundary condition
BE	Blank edge
CFD	Computational fluid dynamics
CPU	Central processing unit
DS	Drum side
DTF	DuPont Teijin Films
EDI	Extrusion Die Industries
FE	Feed edge
HDPE	High density polyethylene
IC	Initial condition
ICI	Imperial Chemical Industries
IV	Intrinsic viscosity
LDPE	Low density polyethylene
LLDPE	Linear low density polyethylene
LOESS	Locally weighted scatterplot smoothing
MAC	Marker and Cell
MD	Machine direction
MLF	Multilayered film
MMD	Multi-manifold die
PC	Polycarbonate
PDE	Partial differential equation

Abbreviations (continued)

Abbreviation	Definition
PE	Polyethylene
PEN	Polyethylene naphthalate
PEPT	Positron emission particle tracking
PET	Polyethylene terephthalate
PISO	Pressure Implicit with Splitting of Operators
PLIC	Piecewise Linear Interface Calculation
PS	Polystyrene
PSI	Phase shifting interferometry
QUICK	Quadratic Upwind Interpolation
SIMPLE	Semi Implicit Method for Pressure Linked Equations
SLIC	Simple Linear Interface Calculation
TD	Transverse direction
TDFJ	Teijin DuPont Films Japan
ToF-SIMS	Time-of-Flight Secondary Ion Mass Spectrometry
VOF	Volume of fluid
VSI	Vertical scanning interferometry
WLI	White light interferometry

Chapter 1

Introduction

1.1 Motivation and purpose

DuPont Teijin Films (DTF [1]) is the world's leading producer of polyethylene terephthalate (PET) and polyethylene naphthalate (PEN) film. Current estimations suggest that the global film production capacity of DTF exceeds 300,000 metric tonnes [2]. DTF is a 50:50 joint venture between E.I. du Pont de Nemours (DuPont [3]) and Teijin Ltd [4] and is a global brand. The company has regional headquarters in Asia, Europe and North America [5]. There are two centres in the UK: a film manufacturing plant in Dumfries, Scotland and a global Research and Development base in The Wilton Centre, Teesside, England.

The major worldwide market regions for DTF polyester film include construction, healthcare, packaging and photovoltaics [6]. *Multilayered films* (MLFs) form a core part of DTF's product portfolio. An MLF is a film consisting of several different polymer layers with applications including photovoltaic backsheets, carton windows, food packaging, reflector film for lighting and liquid-crystal displays and security cards. MLFs are formed via coextrusion, when separately extruded polymer melt layers come together for the first time within coextrusion apparatus, forming a uniformly thin melt curtain (see Sections 1.2 and 2.3). This melt curtain is then rapidly cooled by a casting drum before being stretched in both the machine and transverse directions (MD and TD), producing a

biaxially oriented MLF [7]. Figure 1.1 shows a schematic of the polyester film production process.

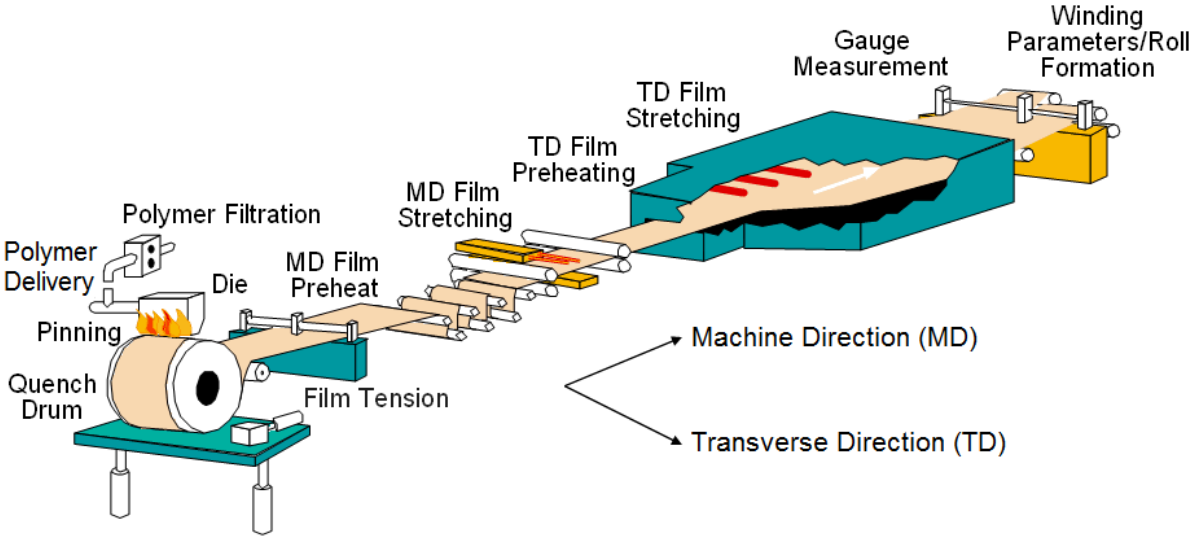

Figure 1.1: A schematic of the polyester film production process. Diagram obtained from the DTF database.

Advantages of MLFs compared with mono-layered structures include the ability to combine the properties of individual layers in a single structure and reduced costs [8–10]. However, as MLF structures become more complex it can be difficult to obtain a film with uniform individual layer thicknesses [11]. A particular problem is when there are large melt viscosity differences between the different polymer streams. This can lead to undesirable thick or thin edges and a curved polymer-polymer interface [9, 11]. Such interfacial curvature would have a deleterious effect upon the optical, mechanical and physical MLF properties [10].

In this thesis, computational fluid dynamics (CFD) is used to model the melt phase of the MLF production process to attempt to show how individual polyester melt phases interact. The volume of fluid (VOF [12]) method is implemented to capture and track the polymer-polymer interface when the melt flows are in contact. Both pilot and production scale coextrusion hardware, typical of DTF operation, are modelled. The purpose of this numerical work is to assess the comparative capability of DTF's current coextrusion geometries, and investigate how the layer thickness control within individual MLFs can

be improved. Furthermore, once the models are in place, it is envisaged that CFD will be used to predict the compatibility of melt flows in potential new MLF products without the need for a trial, as well as forming part of the design process for new coextrusion hardware for the future. This would save DTF considerable time and money.

1.2 Coextrusion background and history

Polymer coextrusion is defined as two or more separately extruded polymer melt streams which come together in either an injector (or feed) block or die to form a single stratified structure with multiple layers [8, 10, 11, 13]. In the coextrusion process, the different melt layers must remain distinct but well bonded (or compatible) when in contact [7, 14]. Assuming that a desirable final coextruded structure is obtained, there are a number of advantages in producing multilayered structures.

The primary advantage of such coextruded products is the ability to combine the properties of different polymers in a single structure with improved features [8, 10, 11, 13, 15]. Another benefit of polymer coextrusion is that it is cost effective and energy efficient compared with a standard off-line lamination process [8, 9, 15]. The cost effectiveness of using multilayered structures is also linked with a reduction in the raw materials required in coextrusion [7, 11, 16].

Further advantages of coextrusion are: the potential to produce structures with secondary (thinner or skin) layers of sub-micron thickness which are thinner than possible via laminating or other coating processes [7–9], the ability to reuse scrap or recycled material in the primary (thicker or core) layer so the product's appearance does not change [7, 9, 11, 16] and the potential for new industrial applications that may challenge traditional materials such as metals, glass and paper [8, 9]. Possible future coextruded products include within photovoltaic cells and in flexible electronics such as organic light-emitting diodes.

A detailed history of polymer coextrusion is shown in [9, 14] amongst other publications. Polymer coextrusion has been used since the 1950's [17, 18]. Beck [19] from

DuPont [3] first patented the use of a dual manifold die to produce two layered flat film in 1955. The dual manifold flat die has since been extended to a multi-manifold die (MMD), where films with more than two different polymer layers can be produced. Co-extruded polymer packaging films were first made commercially available for the United States market in 1964, with 9,000 metric tonnes produced by 1968. During the 1970's and 80's the European coextrusion market had surpassed the United States when considering application (smaller portion packs and longer shelf-life) and market share [9].

Throughout the 1970's there was a large amount of academic and industrial research conducted on polymer coextrusion and associated issues and hardware. In 1971, Chisholm and Schrenk [20] from the Dow Chemical Company [21] first patented the use of an injector block and die combination to produce multilayered structures. This injector block and die composition is now an alternative to the MMD approach and is widely used for flat die coextrusion. Some of the fundamental publications from this era include Southern and Ballman in 1973 and 1975 [22,23], Han in 1973 [24], Lee and White in 1974 [25], Han and Shetty in 1978 [26] and Schrenk *et al.* in 1978 [27].

Coextruded products are now used in a wide variety of markets, with new production lines commonly incorporating a coextrusion capability. Some of the major uses of polymer coextrusion include cast film, blown film, tubing, wire coating, bicomponent fibres and sandwiched foam composites [8,9,13,15–18,28]. The principal commercial application for coextruded film and sheet was in packaging [8,16]. Further coextrusion applications occur in the food packaging, construction and automotive industries [8, 9, 14]. As previously mentioned, there is a large potential for further uses of coextruded products. Polymers can be chosen based on their individual properties to form layers which exhibit specialist features such as antiblock, antislip, light barrier and UV barrier [8, 9].

The author's sponsoring company DTF [1] utilises coextrusion to produce biaxially oriented polyester based multilayered films (MLFs) on a commercial scale. Such MLFs form a component of DTF's whole product portfolio. The individual layers of a DTF MLF are based on either PET or PEN. Typical MLF structures, as produced by DTF, are shown in cross section in Figure 1.2 where A, B and C represent different polymer layers. An

ABA structured film has three layers where the secondary A layers are identical.

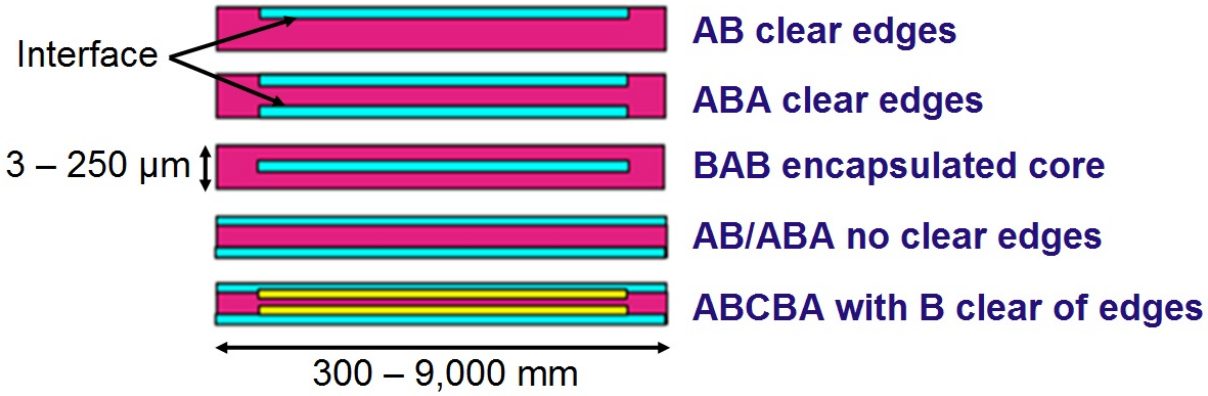

Figure 1.2: Typical DTF MLF structures. Diagram obtained from the DTF database.

Such MLFs in Figure 1.2 are produced by DTF when different polymers are initially extruded, producing separate polymer melt streams. The polymer melt streams then come together for the first time in either an injector block linked to a die or an MMD. The unified melt structure is then rapidly cooled by a casting drum before being stretched in both the machine (forwards) and transverse (sideways) directions, producing a biaxially oriented MLF. In MLF production the choice between an injector block and an MMD depends on a number of factors (see Section 2.3), with a combination of the two potentially used when generating an ABCBA film or another complex structure.

Typical MLFs have two different polymer layers, with the option of increasing this to three [7]. There are certain manufacturing capabilities which allow for layer multiplication and the production of an ABAB...AB MLF, with hundreds of layers and individual layer thickness on the nanoscale [8]. Such films are manufactured by DTF in Japan. It is often desirable to produce a film with *clear edges*. This is when the thinner secondary layers are not at the edges of the MLF (Figure 1.2). The main advantage of attaining clear edges is that trimming the film edges during production leads to monocomponent recycling of the primary polymer. Typical secondary layer thicknesses will account for 15 % of the overall final film thickness [7], although MLFs with only 2 % thick secondary layers have been produced by DTF.

An example of a DTF coextruded film is Mylar® 850, where the secondary polymer

layer has a low melting point, allowing for heat sealing to various substrates. Another MLF produced by DTF is Melinex® 406R, an ABA structured clear handleable coated film used for food carton windows. A schematic of the Melinex® 406R structure is shown in Figure 1.3, where the primary polymer layer contains at least 30 % recycled bottle polymer.

Figure 1.3: The structure of Melinex® 406R. Diagram obtained from the DTF database.

There are a number of limiting factors that one should be aware of when manufacturing coextruded products. A disadvantage of coextrusion is that specialist hardware is required which may need incorporating within a monocomponent extrusion line. Such hardware can be difficult to design and expensive to manufacture [11]. Also more operational skill is required to run a coextrusion line, and knowledge of how different polymers interact is imperative. As previously mentioned, the distinct polymer melt layers should adhere together upon coming into contact [7, 14]. A tie layer may be required to provide compatibility between incompatible melt layers [14]. This would increase the overall cost and the hardware required.

The MLFs depicted in Figure 1.2 are idealised; each individual polymer layer is uniformly thick across the whole film width and the interface between the different layers is linear [29, 30]. This would yield good final product properties. Product requirements of an MLF are generally driven by layer uniformity. An example of such a film is in the ABA structured reflector film. To obtain uniform reflectivity from the film, the individual layers should be uniformly thick across the width. There are a number of coextrusion issues that may arise within the melt processing phase that would cause a deviation from the ideal structure. The main ones are *interfacial deformation* and *interfacial instability*, caused by viscous and elastic effects respectively. If such problems arise they can have

a detrimental effect on the final optical, mechanical, barrier and physical MLF properties [10, 15, 17, 18, 26]. Such non-linear interfaces may also result in a reduction in the quality and manufacturing efficiency and is a limiting factor of coextrusion [15, 26]. Since most polymer melt flows behave viscoelastically (see Section 2.1) both the viscous and elastic components should be considered by a coextrusion operator [9, 14]. The design of the coextrusion hardware used is also an important consideration when trying to obtain a stable interface [9,11,17,18,30,31]. Sections 2.4 and 2.5 contain a more detailed discussion on interfacial issues.

1.3 Objectives

The main aim of this work is to use STAR-CCM+ CFD software to model DTF's coextrusion geometries and improve the layer thickness control of polyester based MLFs. It is envisaged that once the geometries have been created and the accuracy tested, DTF will be able to model potential new MLF products. This will reduce the need for production trials, hence saving the company time and money. There are a number of objectives of this work, based on either an academic or industrial perspective.

1.3.1 Academic objectives

The main academic objectives are as follows:

- Analysis of the ability of the volume of fluid (VOF) method for polymer-polymer interface tracking;
- Further understanding of PET melt rheology and the interaction of different PET melt layers when in contact;
- Conducting both mesh and timestep independence studies to test the accuracy of the CFD results;
- Performing suitable experimental validation methods to test the accuracy and relevance to reality of the numerical results.

1.3.2 Industrial objectives

The primary industrial objectives are:

- Analysis of the accuracy and limitations of the numerical data obtained;
- Comparing the ability of both an injector block and an MMD to handle increasingly wide melt viscosity ratios;
- Investigating the ability of STAR-CCM+ to model industrial scale-up;
- Modelling the use of heat to improve the overall film thickness profile and individual layer thickness control (thermoviscous control).

1.4 Thesis layout

This thesis is structured as follows:

In Chapter 2, previous work on polymer coextrusion relevant to this thesis is critically evaluated. This includes the equations and boundary conditions governing polymer coextrusion, hardware required to produce MLFs and potential issues when manufacturing coextruded products.

Chapter 3 shows both the materials and methods used in this thesis. The Methods section details both numerical and experimental techniques.

A DTF pilot scale coextrusion system is modelled in Chapter 4. Both the ability and limitations of STAR-CCM+ to simulate polymer coextrusion is discussed. Modifications are made to the coextrusion hardware to further investigate the numerical limitations. Mesh and timestep independence studies are then conducted to fully understand the numerical accuracy.

The comparative ability of pilot scale injector block and MMD coextrusion systems to handle increasingly wide melt viscosity ratios is investigated numerically in Chapter 5.

In Chapter 6, experimental work is performed on two different MLFs obtained during pilot scale trials. This is to test the accuracy and relevance to reality of the equivalent numerical results.

Die bolt heaters spanning both pilot and production scale MMDs are modelled in Chapter 7. This is to test the ability of such heaters to improve the final film thickness profile by locally altering the melt viscosity. The final part of Chapter 7 considers thermal non-uniformity in polymer coextrusion.

Finally Chapter 8 summarises the main results shown in this thesis and suggests areas for future work.

1.5 The author's own contributions to the field

Although polymer coextrusion has been studied since the 1970's, the author's work in this area contains some novel features. The finite volume based CFD package STAR-CCM+ by CD-adapco [32] is used to model the full three-dimensional complexity of polyester melt flows in both pilot and production scale geometries. The VOF method is used to capture and track the interface between different polymer melts. This in itself is novel and has never been applied to polymer coextrusion. Also a much finer mesh is used by the author than in any previous publication, implying improved numerical accuracy.

All previous modelling work in this field uses a version of an injector block. In Chapter 5, a DTF MMD is modelled and then compared to the injector block approach, also published in [33]. For experimental validation purposes (Chapter 6), in addition to die plug analysis, both white light interferometry and chloroform washing are used to measure the secondary layer thickness of a final film. Neither of these approaches have been used before for MLF analysis. A combination of thermal and viscous effects are modelled and shown in Chapter 7. Previous publications focus on the relationship between viscosity, shear rate but rarely temperature, whilst never singling out the different thermal and viscous effects. Since PET melts are Newtonian, there is justification in applying this novel thermoviscous approach.

As the product requirements get more complex it becomes difficult to obtain an MLF with both uniform overall thickness and uniformly thin individual layers. This can be due to a number of reasons such as different layer extrusion temperatures, vastly different layer

rheologies and very thin secondary layer thicknesses. CFD has been used to investigate some of these new product requirements and process conditions related to these issues. Using numerical methods is more time efficient and cheaper than running a number of pilot and production scale trials for DTF.

The results obtained during this study have been published as follows:

- J. Champion, M. K. Looney and M. J. H. Simmons, Numerical Modeling of Multilayer Film Coextrusion With Experimental Validation, *Polymer Engineering and Science*, 2014. DOI: 10.1002/pen.24022.

- J. Champion, M. K. Looney and M. J. H. Simmons, Numerical Simulation of the Processing of Multi-Layer Films, *Kunstoffe International magazine*, September 2014.

- J. Champion, M. K. Looney and M. J. H. Simmons, Achieving Better Layer Control in Multi-Layer Polyester Films Through Simulation, *Dynamics magazine*, Issue 35, 2013.

- J. Champion, M. K. Looney and M. J. H. Simmons, Using Computational Fluid Dynamics (CFD) to analyse the limits of the secondary layer thickness in multi-layered polyester film processes, *TAPPI PLACE Europe Conference*, May 2013.

The results obtained during this study have been presented as follows:

- J. Champion, M. K. Looney and M. J. H. Simmons, Improving layer control in multi-layered polyester films using Computational Fluid Dynamics (CFD), *STAR Global Conference*, March 2013.

Chapter 2

Literature Review

This thesis is based on using CFD modelling to improve the layer thickness control of polyester based MLFs. Different polyester melt flows are modelled through various pilot and production scale DTF coextrusion geometries. This Chapter contains a discussion of the fundamental principles behind coextrusion as well as a review of previous published work on the topic. Such work has included experimental, numerical and theoretical attempts at quantifying the common coextrusion issues.

This Chapter is structured as follows: Section 2.1 contains information on polymer melt flow rheology, with focus on both viscous and elastic flow properties. The governing equations and boundary conditions of polymer coextrusion are presented in Section 2.2. Typical coextrusion production hardware and die design is described in Section 2.3. Sections 2.4 and 2.5 show literature based findings on viscous and elastic coextrusion effects respectively. Finally the conclusions of the Chapter are presented in Section 2.6.

2.1 Polymer melt flow rheology

Since polymer coextrusion involves the individual and then combined flow of different polymer melts, knowledge of the flow behaviour of such melts is important. The study of *rheology* involves the study of the deformation and flow of a fluid [9]. The rheology

of polymer melt flows is dependent on a number of factors and forms the basis of this Section. Viscous flow properties are discussed first, followed by elastic effects since most polymer melt flows behave viscoelastically.

2.1.1 Viscous flow properties

Consider a fluid being sheared within two parallel plates, separated by gap h', as shown in Figure 2.1. If the top plate is driven by a velocity in the x direction U_{x} and the bottom plate is stationary, an equation governing the fluid's motion is [9, 34, 35]:

$$\frac{F_{\mathrm{flow}}}{A} = \eta \frac{U_{\mathrm{x}}}{h'} \tag{2.1}$$

where F_{flow} is the force applied in the flow direction, A is the plate area and η is the fluid's viscosity or resistance to flow. Equation 2.1 is based on a lubricator approximation from the Navier-Stokes equations and can be written in a more generalised form as:

$$\tau = \eta \dot{\gamma}. \tag{2.2}$$

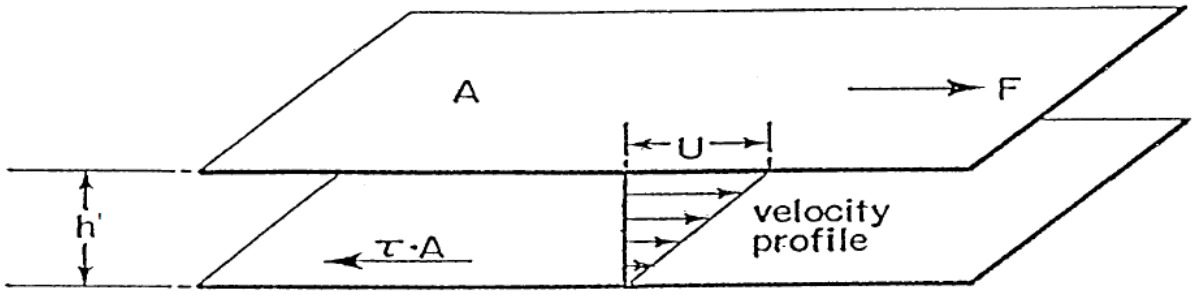

Figure 2.1: Simple shear flow. Diagram obtained from [35].

Equation 2.2 is the mathematical definition of a *Newtonian* fluid. The shear stress exerted on the fluid τ (measured in Pascals, Pa) is the frictional force per plate area acting parallel to the fluid's cross section. The shear rate $\dot{\gamma}$ (measured in reciprocal seconds, s^{-1}) is the rate at which τ is applied. In Equation 2.2, the constant of proportionality is the shear dynamic viscosity η (usually measured in Pa s). Formally, the viscosity of a Newtonian fluid is independent of both the shear stress and the shear rate [34].

A perfectly viscous fluid will stop flowing once an external force acting on the fluid is removed [36]. Newtonian fluids such as water and glycerin exhibit this property. Newtonian fluids have molecular relaxations faster than the time scales of the imposed shear rates and their viscosity is unaffected by the shear rate. Within the melt processing shear rate range found during the film production process ($\dot{\gamma} \leqslant 150\ s^{-1}$), polyester melt flows are considered Newtonian [37–41]. This means that at a constant temperature the rheology of polyester melt flows will not change regardless of the position within the die hardware and the corresponding shear rates here.

The Newtonian aspect of polyester melt flows allows for easier modelling since one less dependent variable ($\dot{\gamma}$) is required and shear thinning models can be omitted. Figure 2.2 shows experimental rheology curves of three different PET grades (investigated in Section 6.3), taken at 280 °C. The intrinsic viscosity (IV) of each grade is shown and is defined fully later. The high viscosity PET, with IV = 0.75, does show some shear thinning behaviour, but is Newtonian up to 150 s^{-1}. The other two grades are film standard PET polymers and show very little shear thinning, confirming the Newtonian assumption.

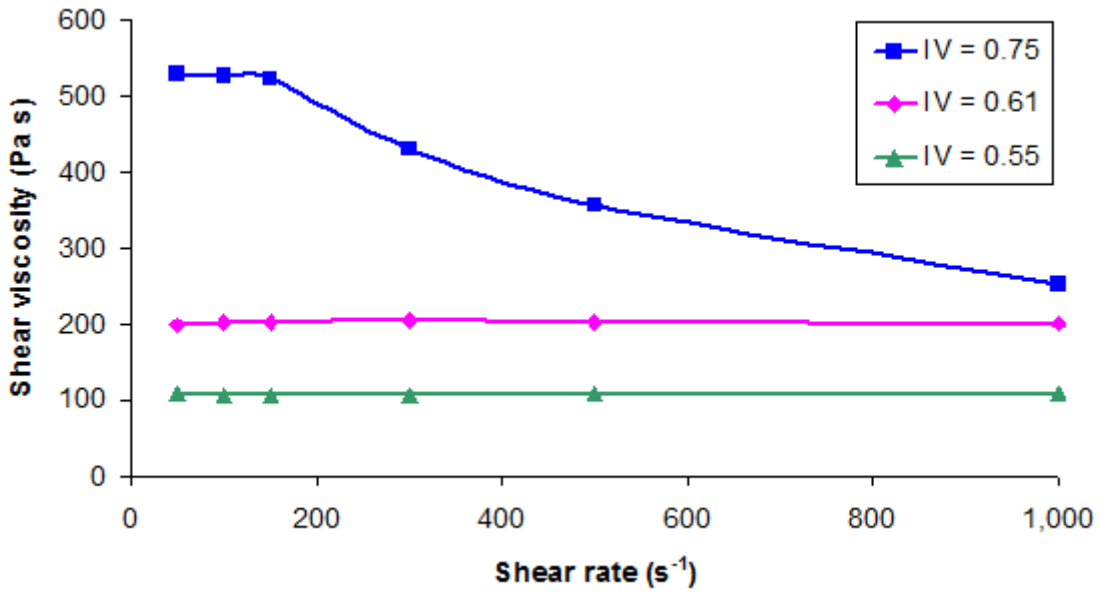

Figure 2.2: The effect of shear rate on the viscosity of three different PET grades. Experimental rheometry performed by David Stocks, Intertek [42] at a temperature of 280 °C.

The majority of polymer melts are *shear thinning*; their viscosity decreases with increasing shear rate [8, 9, 16, 34, 35]. This shear thinning of polymer melts occurs because of molecular alignments and disentanglements after increasing the shear rate [9, 29, 35]. This shear dependent viscosity means that in regions of high shear the resistance to flow decreases and the melt will flow more readily. However, high shear rates can cause flow instabilities and molecular weight reduction [35]. Polyester melt viscosities are largely independent of shear, but some co-polymers used within a DTF MLF are shear thinning and one should be aware of this phenomenon.

For modelling and experimental purposes it is often useful to apply a function that represents the shear thinning behaviour of polymer melt flows. There are a number of constitutive models that polymer rheology data can be fitted to; the simplest and most common is the power-law model [9, 34, 35]:

$$\eta(\dot{\gamma}) = K\dot{\gamma}^{n-1}, \tag{2.3}$$

where K is the consistency index and n the fluid's power-law exponent. The value n ($0 \leqslant n \leqslant 1$) is used to represent the degree of shear thinning, where $n = 1$ implies a Newtonian fluid, whilst a small n, a fluid with a large degree of shear thinning behaviour. Typical values of n for polymer melt flows range from 0.3 (certain grades of polyethylene, PE) to 0.8 (polycarbonate, PC) [35]. The power-law relationship has been fitted to polymer melt rheology data by Dooley in [43] and Prakash in [44] amongst many others.

The power-law model is effective at modelling polymer melt flows for large shear rates. However, at low shear rates the model predicts the viscosity approaching infinity [35]. At both very low and very high shear rates, the viscosity of most polymer melt flows has two Newtonian plateaus: the zero shear viscosity η_0 and the infinity shear viscosity η_∞ [9, 45]. Both the Carreau and Cross models are functions of shear rate and contain η_0 and η_∞ unlike the power-law approach. The Carreau model is given by [45]:

$$\eta(\dot{\gamma}) = \eta_\infty + \eta_0[1 + (\lambda_c\dot{\gamma})^2]^{\frac{n-1}{2}}, \tag{2.4}$$

and the Cross model by [45]:

$$\eta(\dot{\gamma}) = \eta_\infty + \frac{\eta_0}{1 + (\lambda_c\dot{\gamma})^{1-n}}, \tag{2.5}$$

where λ_c is a time constant. The Carreau model or slight variations have been shown to be excellent fits to polymer melt rheology data in [37, 46–48] for example, with the Cross model utilised by Gupta in [49, 50]. The majority of recent publications use the Carreau model for modelling purposes. All the shear thinning models discussed are known as generalised Newtonian models.

Figure 2.3 shows how the melt viscosity decreases with increasing shear rate for four polystyrene (PS) resins at 204 °C [8]. The polymer melt viscosity is a very important parameter for all polymer processing. For film grade PET at standard operating conditions, η typically ranges from 150-300 Pa s (or 1,500-3,000 Poise). The typical viscosity range for all polymer melts is between 100 and 1,000,000 Pa s [9]. As well as being a function of shear rate, polymer melt viscosities depend on other variables such as temperature T, pressure p, time t and molecular weight M_n [16]:

$$\eta = \mathrm{F}(\dot{\gamma}, T, p, t, M_n, ...), \tag{2.6}$$

where some of the dependent variables in Equation 2.6 also depend on each other. Since polyester melts are considered Newtonian, T rather than $\dot{\gamma}$ is the most important contributor to the value of η. The time t arises because of either thixotropy or elastic effects (see later in this Section) exhibited by some polymer melt flows.

As with most liquids, the viscosity of polymer melts *decreases* with increasing temperature [34, 35]. This is because an increase in temperature causes an increase in the average kinetic energy of the liquid molecules, overcoming the attractive forces holding the molecules together and decreasing the resistance to flow [51]. Different polymer melts show varying viscosity effects with increasing temperature. The viscosity dependence on temperature for a DTF PET melt is shown in Figure 2.4, where the viscosity is shown on a logarithmic scale. In Figure 2.4 the shear rate is constant ($\dot{\gamma}$ = 100 s^{-1}) and the approximate polymer IV is 0.57.

The temperature range in Figure 2.4 is from 265 to 375 °C. The melting temperature (T_m) of PET is around 255 °C, and any PET rheology data should be obtained above T_m. Typical PET melt temperatures during extrusion are normally between 280 and 310 °C [7]. Increasing the temperature of either the melt or the hardware reduces the melt

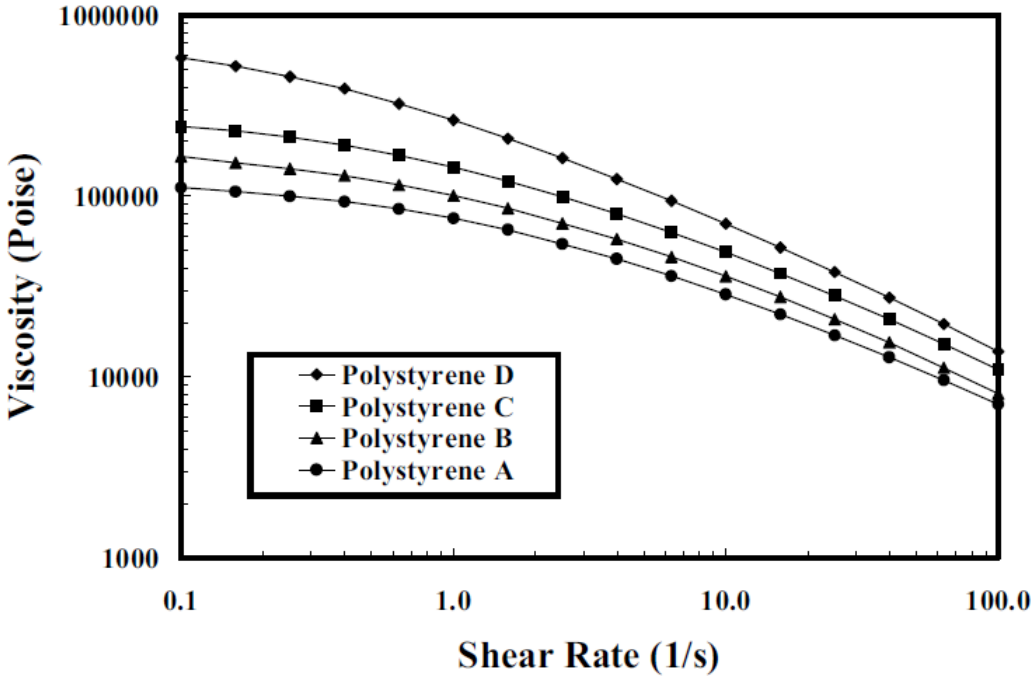

Figure 2.3: The effect of shear rate on the viscosity of four PS resins. Diagram obtained from [8].

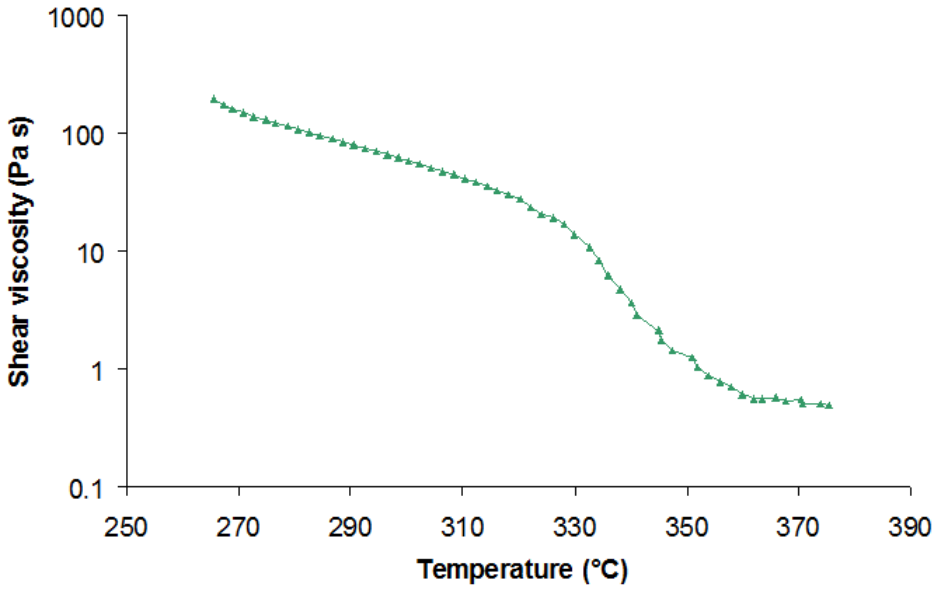

Figure 2.4: The effect of temperature on the viscosity of PET (IV $\approx$ 0.57). Diagram obtained from the DTF database. Experimental rheometry performed by David Stocks, Intertek at $\dot{\gamma} = 100$ s^{-1}.

viscosity and makes processing easier. However, at very high operating temperatures the polymer will thermally degrade and will not be processable as a melt. This is demonstrated in Figure 2.4 where at high temperatures the PET viscosity decreases to below unity.

The viscosity of polymer melts vary with temperature in an exponential manner [35]. Often an Arrhenius type relationship is used to represent this [16, 34]:

$$\eta = \mathrm{A} \exp\left(\frac{E(\dot{\gamma})}{\mathrm{R}T}\right), \tag{2.7}$$

where A is a pre-exponential constant, $E(\dot{\gamma})$ gives the activation energy at constant shear rate and R is the universal gas constant. For a shear thinning, non-Newtonian polymer melt, an increase in temperature will shift the viscosity-shear rate curve downwards [34, 35].

Within DTF the unpublished, internal O'Dell model is used to represent the viscosity-temperature relationship:

$$\eta = 0.1\left[10\text{^}\left\{\frac{5\ln[\eta]}{2.30259} + \frac{2,953}{T} - 0.9508\right\}\right], \tag{2.8}$$

where atmospheric pressure is assumed. In Equation 2.8, T is measured in Kelvin and $[\eta]$ is the intrinsic viscosity (IV) of the polymer. The IV is "*a measure of the ability of a polymer in solution to increase the viscosity of that solution*" [52]. Within DTF, the polymer IV is measured using a Davenport melt viscometer [53], which initially gives a melt viscosity value. The Davenport software then obtains the IV from η using Equation 2.8. The IV is a function of M_n, where an increase in M_n causes an increase in the IV and hence in the shear viscosity η. The typical IV range for film grade PET is 0.6-0.7 or an M_n of around 19,000-23,000. The units of IV are decilitres per gram (dL g^{-1}) but it is often quoted without units. Polymers should be dried prior to unvented extrusion so that they retain their IV as much as possible upon melting. Equation 2.8 has been shown internally to give an excellent correlation to PET rheology and is used for modelling purposes.

Increasing the pressure exerted on the melt can cause an increase in η [34]. However, the effect of pressure is negligible during extrusion [35] and is not considered a major factor. Some polymer melts will show *time dependent* shear thinning (thixotropy [16]) but within DTF polyester melt flows are considered steady state and this is modelled in

this thesis. Figure 2.5 shows the effect of the different variables on polymer melt viscosity. Certain fillers and additives (plasticisers) can be added to the original polymer resin to change its flow behaviour without adjusting the processing conditions, but will influence final film properties.

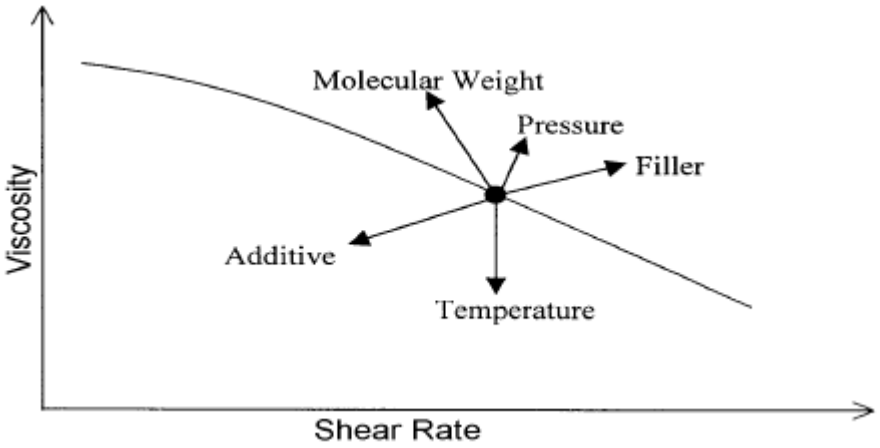

Figure 2.5: The effect of certain parameters on polymer viscosity. Diagram obtained from [35] and also found in [34].

A *rheometer* can be used to measure how the polymer melt viscosity changes with either shear rate or temperature. The two most common rheometers used for polymer processing are the capillary rheometer and the parallel plate rotating rheometer [54]. In the capillary rheometer, the fluid (in this case the polymer melt) is pressure driven through a tube of constant cross section. The flow rate is then converted to a shear rate and the apparent Newtonian wall shear rate is given by [54, 55]:

$$\dot{\gamma} = \frac{4Q}{\pi R^3} = \frac{4\bar{U}}{R}, \tag{2.9}$$

where Q is the volumetric flow rate, R is the tube radius and $\bar{U}$ the superficial velocity.

In the parallel plate rheometer (used in Chapter 6), the fluid is placed between two plates; one that is stationary and one that is rotating, usually in an oscillatory manner. For this instrument the shear rate is a function of the distance r from the disk centre [55]:

$$\dot{\gamma} = \frac{r\Omega'}{h'} \tag{2.10}$$

where Ω' is the angular velocity and h' is the distance between the two disks. At the

centre of the disks ($r = 0$) the shear rate is a minimum and is a maximum at the disk edge ($r = R$).

When comparing the two rheometer geometries, the capillary model is the preferred industry standard as it gives a good representation of the actual extrusion process and the corresponding shear rate values found here [34,54]. The parallel plate or similar rheometer is often used as a complement to the capillary rheometer measurements and is better for scanning a wide range of shear rates. Furthermore, the parallel plate rheometer, unlike the capillary approach, allows for measurement of viscoelastic properties.

The viscous properties of polymer melts have been discussed based on their shear viscosity η. Polymer melts also show some resistance to stretching or extension which makes the structure thinner. This resistance is known as the *extensional* or *elongational* viscosity η_e and can be measured using either a capillary rheometer or a special extensional rheometer [34, 35]. Although a viscous effect, η_e has been shown to contribute to interfacial instabilities that are mainly linked to the elastic properties of polymer melts (see Section 2.5) [56]. Polymer melts are often subjected to extension during processing. For Newtonian fluids, a relationship between η and η_e is given by Trouton's ratio [34,35]:

$$\eta_e = 3\eta. \tag{2.11}$$

2.1.2 Elastic flow properties

Most polymer melts show elastic as well as viscous properties [8,9,34]. In a perfectly elastic solid the strain or deformation relaxes after removal of a force and the material returns to its original shape [36]. The flow behaviour of polymer melts is between that of a Newtonian liquid and an elastic solid. This behaviour is often referred to as *viscoelastic* [57]. Most polymer melts can behave as either a liquid or a solid depending on the processing time [35].

The main parameter used to quantify the elasticity of a fluid is the storage modulus G' (measured in Pa). Oscillatory rheometry, with an angular frequency ω, is often used to characterise elastic fluids. Here, a rheometer will apply a sinusoidal oscillatory strain

γ to a material at a chosen range of ω with a maximum initial strain γ_0 [55]:

$$\gamma = \gamma_0 \sin(\omega t). \tag{2.12}$$

The strain rate $\dot{\gamma}$ may thus be obtained by differentiation of Equation 2.12:

$$\dot{\gamma} = \dot{\gamma_0} \cos(\omega t), \tag{2.13}$$

where $\dot{\gamma_0} = \omega\gamma_0$ is the initial strain rate.

Elastic materials have a linear response as a function of strain (*i.e.* Hookean solids, $\tau = K'\gamma$, where K' is the bulk modulus), whilst viscous materials respond linearly with strain rate (Newtonian fluids, $\tau = \eta\dot{\gamma}$). Viscoelastic fluids thus cause a phase shift in the torque (and thus shear stress) response so that [34]:

$$\tau = \tau_0 \sin(\omega t + \delta), \tag{2.14}$$

or:

$$\tau = (\tau_0 \cos\delta)\sin(\omega t) + (\tau_0 \sin\delta)\cos(\omega t), \tag{2.15}$$

where δ is the phase angle. The proportion in phase is therefore due to the elastic response of the fluid (first term on the right hand side of Equation 2.15) and the proportion 90° out of phase is the viscous response (second term on the right hand side of Equation 2.15).

From Equation 2.15, the storage and loss moduli, G' and G'' respectively, can be derived as:

$$\frac{\tau}{\gamma_0} = G' \sin(\omega t) + G'' \cos(\omega t), \tag{2.16}$$

where:

$$G' = \frac{\tau_0}{\gamma_0} \cos\delta, \tag{2.17}$$

and:

$$G'' = \frac{\tau_0}{\gamma_0} \sin\delta. \tag{2.18}$$

The complex modulus G^* can be split into its real and imaginary parts using complex algebra as:

$$G^* = G' + iG'', \tag{2.19}$$

where i is the imaginary component and G'' shows the fluid's viscous component. Most modern oscillatory rheometers give an output of G' and G'' along with η. Figure 2.6 shows how G' increases with increasing shear rate (converted from ω) for PS, PE and PC resins. The least elastic is PC, which is also the most Newtonian or least shear thinning of the three polymers.

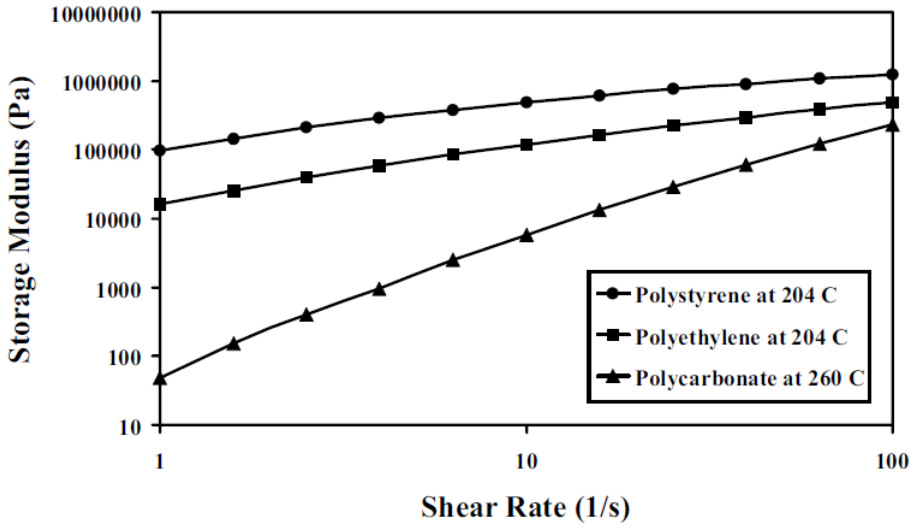

Figure 2.6: The effect of shear rate on the storage modulus of PS, PE and PC resins. Diagram obtained from [8].

Rheological tests by Intertek [42], showing how G' and G'' vary with shear rate ($0.1\ s^{-1} \leqslant \dot{\gamma} \leqslant 100\ s^{-1}$) for two PET blends (denoted PET1 and PET2) at a melt temperature of 280 °C, is displayed in Figure 2.7. For both polymer blends, G'' exceeds G' across the shear rate range, as observed within DTF for all film grade PET. This shows that viscous effects dominate over elastic ones for PET. Polyester resins have low G' values compared with other polymers; the maximum G' of PET1 is far lower than the maximum G' for the three polymers in Figure 2.6. Within the shear rate range of interest ($\dot{\gamma} \leqslant 150\ s^{-1}$), polyester melts have low elasticity. A Newtonian, inelastic modelling assumption for PET is maintained throughout this thesis.

Elastic materials return to their original state after deformation in a time dependent manner [16]. Therefore the flow history experienced by a typical polymer melt can affect the final product properties. If a shear stress is applied to a Newtonian fluid, the

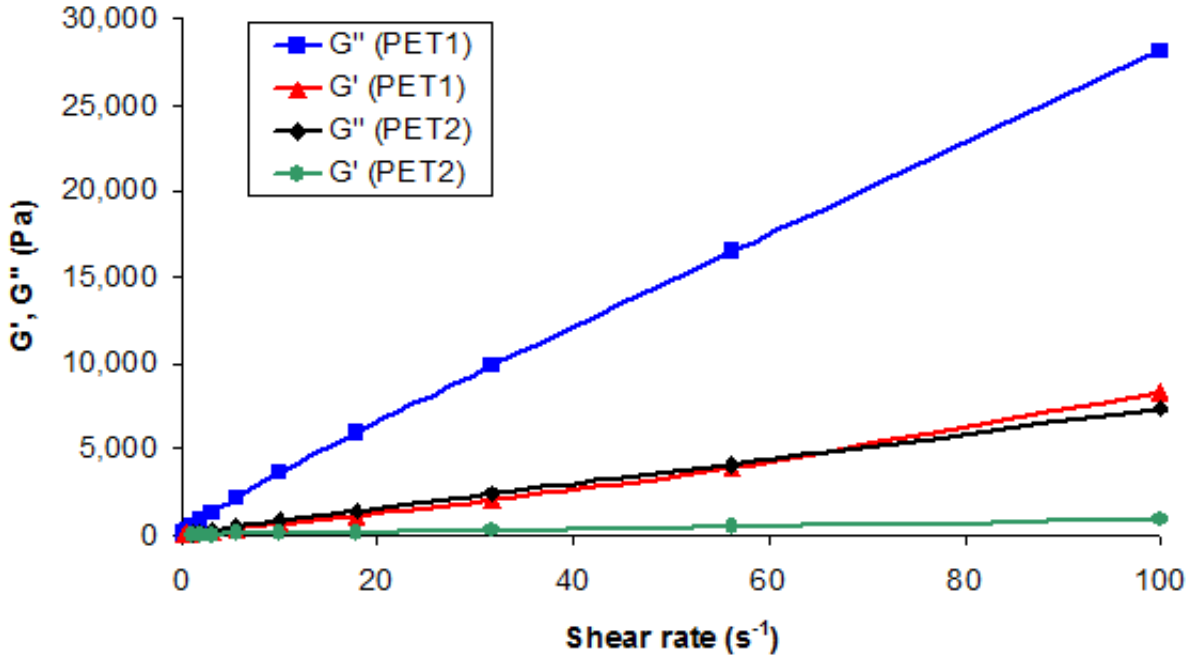

Figure 2.7: The effect of shear rate on G' and G'' for two PET blends. Experimental rheometry performed by David Stocks, Intertek [42] at a temperature of 280 °C.

fluid would only deform in the shear direction (tangential to the flow surface) [34]. A non-Newtonian, time dependent fluid would respond in both the shear *and* normal (perpendicular) directions. Viscoelastic fluids like most polymer melts, therefore, have both normal stresses σ and shear stresses τ in such flows. This is because the shearing of complex long chain molecules generates stresses normal to the flow direction [57].

Both the shear and normal stresses experienced by any fluid can be summarised into a three-dimensional (3D) *stress tensor* $\underline{\Pi}$ [34]:

$$\underline{\Pi} = \begin{pmatrix} \sigma_x & \tau_{xy} & \tau_{xz} \\ \tau_{xy} & \sigma_y & \tau_{yz} \\ \tau_{xz} & \tau_{yz} & \sigma_z \end{pmatrix}. \tag{2.20}$$

The normal stresses for Newtonian fluids are equal to the pressure p and their effect is negligible [57]. The normal stresses of viscoelastic fluids are measurable and their presence must be considered when processing polymer melts. Both the primary (N_1) and secondary (N_2) normal stress differences for an individual fluid have been shown to contribute to

unwanted elastic interfacial instability, where [34, 35]:

$$N_1 = \sigma_x - \sigma_y \tag{2.21}$$

and:

$$N_2 = \sigma_y - \sigma_z. \tag{2.22}$$

The normal stress differences N_1 and N_2 are non-zero for time dependent elastic fluids and must be considered. It has been shown that N_1 is positive and greater in magnitude than the negative N_2 [28, 34, 35]. In polymer coextrusion the difference between N_1 and N_2 of the different melt phases in contact may further contribute to the interfacial shape. The normal stresses can lead to unwanted polymer processing effects even in monocomponent processing. For Newtonian fluids such as PET (for $\dot{\gamma} \leqslant 150$ s^{-1}), the normal stress differences are zero and need not be analysed [34].

2.2 Governing equations and boundary conditions

Polymer coextrusion involves the formation of a unified structure and subsequent flow of two or more different polymer melts through specialised hardware. A number of equations can be used to represent this fluid flow within the coextrusion process. It is common in the literature to model an *isothermal* coextrusion process, with shear thinning effects.

Other assumptions include steady, creeping (very slow moving), incompressible flow with no body forces, as governed by [27, 48, 58–61]:

$$-\nabla p_k + \nabla.\underline{\Pi}_k = 0, \tag{2.23}$$

$$\nabla.\underline{u}_k = 0, \tag{2.24}$$

where $k = 1, 2, ..., N$ corresponds to an individual melt phase within the coextrusion system, ∇ is the gradient operator and $\underline{u} = u_i = (u, v, w)$ is the velocity vector of individual fluids. Equation 2.23 is a simplified version of the Navier-Stokes momentum equations and Equation 2.24 shows incompressibility or mass conservation. Equation 2.23 shows a

simplified model which neglects the convective term in the Navier-Stokes equations. A version of this which considers the convective term is [46]:

$$-\nabla p_k + \nabla.\underline{\Pi}_k = \rho \underline{u}_k.\nabla \underline{u}_k, \tag{2.25}$$

as solved by the author.

If temperature effects are to be included within a coextrusion model, the energy conservation equation must be solved alongside Equations 2.23 or 2.25 and 2.24 [45, 62]:

$$(\rho c_{\mathrm{p}})_k \underline{u}_k.\nabla T_k = \kappa_k \nabla^2 T_k + \underline{\Pi}_k : \nabla \underline{u}_k, \tag{2.26}$$

where ρ is the melt density, c_{p} is the specific heat capacity and κ the thermal conductivity. In a generalised Newtonian case the viscous stress tensor $\underline{\Pi}$ is written for individual melt phases as [58]:

$$\underline{\Pi}_{ij,\,k} = \eta_k \left(\frac{\partial u_i}{\partial x_j} + \frac{\partial u_j}{\partial x_i} \right). \tag{2.27}$$

Often the Carreau model (Equation 2.4) or a slight variant is used to model the shear thinning or generalised Newtonian behaviour of polymer melts.

Two common dimensionless numbers used to quantify the viscous effects of polymer melts in coextrusion are the Reynolds number Re and the capillary number Ca. Re is the ratio between inertial and viscous forces [28]:

$$Re = \frac{\rho |\underline{u}| D}{\eta}, \tag{2.28}$$

and Ca is the ratio between viscous and surface (or interfacial) tension forces:

$$Ca = \frac{\eta u}{\zeta}, \tag{2.29}$$

where D is a length scale and ζ the surface (or interfacial) tension between two fluids.

Calculations by Yue *et al.* [28] show that $Re \approx 10^{-4} << 1$ for a typical polymer melt within coextrusion. This low value is due to the high viscosity of polymer melt flows and implies that inertial effects are negligible within coextrusion. This justifies the creeping flow assumption made in Equation 2.23. The very laminar nature of polymer melt flows is what makes coextrusion possible [29]. When estimating the interfacial tension between

two melts ζ as 0.01 N m^{-1}, Ca is calculated as $\approx 10^3$ [28]. This large value shows that interfacial tension is negligible in coextrusion and is not usually included for numerical purposes [25, 28, 58, 63, 64]. Interfacial tension is not solved for in this investigation.

To numerically model a coextrusion system, both boundary and interfacial conditions must be prescribed. Usually a no-slip boundary condition is enforced, *i.e.* $\underline{u} = 0$ at the geometry walls [61]. At the fluid-fluid interface a number of conditions must also be set. Assuming a two fluid model the interfacial conditions are generally given as [61–63]: Kinematic conditions:

$$\underline{n}.\underline{u}_1 = \underline{n}.\underline{u}_2 = 0, \tag{2.30}$$

$$\underline{t}_1.\underline{u}_1 = \underline{t}_1.\underline{u}_2, \tag{2.31}$$

$$\underline{t}_2.\underline{u}_1 = \underline{t}_2.\underline{u}_2, \tag{2.32}$$

Dynamic conditions:

$$\underline{t}_1.\underline{\sigma}_1 = \underline{t}_1.\underline{\sigma}_2, \tag{2.33}$$

$$\underline{t}_2.\underline{\sigma}_1 = \underline{t}_2.\underline{\sigma}_2, \tag{2.34}$$

$$\underline{n}_2.\underline{\sigma}_1 - \underline{n}_2.\underline{\sigma}_2 = 0, \tag{2.35}$$

No relative slip condition:

$$\underline{u}_1 = \underline{u}_2. \tag{2.36}$$

In Equations 2.30-2.36 the vectors $\underline{n}$ and $\underline{t}$ are the unit normal and tangential interfacial vectors respectively. Equations 2.30-2.32 show the no flow condition across the interface. Equations 2.33-2.35 imply a continuity of stress at the interface and Equation 2.36 is the condition of no relative interfacial slip between the two fluids [61]. In Equations 2.33-2.36, $\underline{\sigma}$ is the *total* stress tensor [61]:

$$\underline{\sigma} = -p\underline{I} + \underline{\Pi}, \tag{2.37}$$

where $\underline{I}$ is the identity tensor.

Since most polymer melts behave viscoelastically (Section 2.1), the elastic, time dependent part of their behaviour must also be considered. A Newtonian, inelastic modelling assumption is maintained throughout this thesis for film grade PET, but one should be

aware of viscoelastic models if investigating polymers other than polyesters. The relaxation time t' is a way of characterising a fluid's viscoelastic response time [36]:

$$t' = \frac{\eta}{G} \tag{2.38}$$

where G is the dynamic modulus of the fluid concerned; $G = |G^*|$. A value of t' between the order of milliseconds and hours implies a viscoelastic material [36].

For a full viscoelastic representation Equations 2.24-2.37 must be solved alongside a constitutive viscoelastic model. One such example is the White-Metzner equation, given as [8, 63, 64]:

$$\underline{\Pi} + t'\underline{\breve{\Pi}} = \eta(\nabla\underline{u} + \nabla\underline{u}^{\mathrm{T}}), \tag{2.39}$$

where $\underline{\breve{\Pi}}$ is the upper convected time derivative of $\underline{\Pi}$ [63, 64]:

$$\underline{\breve{\Pi}} \equiv \frac{\partial\underline{\Pi}}{\partial t} + \underline{u}.\nabla\underline{\Pi} - \nabla\underline{u}^{\mathrm{T}}.\underline{\Pi} - \underline{\Pi}.\nabla\underline{u}. \tag{2.40}$$

A second constitutive viscoelastic model is the more realistic Giesekus equation [8, 37, 59, 60]:

$$\underline{\Pi}\left[\underline{I} + \frac{\alpha t'}{\eta}\underline{\Pi}\right] + t'\underline{\breve{\Pi}} = \eta(\nabla\underline{u} + \nabla\underline{u}^{\mathrm{T}}), \tag{2.41}$$

where for low shear rates [8, 59]:

$$\alpha = -\frac{2N_2}{N_1}. \tag{2.42}$$

It is the inclusion of the normal stress differences that makes Equation 2.41 more realistic than Equation 2.39. Further viscoelastic models have been used, but are not discussed here.

There are a number of dimensionless numbers that can be used to characterise the viscoelasticity of a material. Two of these are the Weissenberg number We [45, 64]:

$$We = t'\dot{\gamma}, \tag{2.43}$$

and the Deborah number De [28]:

$$De = \frac{t'}{t} \tag{2.44}$$

where t is the timeframe of the experiment. For $We < 1$ viscous effects dominate over elastic ones in a fluid whereas for $We > 1$ elastic effects dominate [45].

2.3 Coextrusion hardware and die design

As alluded to in Section 1.2, MLFs are formed via coextrusion when separately extruded polymer melt flows come together in either an injector block linked to a die or a multi-manifold die (MMD) [7–9, 11, 16, 29, 48, 56]. In the injector block approach the separate polymer melt streams come together to form a unified melt structure. This melt composition then enters the die, where it is spread across the die width and then converted into a uniformly thin melt curtain. In an MMD, the polymer melt layers are first spread and retained independently in individual channels *before* coming into contact in the die from which they leave as a uniformly thin melt curtain.

The injector block approach was studied in the 1960's and then patented by Chisholm and Schrenk in 1971 [20]. This type of technology accounts for around 95 % of all flat die coextrusion [8]. Figure 2.8 shows a computational representation of a DTF pilot scale injector block. There are three inlet pipes and the flow direction is from left to right. The melt streams come together in the main part of the heated block to form a unified melt structure. This melt structure then exits the block from the outlet. A die is then used to convert the melt structure into a uniformly thin melt curtain. Die design is discussed later in this Section.

The injector block in standard form (Figure 2.8) is capable of producing either an AB or ABA structured MLF. However, the geometry can be easily modified to produce more complex structures such as an ABC or ABCBA film, representing one of the advantages of this approach. Also an injector block is significantly cheaper than an MMD. Die manufacturers Nordson Extrusion Die Industries (Nordson EDI [65]) and Cloeren [66] both produce injector blocks with varying design features.

The internal injector block features are important to ensure a desirable final film structure. Figure 2.9 shows a two-dimensional (2D) plane section cut through a DTF injector block, as viewed from above. Fins are placed both above and below the secondary channel entrance (see also Figure 2.8) to restrict the flow of the secondary layers and to therefore promote an MLF with clear edges (Figure 1.2). Since the different melt layers are in contact for a long time in the block, clear edges are not always guaranteed. This

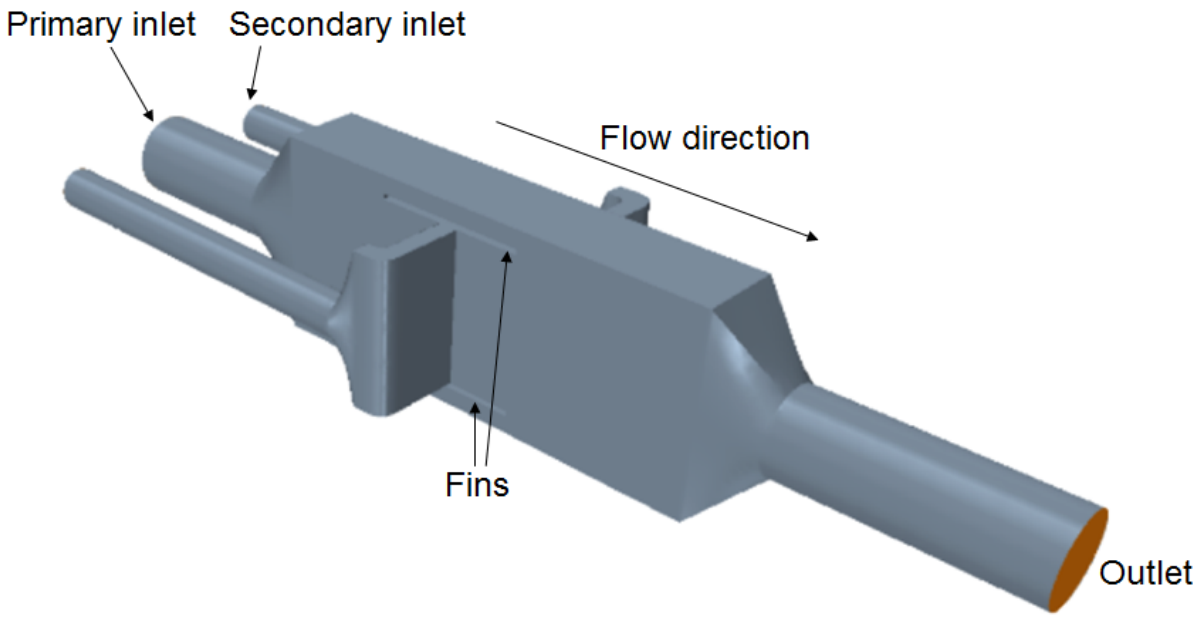

Figure 2.8: A representation of an injector block.

is mainly attributed to too much secondary layer spreading. Cams are installed into the secondary entrance chamber and these alter the inlet port shape to ensure an even spread of the secondary layer(s) across the whole MLF width, allowing for the distortion generated by the end fed die.

The MMD concept effectively acts as a combination of an injector block and a die. An MMD was first used in the 1950's, before the injector block approach [15, 56]. In this system, the different polymer melts are first spread independently across the width of the MMD geometry *before* coming together to form a unified melt structure and again leaving as a uniformly thin melt curtain. The different polymer melt layers are in contact for a much shorter time period in the MMD compared with the injector block. Figure 2.10 shows a representation of a DTF MMD geometry, where the geometry and the internal movement of the fluids within the MMD is displayed. As with the standard injector block approach, the MMD can produce either an AB or ABA MLF. In Figure 2.10 an ABA MLF is produced, with the secondary polymer melt layer (shown in blue) entering the secondary melt channels and being spread across the MMD width. The MMD is used significantly less than the injector block for flat die coextrusion applications.

The choice between an injector block and an MMD for coextrusion purposes depends

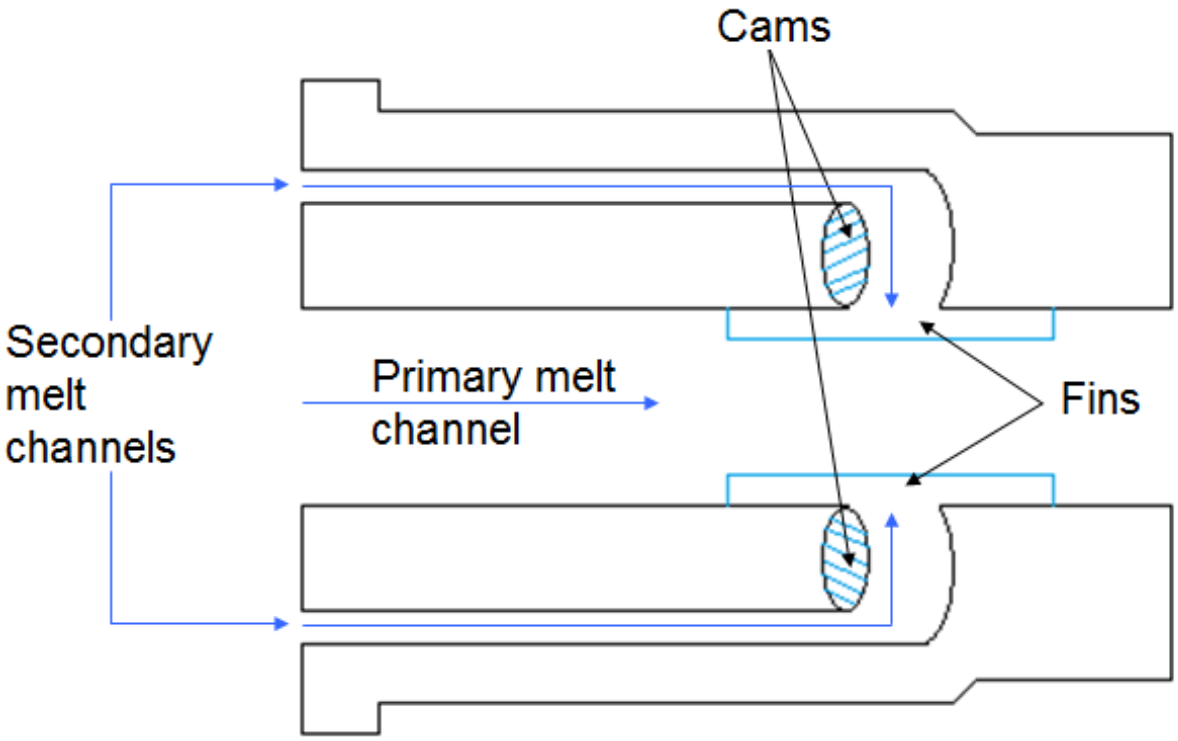

Figure 2.9: The internal features of an injector block. Diagram obtained from the DTF database.

on a number of factors such as: the viscosity ratio between the different polymer melts, the secondary layer thickness and the extrusion temperatures. Since the different polymer melt layers are already spread across the die land and are only in contact for a very short period of time in the MMD, this system can handle a much wider melt viscosity ratio between the different layers than the injector block. The injector block is said to be limited industrially by a melt viscosity ratio of between 2:1 and 4:1 [8, 16]. In Chapter 5, some of the viscosity ratios studied exceed the limit of 4:1 to form the basis of an academic investigation. Also attributed to the separate flow paths taken by the individual melt flows, the MMD is better than the injector block at handling wider mass flow rate ratios, guaranteeing clear edges and effectively controlling the thickness uniformity of individual layers [11, 29, 67].

Conversely the injector block approach is much cheaper and less complex than the MMD [11, 67]. Furthermore, the injector block is more flexible in its ability to produce asymmetric film structures with three or more different layers [9]. The MMD is inflexible

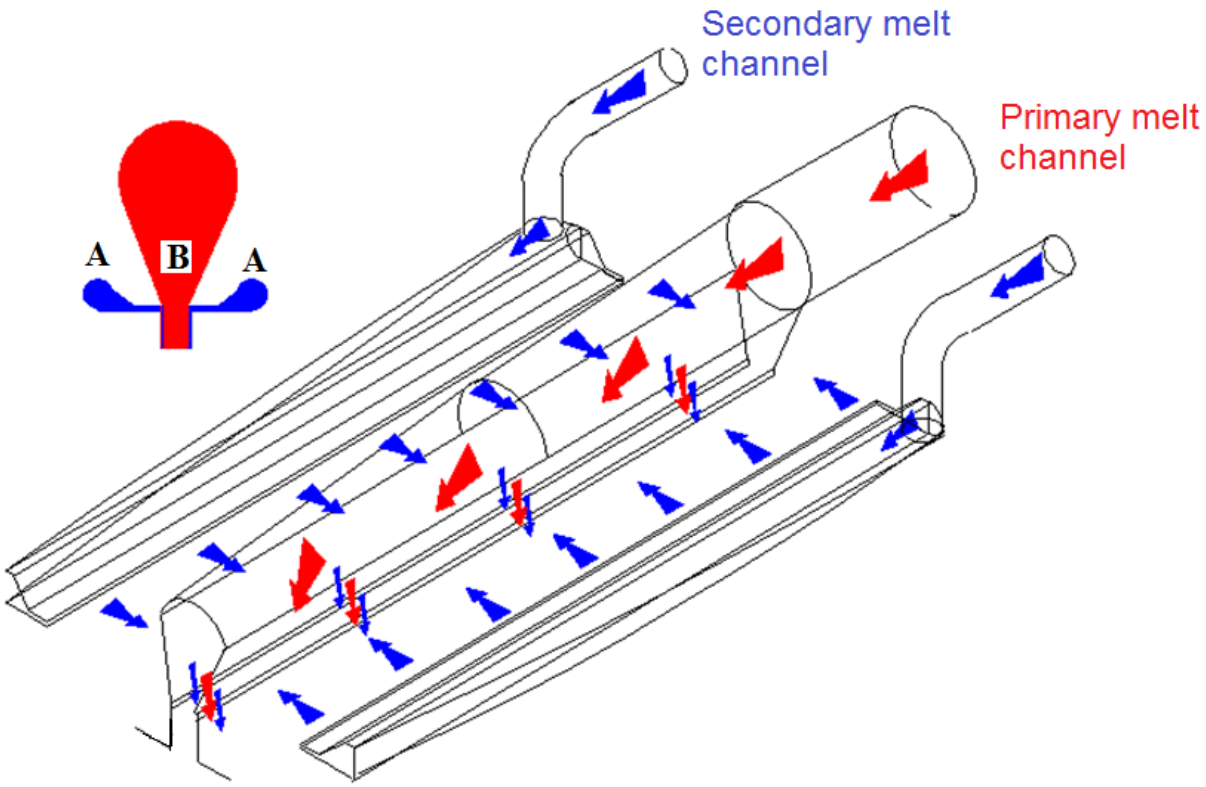

Figure 2.10: A representation of an MMD. Diagram obtained from the DTF database.

in its ability to change the layer sequence of an MLF [67]. The injector block approach is also easily adaptable to most existing film lines and technologies, which is not always the case with the MMD [9]. Table 2.1 summarises the main comparisons between the two coextrusion techniques.

The majority of polymer coextrusion literature uses a modified injector block linked to a die for experimental or modelling purposes. There is little or no literature available showing direct comparisons between the two systems. Work by Champion *et al.* [33] confirms theoretically that an MMD can handle much wider melt viscosity ratios than the injector block system. One of the main project challenges to address was to use CFD to compare the two systems. This work is shown in Chapter 5 for pilot scale geometries. It is possible to combine the two systems to produce film structures with more than three layers such as the ABCBA MLF as shown in Figure 1.2.

An alternative to the traditional injector block and MMD geometries, a *layer multiplication* technique is a way of generating a large number of sub-micron thin layers into a

Table 2.1: Comparisons between the injector block and MMD systems. Information obtained from [8, 9, 11, 16, 29, 67].

Injector block	**Multi-manifold die (MMD)**
Cheap	Expensive
Simple	Complex
Limited to viscosity ratios of 2-4:1	Can handle wide viscosity ratios
Can produce complex structures	Complex structures not easily produced
Inflexible individual mass flow rate ratios	Flexible individual mass flow rate ratios
Adaptable to existing film lines	Not always adaptable
Individual melt temperature limitations	Less temperature limitations
Limited layer uniformity	Good layer uniformity
Clear edges not guaranteed	Clear edges guaranteed

single structure [68]. This approach was patented in 1966 by Tollar of the Dow Chemical company [69]. The layer multiplication approach is a modification of the existing injector block technology and generally involves continually dividing and then recombining an AB structure to produce an ABAB...AB MLF with hundreds of individual layers [8]. DTF in Japan, TDFJ, have published a number of patents where films with 251 alternating layers are produced using a layer multiplication technique [70–72]. Films produced from layer multiplication have increasing applications as packaging films [68]. This is because of the optical differences achieved when producing films with many different layers.

The aim of any die, whether connected to an injector block or used to produce a single layered film, is to convert the incoming melt flow into a uniformly thin melt curtain [31, 47, 54, 73–76]. An ideal die will provide a uniform flow across the whole die exit, achieving this with little pressure drop and streamlining the flow, avoiding any stagnation points. The two main dies used within DTF are the end fed and centre fed dies. End fed dies are used more than centre fed ones within DTF, but centre fed dies are more common for general polymer processing.

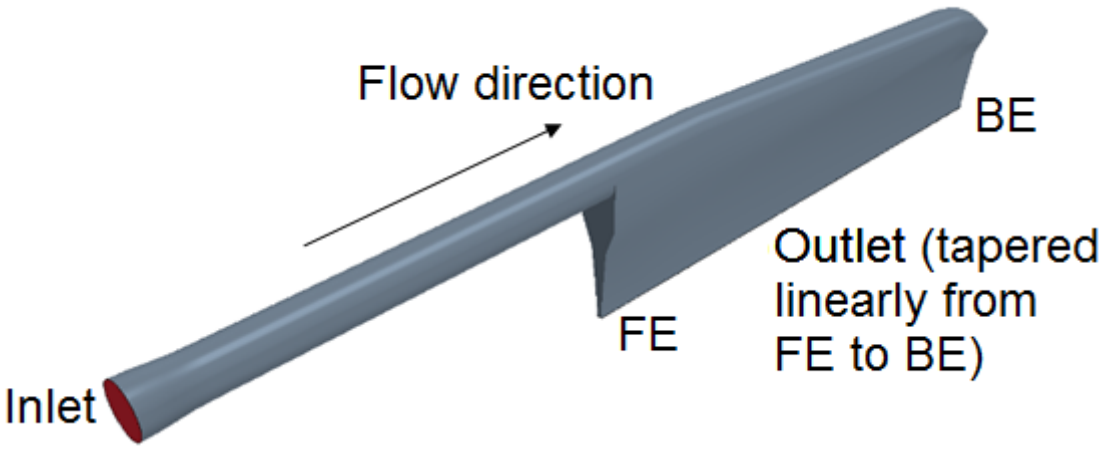

Figure 2.11: A representation of an end fed die.

Figure 2.11 shows a 3D computational representation of an end fed die. A polymer melt structure enters the inlet melt pipe, before entering the main die section at the feed end (FE). The melt then flows through the die and exits as a melt curtain of uniform thickness from the FE to the far end (blank end, BE). For this type of flow to occur there must be a higher pressure at the FE compared with the BE [74]. This makes it easier for material to exit at the FE outlet. To even this out, and to obtain uniform flow, the outlet is tapered *linearly* from FE to BE to produce a higher pressure drop through the FE gap compared to the BE gap, see also Figure 2.12. In an internal, unpublished article, [74], Clifford states that a 1 % variation in the gap will give a 3 % variation in the film profile. The die gap at both the FE and BE will vary depending on the width and scale of the die being used.

Figure 2.12 shows a typical cross section of an end fed die at the FE and BE. The flow area is reduced from FE to BE across the whole die width, allowing for a streamlined melt flow with no stagnation points. The die land is a parallel slot used to deliver a uniform flow out of the die, and the pressure drop and shear rate is at a maximum here. Typically in an end fed die the top half reduces in height and width towards the BE, but the bottom half (the die lips) retain their structure apart from the increasing die land gap.

As well as tapering of the die gap, either heat or local gap changes by forcing bolts can be applied for further final profile improvement [74]. Most end fed dies used by DTF apply

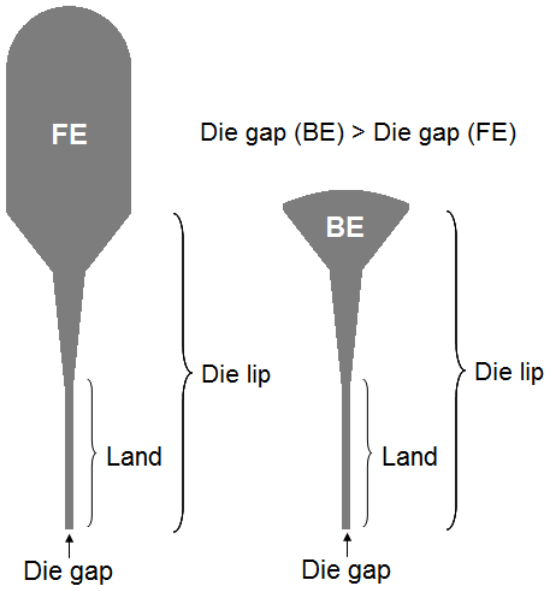

Figure 2.12: The feed end (FE) and blank end (BE) of an end fed die.

heat. This is where heaters are bolted to the internal metalwork of the die land. The heaters (modelled in Chapter 7) are placed a set width apart and span the die width from FE to BE. These heaters are controlled either manually, automatically or a combination of both depending on the die. Increasing the temperature of a heater will cause a localised increase in the film thickness due to a reduction in melt viscosity. A general rule of thumb applied at DTF is that a 1 % change in thickness requires a 5 % increase in heater power.

Centre fed dies are used much more commonly than end fed dies for polymer processing. Also known as coathanger dies, in this geometry the incoming polymer melt flow enters the die centrally before being split equally into two flow paths. Figure 2.13 shows a schematic of a centre fed die, where the red line shows the approximate melt flow path.

The centre fed die is more flexible than the end fed die due to the symmetry of the geometry and therefore requires a smaller taper. However, the centre fed die is more expensive than the end fed technology. A design issue with centre fed dies is that they can sometimes *clamshell* [31, 73]. Clamshelling occurs when the pressure build up in a centre fed die causes the outlet width to be wider in the middle than at the edges, causing an uneven flow distribution.

Typically centre fed dies use force rather than heat for profile control. The Nordson

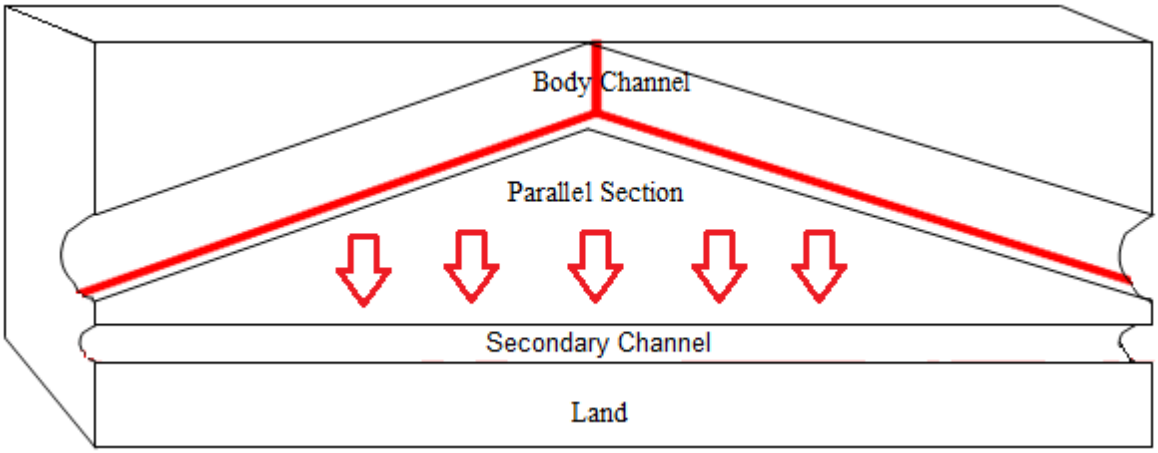

Figure 2.13: A representation of a centre fed die. Diagram obtained from the DTF database.

EDI Autoflex dies have bolts attached to the die land which can be manually tightened or loosened to improve the film profile by changing the local slot width. These bolts also have a thermal aspect to them and are actuated by automatically expanding or contracting depending on the localised film profile.

For a shear thinning polymer melt the pressure drop in a die is an important quantity to monitor to ensure uniform flow at the die exit. The pressure drop is dependent on the polymer melt rheology [54]. The greater the melt viscosity the greater the pressure drop in the die. Polymer rheology must therefore be considered in die design, and the shear thinning nature of most polymer melt flows can lead to further complications [75, 76]. For high shear rate regions such as in the die land, a shear thinning polymer melt will flow with greater ease. However, if the shear rates are not monitored effectively and are too high the polymer may degrade, resulting in a decreased performance.

Due to the geometrical complications of most dies, it is often desirable to use numerical as well as experimental methods for flow analysis in dies. Huang *et al.* [47] used the finite element based CFD package FIDAP to predict the flow behaviour of both high density polyethylene (HDPE) and linear low density polyethylene (LLDPE) melt flows in a centre fed die. The authors found a much more uniform outlet flow for LLDPE compared with that for HDPE. This is attributed to the viscosity of LLDPE being lower at lower shear

rates and being able to fill the whole die. Catherine [54] used 3D CFD to model the velocity distribution of LDPE within a centre fed die. This distribution is shown in Figure 2.14, where a uniform flow is predicted across the whole outlet width.

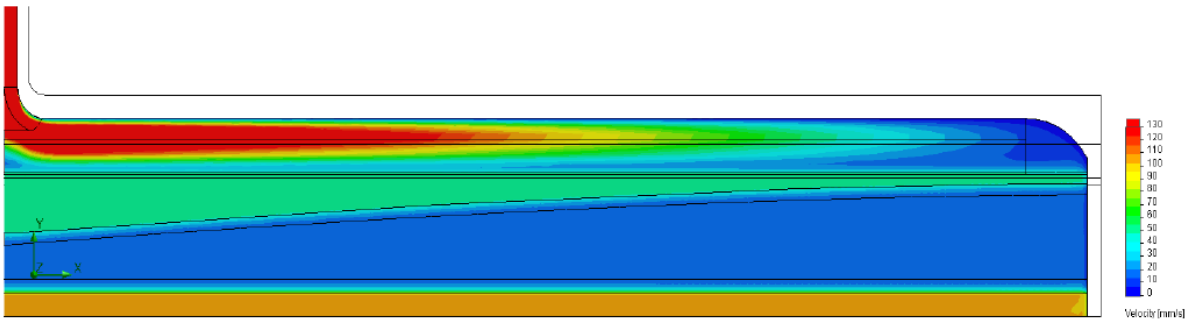

Figure 2.14: The velocity distribution in a centre fed die. Diagram obtained from [54].

Vlcek *et al.* [75] compared the numerically and experimentally predicted outlet flow of a centre fed die. Both the 2D and 3D CFD showed good agreement with each other, but there is poor experimental validation of the CFD data. Kostic and Reifschneider [76], Reifschneider *et al.* [77] and Lee *et al.* [78] used CFD optimisation methods to modify a die design to improve the overall flow uniformity. Most numerical representations of polymer melt flows use the Carreau model or a slight variant of this (see Equation 2.4). Throughout this thesis, CFD is used to predict the flow behaviour within both pilot and production scale DTF dies.

The viscoelastic nature of most polymer melts must also be considered by a die designer. A common phenomenon in polymer processing is the *die swell* (or extrudate swell) of a polymer melt upon exiting the die [14, 35, 76, 79]. Die swell is the enlargement of the melt in the orthogonal direction upon exiting the die; the polymer melt becomes slightly wider than the die outlet width [76]. This swelling can occur in both viscoelastic and Newtonian, low elasticity melts such as PET. Swelling in viscoelastic fluids occurs because of their elastic "memory" which is released as energy or normal stresses upon exiting the die. Newtonian die swell is caused by velocity streamline rearrangement at the die exit [35].

Die swell can lead to processing difficulties further downstream in the film process

and should be controlled as early as possible. Increasing the melt temperature would reduce the polymer viscoelasticity and hence the die swell [14, 80]. Gifford in [81–84] has published a number of findings on the causes and possible solutions of die swell. In [81] the finite element based CFD code DIEFLOW is used to modify the design of die channels to compensate for die swell. In [84] it is shown numerically that die swell decreases with increasing Reynolds number (decreasing viscosity).

2.4 Viscous effects in polymer coextrusion

An ideal MLF (see Figure 1.2) will have good layer thickness control throughout and a linear interface between the different layers. However, this is not always attainable and certain factors can have a negative impact on the final product performance. It has been shown that when polymer melts are flowing as a unified structure, the lower viscosity polymer moves to the geometry walls and flows around the higher viscosity polymer(s), producing a curved final interface [8, 9, 29]. This is because the higher viscosity polymer melt seeks the area of least resistance or shear away from the walls. The higher viscosity material experiences little flow resistance in the middle of the geometry. This curved interfacial phenomenon is also linked with the minimisation of energy (see later).

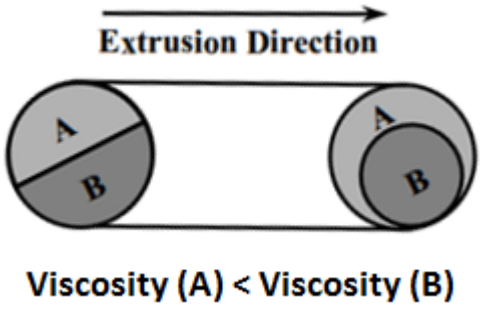

Figure 2.15: A schematic showing interfacial deformation. Diagram obtained from [8].

A curved interface is displayed schematically in Figure 2.15 and this effect is known as *interfacial deformation* or *interfacial curvature*. For large viscosity ratios or wide geometries this can lead to full encapsulation of the lower viscosity melt around the higher viscosity one [8]. Polymer melt viscosity is a function of a number of variables

(see Equation 2.6) which should be considered if interfacial deformation is to be avoided. The effect is more pronounced in an injector block than an MMD. The following Sections contain a review of previous publications on the viscous effects in coextrusion.

2.4.1 Initial developments

Throughout the 1970's, a large amount of research was conducted on the viscous effects in polymer coextrusion. Han [24] studied a number of effects simultaneously during experimental analysis of coextrusion. PS was extruded with both LDPE and HDPE, where η (HDPE) $> \eta$ (PS) $> \eta$ (LDPE) in the shear rate range tested. For approximately equal flow rates in a circular die LDPE curves around PS, forming a concave interface shape. This curvature increases to full encapsulation when one moves further into the die and for increasing LDPE flow rates. Conversely at large flow rates of the more viscous HDPE, Han observes encapsulation of the HDPE around PS. This is the opposite to the general theory of viscous coextrusion and implies that the flow rates are likewise important. It is also found that the die shape can affect interfacial curvature since a circular die gives a much smoother interface than a rectangular one.

In two much cited publications, Southern and Ballman [22, 23] analysed the bicomponent flow of two different PS grades in a capillary rheometer. A dye was applied to one blend for layer visualisation purposes. There is a viscosity crossover at different wall shear rates such that for $\dot{\gamma}_w < 14.9$ s^{-1}, η (PS A) $< \eta$ (PS B) and η (PS B) $< \eta$ (PS A) otherwise. This is shown in Figure 2.16, where at low shear rates and equal flow rates there is interfacial curvature of PS A around PS B. The curvature is reversed for $\dot{\gamma}_w > 14.9$ s^{-1}. This data is obtained at a temperature of 220 °C.

Additional work by Southern and Ballman in [23] at melt temperatures of 240 °C obtained a curtate cycloid interface shape (Figure 2.17) at $\dot{\gamma}_w = 149.5$ s^{-1}. This is where there are multiple regions of interfacial curvature in different flow areas of a single die cross section. Near the walls there is curvature of PS B around PS A and in the middle the curvature direction is reversed. The authors attribute this ambiguous interfacial shape to viscous effects since the viscosity ratio changes from above 1 to less than 1 when moving

towards the middle of the geometry. In more recent publications it is suggested that the curtate cycloid interface shape is due to elastic rather than viscous effects. Southern and Ballman do not present sufficient melt elasticity data to disprove this theory completely. It would have been interesting had they studied a non-isothermal case where each polymer melt entered the geometry at different temperatures, allowing for thermal analysis.

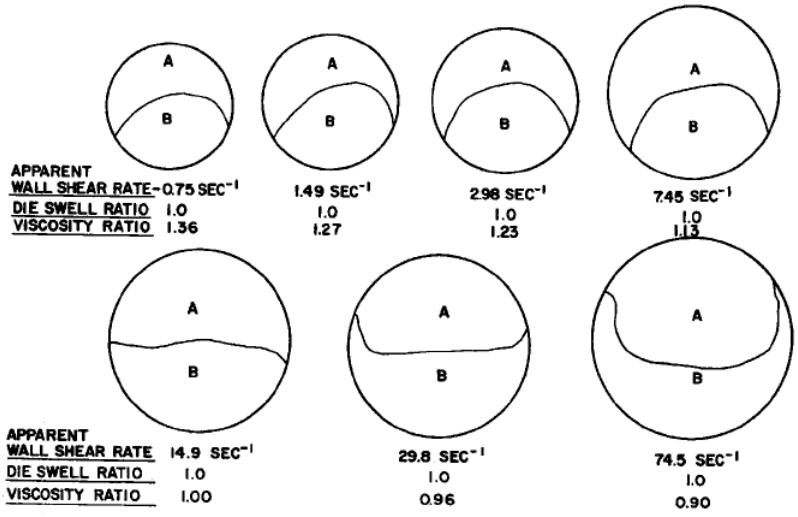

Figure 2.16: Interfacial shapes of two coextruded PS blends at different wall shear rates. Diagram obtained from [22].

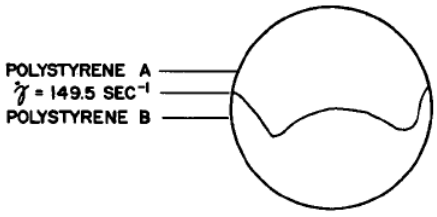

Figure 2.17: A curtate cycloid interface shape. Diagram obtained from [23].

Both Lee and White [25] and Minagawa and White [85] use similar experimental approaches to Southern and Ballman to investigate polymer coextrusion. In both cases there was agreement with the general consensus in that it was found that interfacial deformation occurs when the least viscous polymer melt layer migrates to the geometry walls and bends around the more viscous melt layer. This bending has a negative impact on the final film product and was found to increase with increasing viscosity ratios and

as one moves further into the die (the length/diameter or L/D ratio increases). Curtate cycloid interfaces are found in both [25] and [85] and again attributed to viscous rather than elastic effects.

Southern and Ballman [22], Han [24] and Lee and White [25] present a small section of elastic as well as viscous effects in their analysis. The elasticity investigations are based on either the normal stress differences or the storage modulus of various polymers. In each case it is found that independent of the relative elasticity ratios between the different melt layers, it is always the least viscous melt which bends around the more viscous one. This shows that the polymer melt viscosity ratio, rather than the elasticity ratio, is the primary cause of interfacial curvature.

Based on the previous work presented above it is widely accepted that viscous effects are mainly responsible for interfacial deformation and eventually full encapsulation of the lower viscosity melt round the more viscous one. In [86–88] theoretical analyses, based on an energy interpretation and energetically preferred configurations, are presented. MacLean [86] studied planar layered flow of two materials. Comparisons between a configuration with one fluid on top of the other in a half and half configuration and full encapsulation were made. Everage Jr [87] and to a lesser extent Williams [88] extended this to theoretically compare slight interfacial deformation with full encapsulation.

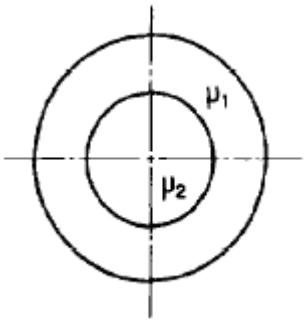

Figure 2.18: Full encapsulation of a lower viscosity polymer melt (η_1) round a higher viscosity one (η_2). Diagram obtained from [87].

In all three cases it is found that full encapsulation, or the sheath core configuration (Figure 2.18), is the most energetically preferred as it has the lowest energy loss overall.

In [88] it is also shown theoretically that encapsulation of the lower viscosity melt round the more viscous one is more energetically efficient than the reverse structure. The work in all three publications outlines why two polymer melts of different viscosities evolve towards full encapsulation. All three publications, while useful, only show simplified viscosity analyses in model geometries and neglect elastic effects.

2.4.2 Further findings

Whilst initial work on viscous effects within polymer coextrusion was mainly of an experimental and theoretical nature, more recent publications have focused on experimental and numerical approaches. Dooley [8] and Dooley and Rudolph [89] experimentally analysed the flow of two polymer melts through a model injector block and die system. The experimental method employed in [8,89] is of interest to the author (see Chapter 6). Here the primary polymer layer is dyed using carbon black, allowing for easy visualisation of the frozen polymer die plug when the die is rapidly cooled.

In [8,89] the same interfacial deformation as detailed in Section 2.4.1 was found. This curvature increased with both increasing viscosity ratios and increasing L/D ratios, eventually leading to full encapsulation. Furthermore, the ambiguous reverse encapsulation as found by Han in [24] is not found at similar flow rates in [8] and other publications, with Borzacchiello *et al.* [90] attributing this to elastic rather than solely viscous effects. In [8], a numerical approach is used to compare with elastic interfacial effects, but not with solely viscous ones, giving the thesis an incomplete feel.

Dooley [43,91] and Dooley *et al.* [92] used a very novel experimental method to measure the rheology of coextruded structures. An experiment was designed, allowing for the rheology of fully encapsulated melt structures to be measured. This multilayer rheology was then compared with the individual melt phases making up the composition, based on their shear thinning behaviour. Either PE or LDPE resins were used, and a similar visualisation method to that in [8] maintained throughout.

A main finding was that the rheology of the fully encapsulated form was similar to the skin layer rheology and this did not change even in four layered structures, as shown

in [92]. This finding was observed because in fully encapsulated form only the skin layer is at the walls and the shear rate is highest here. This explains why changing the skin layer thickness does not alter either the pressure drop or the edge thickness profile during extrusion. The approach in [43,91,92] is of interest due to its unique experimental method, however, it is of little relevance industrially since full encapsulation is rare and only occurs after $100D$ under standard conditions [28], where D is a pipe diameter. It would have been useful had the authors measured the rheology of a structure with slight interfacial deformation and compared this with full encapsulation.

With the increase in computer power and software packages available, numerical methods have been used since the 1980's to study polymer coextrusion. Such techniques are used either as standalone work or in conjunction with experimental evidence. For a full representation of the coextrusion process, one must model large 3D geometries and solve the governing non-linear equations of fluid flow. There are, therefore, a lot of factors one must consider before performing such investigations.

Sornberger *et al.* [93] used a simplified iterative finite difference approach to model polymer coextrusion. Two 2D die geometries were modelled after linking to an injector block: a centre fed die and a slight variant of this. The authors show that viscosity based interfacial curvature occurs and is mainly apparent in the main part of the die geometry, not the die lips. The authors also show good agreement between numerical and experimental work. However, the model is of a simplified nature and is unable to represent full encapsulation.

Unidirectional, 2D coextrusion was modelled by Karagiannis *et al.* in [94]. A finite element, evolving mesh method was used. As expected, it was found that interfacial curvature increases with both increasing viscosity ratios and increasing the flow rate of the less viscous fluid. Full encapsulation was found numerically for large viscosity ratios. 3D studies investigating the viscosity and flow rate ratios were conducted by Gifford in [95]. Similar results to those in [94] were found, although full encapsulation was not predicted. Experimental validation was not used in either publication, making one question the validity of the presented results.

The majority of numerical coextrusion investigations use a finite element CFD technique. A problem with such modelling is in the discontinuity of the viscous stress and pressure at the interface [58]. Mavridis *et al.* [96] and Karagiannis *et al.* [58] investigated this problem by having nodes either side of the interface that the pressure and velocity are solved on. This is known as the *double node method* and is shown in Figure 2.19. Both publications apply 3D finite element modelling to simplified injector block geometries. In each case there is good *qualitative*, but poor *quantitative* agreements with the experimental results from Southern and Ballman in [22, 23].

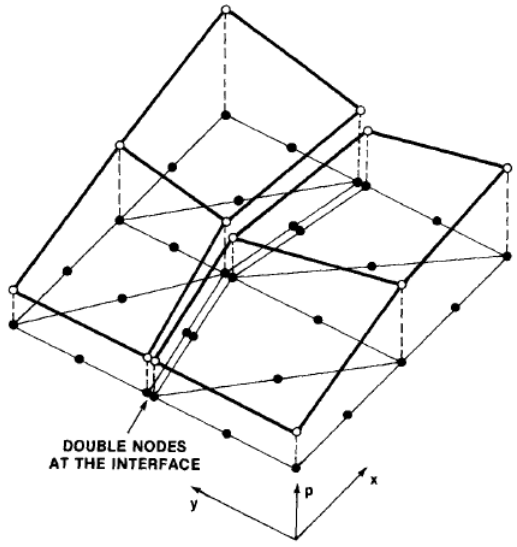

Figure 2.19: A double node numerical approach. Diagram obtained from [96].

One of the suggested reasons in [58] for the slightly ambiguous numerical and experimental correlation is the numerical treatment of *contact lines*. A fluid/fluid/solid contact line is defined as a region between the interface and the wall [58,97]. In finite element simulations, a no-slip condition for contact lines can give an unrealistic multivalued velocity. Also, there is infinite pressure at the three phase contact point since the no-slip condition cannot hold if this contact point is moving. Karagiannis *et al.* [58] used a slight variant of the no-slip contact line. Torres *et al.* [97] extended this to introduce a slip condition (non-zero wall velocity) for the contact line. Although it showed an improvement on the predicted interfacial curvature compared with the no-slip condition there was still not exact agreement with the results in [22, 23].

The main quantitative disagreement between the experimental results in [22, 23] and the numerical results in [58, 96, 97] is that none of the three publications produced the experimentally observed curtate cycloid interface (see Figure 2.17). This is despite replication of the exact *viscous* polymer properties used by Southern and Ballman. Yue *et al.* [28] and Borzacchiello *et al.* [90] fully produced the curtate cycloid interface shape using finite element modelling. Unlike in previous attempts, these publications incorporated elastic effects into their modelling and therefore suggested that elastic and not viscous effects cause the curtate cycloid interface. The author is inclined to agree with Yue *et al.* and Borzacchiello *et al.* because these publications analyse both elastic and viscous effects simultaneously and modern numerical methods are used. Further contact line investigations for viscous properties would be a useful reference.

The above publications looking at numerical viscous effects are only based on isothermal modelling, *i.e.* a single shear thinning viscosity curve is inputted for a polymer melt at constant temperature. Both Sunwoo *et al.* [62] and Mallens and Waringa [37] implemented temperature effects into their finite element models. In [62] it is shown that both viscous heating and changing a fluid's temperature (and hence viscosity) can impact the final interfacial profile by changing the viscosity ratio. PET melts and slight variants in an ABA structure are modelled in [37], implying a relevant publication for the author. It is shown numerically that matching the viscosity via temperature will have a positive impact on the final interfacial configuration. Mallens and Waringa also confirm that PET behaves in a Newtonian, inelastic manner.

Full encapsulation has never been recreated in a full numerical 3D simulation. As with the previous publications mentioned, Gupta [49,50,98] produced interfacial curvature, but less than that experimentally predicted and without encapsulation. The lack of numerical encapsulation in the literature may be due to the wall conditions used, or alternatively finer, movable meshes may also produce full encapsulation. Finite volume modelling, as used by the author, should not have the problematic contact line and pressure issues. This is because mass is conserved at every mesh cell including interfacial ones with the finite volume approach.

Interfacial deformation can have a detrimental effect on the final film properties [10]. To reduce this and produce a desired linear interface either the different polymer melt viscosities should be similar or modifications to existing geometries can be made [9]. A method of viscosity matching of polymer melts is to change the temperature of one of the melts to get similar viscosities at the shear rates of interest. It is also advisable to coextrude polymers with similar viscosity-shear rate gradients so that viscosity matching is possible in all regions of the coextrusion hardware [31, 73].

Rijksen *et al.* [99] demonstrated a Dow based internal software that allows one to predict the compatibility of different polymers through an injector block geometry. The model allows the user to input known viscosity-shear rate curves for different melts and then predict the comparative viscosities at different parts of the geometry. The assumption of a maximum 3:1 viscosity ratio for an injector block is maintained. Although useful from an industrial perspective, the model is simplified and lacking any technical validation or experimental evidence. Also the viscosity of PET is considered shear rate independent so the model would not be especially useful within DTF.

If viscosity matching is not possible or undesirable for the final product, geometrical modifications may be required. An obvious method is to use an MMD rather than an injector block so that wider melt viscosity ratios are possible. However, this is a more expensive approach and changes can be made to the injector block system, and in particular to the primary channel geometry (feedslot) [8, 9, 30, 35]. In a process where the lower viscosity skin layers curve round the core layer, the feedslot geometry could be widened at the edges to promote more flow here of the core layer (Figure 2.20). Conversely if the curvature was reversed, the injector block feedslot could be narrowed at the edges. Within DTF cams are installed to adjust the side port geometry to promote a better spreading of the secondary layer and attain a linear interface.

Rincon *et al.* [48] and Dooley *et al.* [46] used a combination of finite element CFD and experimental methods to show that geometrical modifications can improve the overall MLF structure. In [48] it is shown that both the secondary layer and final film profile can be ameliorated with adjustments made to the secondary layer ports. In [46] different

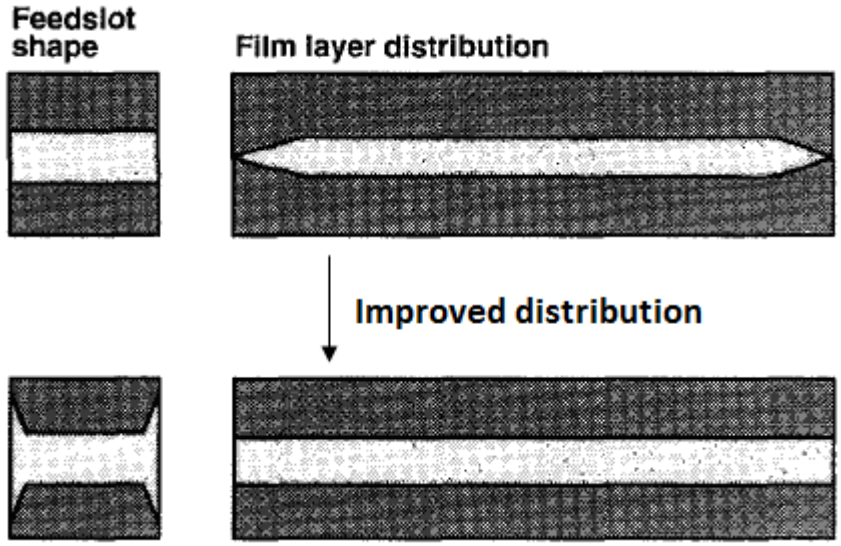

Figure 2.20: Improving the final film structure using geometrical modifications. Diagram obtained from [30].

centre fed die manifolds are compared when producing a PS based ABA structure. It is found that the spreading of the secondary layer improves with the use of symmetric distribution manifolds compared with asymmetric ones. Both publications use the experimental approach of die plug analysis, similar to the technique used by Dooley [8] and Dooley and Rudolph [89].

Throughout this thesis, viscous, inelastic polymers are modelled in DTF coextrusion geometries. The polymer viscosity is assumed to be either constant or temperature dependent. In Chapter 5, constant viscosities are used and the comparative ability of both an injector block and an MMD to handle wide viscosity ratios is analysed. Chapters 6 and 7 show temperature dependent polymer viscosities, based on Equation 2.8, assigned for melt flows through both pilot and production scale geometries. This thermoviscous analysis at a constant shear rate is a novel approach to model polymer melt flows.

2.5 Elastic effects in polymer coextrusion

As shown in Section 2.4, interfacial deformation is primarily caused by viscous rather than elastic effects. However, non-steady state elastic phenomena can influence the final

interface shape in a different way as demonstrated by Yue *et al.* in [28]. Elastic effects, and in particular normal stress differences between different polymer melts (see Section 2.1.2), have been shown to cause *interfacial instability* [8–10,100]. PET melts are Newtonian and inelastic in rheology and therefore the author's work does not use any numerical elastic approaches. This Section contains a brief overview of elastic effects.

Interfacial instability occurs when the interface takes the form of either a *wave* or a *zigzag* and spans the entire film width [8–10, 29, 30, 35, 44]. Wave type instabilities (see Figure 2.21) are low frequency, high amplitude perturbations, and form when the polymer melt flows first come into contact. Zigzag instabilities are high frequency, low amplitude perturbations, forming further into the process in the die land. These time dependent features are believed to be caused by the elastic based primary, N_1, or secondary, N_2, normal stress differences, with N_2 believed to have more of an effect [90].

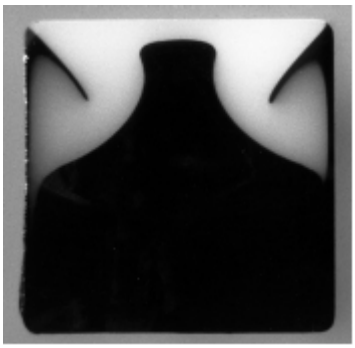

Figure 2.21: A wave type interfacial effect. Diagram obtained from [8].

Interfacial instability will have a detrimental effect on the final MLF properties and should be avoided or reduced as much as possible. Less is known about these effects compared with viscous ones. The wave type interfacial structure occurs when polymer melts merge with vastly different velocities [35]. This can be improved by reducing the extensional viscosity ratio (see Section 2.1.1) or using a symmetric geometry [101, 102]. The more common zigzag defects are caused when the interfacial shear stress is too high in the die land. This can be remedied by reducing this shear stress using methods such as increasing the outlet die gap, reducing the skin layer viscosity, increasing the skin layer thickness and decreasing the overall extrusion rate [9, 30, 35].

PET melts do not exhibit these type of elastic effects and these are generally not considered important by the author nor DTF. Some of the earliest publications on interfacial instability are by Han and Shetty in [26] and Schrenk *et al.* in [27]. For a more detailed study of previous work on elastic instabilities than that presented here, the reader is directed towards these publications as well as work by Dooley and co-workers [8, 13, 28, 59], Martyn *et al.* [10], Zatloukal *et al.* [17, 18, 100, 101, 103] and Borzacchiello *et al* [90].

2.6 Chapter conclusions

This Chapter has contained a literature review of polymer coextrusion and associated issues. Polymer coextrusion is a cost effective process that allows the properties of different polymer blends to be combined into a single product. There are a number of issues associated with polymer coextrusion and the final interface structure that should be avoided. Of particular relevance is the viscosity based interfacial deformation, which has been studied since the 1970's. To reduce this, either the polymer viscosities should be better matched or geometrical modifications made. Work is still ongoing in this field for more understanding. This work should focus on the modelling and consequent experimental validation of more complex geometries at a wider range of processing conditions, and further attempts at recreating full encapsulation on a 3D geometry.

As alluded to in this Chapter, there are a number of project challenges that need addressing. These include:

- *The creation of coextrusion geometries representative of DTF hardware.* The design of the geometrical domain being solved is the first stage of any CFD process. Geometries representing DTF hardware were created and edited using STAR-CCM+'s inbuilt computer-aided design package. Engineering drawings were scrutinised and formed the basis of the geometry creation.

- *The capturing and tracking of the polymer-polymer interface.* When modelling a situation involving different phases, the accurate interfacial capturing and representation is important. The volume of fluid (VOF) method was used throughout this

thesis for this purpose when modelling polymer melt flows. This is a novel approach to model polymer coextrusion. The VOF method is an efficient solver, but relies on a fine mesh to give a sharp interface (see Section 3.2.1.3). Further details of the VOF method and other numerical and experimental methods used are shown in Chapter 3.

- *Comparisons between an injector block and an MMD.* Although much is already known about the relative benefits of both coextrusion systems, CFD is used to give further information on this and confirm what is already known. Chapter 5 and to a lesser extent [33] shows modelling comparisons made on a pilot scale based on increasing viscosity ratios.

- *Industrial scale-up.* The coextrusion geometries shown in this thesis are primarily of a pilot scale. DTF have worldwide production scale operations and modelling of such geometries is imperative to further assist their understanding of the coextrusion process. Production scale geometries were created and modelled on, with the results compared with pilot scale ones. The production scale geometries were created based on engineering drawings. Results based on a production scale MMD are shown in Chapter 7.

- *Experimental validations.* Some form of experimental appreciation is required to complement and compare with CFD modelling results. The experimental methods used in this thesis includes light microscopy, die plug analysis, chloroform washing and white light interferometry (WLI). The latter two techniques are novel when analysing polymer based MLFs. Section 3.2.2 shows more detailed theory and operation technique behind each method used and Chapter 6 shows some experimental results.

- *Thermoviscous modelling.* Since PET melt viscosities are independent of shear rate but dependent on temperature, a form of thermoviscous representation was required for realistic interpretation. The O'Dell model (Equation 2.8) was assigned to different polymer melt flows. Also a variable temperature profile across the die

land width was created to represent a full set of die bolt heaters at different powers. Chapters 6 and 7 show temperature dependent viscosities investigated and Chapter 7 shows die bolt heaters on both pilot and production scale geometries.

Chapter 3

Materials and Methods

3.1 Materials

Both numerical and to a lesser extent experimental methods have been applied in this thesis. For numerical investigations, the finite volume based CFD software STAR-CCM+ was used on a 32GB Dell Precision T7500 Westmere workstation. CD-adapco's STAR-CCM+ was chosen after testing the software on a months' trial. During this trial period, a number of base cases representative of the coextrusion process were solved numerically. Improved accuracy and efficiency was observed when comparing the STAR-CCM+ results with those from other CFD packages. Furthermore, STAR-CCM+ was found to be very user friendly; it offers an "all in one" capability where every aspect of a CFD simulation can be conducted in a single file.

Light microscopy on cast (unstretched) film samples, die plug analysis on a polymer heel obtained after freezing an end fed die, chloroform washing on both cast and final (biaxially oriented) film samples and white light interferometry (WLI) and reflectometry on final film samples were attempted for experimental validations. For light microscopy a Leica DMR microscope [104] was used. A Veeco NT9800, operating in vertical shifting interferometry mode, gave a secondary layer thickness profile across the whole film width when using WLI. A more detailed description of the numerical and experimental methods used is shown in Section 3.2.

3.2 Methods

3.2.1 Numerical methods

This Section contains an overview of some of the theoretical CFD methods applied by the author. Meshing schemes as well as techniques to discretise the governing numerical equations are covered. The volume of fluid (VOF) method is used to capture and track the interface between different polymer melt flows and is reviewed alongside other interfacial capturing techniques here.

CFD is a numerical technique used to solve the Navier-Stokes equations governing fluid flow problems. The equations associated with fluid dynamics are non-linear and heavily coupled with very few analytical solutions. This introduces the need for a numerical solver. To give an outline of the general associated method, CFD discretises a continuous geometrical domain so that the approximated algebraic equations are solved at every mesh cell [105, 106]. CFD can be used in industry to optimise design and vastly reduce experimental time. However, it should not be seen as a complete replacement for experimental work and validation is usually required. Since CFD provides approximate solutions there is always an error between numerical and actual solutions. It requires knowledge and skill by the practitioner to be aware when this is likely to be significant.

As outlined in the STAR-CCM+ training guide [107] and experienced by the author, the general stages of a CFD simulation from start to finish are: design or import of a 3D geometry, repairing this geometry surface, implementing the boundary conditions, meshing the geometry, setting up the physics and post processing properties, running the simulation and remeshing to get a mesh and timestep independent solution. The geometry to be solved on will be made as relevant as possible to the real process equipment, based on actual drawings. Usually different geometrical parts are set as corresponding boundaries such as mass flow inlet, pressure outlet or wall to relate to the physical occurrence at this point. These are available within STAR-CCM+.

3.2.1.1 Meshing and solution scheme

During mesh generation, the different boundary conditions are taken into account and the mesh type may differ at individual sections. The physics set up involves defining the conditions for both the fluid and the geometry, and selecting particular solvers - for example laminar and multiphase flow.

Volume meshing in CFD can be very time consuming. This process involves covering the chosen geometry with a grid that the discretised algebraic equations are solved on. There are three main types of mesh system (Ferziger and Perić [105]): the structured, block-structured and unstructured meshes. In a structured (or regular) mesh, each cell has exactly six neighbours in 3D and consecutive numbering is possible. The mesh is equivalent to a Cartesian one. A block-structured mesh contains various subdivisions between coarse and fine layers. A chimera mesh is one with an overlap between different regions. Such chimera grids are useful when solving problems with multiple or moving parts. In the block-structured approach, regions of importance are covered with a fine mesh to resolve the flow complexity better.

For complex geometries, unstructured meshes are appropriate since these can be wrapped around any geometry type. An unstructured mesh can have any shape and any number of neighbouring nodes. The use of such unstructured meshes increases the non-linearity of the generated algebraic equations and the time taken to solve them. In most modern industrial cases, however, an unstructured, non-orthogonal mesh is required due to the non-Cartesian nature of the geometries.

When meshing geometries it is important to use a suitable mesh to give a relevant, accurate final solution. This can be observed in the author's simulations where different sized meshes are inputted depending on the importance of the solution at a particular section of the geometry. A very fine mesh will lead to an increase in the accuracy of the numerical solution, due to an increase in the number of equations to be solved on the whole geometry. A fine mesh is especially required when capturing the interface between two different fluids. However, simulations with a fine mesh will take a long time to fully converge, particularly on a standard computer. In CFD it is often required to find a

compromise between time and accuracy. STAR-CCM+ is based on the finite volume method to discretise equations and has three main unstructured meshing models. These are the tetrahedral, polyhedral and *trimmer* meshes.

A prism layer mesh (orthogonal layers of prismatic cells next to wall boundaries [108]) can be used along with any of these core mesh models to model heat transfer effectively in non-isothermal simulations. A new feature in the latest version of STAR-CCM+ is the overset meshing option. Here certain parts of the mesh can move within the whole mesh depending on where the important parts of the solution are. The trimmer mesh is used throughout this thesis. This is based on a template mesh from hexahedral cells, which are trimmed to fit the starting surface. Figure 3.1 shows a typical trimmer mesh, as produced by the author. Even though most of the mesh appears structured, there are certain regions where one mesh cell has more than six nearest neighbours in 3D. The mesh is finer towards the geometry outlet (shown in orange) to obtain a smooth interface between different polymer melt layers once they have come into contact.

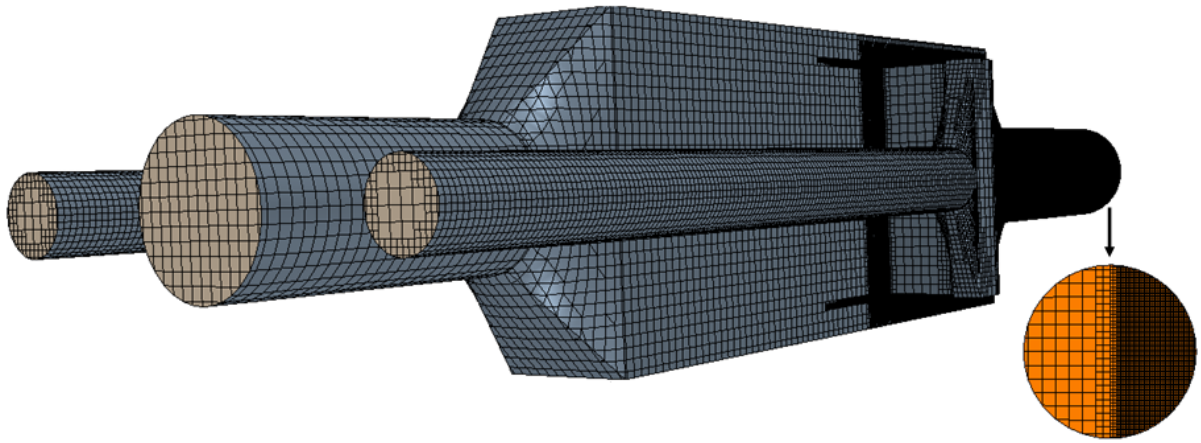

Figure 3.1: A typical trimmer mesh in STAR-CCM+.

For the two 410 mm wide die geometries modelled in Chapter 5, Figure 3.2 shows the velocity magnitude across the outlet die gap at 205 mm for the end fed die (Figure 3.2a) and the MMD (Figure 3.2b), for three different primary:secondary melt viscosity ratios. In each graph, parabolic velocity profiles are observed across the die outlet, and any skew from the standard parabola is caused by increasingly viscous secondary layers. Figure 3.2

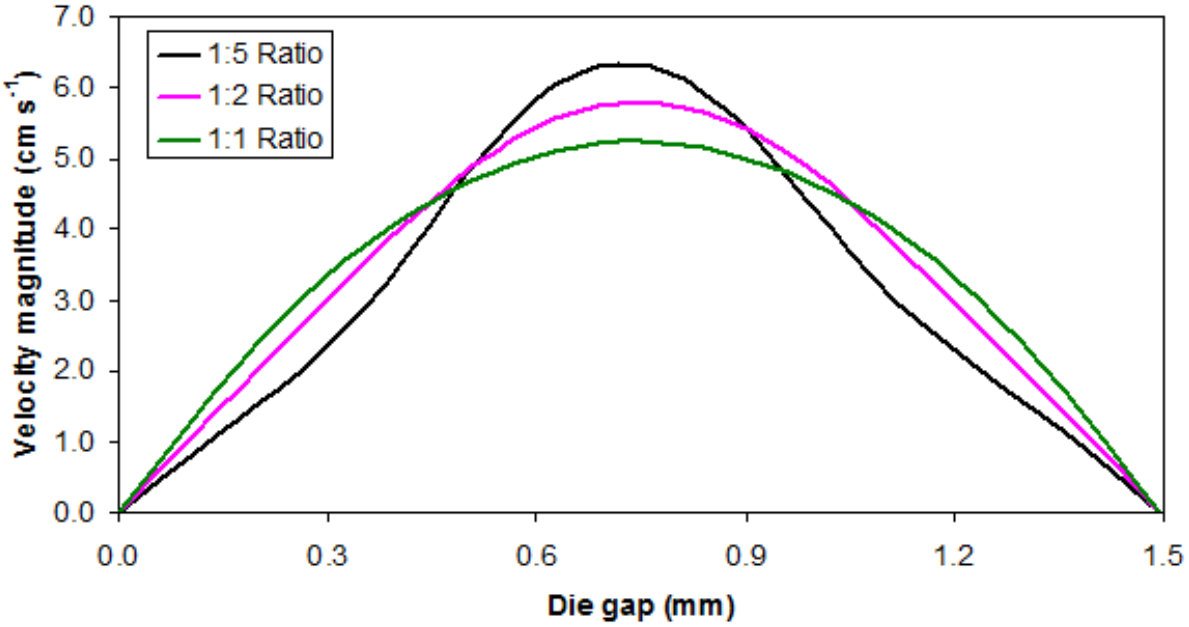

(a)

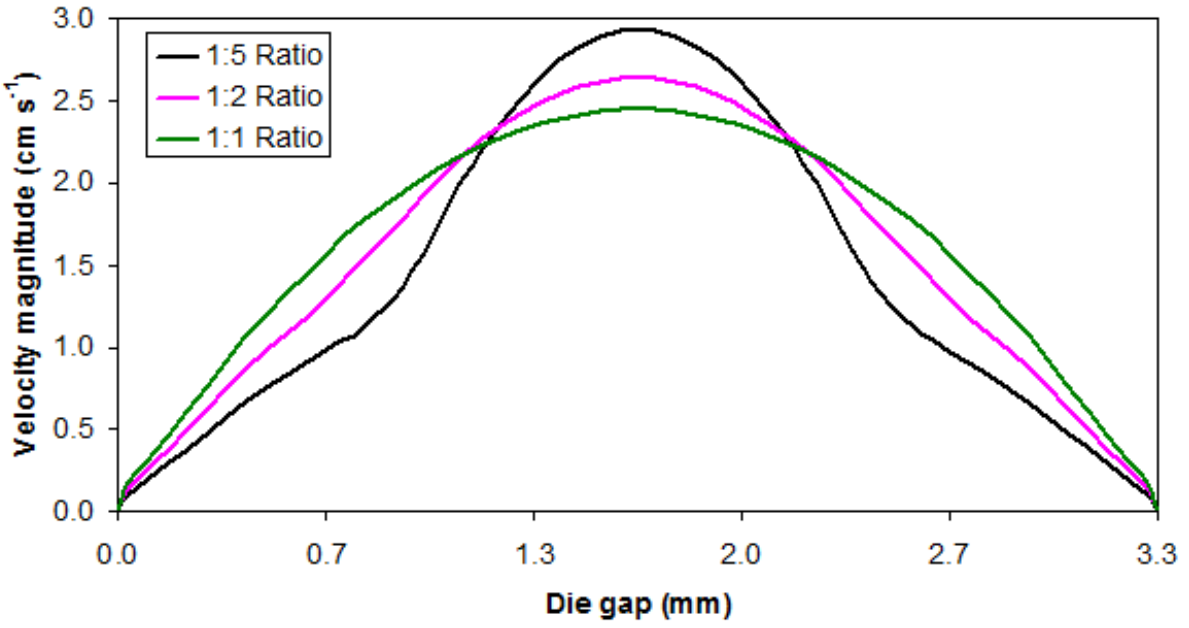

(b)

Figure 3.2: Velocity magnitude plots across the middle of the outlet die gap for three different primary:secondary melt viscosity ratios for (a) the end fed die and (b) the MMD. Both die geometries are modelled in Chapter 5.

shows that the mesh is sufficiently fine across both outlet die gaps to capture thin secondary layers accurately. Such parabolic outlet velocity profiles are obtained throughout.

STAR-CCM+ uses an *iterative* scheme; the discretised governing equations are solved at every single mesh cell in a single iteration. Depending on whether the solution scheme is transient or steady state, an iteration can be set as equivalent to a particular value in time (timestep). For the purpose of this project, polymer melt flows are believed to exhibit steady state behaviour, however, the author uses implicit unsteady physics as a solver with typically 20 inner iterations for a one second timestep. This is to accommodate the VOF method, used to capture and track polymer interfaces. Other physics used includes: laminar flow (an assumption of $Re \ll 1$), Eulerian multiphase, segregated (or uncoupled) multiphase temperature and multiphase equation of state. Even in an uncoupled simulation, there is coupling through the viscosity of different fluids within a single geometry. This is particularly observed when different fluids share the same mesh cell.

3.2.1.2 Governing numerical equations

The five governing equations for any CFD simulation are the three momentum conservation, mass conservation and energy equations [105]. Since the author's simulations are based on a two fluid problem for polymer melts labelled Melts 1 and 2, the VOF equation is implemented alongside these five equations. The VOF equation is solved for the *volume fraction* of Melt 1 (the proportion of Melt 1 in every mesh cell). The combined volume fraction of Melts 1 and 2 is equal to 1 in each cell.

The x, y and z momentum conservation equations (*Navier-Stokes*) in volume integral (Ω) form are given as [105]:

$$\frac{\partial}{\partial t}\int_{\Omega}\rho u_i\,d\Omega + \int_{\Omega}\frac{\partial(\rho u_j u_i)}{\partial x_j}\,d\Omega = \int_{\Omega}\frac{\partial \underline{\Pi}_{ij}}{\partial x_j}\,d\Omega - \int_{\Omega}\frac{\partial p}{\partial x_i}\,d\Omega + \int_{\Omega}\rho g_i\,d\Omega, \tag{3.1}$$

and in differential form:

$$\frac{\partial(\rho u_i)}{\partial t} + \frac{\partial(\rho u_j u_i)}{\partial x_j} = \frac{\partial \underline{\Pi}_{ij}}{\partial x_j} - \frac{\partial p}{\partial x_i} + \rho g_i. \tag{3.2}$$

Equations 3.1 and 3.2 assume that the gravity is the only body force and correspond to three separate momentum equations; one for each velocity component in 3D. It is the

velocity components u_i that are solved in CFD with all other quantities either assumed known (gravity g and density ρ for example) or defined separately (the pressure p). The remaining terms in Equations 3.1 and 3.2 are defined in Chapter 2.

The mass conservation equation is given in volume integral form as:

$$\frac{\partial}{\partial t}\int_{\Omega}\rho\, d\Omega + \int_{\Omega}\frac{\partial(\rho u_i)}{\partial x_i}\, d\Omega = 0. \tag{3.3}$$

Equations 3.1 and 3.3 are the governing equations for any fluid flow problem; when they are coupled together they allow a solution for p to be found computationally. For constant density (incompressible) flows, Equation 3.3 can be written in differential form as:

$$\frac{\partial u_i}{\partial x_i} = 0. \tag{3.4}$$

Equation 3.4 is used for polyester melts as they are assumed to have constant density independent of temperature.

Wesseling in [109] gives the governing energy equation as:

$$\int_{\Omega}\left\{\frac{\partial(\rho E)}{\partial t} + \frac{\partial(\rho u_i E)}{\partial x_i}\right\} d\Omega = \int_{\Omega}\left\{\frac{\partial(u_i \underline{\Pi}_{ij})}{\partial x_j} + \frac{\partial(\kappa \partial T/\partial x_i)}{\partial x_i} + \rho u_i f_i^{\mathrm{b}} + pq\right\} d\Omega, \tag{3.5}$$

where E is the energy term, κ is the fluid thermal conductivity, f^{b} is a body force and q is a source term. The presence of the viscous stress tensor $\underline{\Pi}_{ij}$ in Equation 3.5 implies that even in an isothermal problem the temperature may increase due to friction or shearing.

3.2.1.3 The volume of fluid method and other interfacial capturing schemes

There are many industrially relevant problems that involve a free surface between two fluids. In the most prominent multiphase case, the two fluids are water and air [105]. However, a free surface or *interface* is also observed between two liquids such as polymer melts. Numerical computation of an interface requires further physics and an additional equation to be solved alongside the five governing equations. In particular an iterative method is required to numerically obtain an interfacial shape.

The methods used for computational interfacial generation can be split into two main categories: (i) interfacial tracking and (ii) interfacial capturing such as the VOF technique

[12, 105, 110–112]. For any scheme in (i), the mesh moves with the interface after every timestep or iteration, tracking the interfacial movement. In (ii), scalars are advected to approximate the interfacial position. This is performed on a *fixed* grid and the final interface is found by computing the advection of any interfacial mesh cells. This Section discusses the VOF method (as used in this thesis) and other interfacial capturing schemes.

First published by Hirt and Nichols in [12], the VOF method has a wide range of applications including jet breakup, the motion of large bubbles in a liquid and for interfacial capturing of polymer-polymer interfaces in the author's case. The general approach to solving VOF based problems is as follows: initially every mesh cell is assigned a volume fraction function F, where F shows the amount of (for example) Fluid A present within a particular cell: $F = V_{\mathrm{A}}/V$, where V is the cell volume. A cell full of Fluid A is assigned the value $F = 1$. A cell with no Fluid A (or full of Fluid B in a two fluid model) has the value $F = 0$. Any cell such that $0 < F < 1$ is treated as an interfacial cell.

The $F = 0.5$ contour is treated as the actual interface location and various properties can be monitored here. Figure 3.3 shows how different mesh cells can be labelled based on their respective F values. Cells full of the shaded fluid or Fluid A yield an $F = 1$ value. For a two polymer melt simulation as modelled by the author, $F = 1$ corresponds to a cell full of Melt 1 (or empty of Melt 2). The VOF method enforces conservation of material.

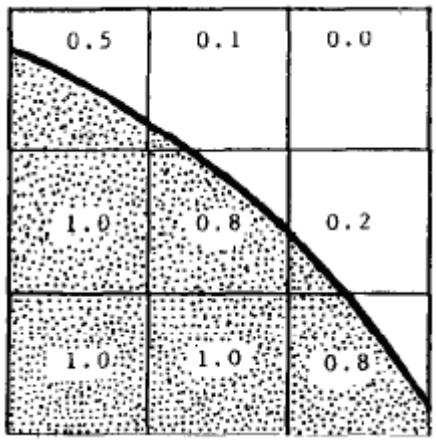

Figure 3.3: A schematic of how F varies within the VOF method. Diagram obtained from [112].

Once all interfacial cells have been found from the function F at an initial timestep for every mesh cell, the evolution of the interface must be tracked at every subsequent iteration to interpret how this changes as the solution progresses. The evolution of F is governed by the equation [12]:

$$\frac{DF}{Dt} \equiv \frac{\partial F}{\partial t} + \underline{u}.\nabla F = 0. \tag{3.6}$$

Equations 3.2, 3.4, 3.5 and 3.6 are the governing CFD equations for the author's multiphase simulations. This is demonstrated in a residual plot (see Section 3.2.1.7). Upon completion of every iteration, the interfacial position is reconstructed based on the fractional volume of neighbouring mesh cells. The formation of the interface is governed by a single equation at every mesh cell like all other variables. This decreases the storage requirements and increases the efficiency of the VOF function compared with alternative schemes discussed later. The unsteady nature of Equation 3.6 requires implicit unsteady physics to be used despite a steady problem in the author's case. The modelling of multiple interfaces, both from two fluids in several layers or with more than two fluids in the same geometry, is possible with VOF, whereby N immiscible fluids require $N-1$ volume fraction functions F_k [111]. The author's work requires the modelling of both multiple fluids and multiple interfaces.

One of the critical aspects of the VOF scheme is in the discretisation of the term F and the convection term $\underline{u}.\nabla F$ in Equation 3.6. In the original approach by Hirt and Nichols [12], the discretisation scheme is parallel to one of the coordinate axes at any position. An upwind scheme discretises the convective term in Equation 3.6 for fluxes parallel to the interfacial axes.

For a perpendicular flux the *donor-acceptor* scheme is used [12,110]. In this scheme a donor cell will give fluid to an acceptor one. The VOF method works alongside the donor-acceptor approach to improve the original VOF algorithm. The information about the slope of the surface and the normal to this slope is used to improve this algorithm [12]. This is related to the original VOF method since this uses an approximate interfacial reconstruction that is parallel to one of the coordinate axes [111].

Surface slope information is therefore beneficial in improving the VOF discretisation.

Also the function F can then be used to define the application of various boundary conditions such as surface tension forces (not modelled by the author). The direction of the velocity u determines the donor and acceptor cells. For positive u (flow direction from left to right), the right hand face of a mesh cell with $(i,\, j)$ coordinates, see Figure 3.4, is considered. Here the left hand cell is the donor and the right cell the acceptor. Mathematically in 2D [113]:

$$(i_{\mathrm{D}}, j_{\mathrm{D}}) = \begin{cases} (i,j) & \text{for} \quad u_{i+0.5,\,j} > 0, \\ (i+1,j) & \text{for} \quad u_{i+0.5,\,j} < 0, \end{cases} \tag{3.7}$$

where $(i_{\mathrm{D}}, j_{\mathrm{D}})$ denotes the donor cell indices. The donor cell must be full before any fluid can enter a downstream cell.

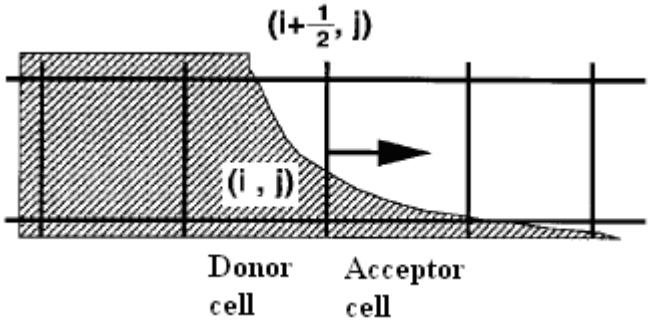

Figure 3.4: The donor-acceptor scheme. Flow direction is from left to right. Diagram obtained from [111].

From Equation 3.7, the sign of u determines the donor and acceptor cells [12]. If u is positive, implying the flow direction is from left to right, the left cell is the donor and the right cell is the acceptor. For a single timestep of duration δt, the amount of the volume fraction function F fluxed across a mesh cell face of width δx is δF multiplied by the cell face cross sectional area A'. Here δF is written as [12]:

$$\delta F = \mathrm{MIN}\{F_{\mathrm{AD}}|u\delta t| + CF, F_{\mathrm{D}}\delta x_{\mathrm{D}}\}, \tag{3.8}$$

where the additional fluid flux CF is given by [12]:

$$CF = \mathrm{MAX}\{(1 - F_{\mathrm{AD}})|u\delta t| - (1 - F_{\mathrm{D}})\delta x_{\mathrm{D}}, 0\}. \tag{3.9}$$

In Equations 3.8 and 3.9 the subscript A represents the acceptor cell and D the donor cell. The notation AD is used to represent either the donor or acceptor cells which can vary depending on the orientation of the interface [12]. The use of the MIN and MAX functions ensures that F stays within the bounds of 0 and 1. The donor cell must fill before any fluid can enter a downstream empty cell, again ensuring boundedness of the donor-acceptor scheme. This scheme is dependent on the interface direction.

Although highly efficient with low storage requirements, the discretisation schemes within the VOF approach may lead to a decrease in accuracy. The basic upwind differencing format (see Section 3.2.1.4) is only first-order accurate and can be numerically diffusive, hence introducing artificial interfacial smudging between the fluids (see Figure 3.5). The VOF method is heavily dependent on the interfacial mesh cell density. Increasing the number of mesh cells would lead to a smoother and more refined interface, but this can vastly increase the time taken for convergence and the overall computational power required.

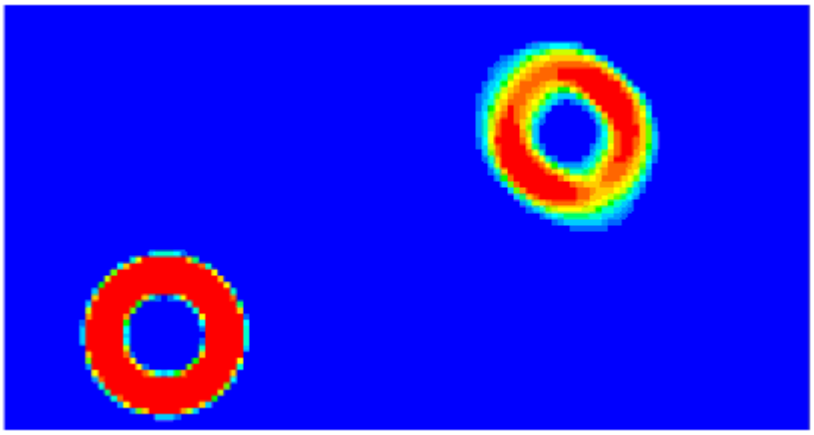

Figure 3.5: Interfacial smudging with the upwind differencing scheme. Diagram obtained from [110].

It is stated in [105] that even for higher order discretisation schemes, the VOF method often leads to unrealistic numerical smearing over one to three mesh cells. Figure 3.6 displays an example of such smudging across several cells for the outlet to a meshed injector block from the author's work. In Figure 3.6 the primary Melt 1 is shown in red and the secondary Melt 2 in blue. To reduce the numerical smearing, mesh refinement

is required in cells with $0 < F < 1$ [105]. However, the difference between coarse and fine meshes should not be too extreme with the change prescribed as gradual [12]. Upon selection of VOF, interfacial details smaller than the mesh size cannot be resolved [110].

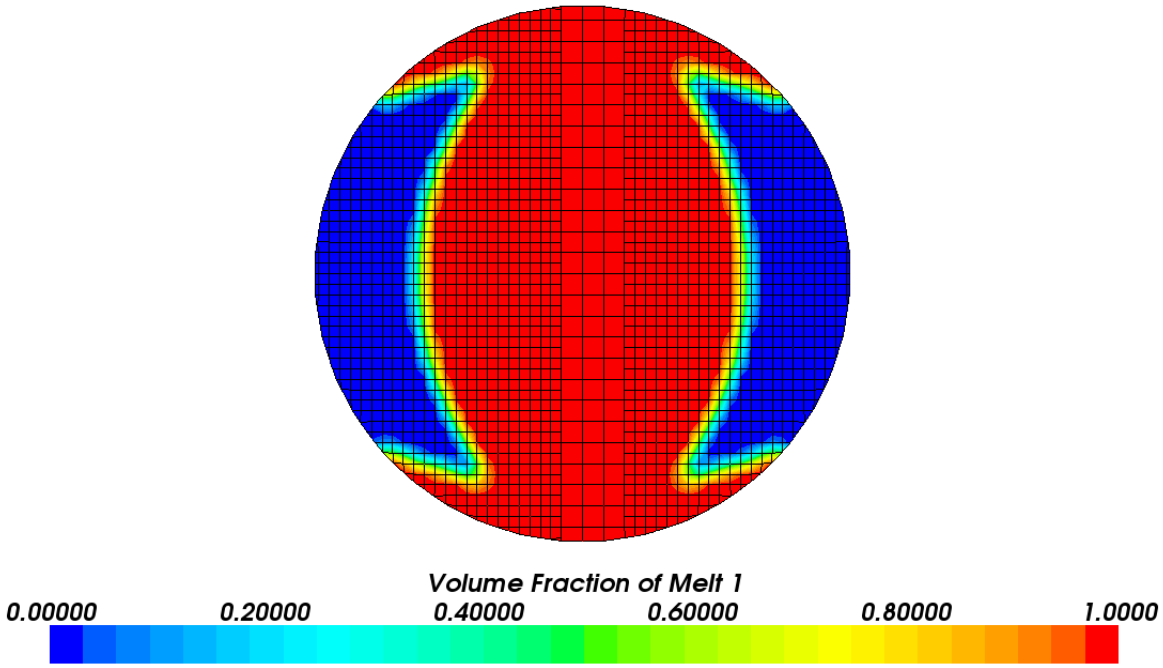

Figure 3.6: Interfacial smudging using the VOF method.

The Courant number (C) is a way of testing the functionality of the fixed mesh at every timestep during the VOF method. This is given as [105, 106, 110]:

$$C = \frac{u_{\mathrm{f}} \Delta t}{\Delta x}, \tag{3.10}$$

where u_{f} is the velocity of the fluid rather than the mesh and Δt and Δx are the global timestep and mesh cell width respectively. For negligible diffusion, the criterion to be satisfied is $C < 1$ [12]:

$$\Delta t < \frac{\Delta x}{u_{\mathrm{f}}}. \tag{3.11}$$

In some cases, the set timestep will affect the final solution and care should be taken when prescribing this to make the simulation timestep independent.

As mentioned, the need for a fine mesh at interfacial cells will increase the size of the overall simulation and hence the central processing unit (CPU) storage space and time - leading to a longer time required for convergence. Another issue with the original Hirt

and Nichols' VOF scheme is that it struggles to recapture a curved interface on a regular structured grid. This is due to the step functional nature of F, which uses a rectangular fractional volume method. An example of this is shown in Figure 3.7, where an attempt to replicate the original interface in Figure 3.3 is presented [112].

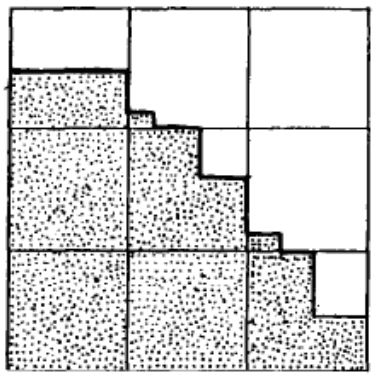

Figure 3.7: An attempt to model the interface from Figure 3.3. Diagram obtained from [112].

In the simulations shown, the accuracy of the solutions is generally of an acceptable level. A curved interface is typically produced with a sufficiently fine mesh. For solution of the Navier-Stokes equations and other scalar transport properties, the different fluids (labelled 1 and 2 here) can be treated as a single fluid with properties varying in space based on the volume fractions [105, 108]:

$$\rho = \rho_1 F + \rho_2(1 - F) \ , \ \eta = \eta_1 F + \eta_2(1 - F), \tag{3.12}$$

where the interface is not treated as a boundary so no prescribed boundary conditions are required. Furthermore, the assumption that all phases share pressure, velocity and temperature fields becomes a discretisation error [108]. This error occurs in interfacial mesh cells where the two prescribed fluids may have different properties and are treated as a single fluid.

To summarise the VOF model, it is an Eulerian fixed grid method ($u_{\text{mesh}} = 0$, [110]) best suited to solving problems where each immiscible fluid constitutes a large structure [107]. If required surface or interfacial tension can be modelled within the VOF equations as an extra body force [105]. However, this is treated as negligible for polymer melt flows

(see Chapter 2). Although efficient from a storage perspective, the VOF scheme suffers from a lack of accuracy with interfacial smudging problematic, especially in coarse meshes.

A pre-curser to the VOF scheme is the Marker and Cell (MAC) algorithm, as first proposed by Harlow and Welch in 1965 [114]. The MAC method assumes a finite difference approximation to the Navier-Stokes equations and an Eulerian, stationary mesh [114,115]. Once this is complete, massless virtual marker particles are introduced to the system to calculate each material region [12, 105, 112, 114, 115]. In particular, these marker particles are placed in cells containing fluid and not elsewhere.

The labelling of such cells is as follows: a cell within the domain but not containing the fluid in question (or any marker particles) is denoted EMPTY (E) [114, 115]. Any cell containing marker particles is denoted as SURFACE (S) if next to at least one cell denoted E. All other cells are denoted F for a cell full of fluid. This labelling scheme is shown in Figure 3.8 for a two fluid system.

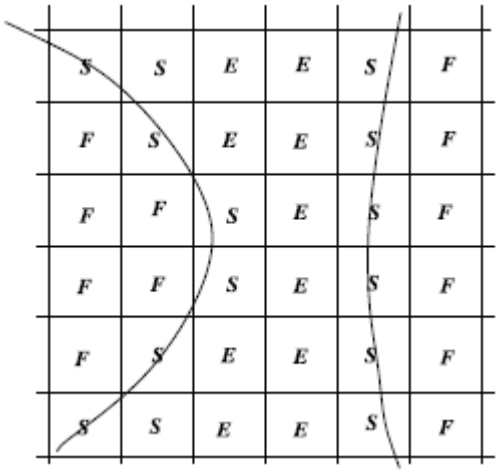

Figure 3.8: The labelling scheme for two fluids as employed in the MAC scheme. Diagram obtained from [115].

In the MAC scheme, the interfacial curvature is approximated by the surface that best fits the surface marker particle positions, and calculating a normal vector position within the cell centre. This curvature is given as [115]:

$$\Upsilon(x, y) = \mathrm{a}x^2 + \mathrm{b}xy + \mathrm{c}y^2 + \mathrm{d}x + \mathrm{e}y + \mathrm{g}, \tag{3.13}$$

where a-e, g are constants to be determined.

The accuracy of the final interface is strongly dependent on the number of marker particles in interfacial cells [12, 105, 112, 114, 115]. Up to 16 particles can be placed in a single interfacial cell, resulting in far more particles than cells [112, 115]. The use and motion of these particles greatly increases the computational storage, when considering this and the Navier-Stokes discretisation at every iteration [12, 105, 112]. It is this low efficiency in the MAC method that led to the VOF scheme [12]. Despite the high storage requirements, MAC techniques offer logical simplicity, especially involving multiple free boundaries [12] and the ability to capture complex phenomena such as wave breaking [105], a broken dam [114] and viscoelastic die swell [115].

A later alternative to the VOF method is the stationary mesh based Simple Linear Interface Calculation (SLIC), which is a fractional marker method like VOF [112]. The SLIC approach was first described by Noh and Woodward in [116]. In the SLIC formulation, the interface is regenerated using a straight line or plane that is aligned to the coordinate axes [111, 117]. The total material volume in each interfacial cell will be conserved. For the SLIC reconstruction, the volume fractions are updated during the calculation using the fractional volume of a cell and its nearest neighbours [111, 112].

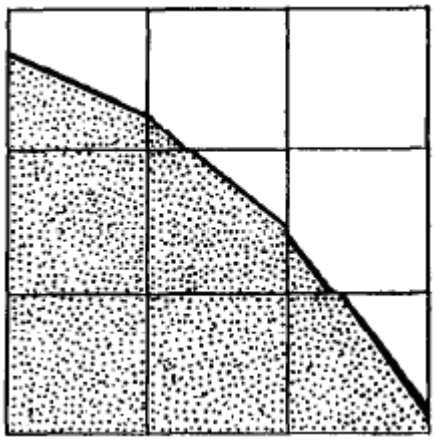

Figure 3.9: Using the SLIC scheme to capture the interface in Figure 3.3. Diagram obtained from [112].

Because of the directional dependent nature of SLIC, the prescribed flux direction

will often lead to a different interface in one direction compared with another [112]. Also curved interfaces are not particularly well defined due to the linear nature of the SLIC. This is demonstrated in Figure 3.9, where SLIC is used to approximate the interface shown in Figure 3.3. In [112] some previous modifications to SLIC are discussed. Chorin [118] modified the original algorithm to allow multiple rectangles in a single cell - this is known as SLICer. Barr and Ashurst [119] combined VOF based ideas with SLICer to create SLICest.

First published by Youngs in 1982 [120], the Piecewise Linear Interface Calculation (PLIC) algorithm is considered more accurate than both the VOF and SLIC methods [111], as shown in Figure 3.10 for the initial interfacial condition (IC). In the PLIC, an estimate is made of the interfacial orientation β [111]. The interface is then constructed using β as a reference, and each cell is partitioned by planes aligned to the fluid position [117]. In a 3D grid a polygonal interface is observed [111, 117].

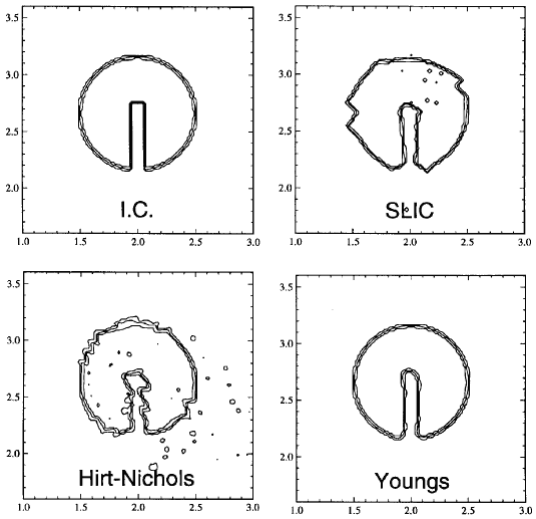

Figure 3.10: Comparisons between the initial condition, the SLIC, the Hirt-Nichols' VOF and Youngs' PLIC schemes. Diagram obtained from [112].

The PLIC scheme is fast and preserves the volume of fluid consistently [117, 121]. However, the PLIC is discontinuous across cell boundaries - making visualisation difficult [117]. There is also a Lagrangian aspect to the PLIC in that large fluid sections are advected through cell boundaries. This is disadvantageous if using an Eulerian approach.

Most modern commercial CFD codes use a combination of the VOF and PLIC algorithms, for example as that described by López *et al.* in [122], where fluid structures thinner than the mesh cell can be tracked using the method described by the authors. This is not possible in original PLIC schemes.

There are a number of publications where improvements to Youngs' PLIC are suggested. Pilliod Jr. and Puckett [123] use a least squares approach to address the approximate linear interface. Dyadechko and Shashkov [124] and Schofield *et al.* [125] described PLIC based interfacial reconstruction algorithms relating to material centroid information.

The more recent level set method, first described by Osher and Sethian [126], uses a *smooth* level set scalar function φ for interface capturing. The value of φ is the normal distance to the interface; the desired value $\varphi = 0$ represents the interface function [105, 115, 121]. Values other than $\varphi = 0$ are considered irrelevant to the interfacial calculation, with positive φ values fluid regions [105]. The discretisation of $\varphi(x,t)$ is governed by [105, 115, 121]:

$$\frac{D\varphi}{Dt} \equiv \frac{\partial\varphi}{\partial t} + \underline{u}.\nabla\varphi = 0, \tag{3.14}$$

at every iteration, where the progression of φ is monitored. The level set equation 3.14 is equivalent to the VOF equation 3.6. However, the differences in the properties of F and φ mean that they are completely different schemes. The level set method has applications in fluid dynamics and materials engineering [115].

Advantages of the level set method include the fact that φ is smooth and can be used to obtain the interface curvature locally [115]. This is because the level set method takes the original interfacial curve and builds it into a surface [127], unlike the discontinuous nature of the VOF function F [12, 105]. Also the nature of this level set technique is simple and easy to implement even in cases of interfacial separation [115]. Disadvantages of this level set approach are that the discretisation of Equation 3.14 can lead to interfacial smudging and errors compared with the VOF approach, especially if there are many interfacial curves [115, 128]. Mass is not conserved since φ is not explicitly contained within the governing CFD equations [105, 115]. This can lead to inaccuracies and greater CPU costs.

Zhang *et al.* [129] modified the standard level set method to allow for mass conservation. Lv *et al.* [121] have presented a novel level set and VOF coupling system. In a paper relevant to the author's studies, Yue *et al.* [28] used a level set interface method to numerically capture the curtate cycloid interface (see Figure 2.17). Borzacchiello *et al.* [90] also used the level set approach to numerically investigate viscous and elastic effects in polymer coextrusion.

In other work relevant to the author's, Dooley [8] and Anderson *et al.* [59] used the mapping method to numerically *track* the interface of identical viscoelastic polymer melt flows. The mapping method, described in detail in [130, 131], is based on tracking rather than capturing, but each material is not tracked separately - hence reducing the computational storage required [8, 59]. The basis of this method is to divide a geometrical domain or volume Ω into N non-overlapping sub-domains, independent of the velocity field discretisation [8, 59]. The sub-domain boundaries are tracked from (for example) $t = t_0$ to $t = t_0 + \Delta t$ or $z = z_0$ to $z = z_0 + \Delta z$, and the grid deformation observed. This takes up a large amount of computational memory, but needs only to be performed once [130, 131]. The result of this tracking is stored in a mapping matrix Φ of size $(N \times N)$, which shows the fraction of each cell of the deformed grid back to the original one [59, 131]. Advantageous properties of the matrix Φ include that mass is conserved and that it is sparse. The mapping method can also produce complex interfaces such as those shown in Figure 3.11.

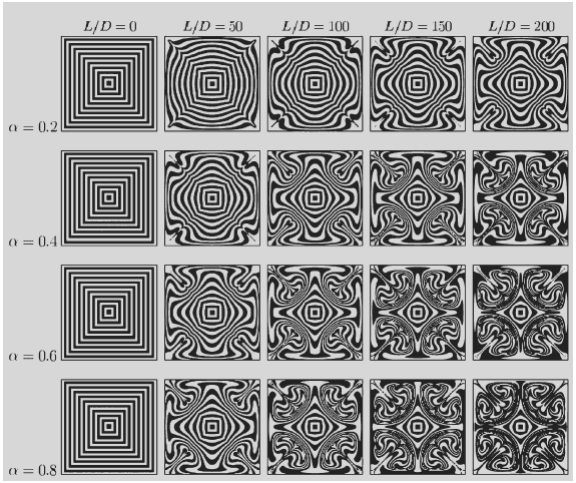

Figure 3.11: The use of the mapping method. Diagram obtained from [8].

In [49, 50, 98] amongst other publications, Gupta used a *mesh partitioning technique* to represent the interface between different polymer melt layers. In these publications, a 3D tetrahedral mesh is used to discretise the full die geometry. The polymer-polymer interface is then captured by a separate surface mesh of linear triangular elements. This decoupling is possible since the polyXtrue software used does not require matching of different mesh elements. The interface is allowed to pass through the core part of the die geometry, and new mesh shapes are created upon such intersection. In these papers by Gupta, an integral form of the no cross flow boundary condition is used:

$$\int_{\Gamma'} (\underline{u}.\underline{n})\, dS = 0, \tag{3.15}$$

over a surface S and interfacial surface Γ'. The initial interface shape is determined by the fluid streamlines within the die and this is a simplistic and inaccurate method to use, particularly for complex geometries.

This Section has discussed some of the main numerical interfacial capturing schemes. As mentioned, this thesis uses the VOF method to capture and track polymer-polymer melt interfaces when producing multilayered films (MLFs) because of the efficiency of the VOF method. Assuming a fine enough mesh within interfacial regions, the author has found the VOF method to give smooth interfacial plots between the different polymer melt layers which is desirable from a modelling perspective. However, it is this mesh dependency that is one of the major disadvantages when using the VOF technique in the author's simulations. For certain coextrusion geometries used in this thesis, more than 15 million mesh cells have been required and this leads to lengthy convergence times.

Although more accurate than the VOF method, the MAC technique requires significantly more additional storage space than the current VOF approach. It is also of the author's opinion that the mapping, SLIC and mesh partitioning techniques would not be effective on full industrial scale geometries such as those used in this thesis. The level set method is not as accurate as the VOF approach and mass is not conserved in this scheme. Having reviewed some of the available interfacial capturing schemes above, it is of the author's opinion that the currently used VOF approach along with PLIC is the best option for the type of modelling work being conducted. The PLIC approach is

very accurate, however this is mainly applicable to Lagrangian type problems which are not modelled in polymer melt flows. Therefore, a combination of VOF and PLIC for an Eulerian approach would be required.

The author feels that the VOF method offers the best compromise between storage requirements and accuracy when considering all the available interfacial capturing schemes. Using the PLIC formulation along with VOF may improve the accuracy further. To reduce the total number of mesh cells required but maintain accuracy, one should coarsen regions that are not of interest numerically. Another option is to input a symmetry plane (see Section 3.2.1.8) into the geometry to halve or quarter the solution domain.

3.2.1.4 Finite volume discretisation methods

Since CFD is a predictive technique, some form of discretisation of the governing equations is required. The main numerical approximations are the finite difference, finite element and finite volume approaches. STAR-CCM+ uses the finite volume method which accounts for around 80 % of usage in all commercially available CFD software [110], and therefore this Section mainly describes this. Summarising the remaining two schemes, the finite difference method approximates partial differential equations (PDEs) in terms of neighbouring nodal values [105]. The finite element method uses a scaled *weight function* as a coefficient of a quantity of interest, for example as a coefficient of the velocity field u. Neither the finite difference nor finite element approaches conserve mass in the way that the finite volume method does.

The governing scalar transport equation, in integral form, for any CFD technique is [105]:

$$\frac{\partial}{\partial t}\int_{\Omega}\rho\phi\, d\Omega + \int_{S}\rho\phi\underline{u}.\underline{n}\, dS = \int_{S}\Gamma\nabla\phi.\underline{n}\, dS + \int_{\Omega}q_{\phi}\, d\Omega, \tag{3.16}$$

where ϕ is an unknown scalar to be solved for and can correspond to any physical quantity, and Γ is the fluid diffusivity. The general form of Equation 3.16 is: the rate of change of an amount + a convection term = a diffusion term + a source. In a typical CFD simulation ϕ is the only unknown and every other value in Equation 3.16 is specified [105]. Equation 3.16 can be modified to represent any of the governing equations 3.2, 3.4, 3.5

and 3.6, where in the continuity and VOF equations, the right hand side of Equation 3.16 is set to zero.

In the finite volume scheme, an unstructured mesh can be generated. Equation 3.16 is solved for ϕ at every single mesh cell. Both surface and volume integrals are approximated for numerical purposes. The value of ϕ is only stored at cell centres (nodes) and therefore discretisation is required to approximate cell edge values from cell centre ones, especially for surface integrals. Figure 3.12 shows a typical structured CFD grid in 2D, where uppercase letters represent cell nodes and lowercase ones cell edges. This structured grid is referred to when describing discretisation schemes. The notation P is used to represent the base cell centre value.

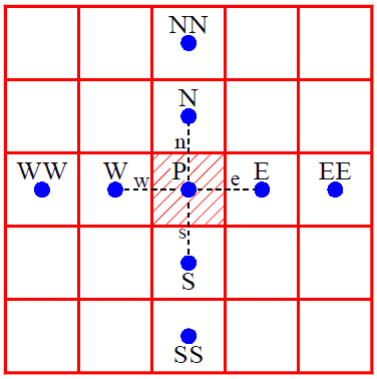

Figure 3.12: A typical structured CFD grid. Diagram obtained from Apsley [132].

The total flux out of any cell is the sum of the flux leaving each of the cell surfaces, denoted n, e, s, w. Using cell face e as an example, there are three common methods of computing the surface integral approximation here - as shown in [105]. These are: the midpoint rule, the trapezoid rule and Simpson's rule. Using f' to denote either the convection or diffusion term in Equation 3.16 and F' the value of the resulting surface integral, the midpoint rule, as used in STAR-CCM+, is simply the product of the integrand at the cell edge centre and length of the cell face:

$$F'_{\mathrm{e}} = \int_{S_{\mathrm{e}}} f' \, dS \approx f'_{\mathrm{e}} S_{\mathrm{e}}, \tag{3.17}$$

a second-order accurate method. The trapezoid rule is written as:

$$F'_{\mathrm{e}} = \int_{S_{\mathrm{e}}} f' \, dS \approx \frac{S_{\mathrm{e}}}{2} (f'_{\mathrm{ne}} + f'_{\mathrm{se}}), \tag{3.18}$$

making use of the ne and se corner values of cell P. The trapezoid rule is also second-order accurate. Simpson's rule is given as:

$$F'_{\mathrm{e}} = \int_{S_{\mathrm{e}}} f' \, dS \approx \frac{S_{\mathrm{e}}}{6}(f'_{\mathrm{ne}} + 4f'_{\mathrm{e}} + f'_{\mathrm{se}}), \tag{3.19}$$

a fourth-order accurate method. There are other techniques used to approximate surface integrals but these are not shown here.

Equation 3.16 contains volume as well as surface integrals, as shown in the source term. The simplest approach for a volume integral is to multiply the integrand at P by the total cell volume, or:

$$Q'_{\mathrm{P}} = \int_{\Omega} q \, d\Omega \approx q_{\mathrm{P}} \Delta\Omega, \tag{3.20}$$

which is second-order accurate. All unknown values are stored at cell centre locations so no further interpolation is required with Equation 3.20. The surface integral approximations 3.17-3.19 still require values of f' and hence ϕ at cell edges and corners, so interpolation from cell centre to cell edge is still required.

One example of such interpolation is the second-order accurate central differencing scheme, which uses the average of the two neighbouring nodes to obtain a value at the cell edge. Using face e as an example, this is written mathematically as [132]:

$$\phi_{\mathrm{e}} = 0.5(\phi_{\mathrm{E}} + \phi_{\mathrm{P}}). \tag{3.21}$$

An alternative approach is the upwind interpolation scheme, which is only first-order accurate. The value at the cell face is directionally dependent based on whether the flow is from left to right or vice-versa. For upwind interpolation, the node chosen is taken as whichever is upwind from the edge required. Mathematically [105, 132]:

$$\phi_{\mathrm{e}} = \begin{cases} \phi_{\mathrm{P}} & \text{for} \quad u > 0, \\ \phi_{\mathrm{E}} & \text{for} \quad u < 0. \end{cases} \tag{3.22}$$

The low accuracy of the upwind scheme is countered by the fact that boundedness (see later) is achieved [105]. This means that non-oscillatory solutions are guaranteed, but Equation 3.22 can lead to numerical smearing [105]. To improve the accuracy of the techniques shown in Equations 3.21 and 3.22, more nodal values need to be used. This is

demonstrated in the CFD results shown throughout this thesis which use a *second-order* version of the upwind scheme. The Quadratic Upwind Interpolation (QUICK) scheme uses the upwind-upwind, upwind and downwind nodes, and is hence directionally dependent. This is third-order accurate and can be written as [105, 132]:

$$\phi_{\mathrm{e}} = \begin{cases} -\frac{1}{8}\phi_{\mathrm{W}} + \frac{3}{4}\phi_{\mathrm{P}} + \frac{3}{8}\phi_{\mathrm{E}} & \text{for} \quad u > 0, \\ -\frac{1}{8}\phi_{\mathrm{EE}} + \frac{3}{4}\phi_{\mathrm{E}} + \frac{3}{8}\phi_{\mathrm{P}} & \text{for} \quad u < 0. \end{cases} \tag{3.23}$$

For implicit unsteady schemes, the QUICK method is recommended to use alongside the VOF approach but it is not used in this thesis. An even more accurate technique is the fourth-order central differencing method [105]:

$$\phi_{\mathrm{e}} = \frac{27\phi_{\mathrm{E}} + 27\phi_{\mathrm{P}} - 3\phi_{\mathrm{EE}} - 3\phi_{\mathrm{W}}}{48}, \tag{3.24}$$

which can be used alongside Simpson's rule (Equation 3.19) to match the accuracy.

There are a number of properties associated with the discretisation schemes, as mentioned in [105, 132] amongst other publications. These include the *order* or accuracy of a method (already mentioned), *consistency*, *conservativeness*, *boundedness* and *stability*. The order defines how fast the residual of the numerical solution decreases as the grid spacing decreases, and can be calculated using a Taylor series expansion. The three main errors in CFD modelling are: modelling errors, discretisation errors and iteration errors [105]. One observes consistency if the discretised equations are an accurate approximation of the governing ones - if the discretised equations are equivalent to the continuum ones as the grid spacing tends to zero [132].

A scheme is conservative if the flux leaving a cell is exactly equal to the flux entering a neighbouring cell. This is automatically embedded in a finite volume approach as used in STAR-CCM+. A bounded scheme implies that the discretised solution always lies between a numerically realistic upper and lower bound, for example temperature in Kelvin should never be negative. Higher order accuracy schemes such as QUICK are unbounded but this can be modified with grid refinement [132]. Finally, a stable discretisation method means that the errors converge rather than diverge when progressing through time (or per iteration). This can be checked through a residual plot, see Section 3.2.1.7.

3.2.1.5 Pressure-velocity coupling

The structure of the three momentum equations 3.1 can result in problematic pressure-velocity coupling [105, 110, 132]. The pressure p appears explicitly in all three momentum equations, and the velocity field u_i appears in these momentum equations as well as the continuity equation 3.3 [110]. This effectively leads to four equations for four variables, although p is not solved for explicitly in CFD. There is a pressure dependence on velocity, based on the force terms in the Navier-Stokes equations [132]. The pressure field needs to be calculated in order to fully solve the governing equations. For compressible flows the continuity equation provides a transport equation for density ρ and p is then obtained using an ideal equation of state. In incompressible flows, as modelled by the author, the density is constant and not linked to pressure [110]. There are a number of different methods available to deal with this coupling, and hence reduce the associated convergence issues with this pressure-velocity coupling.

One possible remedy is to use a co-located system. Here all variables including pressure and velocity are stored at exactly the same set of grid points [105, 132]. The cell face velocities are calculated by linear interpolation using the cell centre velocities as a basis. Since many of the terms in each of the equations are identical, this co-location leads to a reduction in the number of computed coefficients, and hence in the computations required. It can be shown, however, that in a co-located storage system, both the mass and momentum equations only produce links to pressure at alternate nodes. This co-location of velocity and pressure can therefore lead to odd-even decoupling and can cause calculations to crash.

An alternative approach to co-location is to use a staggered grid, as first suggested by Harlow and Welch in [114]. When using a staggered grid, the pressure nodes that are stored at cell centres drive the velocity components which are stored at cell wall faces (see Figure 3.13). Upon using this approach, no interpolation is required for terms in the co-located method that require interpolation due to the separation of pressure and velocity; variables are stored where needed [105, 132]. Furthermore, the separately stored locations of the pressure and velocity fields lead to an eradication of the odd-even decoupling from

the co-located arrangement. A disadvantage of the staggered grid approach is that for non-Cartesian meshes, the velocity nodes may stop lying between the pressure nodes that drive them. For such non-Cartesian meshes, a co-located grid alongside a *pressure correction* approach is highly effective and is the norm in commercial CFD codes.

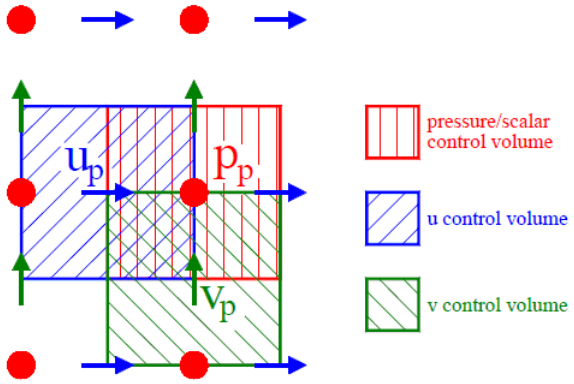

Figure 3.13: The staggered grid approach for velocity and pressure. Diagram obtained from [132].

The most common pressure correction approach is known as SIMPLE (Semi Implicit Method for Pressure Linked Equations), first published by Patankar and Spalding in [133]. The basis of the SIMPLE approach is described by Apsley in [132] and by Bakker in [110]. The main approach behind SIMPLE is to analyse the pressure in every mesh cell at every iteration and if necessary apply a pressure correction term p' to a particular cell. If mass conservation is *not* satisfied in a cell, p' is either increased or decreased here until mass is conserved. The SIMPLE algorithm is iterative and is mainly used to solve steady state problems [132]. SIMPLE is the default solver for most commercial finite volume based CFD codes including STAR-CCM+ [110] and is used in this thesis.

An alternative extension to SIMPLE is the PISO (Pressure Implicit with Splitting of Operators) algorithm, first published by Issa in [134]. The general approach for PISO is the same as SIMPLE, apart from a second corrector step is required to produce a second mass consistent flow field, eliminating the need for iteration. Unlike SIMPLE, PISO is non-iterative and is mainly used to solve time dependent problems [132, 135, 136]. However, PISO has been adapted to solve steady state problems and is efficient computationally

despite the extra step required.

3.2.1.6 Complex geometries

Some of the main computational methods for meshing and hence solving on complex geometries are discussed in [105]. Most realistic engineering flows require non-standard geometries which cannot be meshed using a standard Cartesian grid and non-orthogonal meshes are used. A review of available meshing methods is shown in Section 3.2.1.1. When discretising complex geometries, the mesh should be made as orthogonal as possible and adjacent cell sizes between coarse and fine regions should be kept as similar as possible to avoid any skewed mesh cells or erroneous results. This is particularly important when using the VOF method (see Section 3.2.1.3) in complex geometries.

It is often advisable to use an intermediate mesh cell range between more extreme cell sizes. Even if a mesh is not Cartesian, the accuracy of the solution will be improved if the mesh follows one streamline direction as much as possible. For this purpose, hexahedral rather than tetrahedral mesh cells should be used [105]. A further prevalent mesh issue with complex geometries is the mesh at the walls. For a turbulent flow, a fine mesh with several prism layers is required to correctly resolve the velocity components.

Another way of capturing a complex geometry is to use a set of simple overlapping orthogonal meshes [105]. When such overlapping grids are selected, it is difficult to maintain conservation at the interfaces between the different meshes. Also, the interpolation between the different mesh structures can introduce errors if there is variation here. Commercial codes such as STAR-CCM+ generally use boundary-fitted non-orthogonal grids [105]. This is when the mesh is adapted to fit any geometry and follow the flow direction. Using such schemes can increase the complexity of the governing equations. Also, unphysical solutions, or mesh based errors, can be observed.

For finite volume CFD methods as used here, there is no need for global (Cartesian) coordinate transformations but a local coordinate transformation may be used. Methods for discretising the governing CFD equation 3.16 are shown in [105, 110, 132] amongst many others. For approximating the terms involving surface integral calculations in Equa-

tion 3.16 on a complex geometry, Equations 3.17-3.19 can still be used but modifications are required. In a complex grid the surface vector S for any cell face has several velocity component directions and these all contribute to the overall flux. Using a global to local coordinate transformation, the gradient term within the diffusive term in Equation 3.16 can be written for a 3D coordinate system as [105]:

$$\nabla\phi \equiv \frac{\partial\phi}{\partial x}\,\underline{i} + \frac{\partial\phi}{\partial y}\,\underline{j} + \frac{\partial\phi}{\partial z}\,\underline{k} = \frac{\partial\phi}{\partial n}\,\underline{n} + \frac{\partial\phi}{\partial t}\,\underline{t} + \frac{\partial\phi}{\partial s'}\,\underline{s}', \tag{3.25}$$

where $\underline{s}'$ is a vector orthogonal to both $\underline{n}$ and $\underline{t}$. These three vectors are localised. The vectors $(\underline{i}, \underline{j}, \underline{k})$ are unit vectors in the (x, y, z) directions. Equation 3.25 is calculated at cell faces.

Another way of calculating cell face derivatives is to average the differential at the cell centre and average the result over the whole cell volume:

$$\left(\frac{\partial\phi}{\partial x_i}\right)_{\mathrm{P}} \approx \frac{\int_\Omega \partial\phi/\partial x_i \, d\Omega}{\Delta\Omega}. \tag{3.26}$$

The terms in Equation 3.16 involving volume integral calculations will not change regardless of the complexity of the geometry. This is because Equation 3.20 is independent of the control volume shape [105].

3.2.1.7 Residuals

As mentioned, STAR-CCM+ uses an iterative process. This procedure is based on an initial guess value, which is either set by the software or prescribed as an initial condition by the user. After every iteration the values will change and get closer and closer to the actual solution. Independent of the finite volume discretisation scheme used to approximate Equation 3.16, the final discretisation will be of the form [110]:

$$a'_{\mathrm{P}}\phi_{\mathrm{P}} = \left(\sum_{\mathrm{nb}} a'_{\mathrm{nb}}\phi_{\mathrm{nb}}\right) + b', \tag{3.27}$$

where ϕ_{P} is a physical quantity being solved for at a cell centre P and the subscript nb corresponds to neighbouring nodes of P. The values of the coefficients a' and b' (a source term) will vary from cell to cell.

A measure of the imbalance or *error* in Equation 3.27 is given by the residuals R' [110]. In mathematical form, at point P, the residuals are given as:

$$R'_{\mathrm{P}} = \left| a'_{\mathrm{P}}\phi_{\mathrm{P}} - \left(\sum_{\mathrm{nb}} a'_{\mathrm{nb}}\phi_{\mathrm{nb}} \right) - b' \right|, \tag{3.28}$$

upon rearranging Equation 3.27. When extending to the whole mesh domain or volume Ω, Equation 3.28 is normalised and written:

$$R'_{\Omega} = \frac{\sum_{\text{all cells}} |a'_{\mathrm{P}}\phi_{\mathrm{P}} - (\sum_{\mathrm{nb}} a'_{\mathrm{nb}}\phi_{\mathrm{nb}}) - b'|}{\sum_{\text{all cells}} |a'_{\mathrm{P}}\phi_{\mathrm{P}}|} \tag{3.29}$$

after N iterations.

A residual R' or the normalised R'_{Ω} can be applied to any physical quantity. Ideally as the iterations increase, the residual (or error) will decrease then level off and the CFD solutions have only a negligible error. This shows that the error is not changing as the solution progresses with time. The value of R'_{Ω} is often used to test for convergence and accuracy of simulations. A rule of thumb for convergence is that the residual should decrease by at least an order of three from the initial value before maintaining this level. Typical converged final values for R'_{Ω} in this study will range from 10^{-5} to 10^{-15}. It is stated in [110] that residuals should generally be less than the order 10^{-4}. Another method to test for convergence is to monitor a physical quantity of interest at a computational region within the domain and check that this value reaches an expected one after a certain number of iterations.

Figure 3.14 shows a residual plot obtained from one of the author's simulations, where the simulation was ran for just under 14,000 iterations. After around 3,000 iterations there is no fluctuation in any residual quantity and the final values range from 10^{-5} to 10^{-12}, implying full convergence. The model was ran beyond 3,000 iterations because of the nature of the numerical problem being solved; a viscous, slow moving polymer melt flow is at the geometry walls and needs to be dislodged by another polymer melt. From 3,000 to 14,000 iterations, the only thing changing in the simulation is the amount of melt flow present at the walls. Each individual residual plot shows the error of one of the six governing equations 3.2, 3.4, 3.5 and 3.6. The equations are discretised into the form of Equation 3.16 and solved numerically.

To demonstrate the numerical effort required to dislodge or "flush out" a fluid from the walls, the mass flow rates of the two polymer melts were doubled in the simulation with residuals shown in Figure 3.14. This was from a start of just less than 14,000 iterations with the fluid already fully dislodged. A fully converged solution was obtained after a further 1,000 iterations, with the respective volume fraction and velocity residuals flattening rapidly. This shows that for the type of CFD simulation shown in this thesis, a high proportion of the runtime is on flushing out an initialised fluid from the geometry walls. Further timestep independence considerations are discussed in Section 4.5.2. For the CFD simulations in this thesis, stable flow was assumed to be established upon the reduction and flattening of the residual curves, and when a physical quantity of interest has converged to its expected final value at a plane of interest.

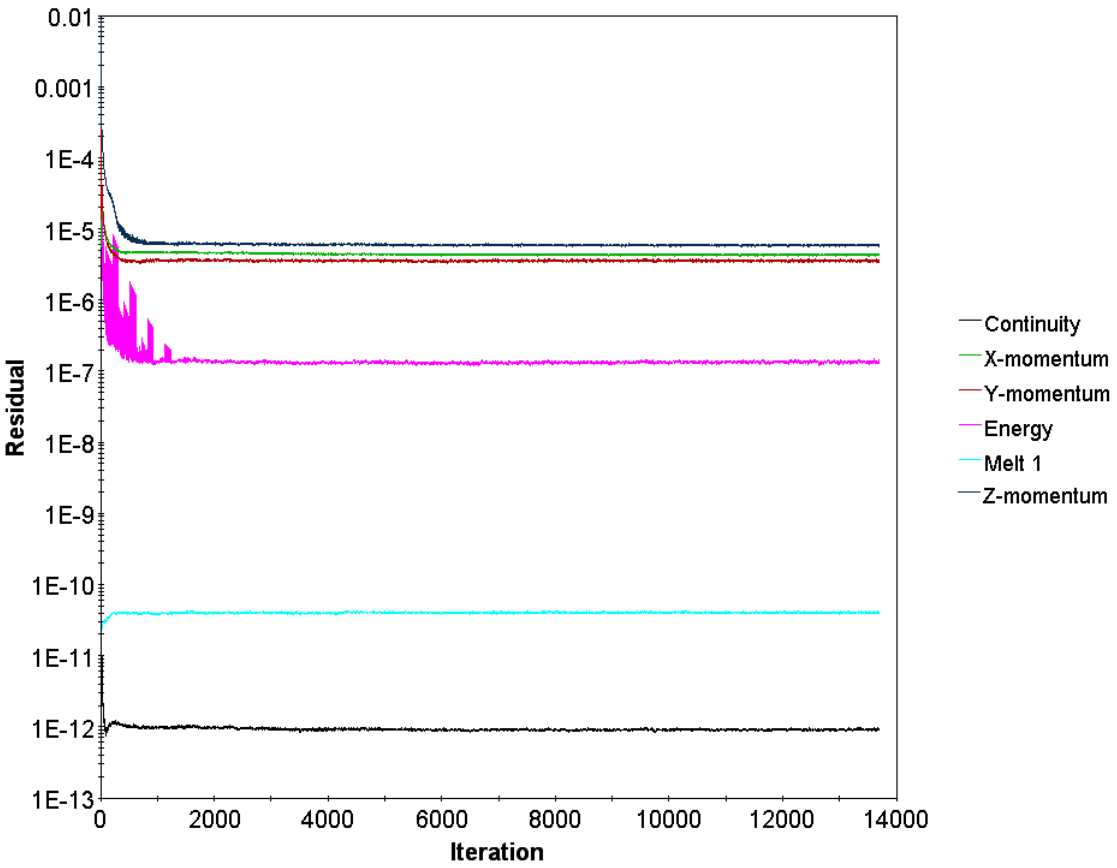

Figure 3.14: A typical residual plot. Diagram obtained from one of the author's simulations.

3.2.1.8 Typical boundary conditions used in STAR-CCM+

In any CFD simulation, boundary conditions (BCs) must be specified to solve alongside the governing discretised equations, forming a complete problem. The number of BCs required is equal to the order of the PDE. Typical BCs are either Dirichlet (where the unknown scalar ϕ being solved for is specified at the boundary of interest) or Neumann (where the gradient of ϕ is specified). On every individual geometry face, the boundary type is set. Typically the author's models utilise a mass flow or velocity inlet, a pressure outlet which is set as an outlet plane, walls and a symmetry plane as the specified boundaries. Certain values can then be specified by the user at each boundary.

At an inlet boundary condition all quantities must be prescribed [105]. For a velocity inlet, the velocity magnitude, temperature, pressure and volume fraction (the proportion of a single melt phase at a boundary surface) are all set by the user. Due to the co-location of pressure and velocity (see Section 3.2.1.5), the pressure at the inlet face is extrapolated from the adjacent mesh cell [132]. For a mass flow inlet, the mass flow rate (in kg hr^{-1}) is inputted and then converted by the software into a velocity. Mathematically a prescribed BC has the form ϕ = constant at this boundary.

Often little is known about the final outlet solution prior to setting up the simulation. As the runtime increases, the final outlet solution develops and replaces what is set as the outlet condition. The solution at the outlet is the most relevant to the majority of simulations and therefore requires constant monitoring. It is recommended in [105] that the outlet boundary be set far away from the prescribed inlet boundaries. In STAR-CCM+, the pressure, temperature and volume fraction are set at the outlet. The temperature and volume fraction values will be overwritten upon full convergence and the pressure remains constant at the outlet plane.

There is an internal, unpublished Imperial Chemical Industries (ICI) paper [137] where the finite element software FIDAP is used to analyse the performance of coextruded products. In [137], the authors suggest that the use of a BC at a plane of interest such as the outlet is not good CFD practice. It is suggested that the free surface condition be used to show the effect of exit from the die outlet. However, free surface CFD flows are

very time consuming and difficult to produce. It would take a separate study to monitor and predict free surface flows out of a die outlet.

For laminar, viscous fluids such as polyester melts a no-slip condition is applied at the walls. This implies that the fluid has a velocity of zero relative to the boundary; $u = 0$ at the wall. This no-slip condition is used throughout this thesis. The wall temperature is set at the walls at a value corresponding to the control temperature for a film production trial. For wall slip conditions, only the velocity component normal to the wall vanishes and the other components remain. There is some literature available whereby the authors use a slip condition to model polymer melt flows, for example Torres *et al.* in [97].

Symmetry planes are used if the geometry exhibits symmetry about this plane. They can dramatically reduce the overall mesh density and hence the processing time. On a symmetry plane the convective fluxes of all quantities are zero [105]. The normal gradient of any physical value is zero, *i.e.* [137]:

$$\frac{\partial \phi}{\partial n} = 0. \tag{3.30}$$

There is no user input required at the symmetry plane.

Initial conditions (ICs) are also required in STAR-CCM+. For the physics used by the author, these are the pressure, temperature, velocity and volume fractions of the different melts. It is advisable to fill the geometry in a manner that will allow for efficient running time. This is mainly relevant to volume fraction values. For a system with two different fluids, the prior filling of the geometry with the core fluid means that the secondary fluid must dislodge the core fluid. For a fine mesh with laminar fluids, this dislodging (or flushing out) will be very time consuming. All ICs correspond to the guessed value and should be specified as close as possible to the already set BCs.

3.2.1.9 Implicit unsteady methods

As previously discussed, the VOF method for interface tracking requires a timestep, so either implicit or explicit unsteady physics is required. In Section 3.2.1.4, only steady state discretisation is shown. For a full approximation, the time dependent form of the

governing scalar transport equation 3.16 must also be solved at every new timestep since the properties can change when progressing through time. In the STAR-CCM+ online help guide [108], it is stated that implicit rather than explicit physics is suitable for the segregated flow solvers used by the author. This Section therefore only focuses on the former, as used in this thesis. Implicit schemes solve a system of algebraic equations in order to calculate the value at all grid points simultaneously [106]. Implicit methods can be efficient at ensuring stability, although this is not guaranteed, and allow for a larger Courant number than explicit ones.

To demonstrate an implicit approach, the one directional, incompressible, differential version of Equation 3.16 without a source term is shown [105]:

$$\frac{\partial \phi}{\partial t} = \text{-}u\frac{\partial \phi}{\partial x} + \frac{\Gamma}{\rho}\frac{\partial^2 \phi}{\partial x^2}. \tag{3.31}$$

The most common implicit methods to solve Equation 3.31 are the implicit (or backward) Euler and the Crank-Nicholson techniques. In the former method, which is useful when solving for steady state, all the flux and source terms are evaluated based on the new variable value at the new time level [105]. When solving Equation 3.31, the Euler approach, as used in STAR-CCM+, has the mathematical form:

$$\phi_i^{n+1} = \phi_i^n + \left[\text{-}u\frac{\phi_{i+1}^{n+1} - \phi_{i-1}^{n+1}}{2\Delta x} + \frac{\Gamma}{\rho}\frac{\phi_{i+1}^{n+1} + \phi_{i-1}^{n+1} - 2\phi_i^{n+1}}{(\Delta x)^2}\right]\Delta t, \tag{3.32}$$

where the derivatives are evaluated by central differencing. In Equation 3.32, $\phi^{n+1} = \phi(t_{n+1})$ and ϕ_i^{n+1} is the desired new value of ϕ. This new term appears on the left and right hand side of Equation 3.32, showing the implicit nature of the scheme. Disadvantages of this method are that it is only first-order accurate in ϕ and requires a large amount of storage as commonly associated with implicit solvers.

The Crank-Nicholson method is second-order accurate and often used when the problem is genuinely unsteady. It is based on the average of ϕ at the old and new timesteps. Mathematically, when solving Equation 3.31 using Crank-Nicholson [105]:

$$\begin{aligned}\phi_i^{n+1} = \phi_i^n + \frac{\Delta t}{2}\left[\text{-}u\frac{\phi_{i+1}^{n+1} - \phi_{i-1}^{n+1}}{2\Delta x} + \frac{\Gamma}{\rho}\frac{\phi_{i+1}^{n+1} + \phi_{i-1}^{n+1} - 2\phi_i^{n+1}}{(\Delta x)^2}\right] + \\ + \frac{\Delta t}{2}\left[\text{-}u\frac{\phi_{i+1}^{n} - \phi_{i-1}^{n}}{2\Delta x} + \frac{\Gamma}{\rho}\frac{\phi_{i+1}^{n} + \phi_{i-1}^{n} - 2\phi_i^{n}}{(\Delta x)^2}\right].\end{aligned} \tag{3.33}$$

There are other schemes available for dealing with the time dependency of Equation 3.31, but these are not discussed here. One clear message is that mesh size and timestep independence cannot be taken for granted and must be tested by the practitioner. Even then errors may arise in a CFD simulation, hence increasing the need for experimental validation.

3.2.2 Experimental methods and theory

Work in this thesis is mainly of a numerical nature. However, in Chapter 6 some experimental validations are presented. Such validation is based on analysis of two different MLFs: one used as a reflector film and the other for heat seal purposes. For the former MLF, light microscopy was used to measure individual layer thicknesses of the cast (not stretched in either direction) film. For the latter film, fluorescence microscopy, die plug analysis, chloroform washing, white light interferometry (WLI) and reflectometry were used. This Section contains an overview of some of the operating principles and theory behind these experimental techniques.

3.2.2.1 Light microscopy

Light microscopy is mainly used by DTF to characterise large areas of a film surface and to a lesser extent to measure individual layer thicknesses of an MLF. The general aim of a light microscope is to use visible light to detect and magnify small images. The basic operating principle of light microscopy is as follows: polarised visible light passes through a glass mounted sample and then through two lenses which brings the sample into focus for the user looking through the eyepiece [138].

The method described above is simplified and would only work for a transparent sample. The microscope used by DTF is the Leica DMR [139], which has two main operational modes. These modes are *transmission* and *reflection* and are shown in a schematic of the Leica DMR (Figure 3.15). In transmission mode polarised light (path 1, Figure 3.15) generated using a bulb passes through the sample of interest (labelled 8 in Figure 3.15) into the eyepiece (labelled 17). This mode relies on a transparent sample. In

reflection mode a filtered light source (labelled 9) is deflected onto the sample surface, and then reflected off it. The light path then passes through the eyepiece. Both modes use magnification of lenses to obtain a more detailed image. The objective lens on the Leica DMR can be chosen as 1X, 5X, 10X, 20X or 50X for magnification. External software is used to characterise and measure any digitised images taken.

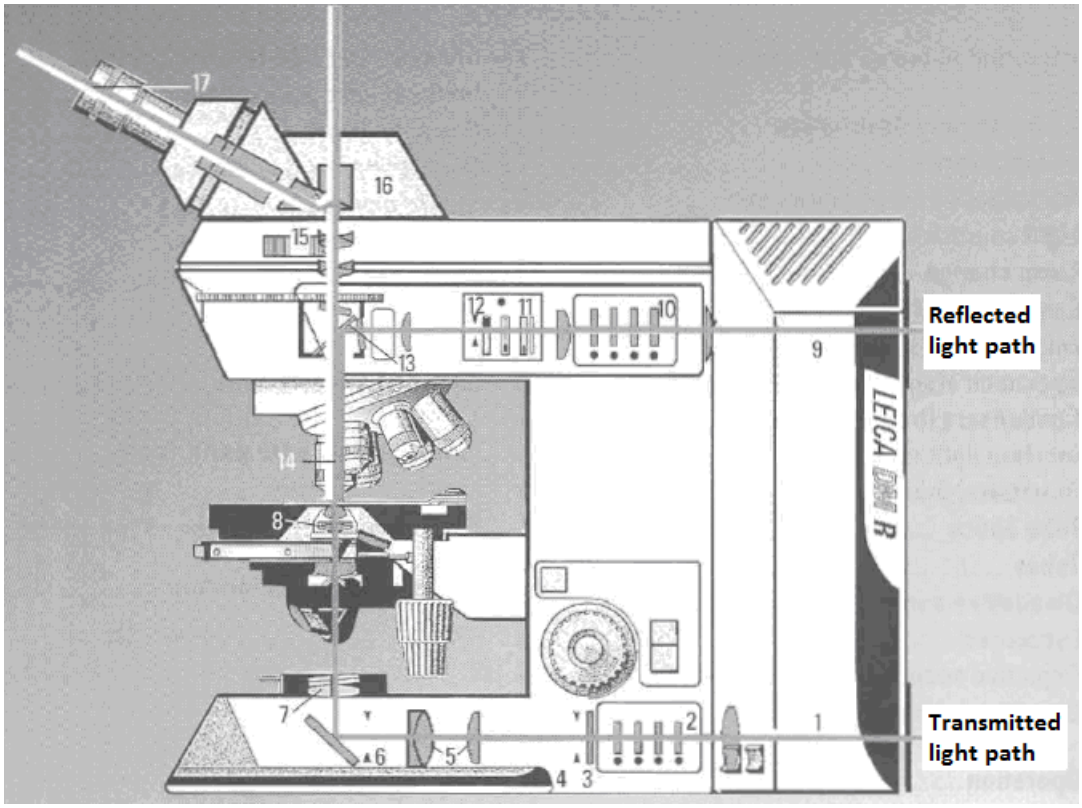

Figure 3.15: A schematic of the Leica DMR microscope. Diagram obtained from [139].

For the purpose of this thesis, light microscopy at 10X magnification was used to measure individual layer thicknesses of an ABA structured MLF, performed by DTF's microscopy technician. For MLF analysis, a cross section rather than the film surface is viewed. A microtome is used to cut a very thin material slice of the film. This sample is then mounted with blue-tac onto a glass slide and scrutinised. The individual layers of an MLF are found as light reflects off them via different paths. Using this approach the Leica DMR, operating in reflective mode, was used to characterise the reflector film across the whole film width. This is shown in Section 6.2.2. The individual layer composition, rather than the film surface, is important for this work. Polarised light microscopy has

been used to analyse multilayered structures before - as shown in [25, 85].

For the second MLF (used as a heat seal), the individual layers could not be distinguished from each other with standard light microscopy. This is because the two polymer layers were too similar optically. Fluorescence microscopy, performed by Intertek [42], was instead used to analyse the layers of a cast sample. The general operating principle of fluorescence microscopy is: light of a certain wavelength is absorbed by the sample, which then emits light at a longer wavelength and different colour upon excitation [140,141]. The contrasting layers of the MLF emitted light at different wavelengths, showing contrasting colours and making analysis possible.

Advantages of light microscopy are that it is quick, easy to learn and contact free. However, light microscopy offers a low resolution compared with surface metrology techniques and only 2D images are possible. Furthermore, it is only feasible to section and view cast, unstretched film under a microscope and individual layer thicknesses within final, biaxially oriented film samples cannot be viewed.

3.2.2.2 Die plug analysis

At the end of the pilot scale trial producing the AB structured heat seal film, the end fed die was rapidly cooled, causing solidification of the melt. This allowed the die to be stripped and the frozen die plug obtained. A small amount of red polymer (denoted red-PET) was added to the secondary layer, turning it pink in colour. This allowed the two layers to be distinguishable from each other as the primary layer was white. The aim of the die plug analysis was to observe how the different melt layers interact and evolve across the whole die width, and compare these findings with CFD. Photographs were taken of the die plug at certain widths across the die, hence allowing for a direct comparison with the CFD predicted melt composition at these widths. Similar die plug analysis (see Figure 2.21) has been conducted in publications such as [8, 46, 58, 89].

3.2.2.3 Chloroform washing

Chloroform (obtained from Sigma-Aldrich [142] and used as received) was used as a solvent for analysis of the heat seal film, applied to both cast and biaxially oriented samples. A small amount of chloroform was applied using a cotton bud, across the film width, to the film surface containing the secondary polymer. Since the secondary polymer is soluble in chloroform, but the primary PET based polymer is not, application of chloroform dissolves the secondary layer, leaving just the primary polymer. At each point of chloroform application, the film thickness was measured using a Sylvac D100S thickness gauge (calibrated using feeler gauges) before and after solvent application. This allowed the thickness of individual layers to be calculated and a secondary layer profile was obtained. For every sample analysed, three chloroform washes at each measurement location were conducted with the mean average taken. To the author's best knowledge there is no literature showing chloroform washing being used this way, demonstrating novelty in this work.

Chloroform washing is quick and easy to learn. However, this method can lead to errors in the thickness measurements. If the secondary layer is not cleaned effectively and there is still some on the surface the thickness calculation will be erroneous. Alternatively the chloroform may be applied too vigorously, causing a small removal of the primary polymer. The accuracy of this method is limited to the accuracy of the thickness gauge, which quotes results to a lower limit of 0.1 μm.

3.2.2.4 White light interferometry

White light interferometry (WLI, see Figure 3.16) is used at DTF to provide detailed film surface metrology at a higher resolution than light microscopy. The basic operating principal of WLI is as follows [143–145]: visible white light is split into two paths using a beamsplitter. One beam is reflected off a reference mirror (the reference beam) and the other off the glass mounted sample of interest (the test beam). These beams are then recombined using the beamsplitter. This rejoining of the two beams leads to interference or superposition of the waves. Since white light is a sinusoidal wave, the cumulative

amplitude will either increase or decrease on combination of the beams.

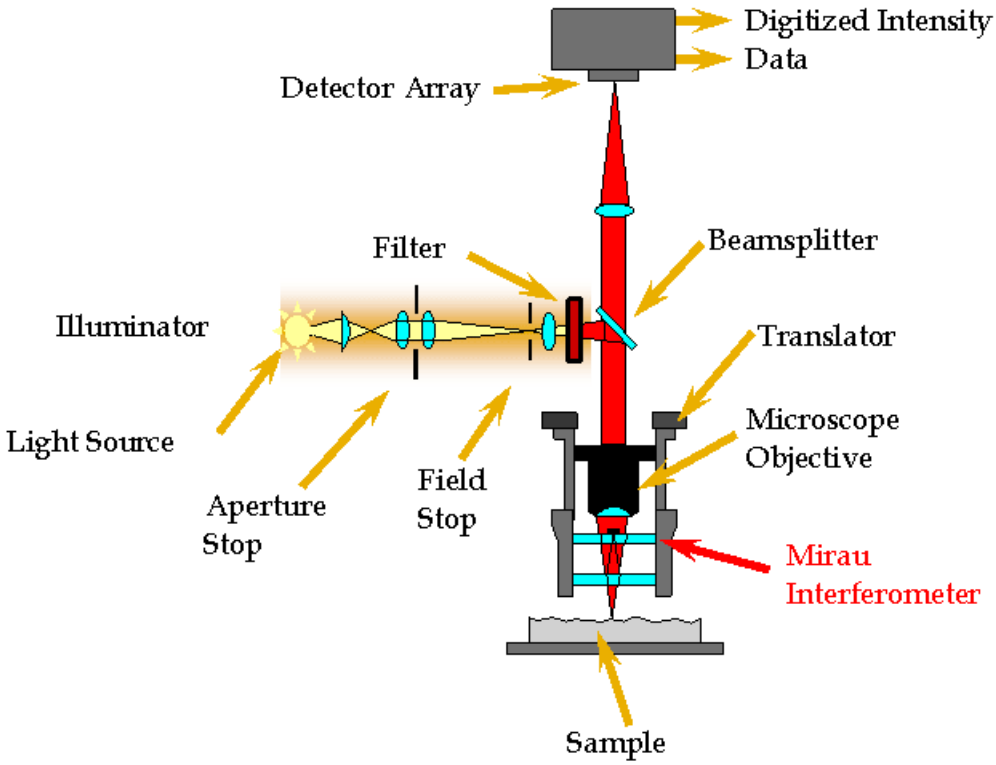

Figure 3.16: A schematic showing white light interferometry. Diagram obtained from [143].

The phase difference between the two waves results in an *interferogram*: a diagram showing the fringe separation between the waves [143,146]. The fringes of an interferogram will be either white or black, and the distance between two fringes is the wavelength between the wavefronts. A white fringe is *constructive*, where the amplitude has increased. Black fringes are *destructive* and show a decrease in amplitude. Figure 3.17 shows an example of an interferogram. When the interferogram appears in focus on a computer monitor, the aperture is tilted until only one wavelength covers the monitor and hence the sample [143]. Surface analysis is now possible and software converts the interferogram to produce surface data.

There are two main scanning techniques for WLI: phase shifting interferometry (PSI) and vertical shifting interferometry (VSI). PSI relies on a phase difference between the test and reference beams, caused by a shift in the interferometer by a known amount

Figure 3.17: An example of an interferogram. Diagram obtained from [143].

using a piezoelectic transducer [144, 145]. There is a minimum allowable quantity for the shift across a film surface and features too close together may not be captured. When the surface height difference between two adjacent points (or pixels) exceeds $\lambda/4$, where λ is the wavelength of the sample light, large height errors become evident. PSI is therefore suited to very smooth and flat surfaces [143–146].

In VSI, which is a more recent development than PSI, the interferometric objective moves vertically up and down near the sample to scan the surface at various heights, capturing more of the film surface slope information than PSI. To quantify the two techniques, PSI can measure pixel-to-pixel steps and slopes up to ≈ 135 nm whereas VSI can measure these up to 10 mm [145]. VSI is mainly used for rough surfaces that PSI cannot handle, for example a film surface full of a wide range of particle sizes [143–146]. VSI has an ability to scan rougher surfaces, but takes considerably longer to scan than PSI. If the surface has both rough and smooth parts, separate scans and a comparison between PSI and VSI is often made.

The author used the Veeco NT9800 WLI system [144], operating in VSI mode at 2.5X magnification, to measure the secondary layer thickness across the heat seal film width. WLI was applied to final, biaxially oriented film samples but *not* cast film because the secondary layer cast thickness is beyond the measurable limits of WLI. The thickness was calculated using the following method: an interferogram of the film surface, showing only one wavelength, was obtained. The interferometric objective was then lowered until a secondary interferogram showing the interface between the two layers appeared.

The software then calculates the *average* vertical distance between the two single wavelength interferograms, which equates to the secondary layer thickness. This is an average value because in the area being measured, the distance between individual pixels

is calculated with an average taken. This is in contrast with the chloroform washing method where a *single* thickness value was obtained. In every point where WLI was used, the total film thickness was measured using a thickness gauge, and the primary layer thickness calculated. For every sample analysed, WLI was performed three times at each measurement location, with an average secondary layer thickness profile obtained, thus allowing for a direct comparison with the chloroform washing results. WLI has never been used before to measure the individual layer thicknesses of an MLF. The minimum vertical resolution of the Veeco NT9800 when operating in VSI mode is 3 nm [144].

WLI is an efficient, non-contact technique where 3D images can be generated. Particles larger than 200 nm can be detected using WLI, allowing for significantly more detail than light microscopy. However, WLI requires a large amount of CPU storage and it can be difficult for a beginner to get the surface into focus. Also secondary layer thickness measurements are not always possible and rely on a refractive index mismatch between the different layers.

3.2.2.5 Reflectometry

The method of thin film reflectometry for secondary layer thickness measurements was attempted, but the results obtained were unrealistic (too thin secondary layers measured) and are not considered of much relevance for the purpose of this thesis. Reflectometry is only described briefly here. For a more detailed review of the principles of reflectometry, the reader is directed towards [147–149].

An MLF sample is cleaned and mounted with white light directed towards the surface. Assuming a sufficient optical contrast between the polymer layers, light is reflected off each surface and interface, producing different paths. This multiple reflectance produces interference fringes since the light paths are out of phase. The more fringes observed, the thicker the secondary layer. Software is used to convert the fringe pattern into a secondary layer thickness measurement. This type of reflectometry relies on *specular reflection*; when the angle of incidence is equal to the angle of reflection from a surface [150].

Reflectometry requires a flat surface and a uniformly thin secondary layer. This tech-

nique was attempted alongside chloroform washing and WLI (see Section 6.3.2.2). However, reflectometry gave secondary layer thicknesses significantly less than what was expected, especially when compared with results for the other two techniques, and were believed to be erroneous. These errors are believed to be due to either the polymer layers being too optically similar or partial crystallisation of the secondary layer.

3.2.2.6 Time-of-Flight Secondary Ion Mass Spectrometry

When applying chloroform washing to final, biaxially oriented film samples, the secondary layer thickness was found to be too low compared with the equivalent WLI and CFD results. A suggested reason for this is partial crystallisation of the secondary layer at the polymer-polymer interface when stretching and heating the film. Partial crystallisation of the amorphous secondary polymer would have resulted in a thin crystalline region that was insoluble in chloroform.

A method used to test the partial crystallisation theory was Time-of-Flight Secondary Ion Mass Spectrometry (ToF-SIMS) surface analysis. The general operating principal of ToF-SIMS is as follows [151, 152]: a primary positive ion source is directed towards a surface of interest. This causes charged secondary ions of varying size characteristic of the surface to be emitted. These secondary ions are detected by a time-of-flight detector and hence converted into a positive ion spectrum. The resulting spectrum can distinguish between different sized molecules because of their difference in mass and is then analysed to determine the overall surface composition.

ToF-SIMS, using a Bi_3^{2+} ion source, was applied to three different surfaces on the AB structured heat seal film: the untreated primary and secondary sides and the secondary side *after* applying chloroform (the polymer-polymer interface). The spectrum for the chloroform treated secondary side was then compared with the primary and secondary spectra to determine whether any secondary polymer was present at the interface. The three ToF-SIMS spectra were recorded with 200 μm × 200 μm analysis areas.

ToF-SIMS is a high resolution method, also offering high detection sensitivities [153]. The lateral resolution of this technique is 50 nm and the surface depth resolution is 1 nm.

The ToF-SIMS detection sensitivities are in the low parts per million range.

3.2.2.7 Experimental methods explored but not used

For analysis of MLFs and polyester coextrusion in general, a number of further experimental validation methods were explored but not used. An example of this is spectroscopic ellipsometry [154], which is used by DTF to measure individual layer thicknesses. However, for both the reflector and heat seal films investigated, the secondary layers were too thick to be characterised this way. Atomic force microscopy (AFM [155]) was also considered for individual layer thickness calculations of the heat seal film. AFM is, however, expensive and difficult to learn, and is beyond the scope of this study. For experimental interpretation of the flow and subsequent combination of polymer melt layers within the coextrusion process, the introduction of radioactive tracer particles to DTF's extrusion systems, via positron emission particle tracking (PEPT [156]), was contemplated. Due to the heated metal walls of DTF dies being very thick, likely to be difficult to bypass with PEPT, and safety concerns relating to the radioactive nature of PEPT, this was not attempted.

Chapter 4

Using Computational Fluid Dynamics to model a pilot scale geometry

4.1 Introduction

In this first results Chapter, a pilot scale DTF coextrusion system is modelled using CFD. The geometries investigated are an injector block linked to a 330 mm wide end fed die. The modelled geometries are representative of DTF equipment used in The Wilton Centre. As well as modelling the coextrusion domain in standard form, geometrical modifications such as increasing the die land length and altering the injector block are also shown.

The aim of the work in this Chapter is to analyse the ability and limitations of STAR-CCM+ to model simple DTF geometries. Numerical accuracy is also investigated, with both the mesh and timestep size altered. This Chapter provides a foundation for the remaining results Chapters, where more complex geometries and polymer properties are modelled.

This Chapter is structured as follows: Section 4.2 shows CFD modelling of an injector block linked to a *standard* die. Modelling of a *high-resolution* die is presented in Section 4.3. The effect of modifying both the injector block and the die is shown in Sec-

tion 4.4. Numerical accuracy, in the form of mesh and timestep independence studies, is investigated in Section 4.5.

4.2 Standard die

The die modelled in this Section is a narrow DTF pilot scale die. Using engineering drawings, the injector block and 330 mm wide end fed die were created and meshed in STAR-CCM+. Figures 4.1 and 4.2 show the coextrusion domain, where Figure 4.1 displays the meshed injector block and Figure 4.2 shows the end fed die in both geometry (Figure 4.2a) and mesh form (Figure 4.2b). The flow direction in both figures is from left to right.

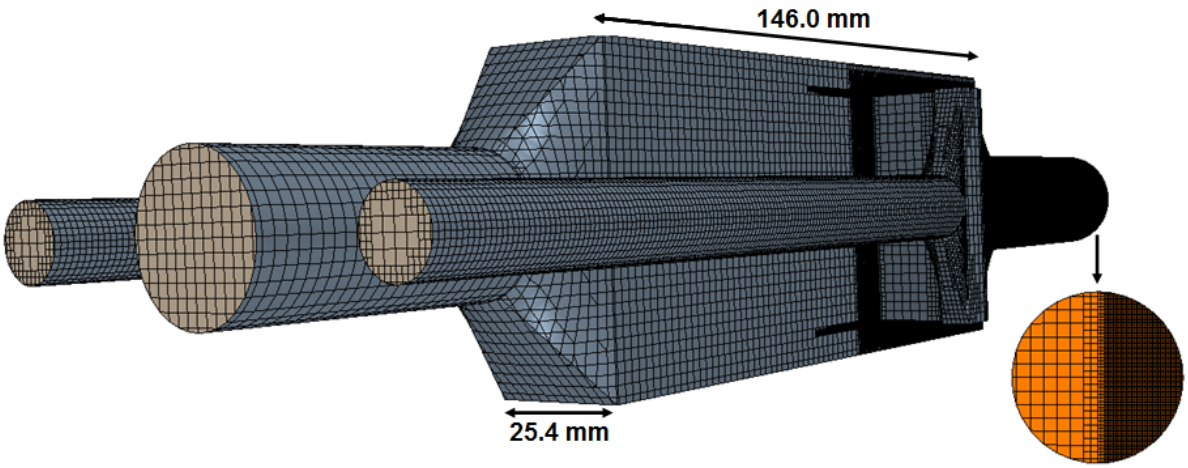

Figure 4.1: The meshed injector block geometry used in CFD. The flow direction is from left to right.

Throughout this Chapter, AB structured MLFs are produced, where B is the primary polymer and A is the secondary polymer. In the injector block, B enters via the central and left inlet ports with A entering from the right. For all the simulations in this thesis, B is used to initialise the problem and fill the geometry. The secondary A layer then dislodges or "flushes out" B upon entering the geometry. The melt layers come into contact in the main part of the block and leave as a unified AB melt structure. Four fins (see Figure 2.9, Section 2.3) are placed both above and below the secondary channel

entrances to promote clear edges. The width of each fin is 8.0 mm, together making up 63.0 % of the injector block width.

Around 4.5 million mesh cells were required to discretise the injector block geometry. A trimmer mesh with hexahedral template cells was used. A base mesh cell size of 2.0 mm was used alongside a minimum mesh cell size of 0.1 mm. This finer mesh was selected in the region where the different melt layers are in contact with each other, trying to maintain as smooth an interface as possible and reduce any numerical smearing. There are 57 mesh cells across the width of the outlet port, compared with 13 across the width of the primary inlet port. The outlet diameter is 23.75 mm. A finer injector block mesh is shown in Section 4.4.1.

The injector block outlet solution (volume fraction, velocity and temperature) was taken as an initial condition into the end fed die (Figure 4.2). This is then converted into a uniformly thin rectangular outlet plot representative of the final film solution. The injector block and die were modelled separately as modelling them together is very expensive computationally. The exit die gap increases linearly (is tapered) from 3.2 to 3.3 mm across the 330 mm width to ensure a uniform exit flow across the die width. The inlet duct diameter is 23.75 mm, reducing to 22.25 mm, and the *land* length (see Figure 2.12) is 6.3 mm.

Around 8 million mesh cells were used for the end fed die (shown via plane sections in Figure 4.2b), again using a trimmer mesh with hexahedral template cells. Tetrahedral and polyhedral meshes are also available in STAR-CCM+. All simulations in this thesis use the trimmer mesh rather than the other two options. This is because trimmed meshes offer faster convergence times for large cases [107, 108]. Furthermore, for multiphase systems using the VOF method, the trimmer mesh is aligned with the flow direction in geometries such as those modelled here. This allows for excellent interfacial capturing and easy refinement of the interface. A mesh independence study is shown in Section 4.5.1.

For the end fed die, a base mesh cell size of 0.75 mm was used alongside a minimum mesh cell size of 0.188 mm. Fine mesh regions were selected in the transition region from horizontal to vertical flow, since this sharp directional change is difficult to resolve numer-

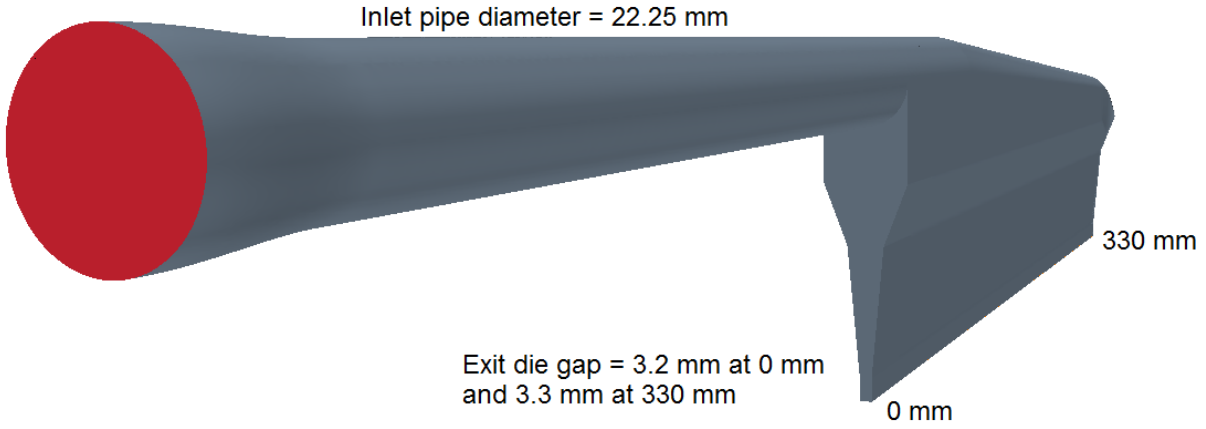

(a)

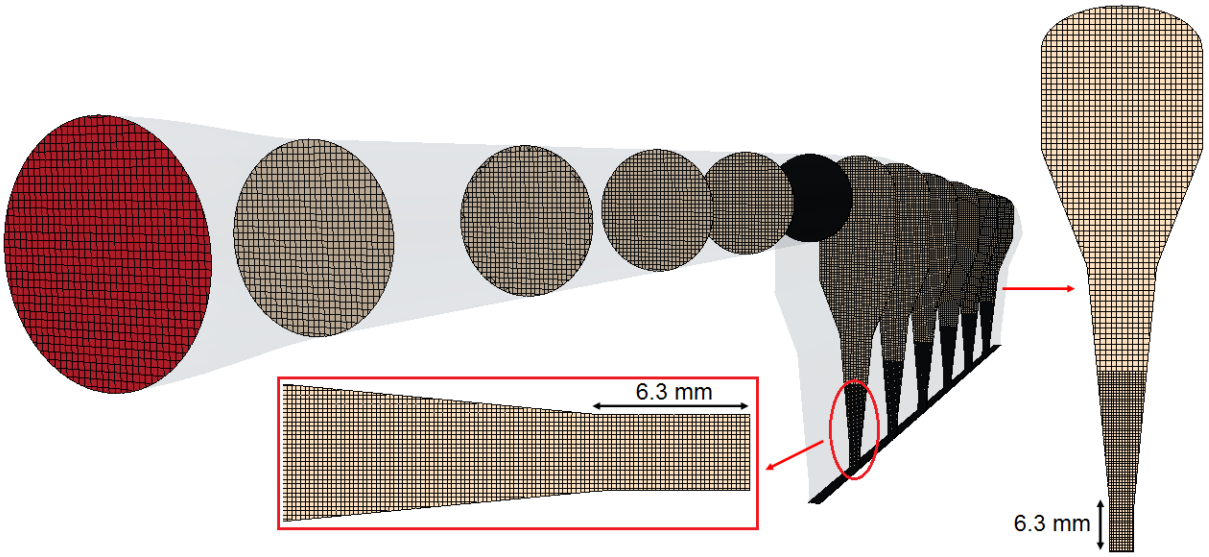

(b)

Figure 4.2: The end fed die used in CFD where (a) shows the geometry and (b) shows the mesh. The flow direction is from left to right.

ically, and across the thin rectangular outlet. An outlet volume fraction plot corresponds to the CFD predicted final film layer thickness solution and the mesh should be as fine as possible here. There are 16 mesh cells across the *feed edge* (FE, see Section 2.3) outlet at 0 mm and eight cells across the blank edge (BE) outlet at 330 mm. The two polymer melt layers are in contact within the end fed die, changing direction along its length. Therefore, to maintain a smooth interface the mesh cell density is kept fine throughout rather than trying to locally refine along the interface.

Implicit unsteady physics was used with a timestep of 0.05 seconds per iteration. This compares with a mean pipe velocity of > 100 mm s^{-1} through a base mesh cell size of 2 mm or < 0.02 s (see Section 3.2.1.1 for further information). Other physics used includes the VOF method, laminar flow and Eulerian multiphase. These timestep and physics conditions are used throughout this thesis unless otherwise stated. It was assumed that uniform flow from each extruder was delivered to each of the injector block inlet ports as development length scales are short.

Table 4.1 shows the physical characteristics assigned to both B and A throughout this Chapter unless otherwise stated, where standard PET melt properties are used and a Newtonian assumption is maintained. For these base cases, the melt layers are identical except for a 10 Pa s melt viscosity difference, with the more viscous A making up 15 % of the overall flow rate. The mass flow rate of B is split between 70 kg hr^{-1} into the main injector block inlet port (Figure 4.1) and 15 kg hr^{-1} through the left port. Viscosity is a function of temperature for PET melt flows, but is taken to be temperature and shear rate independent here. The viscosities quoted in Table 4.1 are observed within a shear rate range of $\dot{\gamma} \leqslant 150$ s^{-1}. The temperature of both the injector block and end fed die is 285 °C, an isothermal problem.

Table 4.1: The modelled fluid properties for B and A.

	B	**A**
Temperature (T)	285 °C	285 °C
Density (ρ)	1,250 kg m^{-3}	1,250 kg m^{-3}
Viscosity (η)	170 Pa s	180 Pa s
Thermal conductivity (κ)	0.2 W m^{-1} $°C^{-1}$	0.2 W m^{-1} $°C^{-1}$
Mass flow rate ($\dot{m}$)	85 kg hr^{-1}	15 kg hr^{-1}
Final volume fraction	85 %	15 %

The progressive volume fraction of Polymer B is shown in Figure 4.3, for 4.3a the injector block and 4.3b the end fed fed die, where the flow direction is from left to

right. There is a relatively smooth interface between B and A in each figure, with both polymers clearly defined and distinguishable. This implies that the mesh is sufficiently fine for each geometry and the interfacial region between B and A is confined to one or two mesh cells.

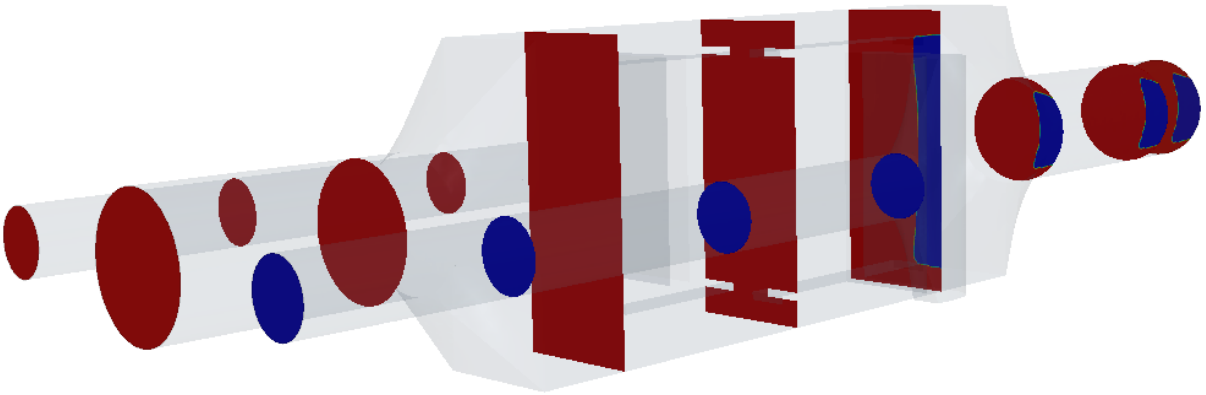

(a)

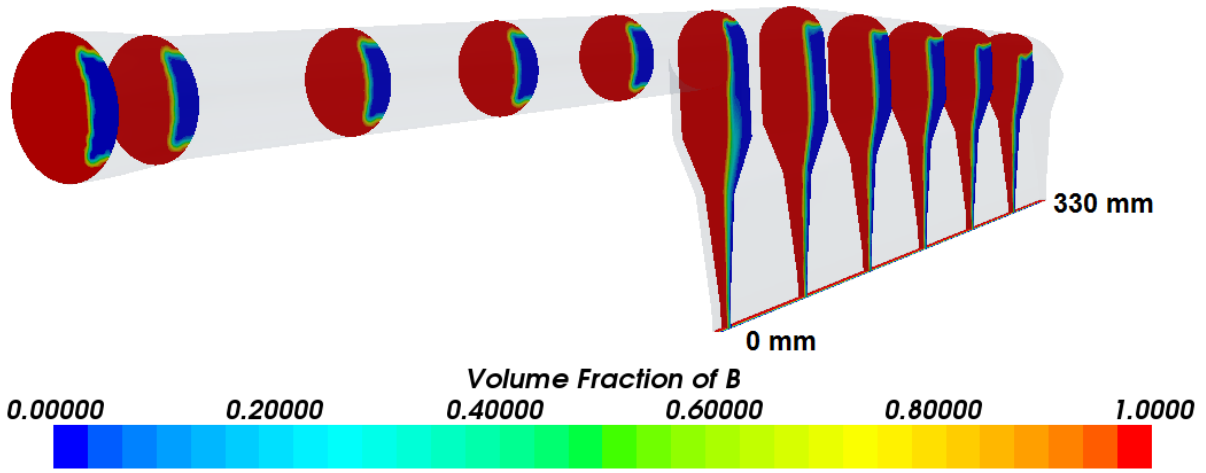

(b)

Figure 4.3: The progressive volume fraction of B (shown in red) through both (a) the injector block and (b) the 330 mm wide end fed die. The flow direction is from left to right. The volume fraction of A is shown in blue.

The interface is sharper within the injector block. This is because the minimum mesh cell size is smaller in the block, which is possible because the fluids are only in contact for the final section of the geometry. The amount of interfacial smearing between B and A is

a direct function of the mesh cell size and would be reduced with a finer mesh across the die. In this study, as with all CFD investigations, one must make a compromise between mesh density and convergence times. Using 8 million mesh cells to discretise the end fed die geometry resulted in a convergence time of approximately four days. Significant mesh refinement and hence smoothing of the interface in Figure 4.3b to match that in Figure 4.3a would dramatically increase the convergence time. It is not feasible to use very fine meshes for this project and the interfacial smearing within the 8 million cell mesh is taken to be acceptable given the already high convergence time observed.

Constant mass flow rates rather than parabolic velocity profiles were implemented at the three injector block inlets, see Table 4.1. For laminar flow in a pipe of diameter D, the development length for a parabolic velocity profile, L_D, is given as [157]:

$$L_D = 0.06 \times D \times Re, \tag{4.1}$$

where Re is the Reynolds number. For $D = 23.75$ mm and $Re = 8.0 \times 10^{-3}$ (modelled here), $L_D < 1$ mm. This justifies the use of constant mass flow rates, since a parabolic velocity profile develops almost immediately within the three injector block inlet pipes.

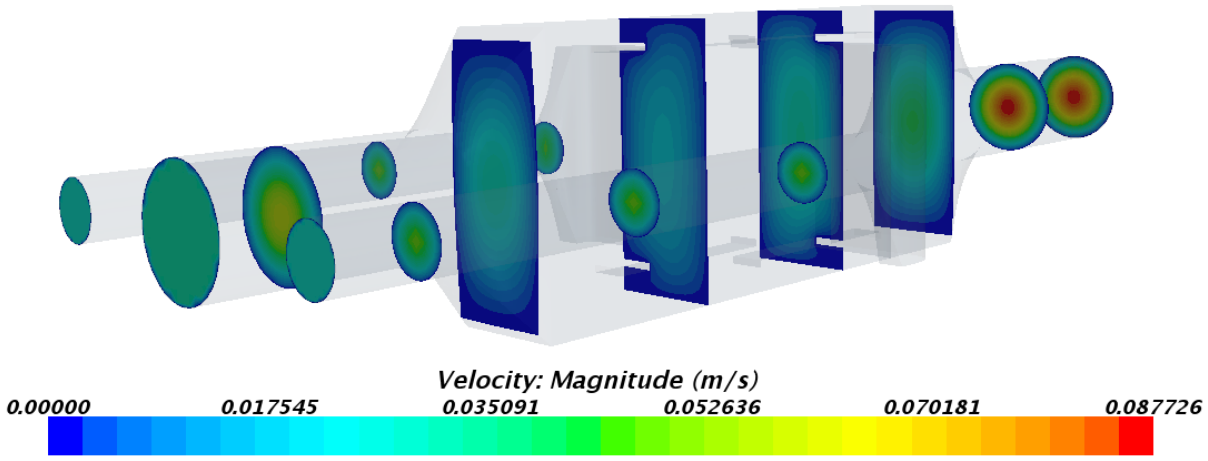

Figure 4.4: The progressive velocity magnitude through the injector block. The flow direction is from left to right.

Figure 4.4 shows the progressive velocity magnitude through the injector block. A fully developed parabolic velocity profile is observed very near to the inlet planes, again confirming the short development length. The parabolic velocity profile at the injector block

outlet is taken as an initial condition into the end fed die geometry, which is maintained across the die width (see Figure 4.9).

4.3 High-resolution die

The die analysed in Section 4.2 is a DTF die that is no longer used very frequently. A *high-resolution* die, with a 25 mm land length, is modelled in this Section. Since this is more commonly used at DTF, results for this die are shown in greater detail. The injector block used to feed this high-resolution die is shown in Figure 4.1. The work shown in Section 4.2 was conducted to provide a base case for the more relevant high-resolution die modelling. Furthermore, a finer mesh was selected for the high-resolution die compared with the standard die, showing the effect of increasing the mesh density on the final film structure.

Figure 4.5 shows the high-resolution die used in CFD, where Figure 4.5a shows the geometry and Figure 4.5b displays the mesh via a number of plane sections. The (unmeshed) FE for this geometry is also shown in Figure 2.12. The degree of tapering between the FE and BE has increased to improve the flow uniformity for this geometry. The inlet pipe leading to the die is 196 mm long.

Approximately 16.5 million mesh cells were used for the die in Figure 4.5b. Although this is more than double the number of mesh cells used for the die in Section 4.2, the mesh density is within the limits of the computational capability available to the author (an approximate convergence time of seven days) and a finer mesh was required to give a more accurate solution. A base mesh cell size of 0.5 mm was used alongside a minimum of 0.125 mm, where this finer mesh was selected to cover the bottom half of the land region and the outlet from FE to BE. It was observed that having a uniform mesh density across the outlet width gives a constant film solution and is advantageous for the purpose of this work. There are 24 mesh cells across the outlet FE and 26 across the BE, where this increase is caused by the tapering.

Figure 4.6 shows the progressive volume fraction of B through the high-resolution die.

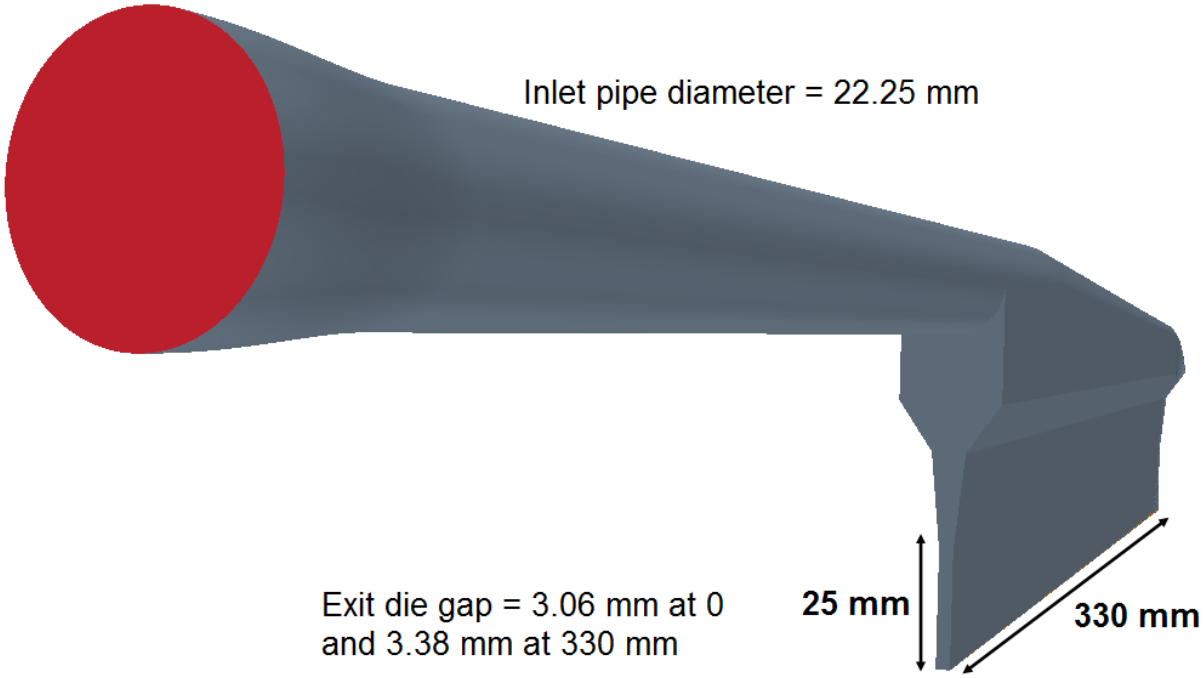

(a)

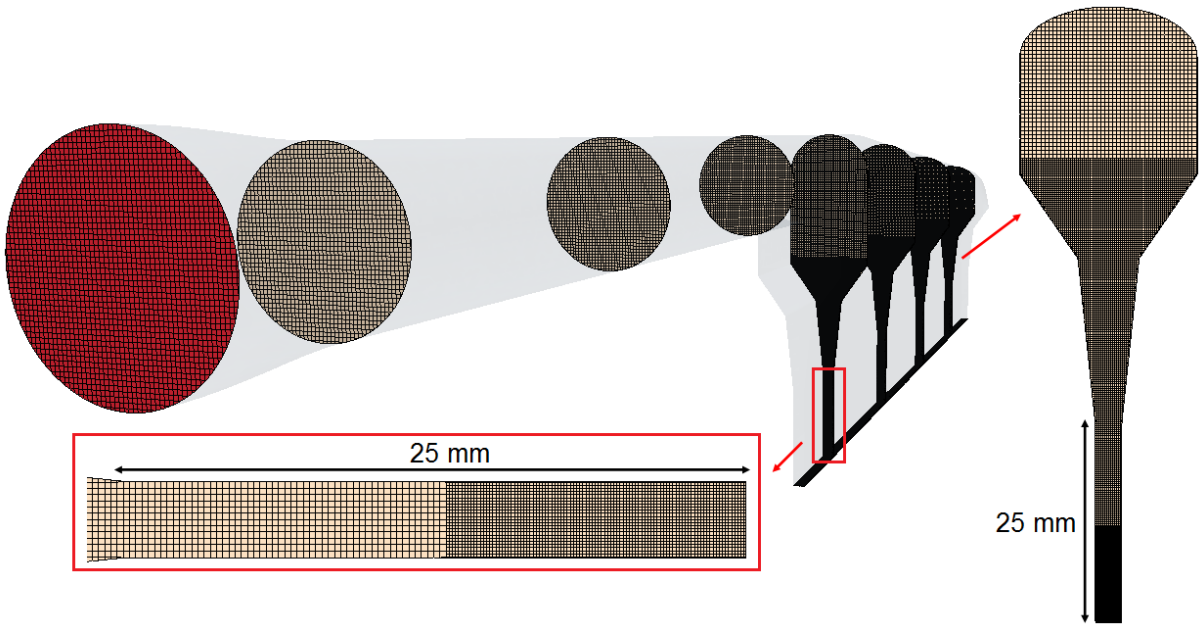

(b)

Figure 4.5: The high-resolution end fed die used in CFD, where (a) shows the geometry and (b) shows the mesh. The flow direction is from left to right.

Here, a smooth interface between B and A is observed throughout the geometry. This interface is sharper than that in Figure 4.3b, attributed to the finer mesh used for the high-resolution die. Figure 4.7 shows the volume fraction plot at the die outlet, where Figure 4.7a shows the FE to 50 mm, Figure 4.7b shows the middle, from 140 to 190 mm and Figure 4.7c displays the far edge, from 280 to the BE at 330 mm.

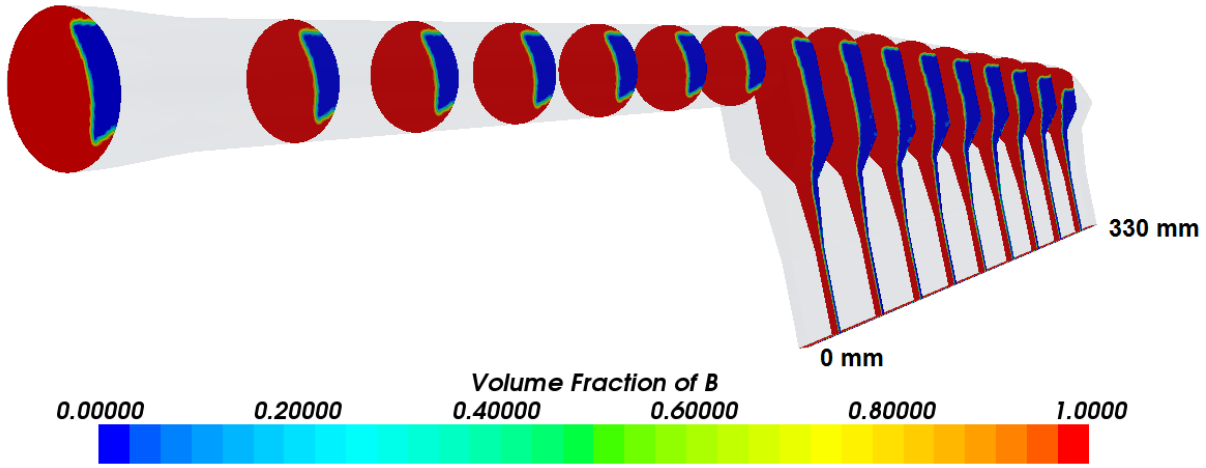

Figure 4.6: The progressive volume fraction of B (shown in red) through the high-resolution end fed die. The flow direction is from left to right. The volume fraction of A is shown in blue.

The outlet plot in Figure 4.7 represents the CFD predicted final film structure. Polymer A is present at the FE, showing that clear edges are *not* attained for this problem. The lack of numerically predicted clear edges is despite previous DTF pilot scale trials showing that clear edges are attainable with this geometry and polymer properties modelled. The presence of Polymer A at 0 mm is believed to be caused by numerical diffusion errors, which are particularly prevalent at the sharp 90° transition from horizontal to vertical flow upon entering the die body [33]. Near the FE, the amount of A decreases and seems to be approaching zero as one would expect, but then it increases at the extreme edge and it is around this region where the numerical diffusion errors are believed to occur. The lack of clear edges predicted numerically at the FE is investigated further in Sections 4.4 and 4.5.

Numerical diffusion errors occur in convection dominated flows [105, 110, 132]. The

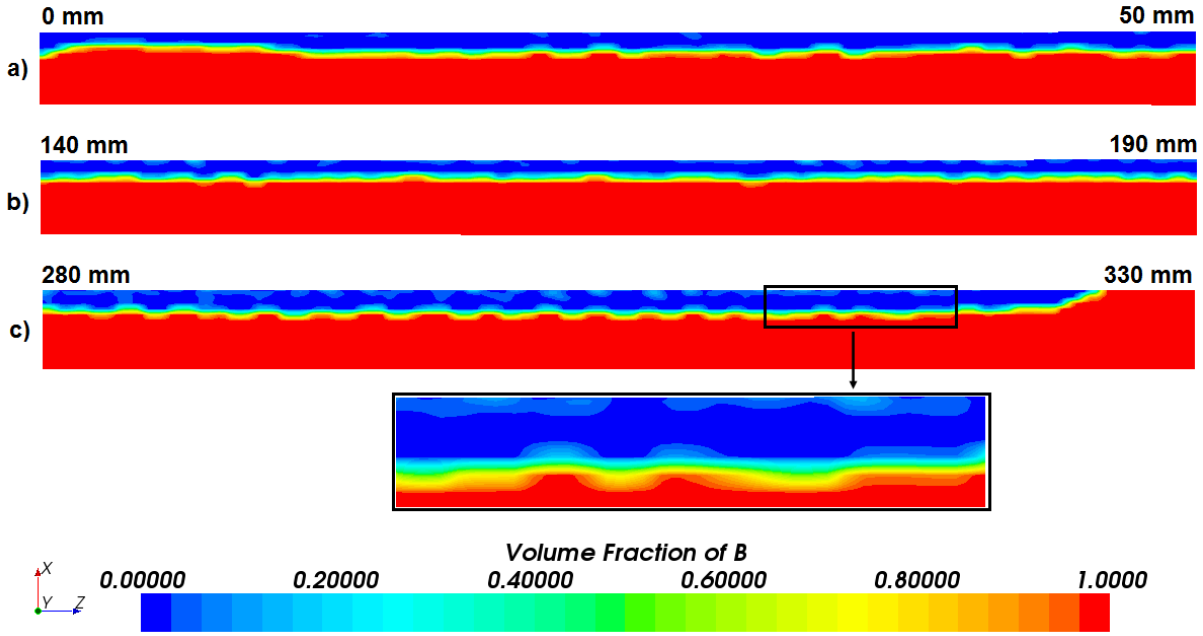

Figure 4.7: The volume fraction of B (shown in red) at the die outlet showing: (a) the 0 mm edge, (b) the middle and (c) the 330 mm edge. The volume fraction of A is shown in blue.

sharp change in direction from horizontal to vertical flow in the end fed die is convection dominated, and it is here that the diffusion errors are believed to occur. Implementing a higher order discretisation scheme has been shown to reduce such errors [110]. For all the CFD simulations in this thesis, a second-order accurate version of the upwind discretisation scheme (see Equation 3.22 for a first-order version of this) is used. It is possible that using the VOF method alongside the third-order accurate QUICK approach (see Equation 3.23) would have yielded clear edges. QUICK is not currently available within STAR-CCM+, but this and other high-order accuracy schemes should be tested in the future. Another approach to reduce numerical diffusion errors is to refine the mesh in problematic regions [105, 110, 132]. Certain software packages other than STAR-CCM+ offer automatic re-meshing of problematic sections of a geometry based on preliminary solution gradients. This study relies on *manual* mesh refinement and would have benefited from a degree of automatic meshing.

A progressive normal stress plot (see Equations 2.20 and 2.27) through the die in

Figure 4.8 shows a large increase in stress at the transition region, again highlighting the difficulties in capturing the flow here and justifying the theory of numerical diffusion errors causing the lack of clear edges. Increasing the mesh density around the transition point may reduce the numerical error here and lead to clear edges at both the FE and BE. However, the mesh used here is near the limit of the computational power available to the author and such refinement would vastly increase convergence times. In Section 4.4, modifications are made to both the injector block and end fed die to investigate this clear edge problem further.

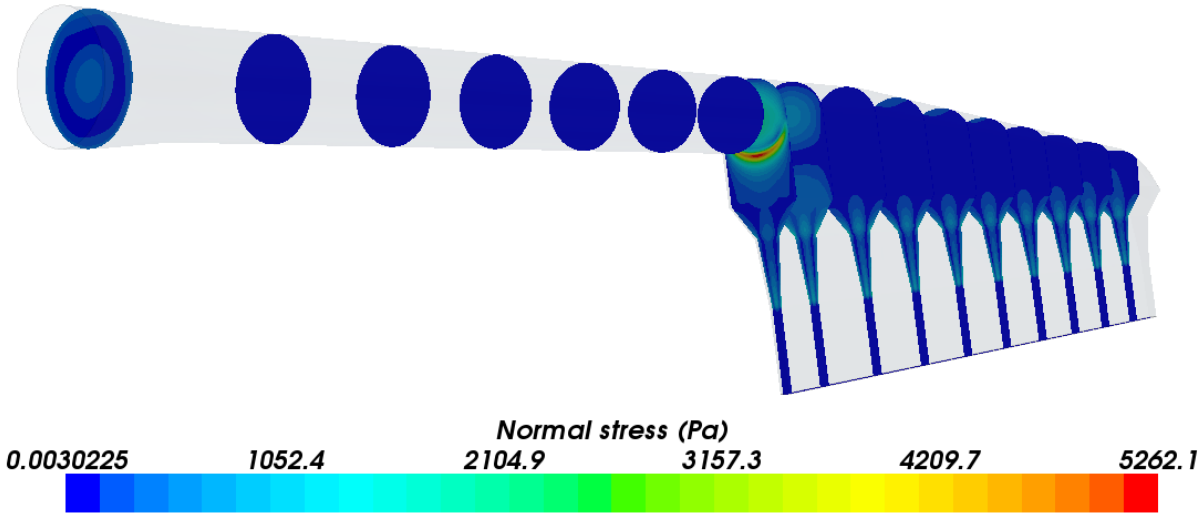

Figure 4.8: The progressive normal stress through the end fed die.

Apart from the presence of A at the FE, the outlet plot and other results within this Section are representative of what one would expect of a DTF AB MLF. There is a BE clear edge width of 4.1 mm and the interface is linear and well defined. Within the blue A layer near the wall, there are some slightly different coloured regions (see Figure 4.7c), caused by Polymer B not being fully dislodged by Polymer A. The polymer melt layers used throughout this thesis are slow moving, highly viscous and it is therefore time consuming to fully displace one fluid with another at the wall where the velocities are very low. The outlet volume fraction plot in Figure 4.7 was obtained after 8,203 seconds, far exceeding the mean residence time of 18 seconds in such a die (a multiple of 455.7). The patches within the A layer are of a very low volume fraction and are assumed to

make up this layer.

The progressive velocity magnitude through the high-resolution die is shown in Figure 4.9. Here, typical laminar flow is observed with a maximum velocity of 11.3 cm s^{-1} found in the middle of the inlet pipe. The velocity increases from the inlet duct to the pipe because of a reduction in diameter. There is a minimum velocity of zero at the geometry walls, found because of the no-slip condition imposed here.

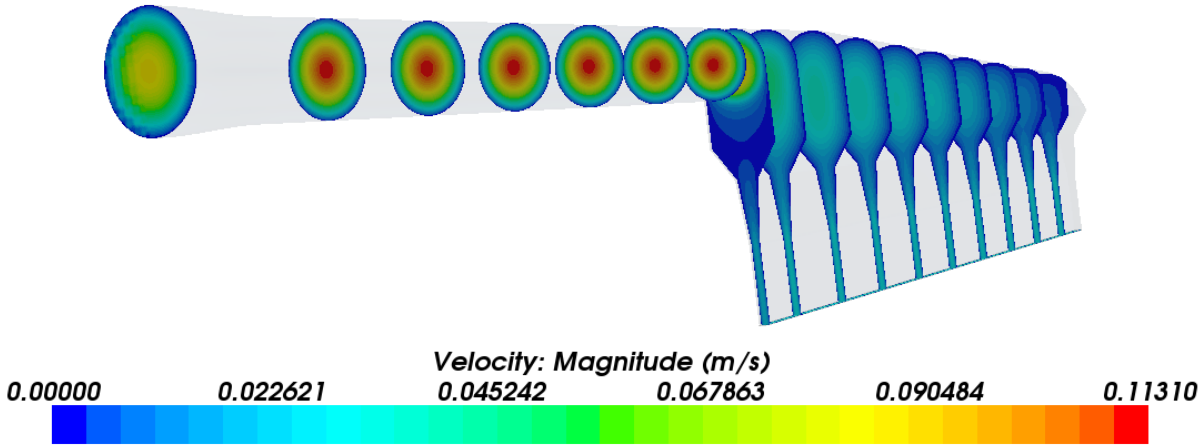

Figure 4.9: The progressive velocity magnitude through the end fed die.

The volumetric flow rate per unit width was derived for both the total and Polymer A flows, with the flow curves plotted in each case. These curves correspond to the CFD predicted total film and A layer thickness profiles across the die width. To derive the *total* flow curve, lines were created in the CFD domain across the exit die gap from 0 to 330 mm in increments of 2 mm near the edges and increments of 5 mm in the middle of the die. The outlet velocity magnitude was then integrated across each line using STAR-CCM+, yielding the total volumetric flow rate per unit width (measured in m^2 s^{-1}) for every line. For the *Polymer A* flow curve, the same procedure was performed on lines spanning the A outlet location from the top outlet wall (see Figure 4.7) to the $F = 0.5$ interfacial location, where F is the volume fraction function.

For such flow curves presented throughout this thesis, the velocity profiles are integrated within the total, primary and secondary flow regions across the die land outlet width, yielding individual flow rates (in m^2 s^{-1}). It is assumed that these flow values cor-

relate with the ratio of the individual layer thicknesses in the *final* film. This assumption is justified since in the film process, the die exit melt curtain is frozen by a casting drum before being stretched. Therefore, flow rate will correlate to volume for a given density.

These total and Polymer A flow curves are shown graphically in Figure 4.10. Interpretation of the *total* flow curve shows that the film is predicted to be thicker at the BE than the FE. The percentage difference between the flow values at 8.5 and 317.5 mm is 8.24 % with respect to the thicker value. This suggests a slight over tapering of the die gap from FE to BE which is causing a thicker film at the BE. The exit die gap values used for the CFD geometry were based on DTF engineering drawings. As well as tapering the die, DTF also use profile heaters to modify melt viscosity locally in the die land to improve the thickness profile. Another feature of high-resolution dies is that there are more heaters across the land than in standard dies, allowing for finer control of the film thickness. Such heaters are modelled in Chapter 7 and would be used to give a flatter film profile.

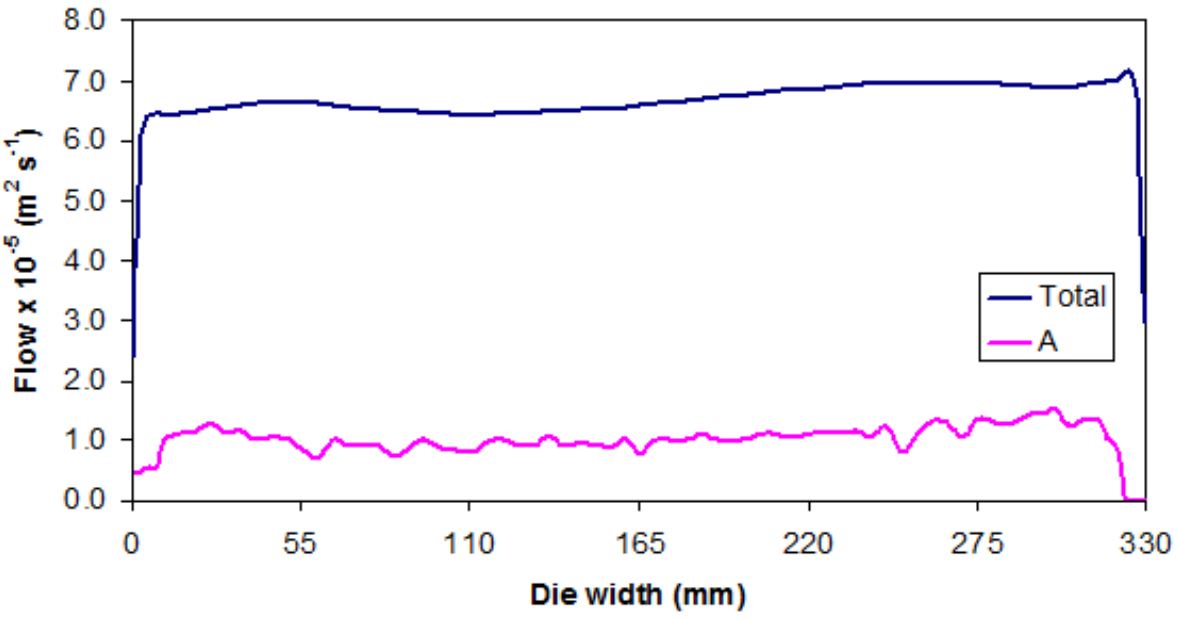

Figure 4.10: The total and A outlet flows across the 330 mm die width.

The A flow curve in Figure 4.10 highlights the non-symmetrical nature of the film produced numerically; Polymer A is present at the FE but *not* the BE (see also Fig-

ure 4.7). An equivalent percentage flow difference calculation for A yields 2.0 %, which is less extreme than the total flow. There is significantly more noise in A than the total data. This is because the flow calculations to obtain the A curve are based on numerical approximations of the exact interfacial location. At the die outlet, the $F = 0.5$ interfacial contour changes position within a mesh cell when moving from 0 to 330 mm across the die. The outlet mesh is coarse with respect to the $F = 0.5$ contour so the exact $F = 0.5$ interfacial location cannot be determined precisely. To amend for this, STAR-CCM+ uses a smoothing function (linear in the flow direction) to estimate the $F = 0.5$ position in every mesh cell. This leads to noisy data which would be ameliorated with a finer mesh or smoothing the data in the axial direction (such smoothing is demonstrated in Section 4.5.1), showing numerical limitations of this work. For the purpose of this thesis, the overall trend of Polymer A rather than the noise is important.

4.4 Geometrical modifications

The CFD results in Section 4.3 are what one would expect apart from the lack of a clear edge at the FE. As mentioned, this is believed to be caused by numerical diffusion errors at the sharp transition point from horizontal to vertical flow. In this Section, modifications are made to both the injector block (Section 4.4.1) and the end fed die (Section 4.4.2) to further investigate this clear edge problem.

4.4.1 Modifying the injector block

To try obtaining numerical clear edges, the height of the injector block secondary channels was reduced from 48.0 (as used in Sections 4.2 and 4.3) to 30.0 mm and the width of each fin was increased from 8.0 to 10.0 mm, now separately making up 39.4 % of the block width. These changes are speculative and not representative of a DTF injector block. The aim of these alterations is to keep A confined to the middle of the block. Furthermore, the mass flow rate of A was reduced from 15 to 5 kg hr^{-1}, again promoting clear edges.

Figure 4.11 shows the meshed modified injector block, where the reduced secondary

channel height compared with that in Figure 4.1 is observed. A total of 7 million mesh cells were used for this new injector block, with a base cell size of 2.0 mm and a minimum cell size of 0.08 mm. This finer mesh at the injector block outlet compared with that used in Sections 4.2 and 4.3 also encourages clear edges since the interface will be finer leading into the die and thus the solution should be more accurate.

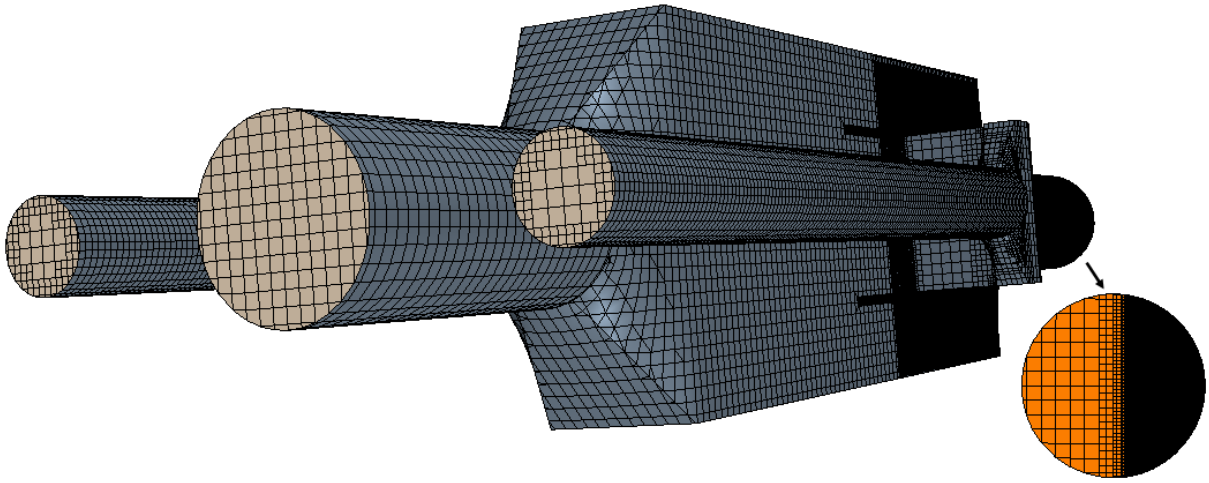

Figure 4.11: The meshed modified injector block geometry.

The progressive volume fraction of B through the modified injector block is shown in Figure 4.12. The outlet solution shows that the geometry and flow rate changes have caused the blue A layer to remain confined to the middle of the pipe. Therefore, one would expect clear edges to be produced since A is very far from the top and bottom of the pipe and this should promote the flow of A towards the middle of the die outlet.

The injector block outlet solution was then taken as an inlet condition into the end fed die from Section 4.3 and then converted into a melt curtain. Figure 4.13 shows the die outlet volume fraction plot where Figure 4.13a shows the FE to 45 mm, Figure 4.13b shows the middle, from 140 to 185 mm and Figure 4.13c displays the far edge, from 285 to the BE at 330 mm.

Figure 4.13a shows that there is still some A present at the FE and clear edges are not attained. This is despite the modifications made and the injector block outlet solution (Figure 4.12) suggesting that clear edges will be found. The flow composition is symmetric at the injector block outlet, but not at the die outlet, which shows a clear edge width

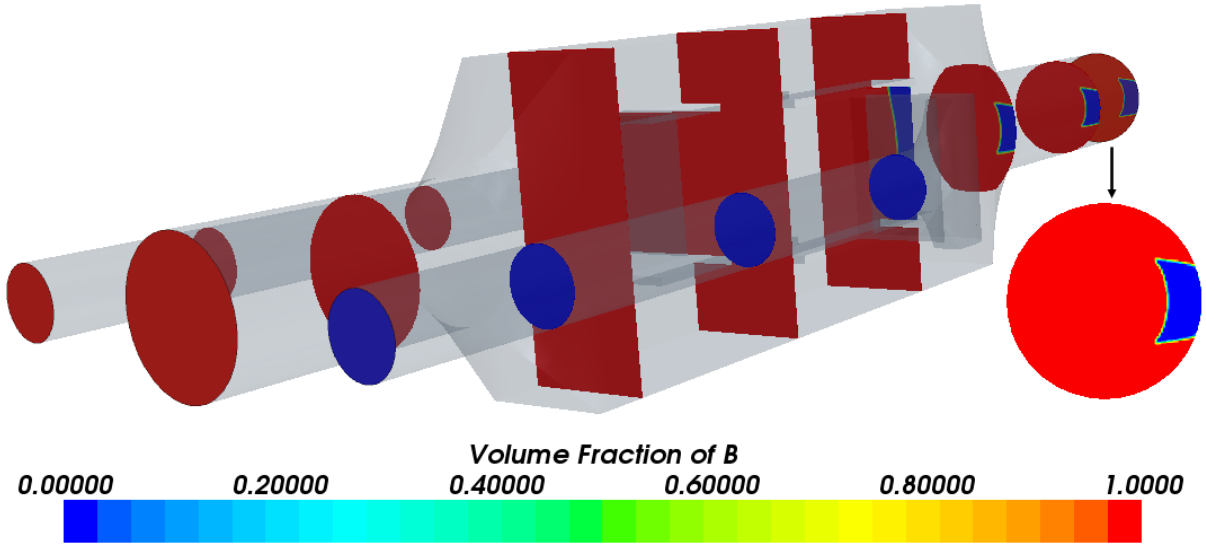

Figure 4.12: The progressive volume fraction of B (shown in red) through the modified injector block. The flow direction is from left to right. The volume fraction of A is shown in blue.

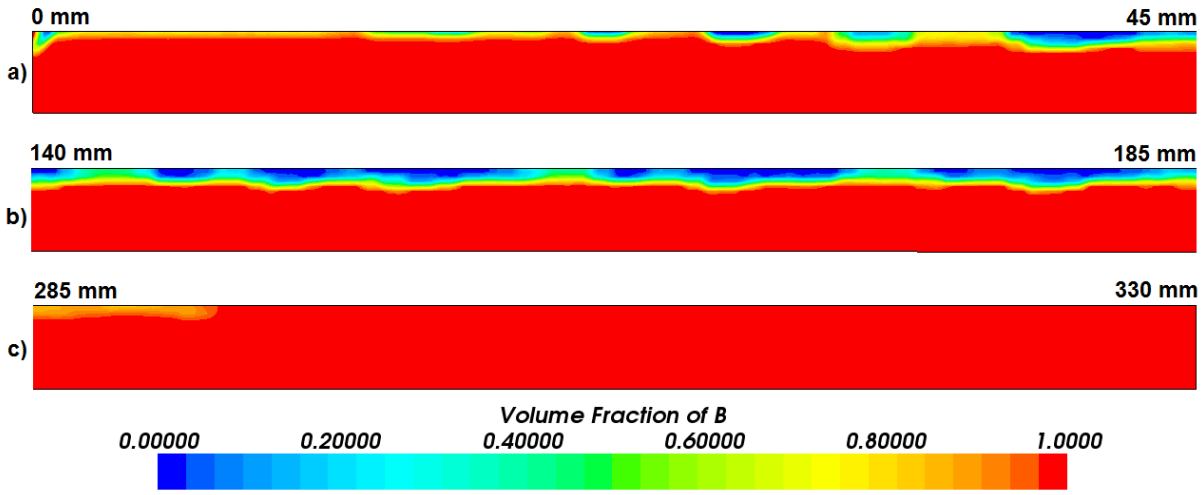

Figure 4.13: The volume fraction of B (shown in red) from the modified injector block at the die outlet showing: (a) the 0 mm edge, (b) the middle and (c) the 330 mm edge. The volume fraction of A is shown in blue.

of over 40 mm at the BE. In an end fed die system, the secondary layer flow will be biased towards the FE in reality. However, the amount of A present at 0 mm has been exaggerated numerically. Numerical diffusion errors at the sharp transition region in the end fed die are again believed to cause this erroneous A layer at the FE. This theory of

diffusional errors mentioned throughout this Chapter is further justified given that there is only 5 % of A in the film and A is still present at the FE.

4.4.2 Modifying the end fed die

For some of DTF's production scale end fed dies, there is a curved transition point between the end of the inlet pipe and the beginning of the die. Such a curve, seen via a frozen die plug obtained after rapidly cooling one of DTF's production dies in Figure 4.14, is designed to ease the transition from horizontal to vertical flow through the die.

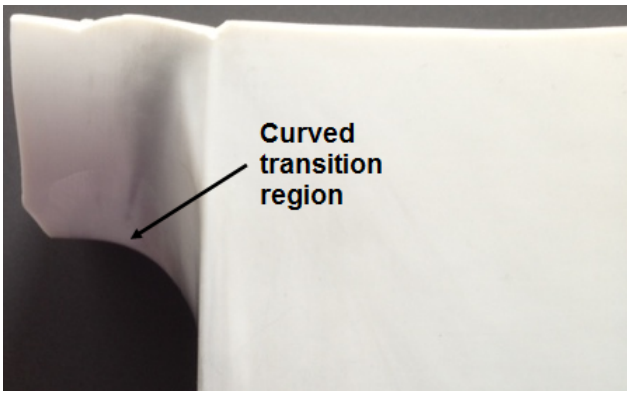

Figure 4.14: A curved transition region on a DTF production die. The flow direction is from left to right.

Here, a curved transition region similar to the one in Figure 4.14 is incorporated into the high-resolution die modelled in Section 4.3. Such curvature is not used on any of DTF's pilot scale facilities, with the geometry shown in Figure 4.5 with a sharp transition point representative of the actual die. The curvature is implemented artificially to try improving the problematic region and obtaining clear edges on each side.

Figure 4.15 shows the meshed end fed die with a curved transition region for CFD analysis. The curved section has a radius of curvature equal to 6.9 mm, where this part is the only modification made to the die in Figure 4.5. Approximately 19 million mesh cells were used for this geometry, using a base mesh cell size of 0.5 mm and a minimum cell size of 0.125 mm. These are the same dimensions as those used for the high-resolution die in Figure 4.5. A finer mesh is required here due to an increased number of cells implemented

around the curved transition point (a mesh cell size of 0.225 compared with 0.25 mm). The injector block used to feed this die is the one shown in Figure 4.1. The flow rate of A was reduced from 15 to 10 kg hr^{-1}.

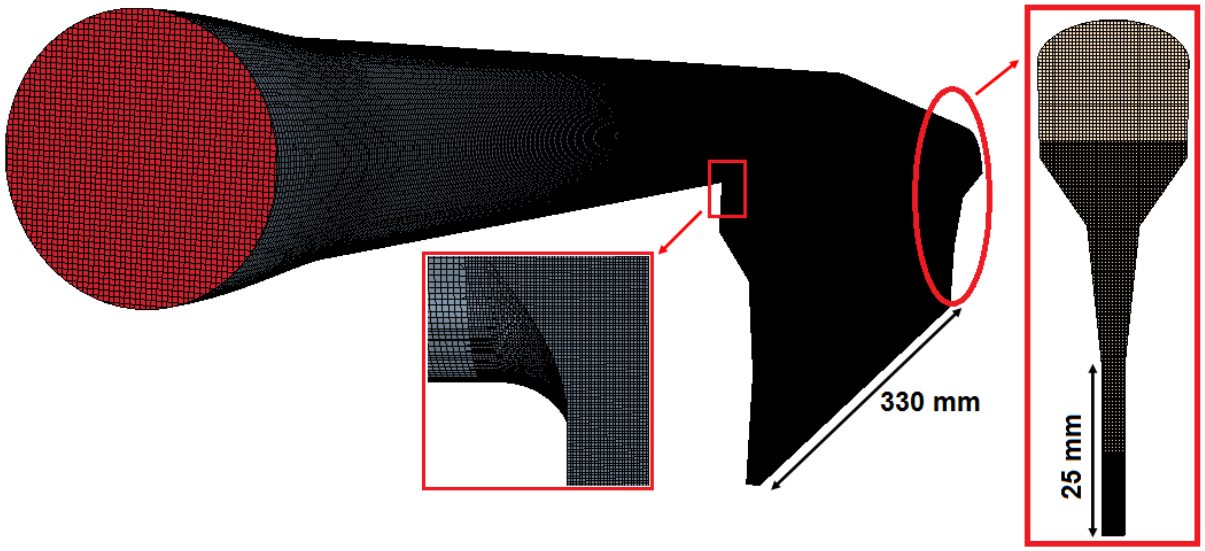

Figure 4.15: The meshed modified end fed die geometry. The flow direction is from left to right.

Figure 4.16 shows the progressive volume fraction of B through the modified end fed die geometry. The fifth plot from the left shows the volume fraction immediately after the curved transition region from horizontal to vertical flow. This plot shows that the secondary A layer has already moved towards the die outlet. This is despite the volume fraction compositions through the inlet pipe showing a region of B between the bottom of A and the bottom of the pipe. One would therefore expect a volume fraction plot at the transition region to be clear of A. Since this is not observed numerically (see also Figure 4.17), it is attributed to numerical diffusion errors at the curved transition section.

For this modified end fed die, Figure 4.17 shows the volume fraction of B at the outlet, observed at the same three locations shown in Figure 4.7. There is still no clear edge at the FE, with A present here. As mentioned, this is believed to be caused by numerical diffusion errors at the transition region. It appears that the added curvature does not sufficiently ease the directional change in the die. A progressive normal stress plot through the modified end fed die (see Figure 4.18) again shows a maximum at this problematic

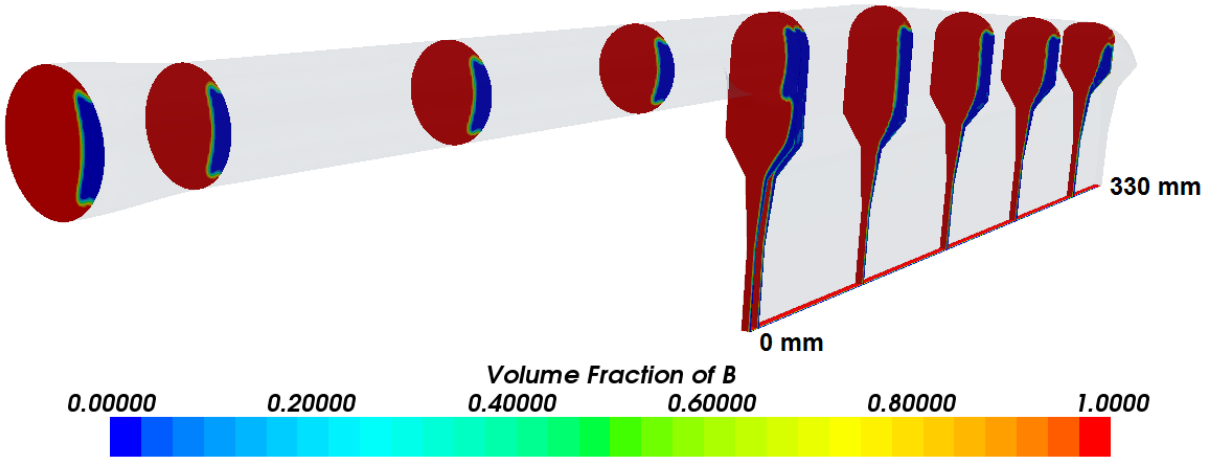

Figure 4.16: The progressive volume fraction of B (shown in red) through the modified end fed die geometry. The flow direction is from left to right. The volume fraction of A is shown in blue.

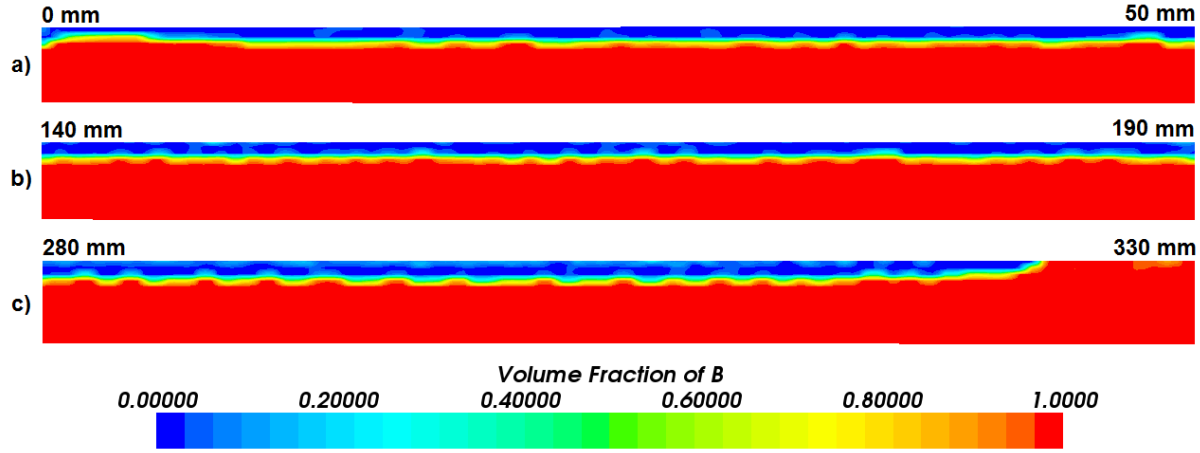

Figure 4.17: The volume fraction of B (shown in red) at the modified die outlet showing: (a) the 0 mm edge, (b) the middle and (c) the 330 mm edge. The volume fraction of A is shown in blue.

region, showing the difficulty in capturing the flow here and justifying the assumption that numerical diffusion errors at the FE are causing a lack of clear edges here. The BE clear edge width is 6.2 mm.

Figure 4.19 shows the total and A flow curves across the modified die of width 330 mm. The derivation method for these curves is described in Section 4.3. As found for the original high-resolution die flow curves (see Figure 4.10), the die seems to be over tapered,

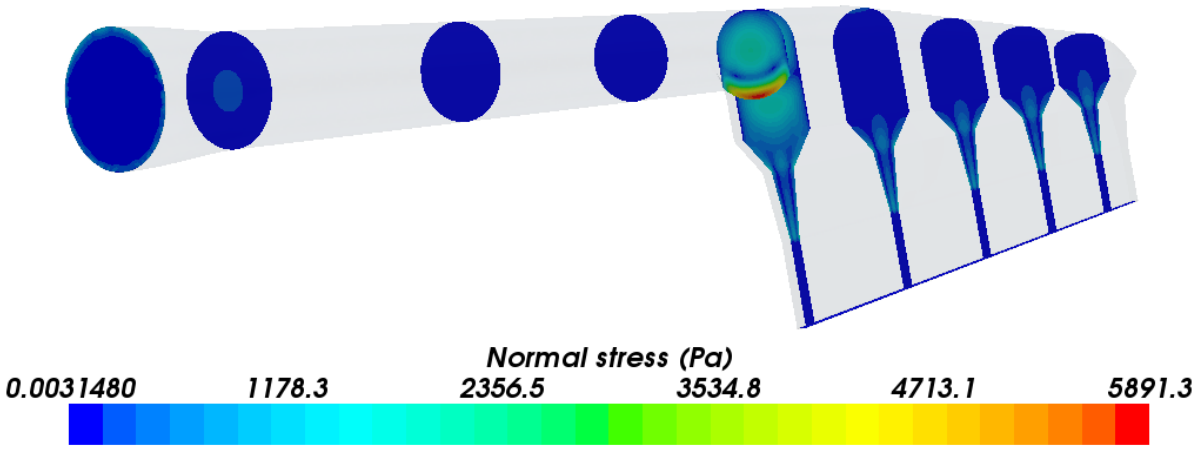

Figure 4.18: The progressive normal stress through the modified end fed die.

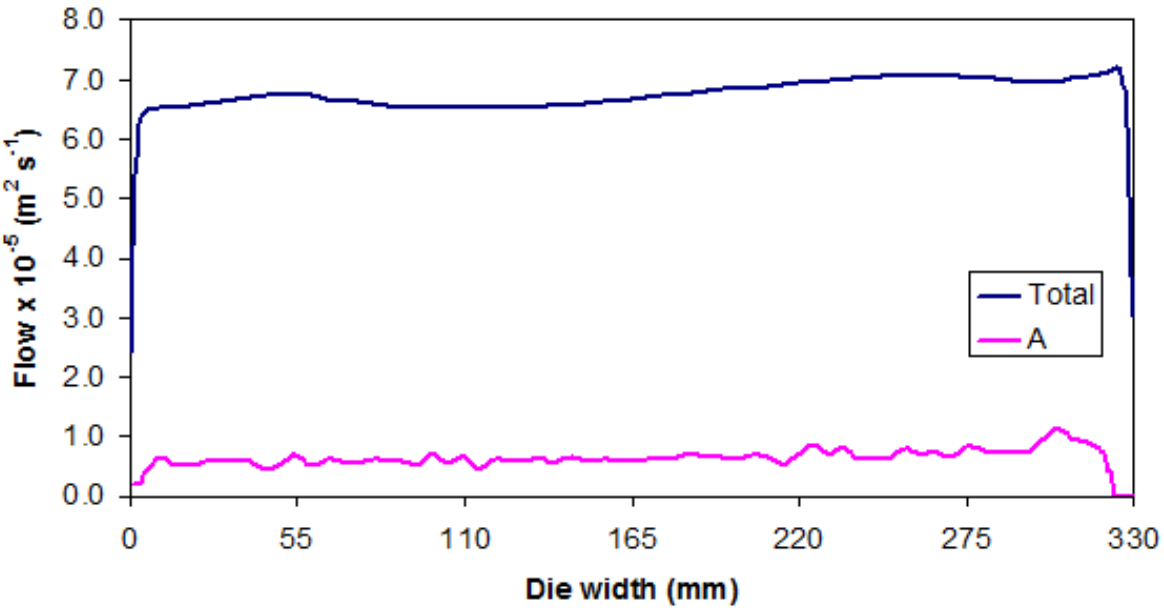

Figure 4.19: The total and A outlet flows across the modified die width.

with 9.5 % more flow at the BE compared with FE. This confirms that the tapering of the outlet rather than the transition region governs the film thickness uniformity. The A flow curve is again noisier than the total curve because of numerical approximations made of the $F = 0.5$ interfacial location. Neither reducing the injector block secondary layer entrance height, adding a curvature to the die transition point nor reducing the secondary layer flow rate has produced a film with clear edges. This is believed to be caused by numerical diffusion errors at the die transition region from horizontal to vertical flow.

Throughout this thesis, clear edges at the FE are not attained numerically within end fed die geometries. Since the CFD results show a good agreement with reality, *apart from at the FE*, the clear edge problem is assumed to be an acceptable error and is factored into the interpretation when considering the overall numerical solution in later Chapters.

4.5 Understanding numerical accuracy

As mentioned in Section 3.2.1, a CFD simulation should be both mesh and timestep independent. In this Section, modifications are made to the mesh and timestep size to test for independence. Another aim of this mesh refinement is to obtain clear edges on each side of the film.

4.5.1 Mesh independence studies

A comparison between numerical and theoretical pressure drop calculations allows one to test both the accuracy and uniformity of the mesh used. For the original high-resolution die modelled in Section 4.3, but with a *constant* die gap of 1.5 mm and *constant* mesh cell size of 0.2 mm across the land region of length 25 mm, a single component CFD simulation was formulated. Polymer A (see Table 4.1) was modelled to enter the die at a mass flow rate of 100 kg hr^{-1}. Figure 4.20 shows the CFD predicted progressive gauge pressure plot for this case. Here the pressure decreases from 14.0 bar at the die inlet to atmospheric pressure at the outlet. The numerically calculated average pressure drop between a section 20 mm above the outlet (labelled in Figure 4.20) and the outlet itself is 853,681 Pa to the nearest whole number.

The theoretical pressure drop (Δp) for laminar flow between two parallel plates is given as [158]:

$$\Delta p = \frac{12\eta QL}{WB^3}, \tag{4.2}$$

where L is the distance between the two planes (20 mm in this calculation), W is the length of the planes (330 mm) and B is the average width of each plane (the die gap, 1.5 mm). Substituting the relevant values into Equation 4.2, the theoretical pressure drop

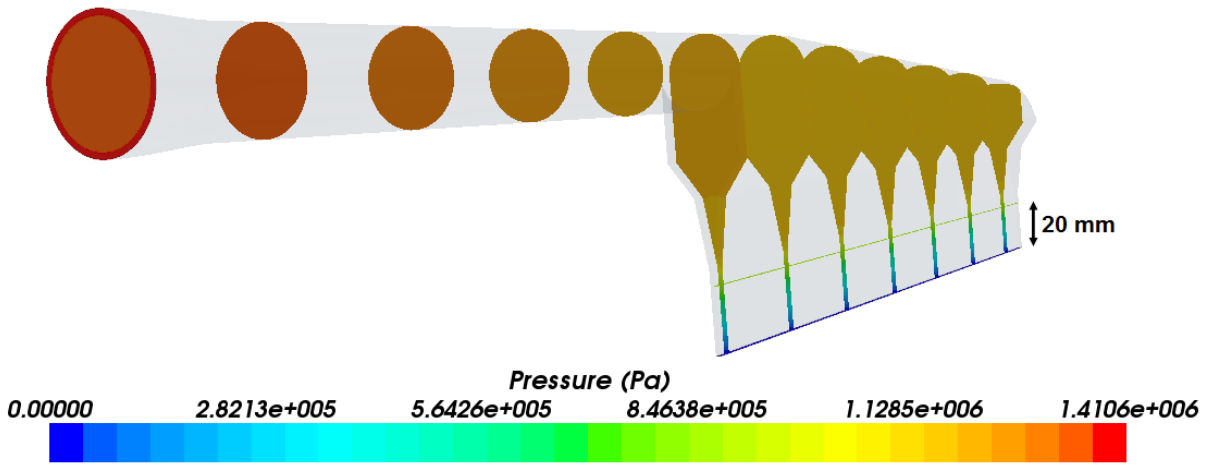

Figure 4.20: The progressive pressure plot through the high-resolution die.

between the two planes 20 mm apart is calculated as 8.6 bar or 861,953 Pa. The percentage difference between the numerical and theoretical pressure drop is 0.96 %. This is less than a 1 % difference between the values and implies that the mesh is sufficiently fine across the high-resolution die outlet. The 0.96 % error value is caused by both non-uniform exit flow and the no-slip condition imposed at the die walls. For a 2D simulation using a template geometry (see Section 7.2) where uniform flow is guaranteed and symmetry planes rather than end walls are used, the error reduces to 0.15 %.

The pressure drop calculation above implies a sufficiently accurate mesh is used for the high-resolution die. Despite this accuracy clear edges are not obtained at the FE die outlet. To further investigate this problem and test for mesh independence, the number of mesh cells used to cover the high-resolution die was increased from 16.5 to 26 million, where a minimum cell size of 0.1 mm across both the die outlet and the transition region is used. The number of mesh cells used here is at the maximum limit of the author's internal computational capabilities. Using a mesh of this magnitude yielded approximately 1 iteration per hour and it is not feasible to use such a mesh for this project.

For the refined mesh, Figure 4.21 shows the outlet volume fraction of B at the same three locations as in Figure 4.7, where the polymer properties modelled are also the same. Polymer A has not fully flushed out B, due to the very long running time for this fine mesh problem. This is observed with a minimum volume fraction of 0.13 rather than

0. The overall outlet composition would not change with increasing time and it is apparent that clear edges are still *not* predicted despite a finer mesh in regions of importance. The die solution is based on the same injector block and conditions used in Section 4.3. The interface in Figure 4.21 appears better defined than in Figure 4.7 (see also Figure 4.22), implying a more accurate and desirable solution with this new mesh.

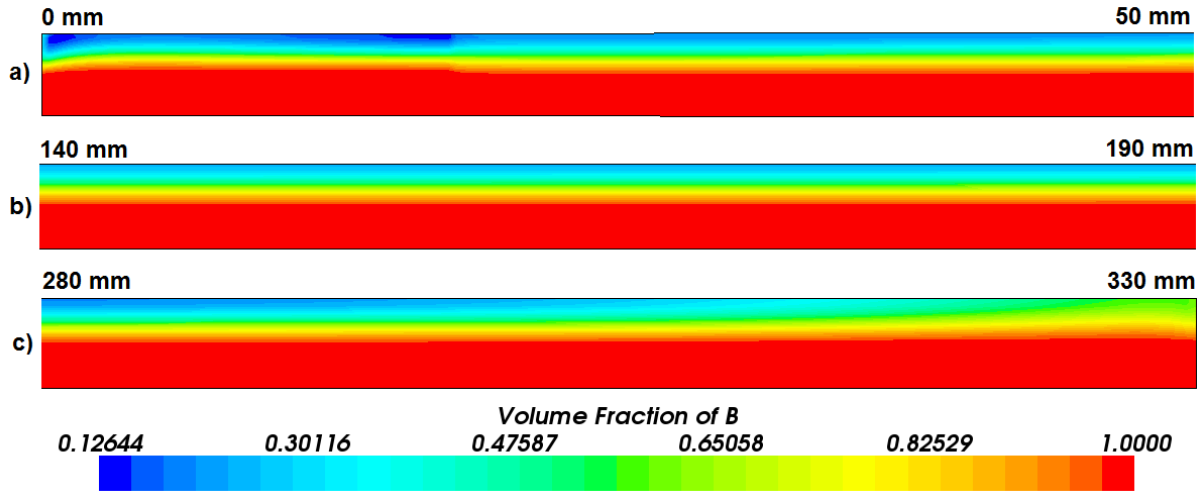

Figure 4.21: The volume fraction of B (shown in red) at the die outlet with a fine mesh showing: (a) the 0 mm edge, (b) the middle and (c) the 330 mm edge. The volume fraction of A is shown in blue.

In this Chapter, modifications made to both coextrusion geometries, reducing the secondary layer flow rate and refining the mesh have not produced a clear edge at the FE. This is despite clear edges being attainable and produced in reality using the geometries modelled. The clear edge problem remains and is observed for any end fed die model in this thesis. It is possible that further mesh refinements would improve the FE solution, but this is beyond the computational power available to the author and would further increase the convergence time. Apart from the numerical diffusion errors at the transition point, the CFD solutions are later shown by the experimental validation methods used in Chapter 6 to be representative, with excellent agreement apart from at the FE.

For the high-resolution die modelled, Figure 4.22 shows the total and Polymer A flow curves using both the original, 16.5 million cell mesh and the finer, 26 million cell structure. There is very little difference between the *total* flow curves, implying mesh

independence for the CFD predicted overall film thickness. Mesh independence is also observed via the lack of a clear edge at the FE in each case. Comparing the *A* flow curves, the BE clear edge width is the same regardless of the mesh used. For the finer mesh, the volume fraction of B exceeds 0.5 near the 330 mm edge (see Figure 4.21c). This is therefore classed as containing B and being a clear edge despite not being fully converged.

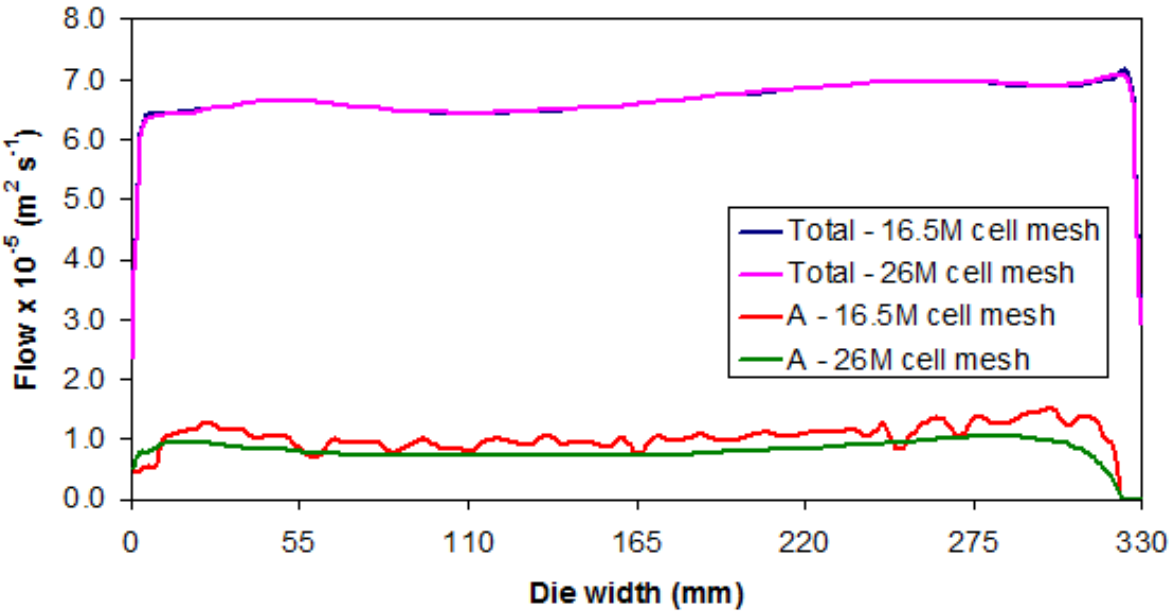

Figure 4.22: The total and A outlet flows across the die width for both the original (16.5 million cell) and finer (26 million cell) meshes.

It is clear from Figure 4.22 that the A flow curve is a function of the mesh cell size; the A layer has a more uniform thickness upon mesh refinement. As discussed in Section 4.3, any curve showing the secondary A layer flow relies on numerical approximations of the exact $F = 0.5$ interfacial location at the die outlet. For the finer mesh, there are more cells across this outlet, leading to less variation of the interfacial contour within a single cell and therefore a more accurate interface approximation. This greater accuracy is observed in Figure 4.22 where a smooth A curve is observed and the noise is reduced. The lack of fit between the two A flow curves is attributed to a lack of temporal convergence in the fine mesh simulation. This is despite running this case for over 3,000 hours.

Despite yielding a greater interfacial precision, using a 26 million cell mesh leads to

vastly increased convergence times and it is not feasible to use in this thesis. A fully converged solution using the 26 million cell mesh would take over 6,000 hours, or over 35 times longer than when using the original, 16.5 million cell mesh. Ideally, meshes such as the 26 million cell one would be used throughout this thesis, but this is not possible due to the very large convergence times. It is feasible that an even finer mesh would produce clear edges at the FE, but this has not been tested. One must make a compromise between mesh density and convergence time and the results from the 16.5 million cell mesh are therefore assumed to be valid and sufficiently accurate. This assumption is justified due to the mesh independence found for the total flow curves in Figure 4.22, clear edges still not being produced despite this finer mesh and the pressure drop calculation made earlier in this Section. Since the coarser mesh gives noisier flow curves for Polymer A, it is important to be aware of the methods used by STAR-CCM+ to estimate the interfacial location since these results are taken to be sufficiently accurate.

For a 410 mm wide end fed die with a similar mesh composition to the coarser mesh used in Section 4.3, Figure 4.23 shows the CFD predicted interfacial position (based on the $F = 0.5$ contour) from the FE to BE for an AB structure. Here, the y-axis shows the interfacial variation between the middle of the outlet at $x = 0$ (see Figure 4.7) to the top wall at $x = 0.75$ mm (a 1.5 mm die gap) and the x-axis shows the die width. The interfacial smoothing function used in STAR-CCM+ generates noisy data and there is significant variation within a single mesh cell. This unstructured result causes the noisy flow curves for Polymer A, such as that observed in Figure 4.10 for a similar type of mesh.

To appreciate the smoothing mechanism used in STAR-CCM+ to approximate the interfacial position, raw data showing the outlet volume fraction of B was imported into a spreadsheet. For every 1 mm between 0 and 410 mm, a manual linear interpolation was performed on adjacent mesh cells in the direction normal to the flow (y-axis, Figure 4.23) to approximate the $F = 0.5$ position. From Figure 4.24, the manual interpolation is almost identical to the STAR-CCM+ smoothing function. This implies that the interfacial approximation using CFD is also based on a linear interpolation between two or three adjacent mesh cells in the direction normal to the flow.

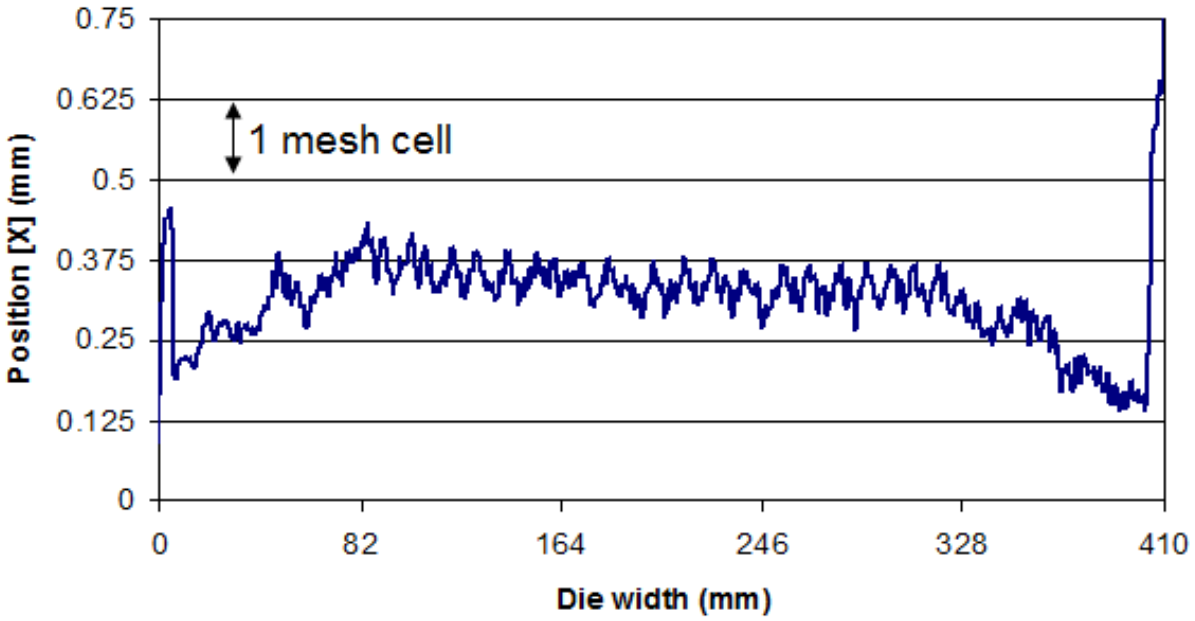

Figure 4.23: The CFD predicted outlet interfacial variation across a 410 mm wide end fed die.

Numerical approximation of the interfacial position such as that shown in Figure 4.23 causes a noisy secondary layer thickness profile. The CFD data can be smoothed in the axial direction (from 0 to 410 mm), hence ameliorating the interface plot and the Polymer A flow curve since this is a function of the interface position. Figure 4.25 shows the original CFD interface position and two smoothing techniques applied to this. The smoothing algorithms used are locally weighted scatterplot smoothing (LOESS [159–161], using a smoothing parameter of 0.33) and manual smoothing using a weighted average of nine mesh cells either side of every interfacial cell across the die width.

From Figure 4.25, applying smoothing in the axial direction improves the original CFD prediction of the interfacial profile. The average absolute percentage difference between the CFD predicted interfacial profile and that obtained using manual smoothing is 1.8 %. This increases to 7.6 % when comparing the CFD and LOESS approximations. It has been shown in this Section that both mesh refinement and axial smoothing of the raw data can significantly reduce the noise in a secondary A layer flow curve, provided it is weighted across at least nine mesh cells either side of each interfacial mesh cell. Increasing

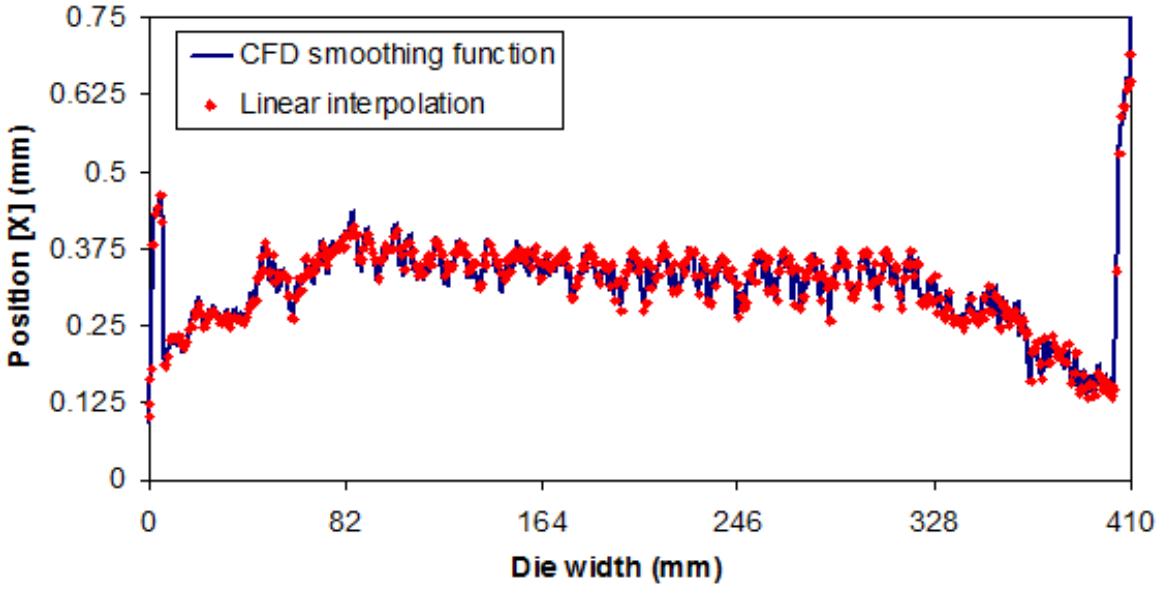

Figure 4.24: The interfacial variation across a 410 mm wide end fed die using CFD and a linear interpolation.

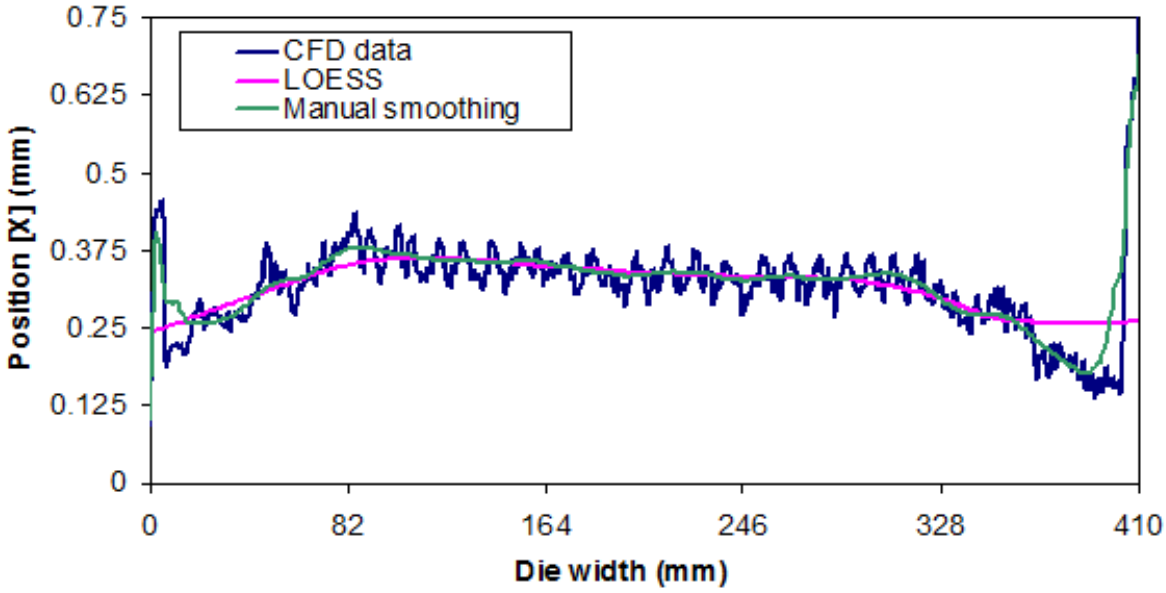

Figure 4.25: Two different smoothing algorithms applied to the original CFD interface data.

the mesh cell quantity much above 16.5 million is not feasible for this study and therefore smoothing is the more viable option. Axial smoothing is not currently available in STAR-CCM+ and it would benefit this work if it were to be implemented. Other end fed die

results throughout this thesis show a noisy secondary layer flow curve where neither a fine mesh nor axial smoothing is used. This noise is a numerical limitation of this work, but the overall trend of A rather than the noise is important for this thesis and such flow curves are assumed to be sufficiently accurate. This is justified given the relatively low percentage error values quoted.

In this Section, mesh independence was found for the total flow curves (almost identical solutions, see Figure 4.22) but *not* for the Polymer A flow profiles. The finer, 26 million cell mesh gave a smoother, more accurate representation of the interfacial position than the 16.5 million cell mesh. For the Polymer A flow curves in Figure 4.22, there is an average absolute percentage difference of 25.2 % for the two mesh structures, caused by a lack of temporal convergence for the higher mesh density system. Given the vastly increased convergence times with this 26 million cell mesh (over 35 times longer), a compromise is made between runtime and accuracy since it is not feasible from a processing perspective to use a 26 million cell mesh. Polymer A was still present at the FE despite this finer mesh. It is possible that clear edges would be attained with even greater mesh refinement. However, this is beyond the computational capability available to the author and the lack of clear edges is assumed to be an acceptable numerical error for end fed die simulations in this thesis. Both the noisy Polymer A flow curves and lack of clear edges at the FE are part of the consideration between acceptable error and runtime.

4.5.2 Timestep independence studies

The default timestep used throughout this thesis is 0.05 seconds per iteration. For all CFD simulations, this timestep is used to initialise the problem and is maintained until the residuals (see Equation 3.29) decrease by at least an order of 3 and remain unchanged. Modelling polymer coextrusion involves dislodging the primary polymer melt layer used to fill the geometry with a secondary polymer melt. Since both polymers are very viscous and slow moving and a no-slip condition is used at the geometry walls, it often takes a long time to fully flush out the primary polymer, despite convergence being observed. This is particularly prevalent for end fed die modelling, where the different melt layers

are in contact with each other throughout. In such cases, the timestep per iteration is increased to aid the dislodging of the primary polymer.

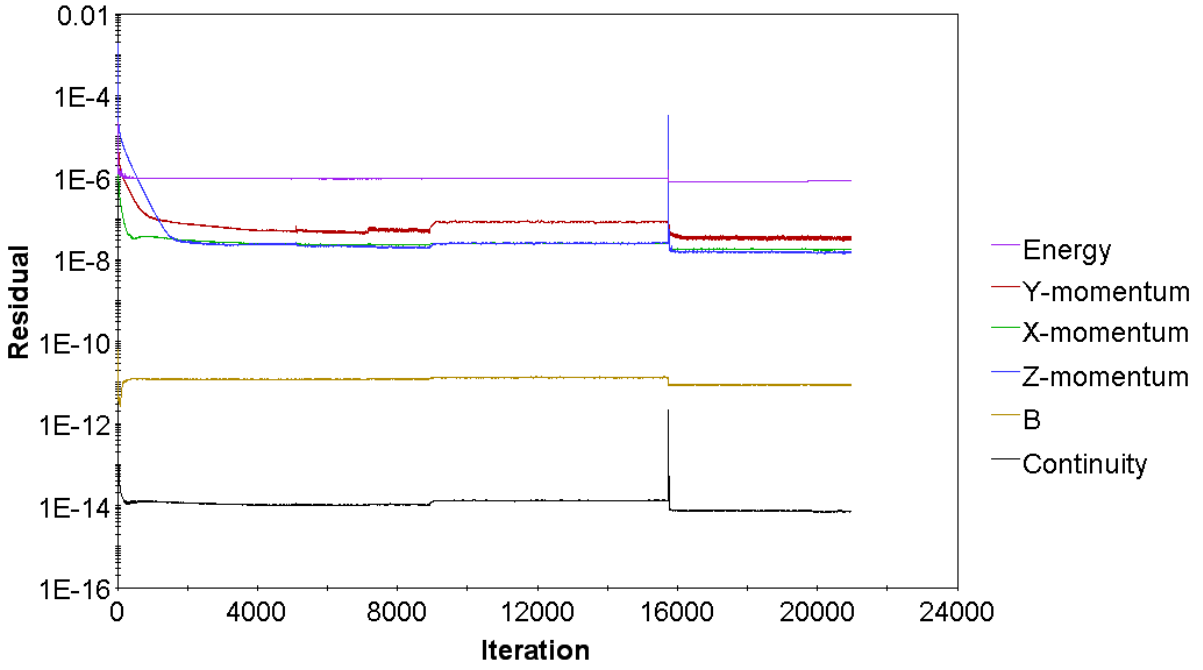

Figure 4.26: The residuals for the modified end fed die geometry.

For the modified high-resolution end fed die case (see Section 4.4.2), the timestep was increased from 0.05 to 0.1 seconds per iteration to attempt to flush out the primary B polymer. This increase was made after 15,800 iterations when full convergence was attained, as shown in the residual plot in Figure 4.26. There is a sharp increase (or "spike") in the z-momentum and continuity residual monitors, caused by the system readjusting to the change in timestep. All six residuals then decrease to slightly lower than the converged value before flattening. This slight decrease in the residual values shows that the errors have reduced when moving faster with time, as one would expect.

Despite changing the residual values, the overall solution does *not* change with increasing timestep. Figure 4.27 shows the total flow curves for the modified end fed die from 0 to 15,800 iterations (a timestep of 0.05 seconds per iteration) and from 15,800 to 21,000 iterations (0.1 seconds per iteration). There is very little difference upon increasing the timestep and the CFD predicted film thickness does not change. This implies that the modified end fed die simulation is timestep independent. Such independence of time

confirms that steady state simulations are modelled, with a timestep required for interface tracking with the VOF method.

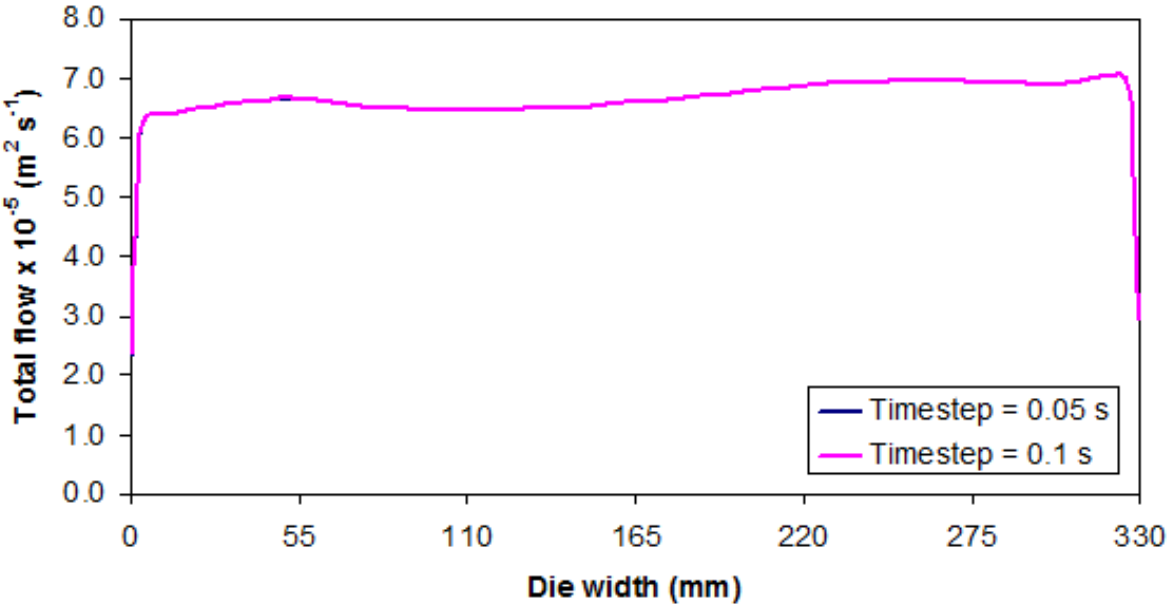

Figure 4.27: The total flow curves for the modified end fed die simulation using two different timesteps.

For all CFD simulations in this thesis, both mesh and timestep independence studies like those in this Section are conducted, but not explicitly shown.

4.6 Chapter conclusions

This Chapter has shown CFD modelling of a DTF pilot scale injector block linked to a 330 mm wide end fed die. Standard PET melt properties were used. The effect of modifying both coextrusion geometries was also investigated.

The main finding in this Chapter is that clear edges were *not* attained, with the secondary layer present at the outlet FE. This erroneous result at the 0 mm edge was observed despite refining both geometries and the mesh, and reducing the secondary layer flow rate; all of which were aimed at promoting clear edges. The lack of clear edges is believed to be caused by numerical diffusion errors at the sharp transition region in the end fed die and is a numerical limitation. It is possible that further mesh refinement

would lead to clear edges, but this would vastly increase convergence times. The lack of clear edges at the FE is part of a consideration between runtime and accuracy, and is taken to be an acceptable error. From a process perspective, this is justified in Chapter 6, where apart from at the FE, the CFD data is shown to give an excellent representation of reality. This clear edge problem is therefore not considered relevant in the remainder of this thesis.

The number of mesh cells in the end fed die and the timestep was increased to check how this changes the numerical results. The CFD predicted total film thickness did *not* change upon these alterations, implying both mesh and timestep independence. Increasing the mesh density and axial smoothing of the raw data reduces the noise of the secondary layer thickness profile. Neither of these are viable to maintain for every CFD case shown in this thesis and the noisy data is another numerical limitation. The secondary layer thickness profile is a further consideration between runtime and accuracy. However, it is the secondary layer thickness trend rather than noise that is important and this thickness is realistic.

Chapter 5

Comparing pilot scale injector block and multi-manifold die geometries

5.1 Introduction

In this Chapter, CFD is used to model an injector block linked to a 410 mm wide end fed die and a 410 mm wide multi-manifold die (MMD, see Figure 2.10), shown in Sections 5.2 and 5.3 respectively. Both these systems are typical of DTF's pilot scale operations. The comparative ability of each coextrusion technique to handle increasingly wide melt viscosity ratios is analysed. ABA structured MLFs are modelled, with the secondary A layer making up 20 % of the overall flow rate. Table 5.1 shows the initial modelled fluid properties for B and A in STAR-CCM+, where standard PET melt properties are assumed.

From Table 5.1, B is initially modelled to be identical to A. The melt viscosity ratio between the two layers is then altered by firstly increasing the viscosity of A relative to B (Sections 5.2.1 and 5.3.1) and then increasing the viscosity of B relative to A (Sections 5.2.2 and 5.3.2). The primary:secondary melt viscosity ratio is modelled up to a maximum of 1:5 and 5:1 through the injector block and end fed die and a maximum of 1:10 and 10:1 in the MMD. Such wide viscosity ratios are not used at DTF, but are studied here for academic purposes. The other fluid properties in Table 5.1 remain as quoted. Constant viscosities are implemented in this Chapter despite PET melt viscosity relying

Table 5.1: The modelled fluid properties for B and A.

	B	**A**
Temperature (T)	285 °C	285 °C
Density (ρ)	1,250 kg m^{-3}	1,250 kg m^{-3}
Viscosity (η)	170 Pa s	170 Pa s
Thermal conductivity (κ)	0.2 W m^{-1} $°C^{-1}$	0.2 W m^{-1} $°C^{-1}$
Mass flow rate ($\dot{m}$)	80 kg hr^{-1}	20 kg hr^{-1}
Final volume fraction	80 %	20 %

on temperature in reality. This ensures that viscosity is the sole dependent variable. The wall temperature used throughout this Chapter is 285 °C, hence an isothermal problem is modelled. Energy effects are still solved for in this Chapter to account for any small amount of viscous heating of the polymer melts.

The maximum melt viscosity ratios considered exceed those in any of DTF's MLFs. However, with coextruded products increasing in complexity, more extreme viscosity ratios are required and it is important to be aware of the ability of DTF's geometries to handle this. It is envisaged that CFD will predict the MMD to be more effective than the injector block and end fed die at producing films requiring high viscosity ratios. This is observed in reality and is because the different polymer melt layers are in contact for a shorter period of time in the MMD [8, 9, 11, 15, 16, 76].

5.2 Injector block linked to a 410 mm wide end fed die

Figure 5.1 shows the meshed injector block used for CFD analysis. The primary B layer enters the block through the central inlet channel and the secondary A layer flows through both the left and right inlet pipes (10 kg hr^{-1} through each pipe). These melt layers come

together for the first time in the main part of the block before leaving as a unified ABA melt structure. This structure exits the block and enters the die (see Figure 5.2) where it is converted into an outlet representative of the final film solution.

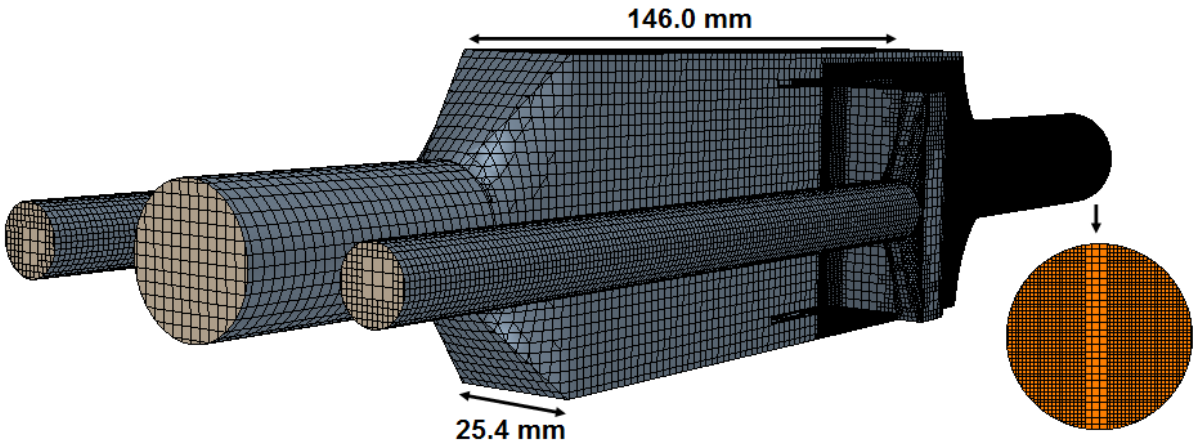

Figure 5.1: The meshed injector block geometry. Flow direction is from left to right.

The injector block modelled here is the same as that in Figure 4.1. However, the number of mesh cells used is 1.5 million rather than 4.5 million. A base mesh cell size of 2.0 mm was used alongside a minimum mesh size of 0.5 mm. This finer mesh region was implemented once the different melt layers were in contact, with the aim to produce as smooth an interface as possible. The coarser mesh used for the injector block in this Section compared with that shown in Figure 4.1 results in a slightly less accurate solution; there is more interfacial smearing between the two polymers. Using this coarser mesh is justified by the reduction in convergence times for such injector block solutions from two days to one day. The interfacial configuration between the two melt layers is a direct function of the mesh size and this forms part of the consideration between solution accuracy and runtime and the degree of interfacial smearing is assumed to be acceptable.

Figure 5.2 shows the 410 mm high-resolution die used for CFD analysis, where Figure 5.2a shows the geometry and Figure 5.2b displays the mesh via a number of plane sections. The end fed die is used to convert the outlet solution from the injector block into a solution representative of the final film. Around 14.5 million mesh cells were required to discretise the end fed die (Figure 5.2b). A base mesh cell size of 1.0 mm was selected

with a minimum mesh cell size of 0.125 mm. Finer mesh regions were used once the die narrowed and also across the thin outlet. The meshed geometries shown in Figure 5.1 and 5.2b are also used for CFD modelling throughout Chapter 6.

Figure 5.3 shows the progressive volume fraction of Polymer B through both the injector block (Figure 5.3a) and the end fed die (Figure 5.3b). These results were obtained using the modelled fluid properties for B and A in Table 5.1. The combined injector block and die system converged after around 10,000 iterations; a runtime of approximately seven days. From the injector block solution in Figure 5.3a, the left secondary channel enters the main block slightly before the right channel - see the plane section marked with a star. This feature is designed to avoid flow disturbances when the A layers first enter the geometry. Such an offset in the channel entrances is believed to cause the left A profile (denoted AS, see later) to be longer but thinner than the right one at the injector block outlet (DS).

Both results plots in Figure 5.3 have a sufficiently smooth and well defined interface throughout. The interface is sharper within the injector block. This is because the minimum mesh cell size is 0.5 mm in the block and in the main part of the inlet pipe and die, where the melt layers are in contact, the mesh size is 1.0 mm. The degree of interfacial smearing is a direct function of the mesh cell size. Further mesh dependency studies are discussed in Section 4.5.1.

The volume fraction of B at the end fed die outlet is shown in Figure 5.4, where Figure 5.4a shows the FE to 30 mm, Figure 5.4b shows the middle, from 190 to 220 mm and Figure 5.4c displays the far edge, from 380 mm to the BE at 410 mm. From Figure 5.4a, clear edges are not attained at the FE with A present here from both layers. This lack of clear edges is taken to be an acceptable numerical limitation, see Chapter 4.

The air side (AS) and drum side (DS) are labelled in Figure 5.4 according to the side of the melt curtain touching the casting drum. Clear edges are predicted at the BE, where the AS clear edge width is 7.2 mm and the DS clear edge width is 4.3 mm. This width difference is believed to be caused by the unsymmetric injector block secondary channels (see Figure 5.3a). Although it has spread further through the injector block, the AS A

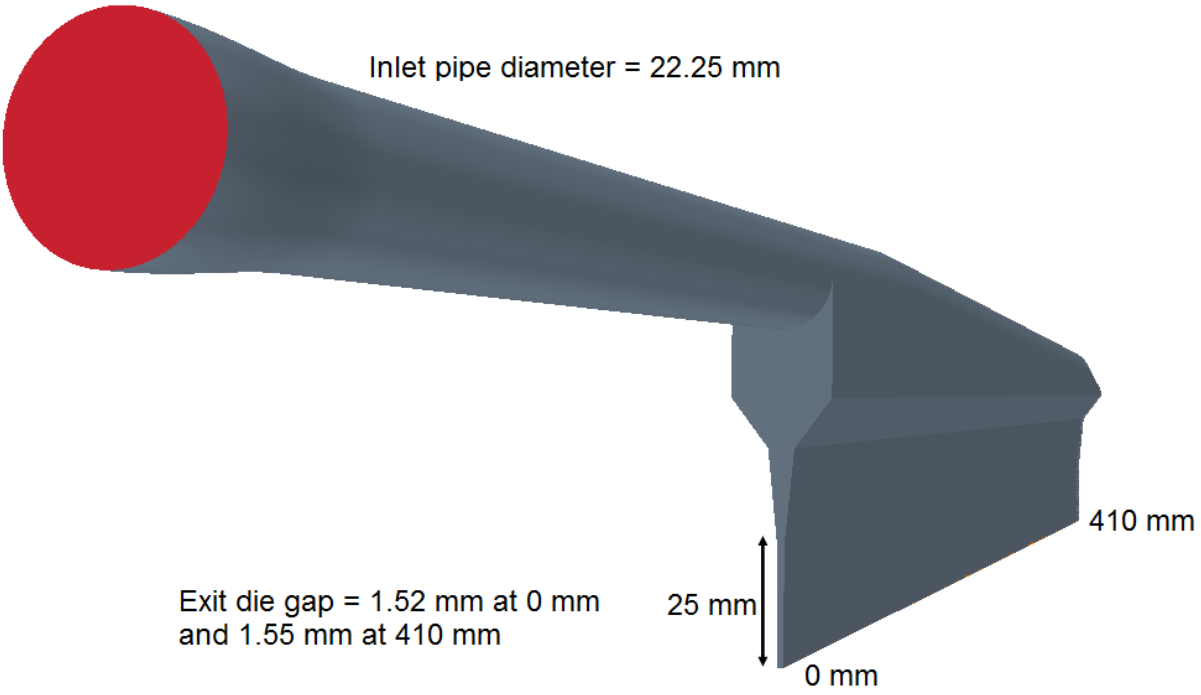

(a)

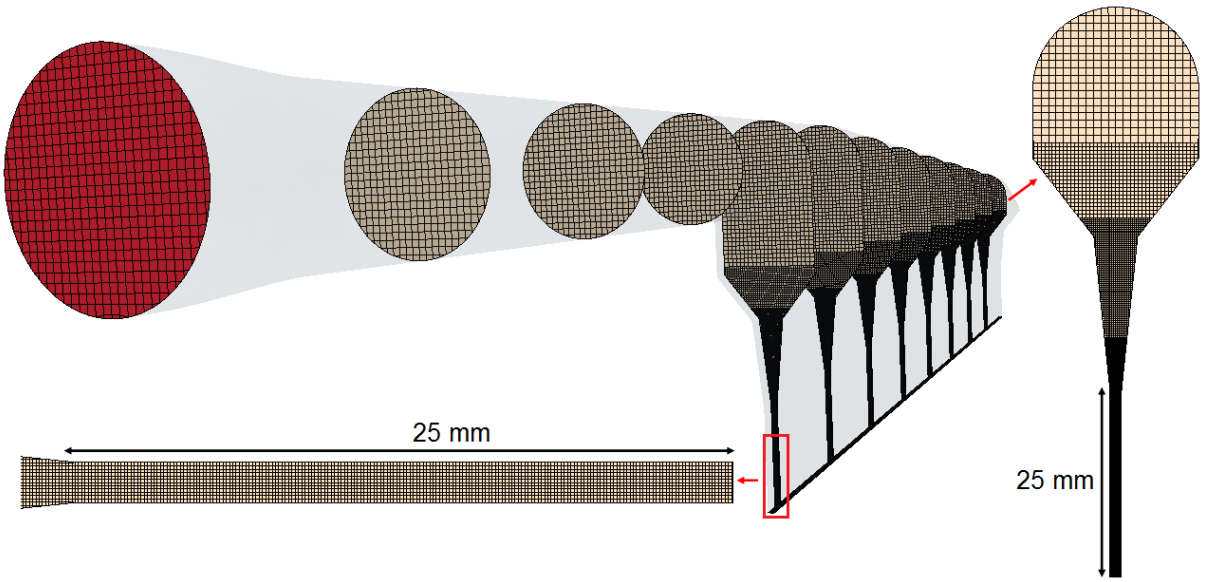

(b)

Figure 5.2: The 410 mm wide end fed die where (a) shows the geometry and (b) shows the mesh. The flow direction is from left to right.

layer at the die outlet is predicted to spread *less* than the DS A layer towards the BE.

Figure 5.5 shows the total, B, A DS and A AS flow curves across the end fed die

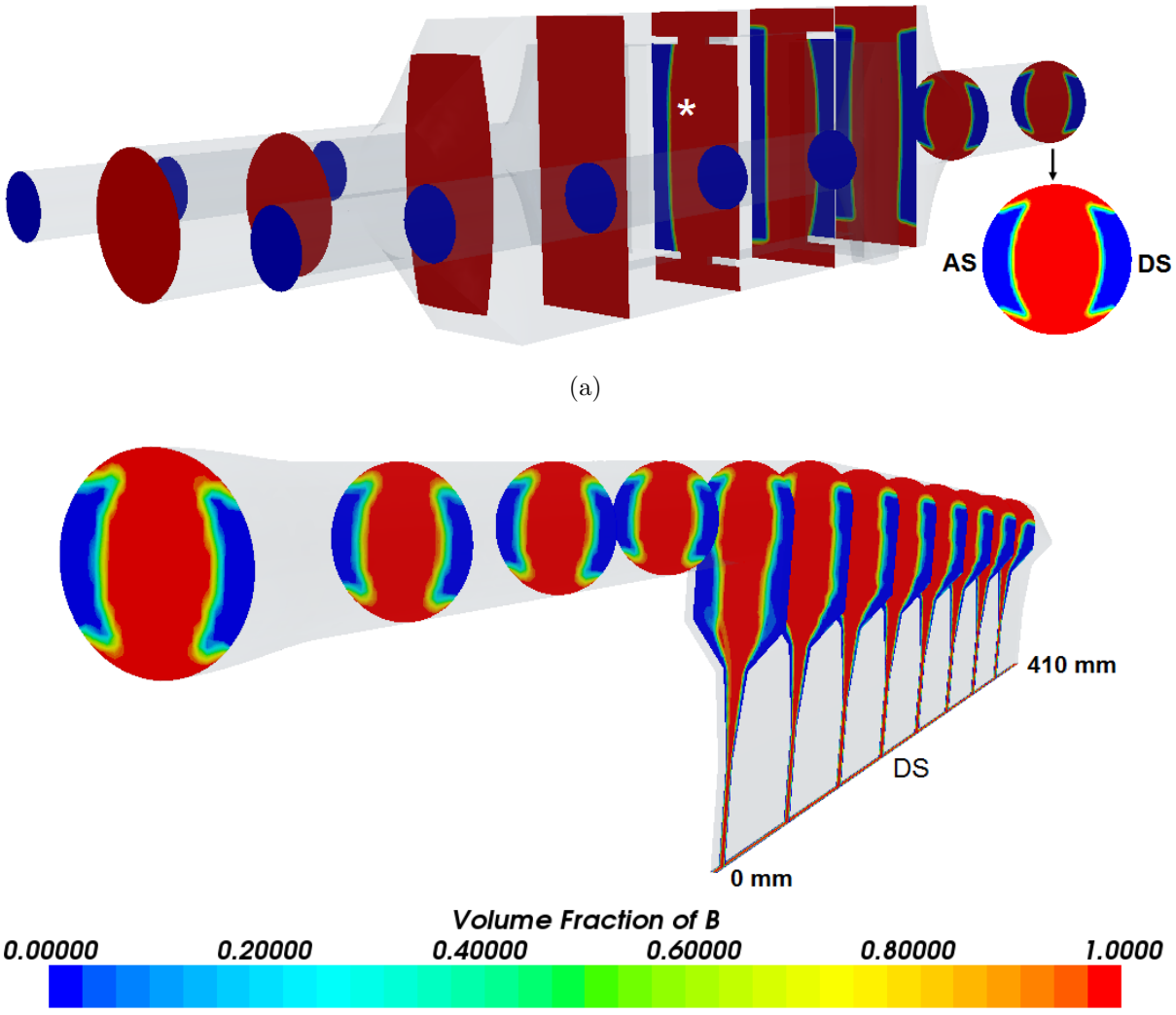

(a)

(b)

Figure 5.3: The progressive volume fraction of B (shown in red) through both (a) the injector block and (b) the 410 mm wide end fed die. The flow direction is from left to right. The volume fraction of A is shown in blue.

outlet width for the 1:1 viscosity ratio. The total flow curve is flat and a uniformly thin final film is predicted numerically. For the *total* flow solution between 19.5 and 390.5 mm (ignoring the edge solutions because these would be trimmed in reality), the mean flow ($\bar{x}_{\text{flow}}$) is 5.4×10^{-5} m^2 s^{-1}, and the standard deviation (σ_{flow}) is 1.5×10^{-7} m^2 s^{-1}. This flow uniformity is desirable from a commercial perspective and implies a sufficient tapering of the die outlet for the geometry modelled.

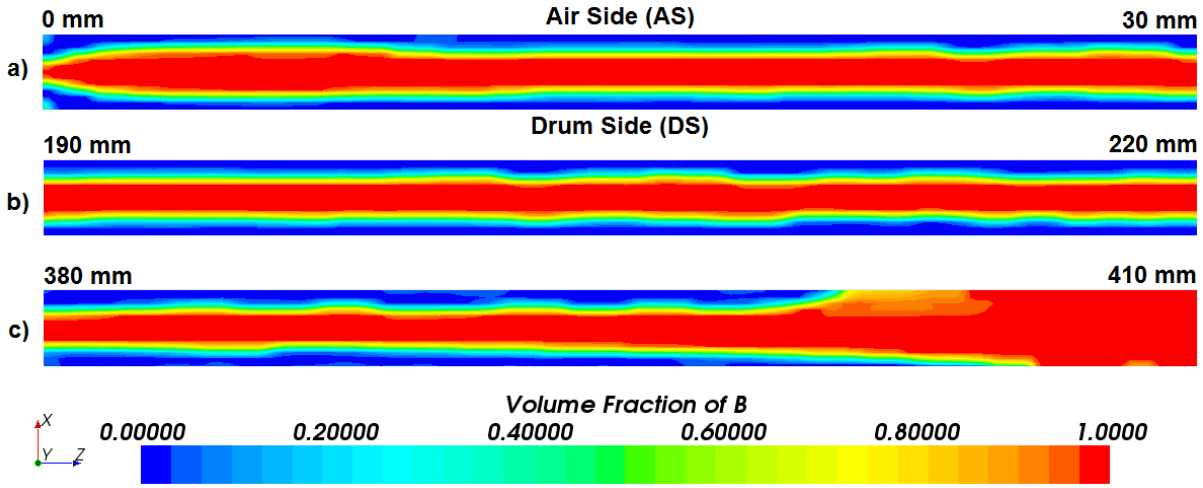

Figure 5.4: The volume fraction of B (shown in red) at the die outlet showing: (a) the 0 mm edge, (b) the middle and (c) the 410 mm edge. The volume fraction of A is shown in blue.

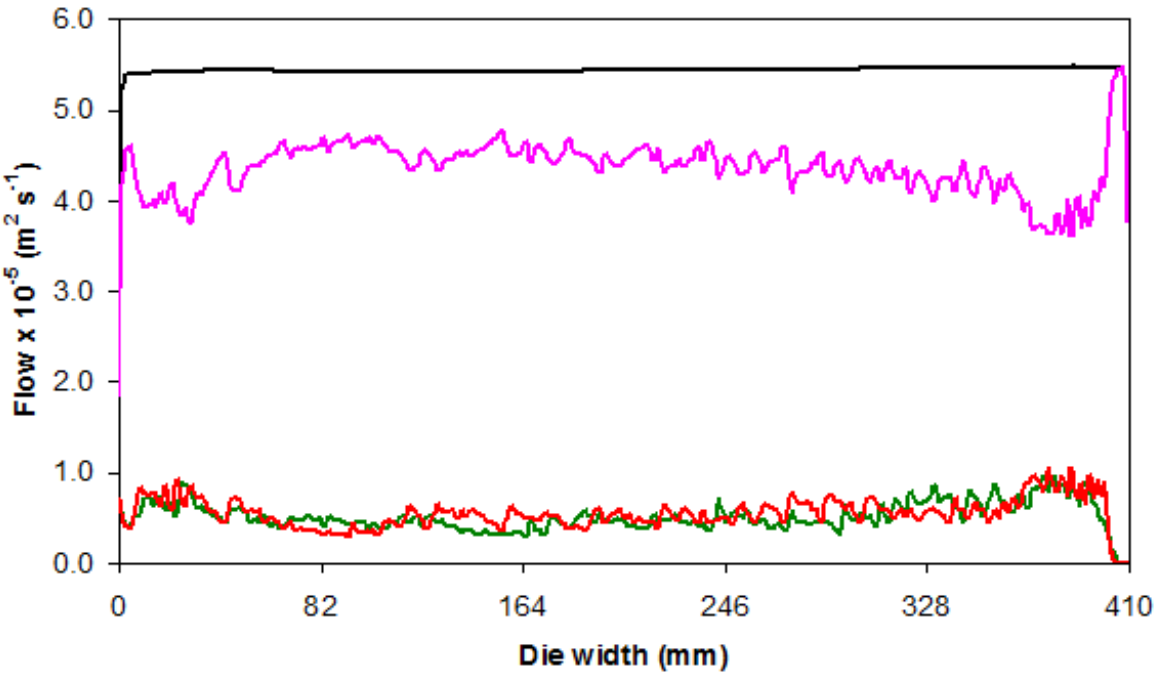

Figure 5.5: The total (shown in black), B (shown in pink), A drum side (shown in green) and A air side (shown in red) flow curves across the die outlet width.

The thickness of B increases near the BE at 410 mm since clear edges are attained here. Non-uniform individual layer thicknesses (noisy data) are observed because of numerical

approximations of the exact interfacial location, see Chapter 4 for more detail and the derivation method to obtain such flow curves. For the two Polymer A layers, the standard deviation of the flow is 1.5×10^{-6} m^2 s^{-1}; there is ten times more noise for each A layer compared with the total flow curve. There are 12 mesh cells across the outlet width and this disjointed data shows that the interfacial position varies significantly within a single mesh cell. This noisy secondary layer thickness data is assumed to be an acceptable numerical limitation for the mesh density used.

5.2.1 The effect of increasing the secondary layer viscosity

The viscosity of A was then increased to both two and five times that of B within the injector block and die. It is envisaged that the more viscous, slower moving A layers will remain confined to the geometry walls and spread *less* to the die edges compared with the 1:1 viscosity ratio simulation [9].

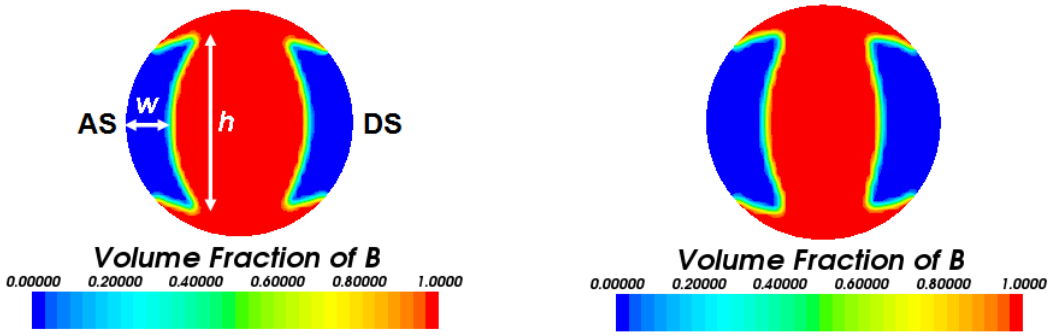

(a) (b)

Figure 5.6: The volume fraction of B (shown in red) at the injector block outlet for (a) a 1:1 B:A melt viscosity ratio and (b) a 1:5 viscosity ratio. The volume fraction of A is shown in blue.

Figure 5.6 shows the volume fraction of B at the injector block outlet, for the 1:1 viscosity ratio (Figure 5.6a) and the 1:5 ratio (Figure 5.6b). At the AS, the maximum height of A (marked h in Figure 5.6a) *decreases* from 19.0 to 18.0 mm upon increasing the viscosity ratio. The spreading of A at the wall has decreased for a more viscous A melt as

expected. The maximum width of Polymer A (marked w in Figure 5.6a) *increases* from 4.9 to 6.3 mm when increasing the secondary layer viscosity. This again shows that the spreading of A has reduced and it remains more confined to the middle of the injector block. Equivalent velocity magnitude outlet plots (see Figure 5.7) shows that the region of maximum velocity is squeezed towards the middle of the outlet for the 1:5 ratio, due to the presence of the more viscous secondary layers. From Figure 5.7, the maximum velocity of the unified structure increases from 8.8 to 11.0 cm s^{-1} when increasing the viscosity of A. This is because Polymer B has been squeezed to the middle of the geometry.

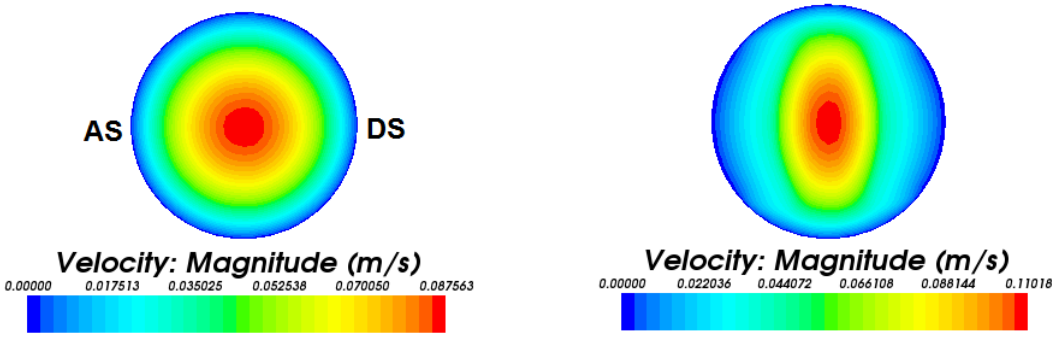

(a) (b)

Figure 5.7: The velocity magnitude at the injector block outlet for (a) a 1:1 primary:secondary melt viscosity ratio and (b) a 1:5 viscosity ratio.

For the 1:5 viscosity ratio, Figure 5.8 shows the volume fraction of B at the end fed die outlet for the same three locations as in Figure 5.4. The A layers spread less upon increasing their viscosity. A is present at the FE (Figure 5.8a) but in a smaller quantity compared with the case of equal viscosity fluids (Figure 5.4a). At the BE, the clear edge width has increased from 7.2 to 7.6 mm at the AS and from 4.3 to 9.6 mm at the DS at this increased viscosity ratio. This reduced spreading of the secondary layers is expected due to their increased viscosity and slower movement at the walls.

Figure 5.9 shows the three die outlet flow curves for the three viscosity ratios modelled, where Figure 5.9a shows the total flow curves and Figure 5.9b displays the flow curves for Polymer A as a sum of both the AS and DS layers. The film edges increase in thickness

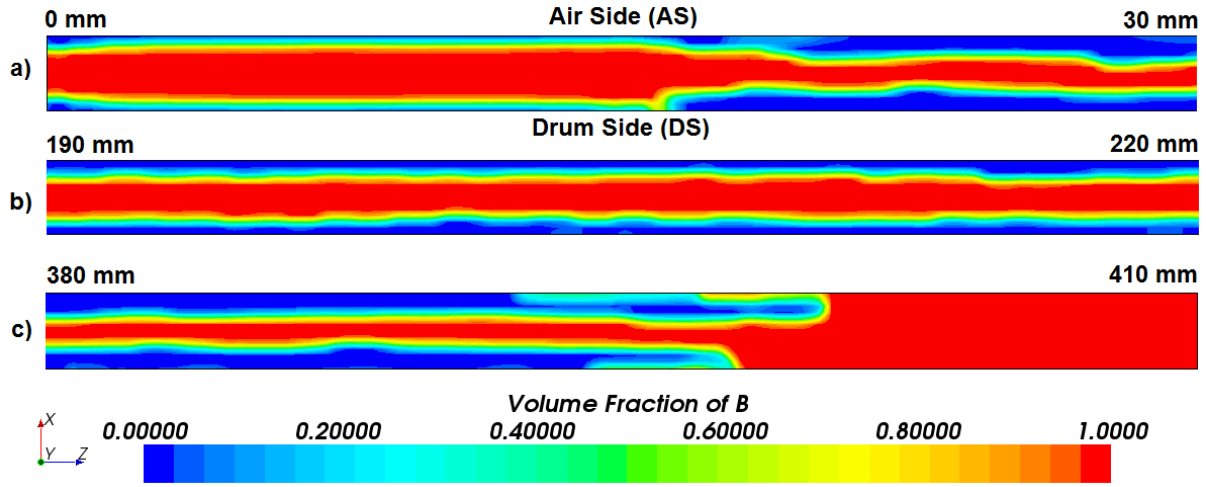

Figure 5.8: The volume fraction of B (shown in red) at the die outlet showing: (a) the 0 mm edge, (b) the middle and (c) the 410 mm edge for a 1:5 B:A viscosity ratio. The volume fraction of A is shown in blue.

(Figure 5.9a) upon increasing the viscosity of A, particularly at the BE. This is because clear edges are attained here and only the less viscous B layer is present. Between 19.5 and 390.5 mm, The mean total flow ($\bar{x}_{\text{flow}}$) is 5.3×10^{-5} and 5.1×10^{-5} m^2 s^{-1} for the 1:2 and 1:5 viscosity ratios respectively. This decrease in film thickness upon increasing the viscosity ratio is due to the flow increase at the edges. Compared with the uniformly thin film at the 1:1 viscosity ratio, less uniformity and more noise is observed at both the 1:2 and 1:5 ratios. Between the solutions at 19.5 and 390.5 mm, there is a total flow standard deviation (σ_{flow}) of 1.7×10^{-6} and 4.2×10^{-6} m^2 s^{-1} for the 1:2 and 1:5 viscosity ratios respectively (see also Table 5.2), showing an order of magnitude more noise than the case of equal viscosity polymers.

The flow curves for Polymer A (Figure 5.9b) show very noisy data; there is a standard deviation of 2.6×10^{-6} m^2 s^{-1} for the three viscosity ratios. As mentioned in Chapter 4, this noise is a function of the mesh cell size and is assumed to be an acceptable numerical limitation. For the 1:5 viscosity ratio, the *total* flow standard deviation exceeds the Polymer A standard deviation. Between 19.5 and 390.5 mm, the amount of A as a percentage of the total film thickness is 20.0, 20.7 and 22.6 % for the 1:1, 1:2 and 1:5 viscosity ratios respectively. This shows that the secondary layers spread less upon increasing their

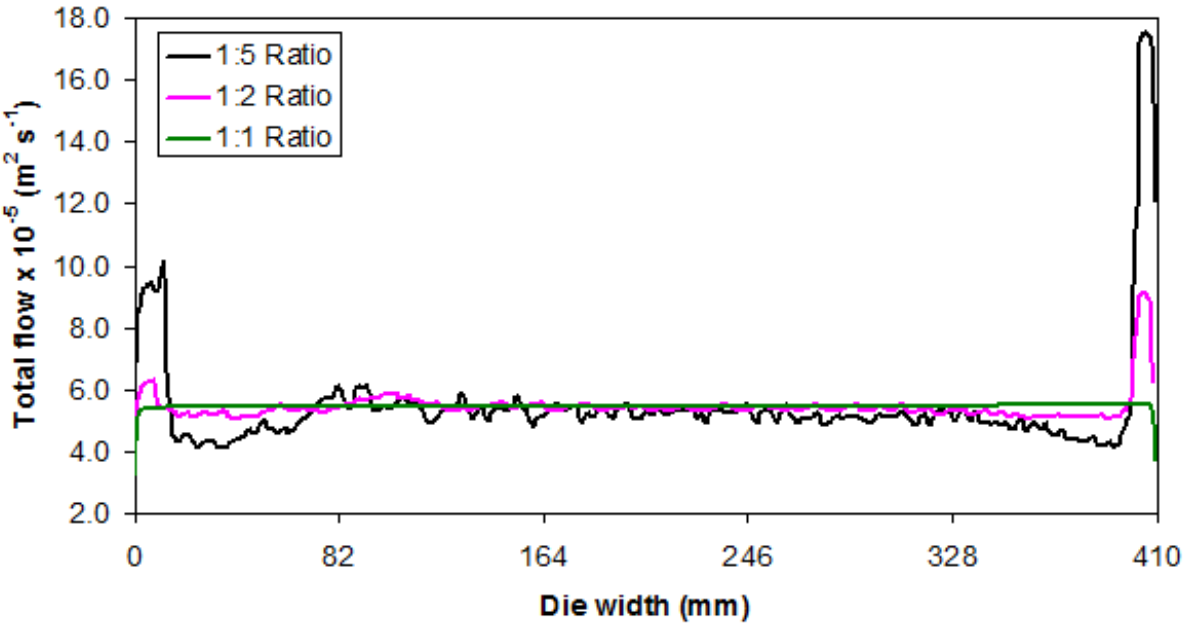

(a)

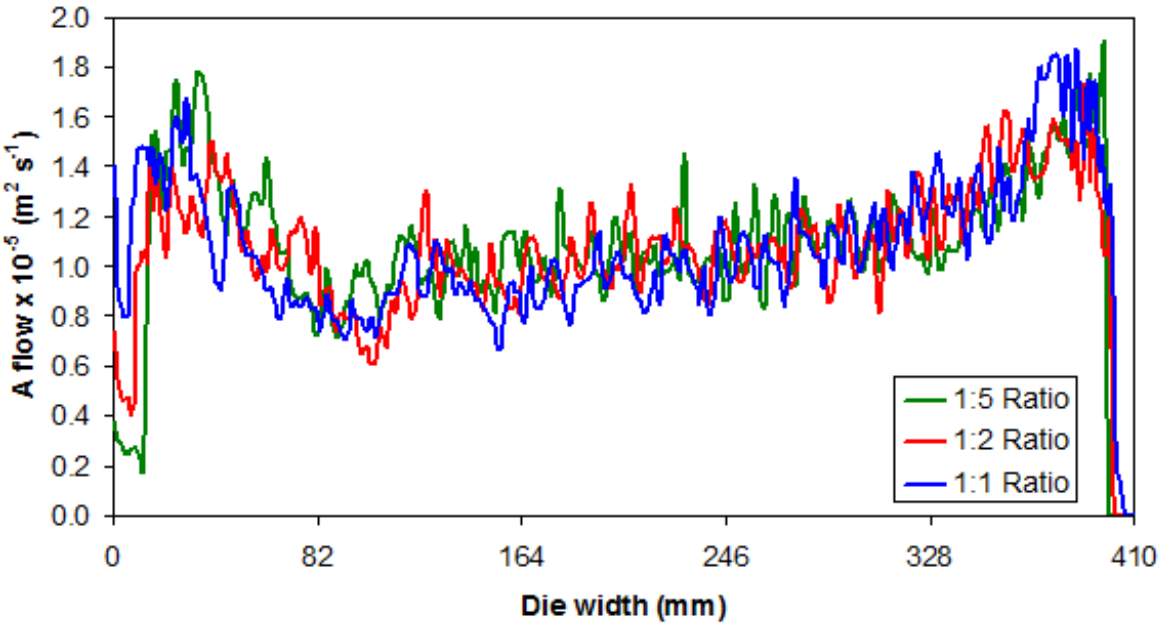

(b)

Figure 5.9: The end fed die outlet flow curves for the three primary:secondary melt viscosity ratios modelled, where (a) shows the total flow curves and (b) shows the Polymer A flow curves.

viscosity, as expected.

The decrease in total flow uniformity at increasing viscosity ratios (Figure 5.9a and Table 5.2) implies that the injector block and end fed die approach struggles at such ratios, which is consistent with literature findings [8, 9, 15, 16, 76]. In particular, in [8, 16] it is stated that the injector block and end fed die approach is limited by a viscosity ratio of 1:4 or 4:1. The large standard deviation at the 1:5 ratio confirms this assertion. This is because the different melt layers are in contact throughout the die and flow deformations can occur.

Table 5.2: Summary results for the three modelled viscosity ratios using the injector block and die.

Viscosity (Pa s)		**BE clear edge width (mm)**		**Total flow $\times$ 10^{-5} (m^2 s^{-1})**	
B	**A**	**AS**	**DS**	$\bar{x}_{\mathbf{flow}}$	$\sigma_{\mathbf{flow}}$
170	170	7.2	4.3	5.4	0.01
170	340	7.3	6.9	5.3	0.2
170	850	7.6	9.6	5.1	0.4

5.2.2 The effect of increasing the primary layer viscosity

Compared with the base conditions shown in Table 5.1, the viscosity of B was increased to two and five times that of A within the injector block and die system modelled. One would expect the less viscous A layers to spread *more* across the film width compared with the case of equal viscosity fluids. It is more common within DTF for the primary melt layer to be more viscous than the secondary melt for MLF production.

Figure 5.10 shows the volume fraction of B at the injector block outlet, for the 1:1 (Figure 5.10a) and 5:1 viscosity ratios (Figure 5.10b). At the AS, the maximum height of A (marked h in Figure 5.10a) *increases* from 19.0 to 20.0 mm upon increasing the viscosity ratio. The spreading of A at the wall has increased for a less viscous A melt as

expected. The maximum depth of Polymer A (marked w in Figure 5.10a) *decreases* from 4.9 to 3.5 mm. Equivalent velocity magnitude outlet plots (see Figure 5.11) shows that the region of maximum velocity has spread further to the edge of the outlet, due to the presence of the less viscous secondary layers. The maximum velocity decreases from 8.8 to 7.3 cm s^{-1} when increasing the viscosity of B.

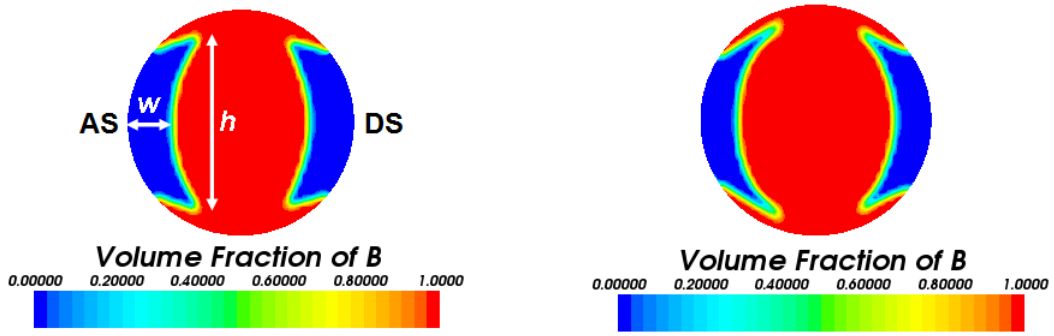

(a) (b)

Figure 5.10: The volume fraction of B (shown in red) at the injector block outlet for (a) a 1:1 B:A melt viscosity ratio and (b) a 5:1 viscosity ratio. The volume fraction of A is shown in blue.

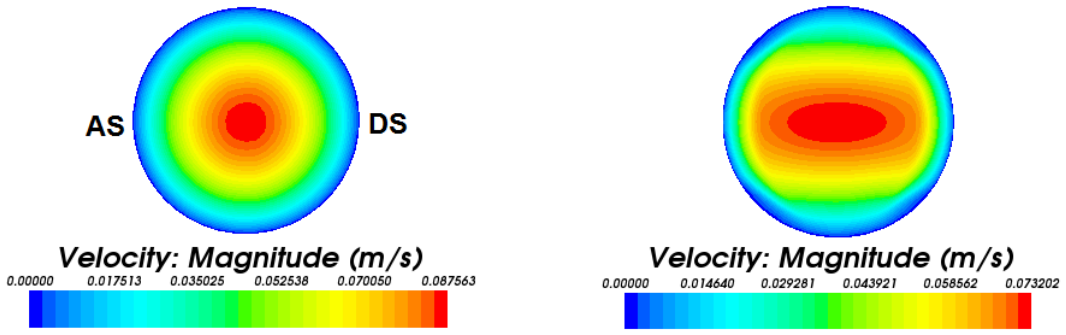

(a) (b)

Figure 5.11: The velocity magnitude at the injector block outlet for (a) a 1:1 primary:secondary melt viscosity ratio and (b) a 5:1 viscosity ratio.

For the 5:1 viscosity ratio, Figure 5.12 shows the volume fraction of B at the end

fed die outlet for the same three locations as in Figure 5.4. The A layers spread more upon increasing the viscosity of B, as expected. A is present at both the FE and BE (Figures 5.12a and c) and full encapsulation of A around B is observed. The presence of A at both edges is caused by the wide melt viscosity differences between the two polymers and such differences are the dominating factor within the die solution. In the middle of the film (Figure 5.12b), the amount of A has significantly reduced compared with the two edges.

The full encapsulation and lack of clear edges is undesirable for a final film product in many cases since the A layers would contaminate the clips during the film production process. This finding again confirms that the injector block and end fed die system is unable to handle wide viscosity ratios such as 5:1.

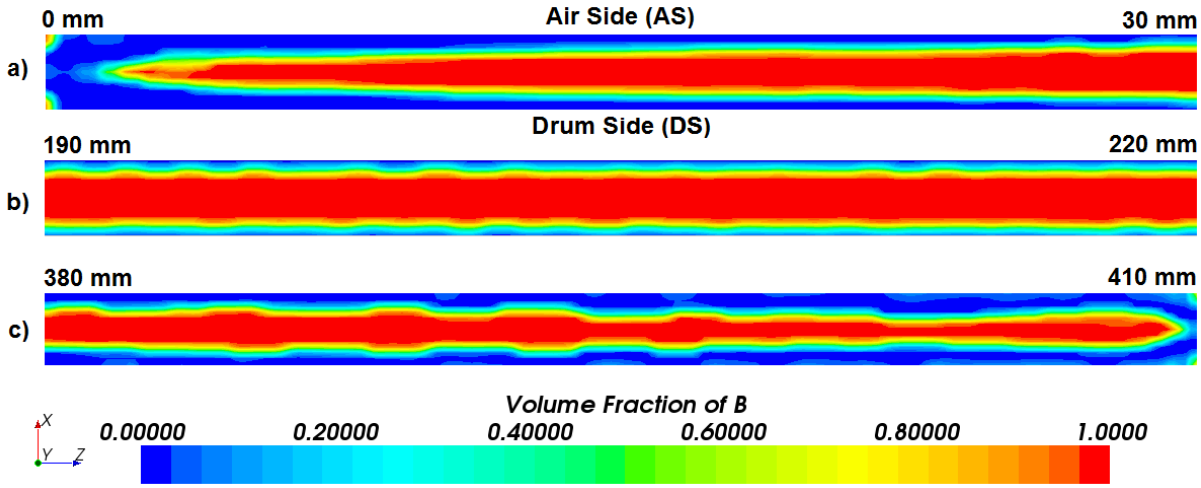

Figure 5.12: The volume fraction of B (shown in red) at the die outlet showing: (a) the 0 mm edge, (b) the middle and (c) the 410 mm edge for a 5:1 B:A viscosity ratio. The volume fraction of A is shown in blue.

Figure 5.13 shows the effect of increasing the primary layer viscosity on the final film (Figure 5.13a) and Polymer A (Figure 5.13b) thickness. From Figure 5.13a, the edges are thicker than the core part of the film for increasing viscosity ratios. This is because the less viscous A layers are present in large quantities at both the FE and BE, causing this thickness increase. In the middle of the film, the total thickness decreases with increasing viscosity ratio (see also Table 5.3) because the more viscous B layer takes up a wider

section of the outlet and dominates the thickness here.

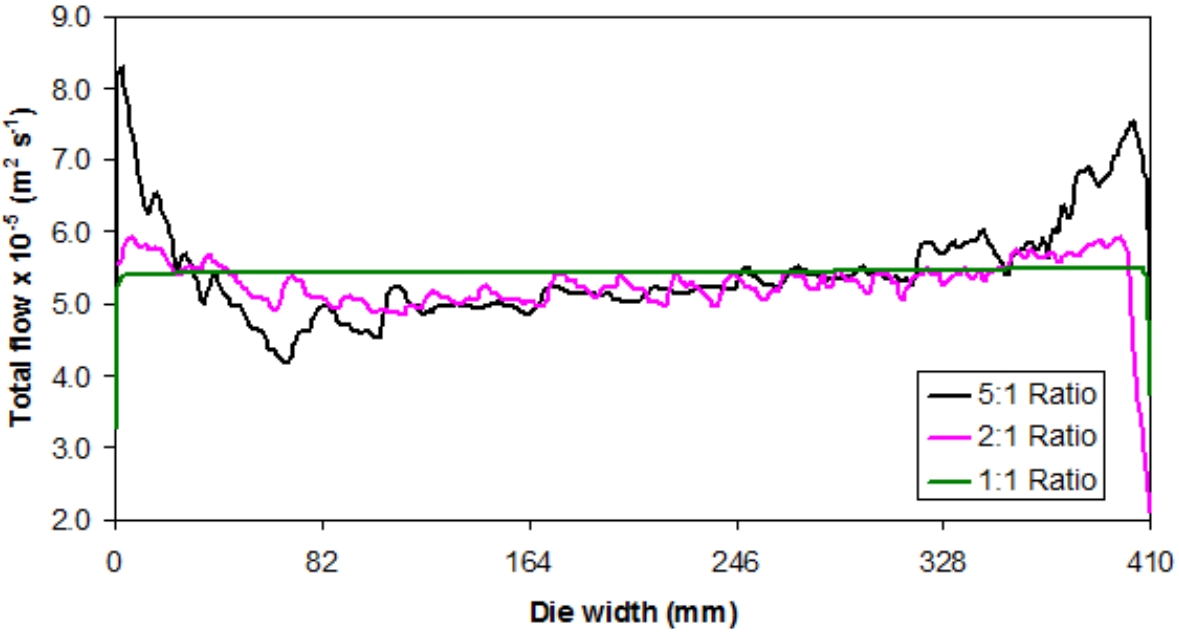

(a)

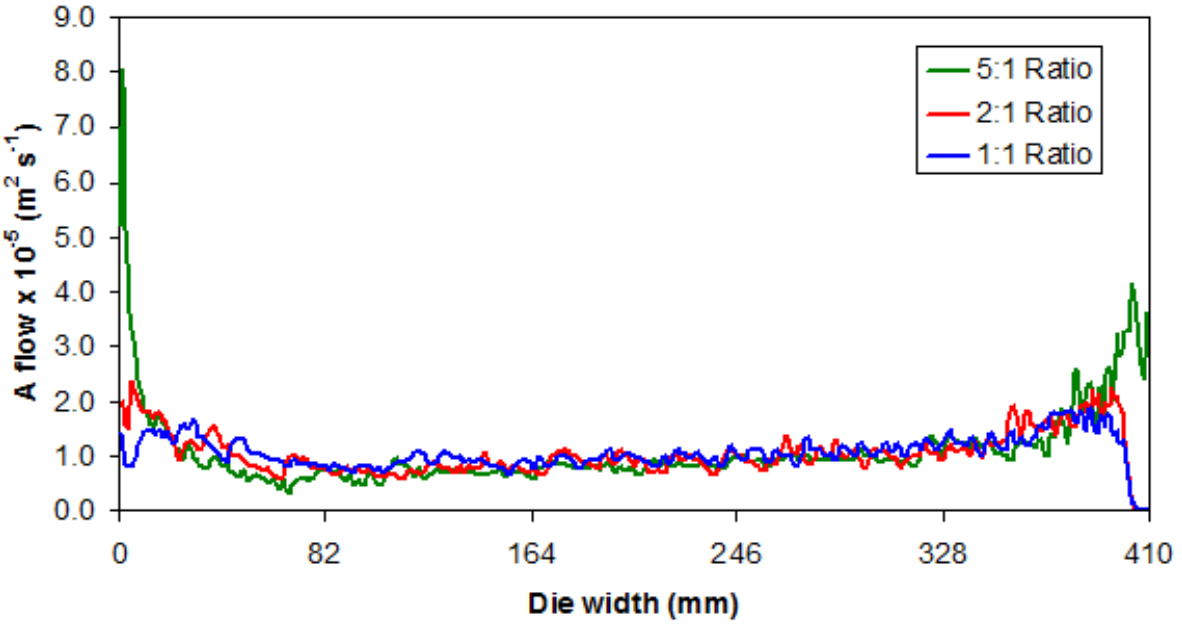

(b)

Figure 5.13: The end fed die outlet flow curves for the three primary:secondary melt viscosity ratios modelled, where (a) shows the total flow curves and (b) shows the Polymer A flow curves.

From Figure 5.13a, less uniformly thin final films are obtained with increasing primary layer viscosity. Between the flow solutions at 19.5 and 309.5 mm, the standard deviation increases from 1.5×10^{-7} to 5.0×10^{-6} m^2 s^{-1} for the 1:1 and 5:1 viscosity ratios respectively. Table 5.3 shows the summary results for a more viscous B layer. The spreading of A and the increased total flow standard deviation with increasing viscosity ratio again suggests that the injector block and die concept is ineffective at handling such wide ratios.

The flow curves for Polymer A (Figure 5.13b) confirm the greater spreading of the secondary layers when increasing the primary layer viscosity. In the die width between 19.5 and 390.5 mm, the amount of A as a percentage of the total flow is 20.0, 19.1 and 17.0 % for the 1:1, 2:1 and 5:1 viscosity ratios respectively. The Polymer A flow standard deviation is 3.5×10^{-6} m^2 s^{-1} for the 5:1 ratio.

Table 5.3: Summary results for the three modelled viscosity ratios using the injector block and die.

Viscosity (Pa s)		**BE clear edge width (mm)**		**Total flow $\times$ 10^{-5} (m^2 s^{-1})**	
B	**A**	**AS**	**DS**	$\bar{x}_{\mathbf{flow}}$	$\sigma_{\mathbf{flow}}$
170	170	7.2	4.3	5.4	0.01
340	170	4.4	3.3	5.3	0.2
850	170	0.0	0.0	5.3	0.5

5.3 410 mm wide multi-manifold die

A second, less widely used coextrusion option is the multi-manifold die (MMD). Figure 5.14 shows the MMD used for CFD analysis, where Figure 5.14a shows the geometry and Figure 5.14b displays the mesh. The primary B layer enters via the middle inlet pipe with the two A layers entering the side pipes. The different melt streams are spread *independently* of each other before coming into contact near the exit and leaving as a unified melt structure. Because of this short contact time, it is envisaged that the MMD will be

better than the injector block and die at handling wide viscosity ratios [8, 9, 11, 15, 16, 76].

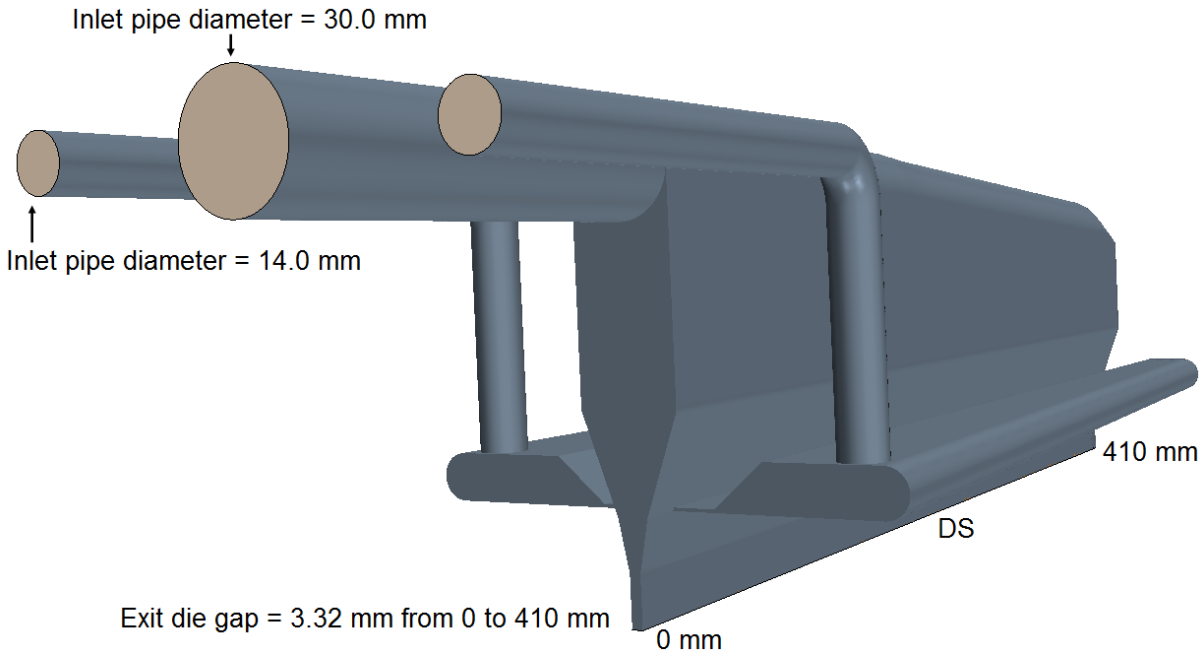

(a)

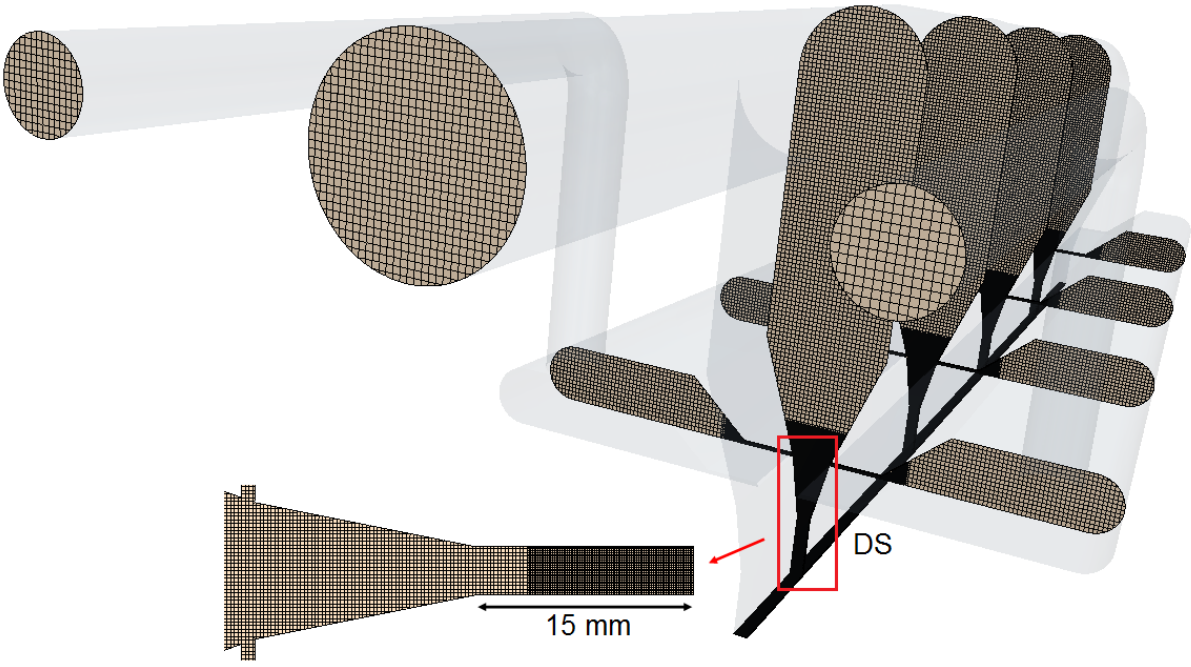

(b)

Figure 5.14: The 410 mm wide MMD used in CFD where (a) shows the geometry and (b) shows the mesh. The flow direction is from left to right.

The pilot scale MMD width is equal to that of the end fed die modelled in Section 5.2. The MMD outlet is *untapered*; the gap remains constant across the width. This setting is based on a configuration used at the time of modelling and it is possible within DTF to alter the die gap settings and implement a taper if required. The width of both secondary channels is 384 mm, giving a projected clear edge width of 13 mm at both the FE and BE. The MMD land length is 15 mm and the DS is marked in Figure 5.14.

Approximately 12 million mesh cells were required to discretise the MMD, 4 million less than used for the system in Section 5.2. Less mesh cells were used for the MMD geometry compared with the injector block and end fed die approach because there is significantly less contact time between the two melt layers in the MMD. Therefore, a finer mesh is required in a smaller fraction of the geometry to maintain a smooth interface. A base mesh cell size of 1.0 mm was used alongside a minimum cell size of 0.2 mm for the MMD. Finer mesh regions were selected once the different fluids were in contact, with an especially fine mesh implemented across the MMD outlet width.

For the conditions in Table 5.1, *i.e.* a B:A viscosity ratio of 1:1, Figure 5.15 shows the progressive volume fraction of B through the MMD. A smooth interface is observed between A and B (see a close-up of the plane section marked with a star), implying a sufficiently fine mesh used. The MMD simulations fully converged within 2,500 iterations, which is significantly less than the running time required for the injector block and die approach (approximately two days runtime compared with seven days). This alongside the lower number of mesh cells implies a greater numerical efficiency with the MMD. The flushing out effect when the secondary layers enter the geometry is not significant for the MMD as the initial condition of the volume fraction is closer to the final solution.

Figure 5.16 shows the volume fraction of B at the MMD outlet, where Figure 5.16a shows the FE to 50 mm, Figure 5.16b shows the middle, from 180 to 230 mm and Figure 5.16c displays from 360 mm to the BE.

The MMD final film solution is better from a commercial perspective than the equivalent end fed die outlet plot (see Figure 5.4). Clear edges of equal width (11.5 mm) are produced which were not obtained using the end fed die. Although the lack of clear edges

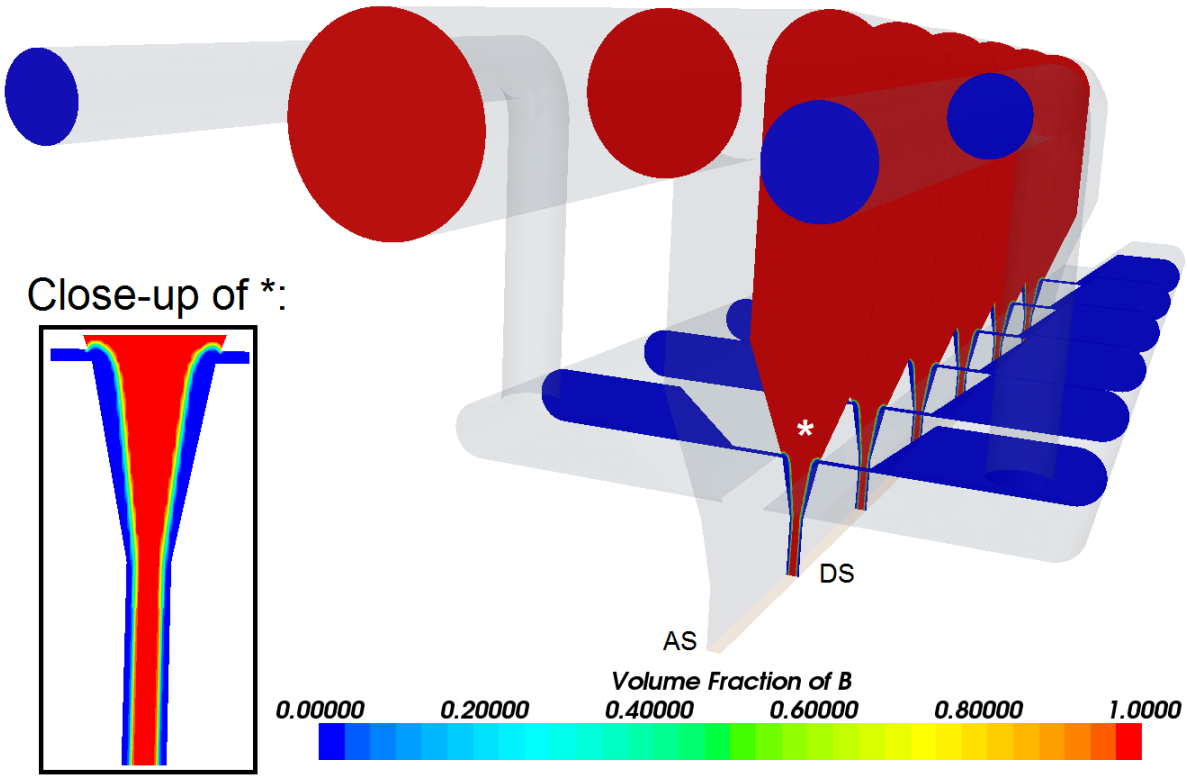

Figure 5.15: The progressive volume fraction of B (shown in red) through the MMD. The flow direction is from left to right. The volume fraction of A is shown in blue.

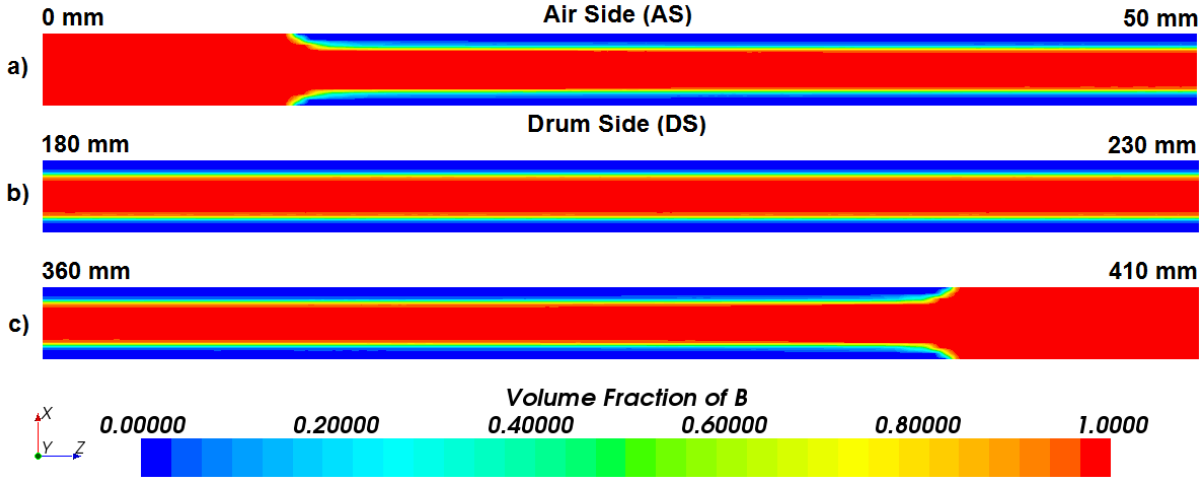

Figure 5.16: The volume fraction of B (shown in red) at the MMD outlet showing: (a) the 0 mm edge, (b) the middle and (c) the 410 mm edge. The volume fraction of A is shown in blue.

at the FE in Figure 5.4 is a numerical artefact, the secondary layers spread unevenly at the end fed die BE and the MMD is shown to be the better coextrusion option at producing a symmetric MLF. The clear edge width is less than the predicted 13 mm value. This spreading of the A layers towards the film edges is believed to be caused by the higher merging velocity due to forcing these layers through narrow secondary inlet channels before coming into contact with B. The MMD outlet solution also shows a smooth, well defined interface which is sharper and more linear than that in Figure 5.4.

For any MMD approach, the individual melt streams flow through separate channels and not as a unified melt structure. It is therefore important to control the velocity of each polymer upon initial contact. Ensuring well matched individual velocities is beneficial to the final film structure. Figure 5.17 shows the velocity magnitude on a plane section 205 mm into the MMD. At the point of initial contact, the maximum velocity of A is 7.63 mm s^{-1} and that of B is 7.57 mm s^{-1}. This equates to a 0.8 % velocity difference which implies very little flow deformation upon initial contact of the layers. Such closely matched velocity values cause the uniform film structure in Figure 5.16.

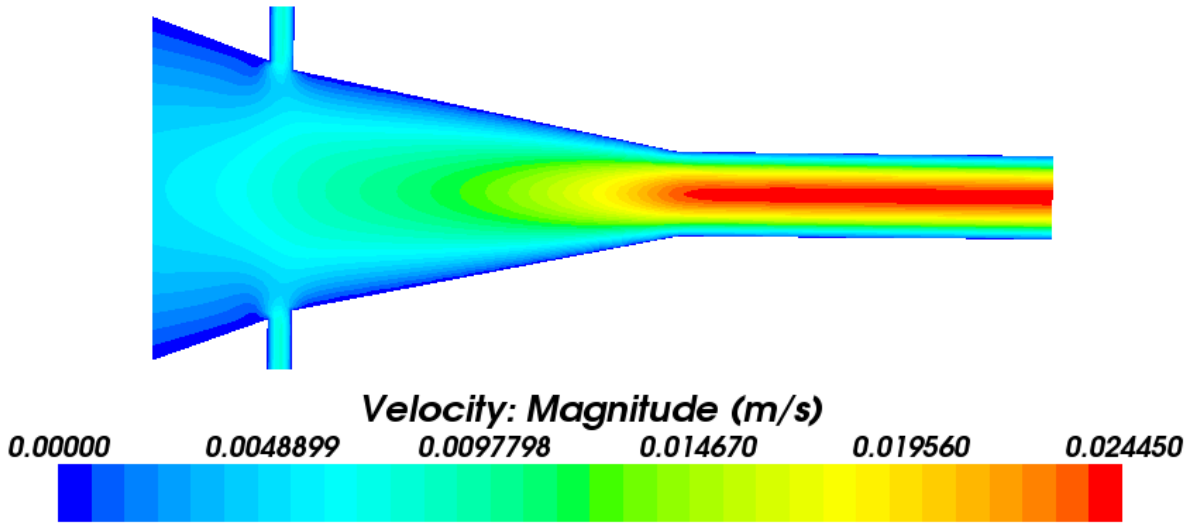

Figure 5.17: The velocity magnitude on a plane section 205 mm into the MMD geometry.

Figure 5.18 shows the total, B, A DS and A AS flow curves across the MMD outlet width. The film produced is *not* uniformly thin; there is a 5.0 % decrease in thickness between the values at 19.5 and 390.5 mm. This uneven thickness is due to the constant

MMD outlet gap (see Figure 5.14). It is possible to widen the die gap of DTF dies which would have improved the thickness uniformity by promoting more flow towards the BE. Another way of ameliorating the flow profile is the use of die bolt heaters, as modelled in Chapter 7. There is very little noise in the total flow curve (a standard deviation of 9.4×10^{-7} m^2 s^{-1}), which is desirable from a commercial perspective.

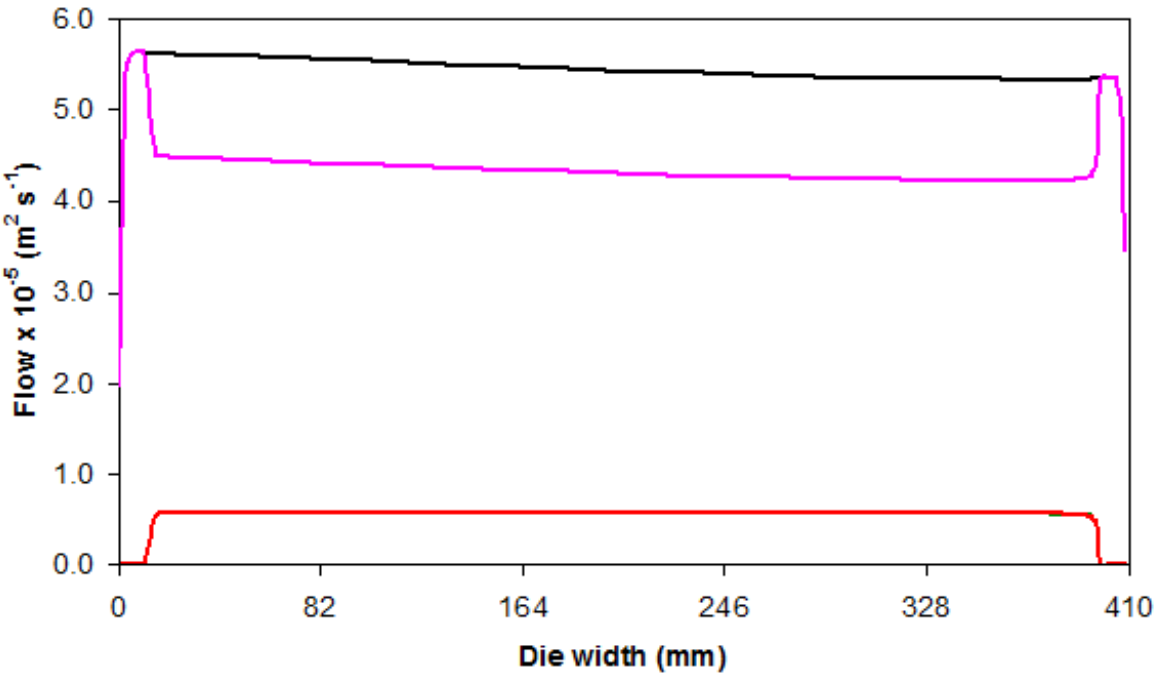

Figure 5.18: The total (shown in black), B (shown in pink), A drum side (shown in green) and A air side (shown in red) flow curves across the MMD outlet width.

The individual layer thickness curves are very well defined and are significantly less noisy than the equivalent end fed die results in Figure 5.5; each individual A layer has a flow standard deviation of 7.4×10^{-8} m^2 s^{-1}. This is because the interfacial contour is confined to a single mesh cell and remains constant in the MMD. The two A flow curves are almost identical, showing the symmetrical final film produced by the MMD. Equal individual A layer thicknesses were not obtained using the injector block and end fed die, and the MMD is the better coextrusion option for individual layer thickness control.

5.3.1 The effect of increasing the secondary layer viscosity

The viscosity of A was increased to two, three, five and ten times that of B within the MMD, using the conditions in Table 5.1 as a reference. The outlet volume fraction at the same three locations as in Figure 5.16 for the 1:10 viscosity ratio is displayed in Figure 5.19.

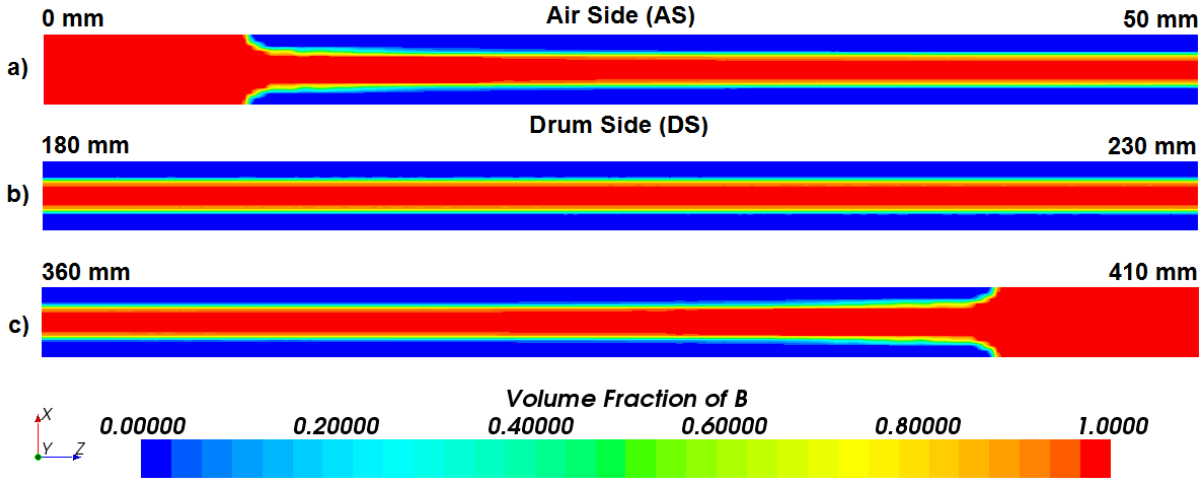

Figure 5.19: The volume fraction of B (shown in red) at the MMD outlet showing: (a) the 0 mm edge, (b) the middle and (c) the 410 mm edge for a 1:10 B:A viscosity ratio. The volume fraction of A is shown in blue.

A smooth interface is again maintained for the MMD solution. Compared with the 1:1 viscosity ratio case, the clear edge width has *reduced* from 11.5 to 9.7 mm when increasing the viscosity of A to 1,700 Pa s. This increased spreading of A when increasing its viscosity is the opposite to what one would expect and is attributed to the nature of the MMD geometry. Very viscous secondary layers are forced through narrow channels and it is believed that this causes them to dislodge B and spread further upon initial contact. Figure 5.19 shows that clear edges are guaranteed with an MMD for very large viscosity ratios.

Figure 5.20 shows the flow curves for the five viscosity ratios modelled, where Figure 5.20a shows the total flow curves and Figure 5.20b displays the Polymer A flow curves. The middle part of each film (Figure 5.20a) is uniformly thin. This is desirable and confirms that the MMD is excellent at handling increasingly wide secondary layer

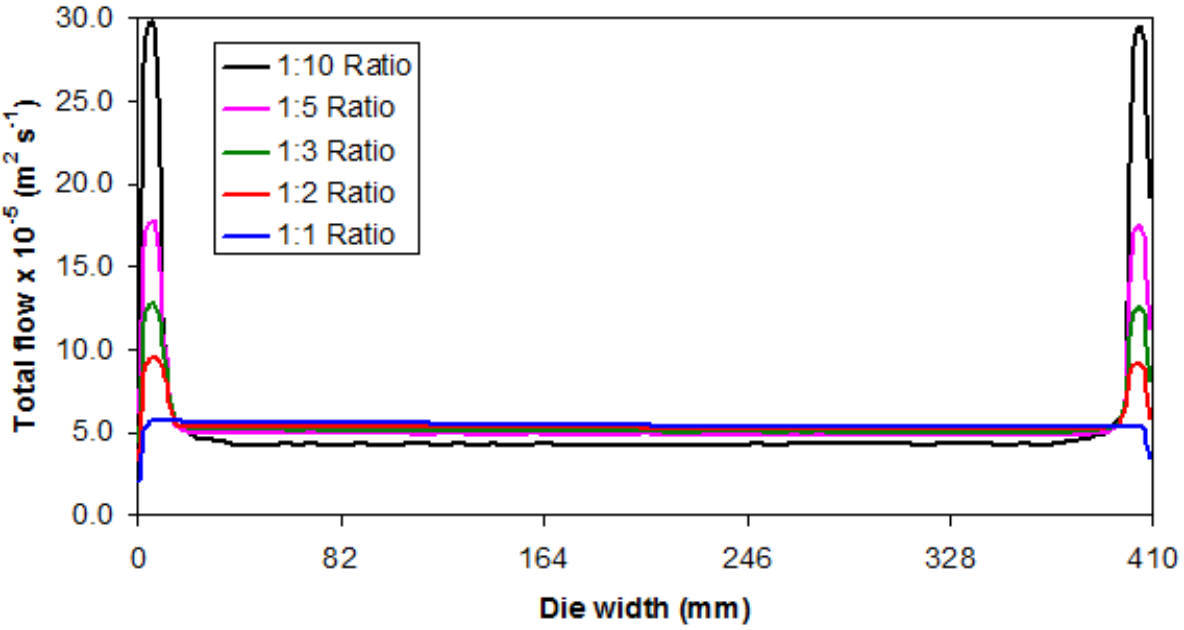

(a)

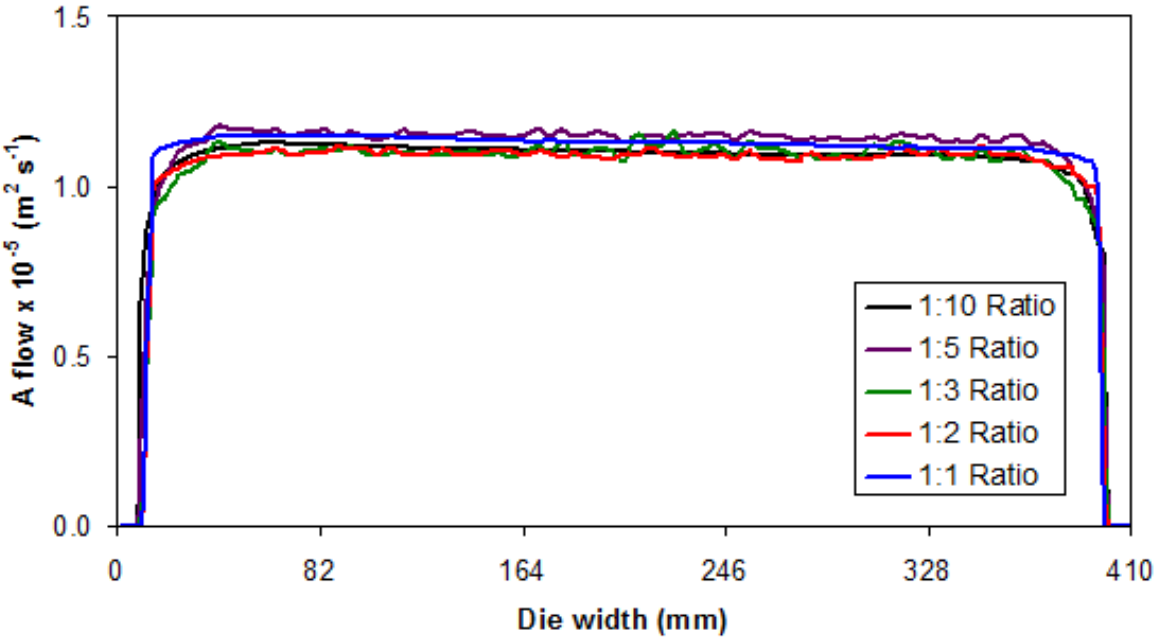

(b)

Figure 5.20: The MMD outlet flow curves for the five primary:secondary melt viscosity ratios modelled, where (a) shows the total flow curves and (b) shows the Polymer A flow curves.

melt viscosities. Such linear thickness profiles are not observed for the equivalent end fed die solutions in Figure 5.9a, showing the MMD to be the better coextrusion option for wide viscosity ratios. The mean total flow between 19.5 and 390.5 mm *decreases* with increasing secondary layer viscosity (see Table 5.4). This is due to the increase in edge thickness for large viscosity ratios, with mass conservation causing a decrease in the middle of the film. The edges increase in thickness compared with the core part of each film because clear edges are attained and only the less viscous B is present here. The edges are trimmed during the film production process, and the core part of the film is of more importance. However, thick cast edges can cause operational issues and need to be managed using die bolt heaters.

The secondary layer flow curves in Figure 5.20b show increased spreading of Polymer A to the edges upon increasing its viscosity. Between 19.5 and 390.5 mm, the amount of A as a percentage of the total film *increases* from 20.7 to 25.3 % for the 1:1 and 1:10 viscosity ratios respectively. This increase in proportion of Polymer A in the middle of the film is due to the decrease in the mean total film thickness, caused by thicker edges. The thickness curves for Polymer A are significantly less noisy than the equivalent end fed die curves in Figure 5.9b; the standard deviation for the 1:5 viscosity ratio is 3.1×10^{-7} m^2 s^{-1}. This is because the interfacial contour is confined to a single mesh cell and remains constant in the MMD.

Table 5.4: Summary results for the five modelled viscosity ratios using the MMD.

Viscosity (Pa s)		**Clear edge width (mm)**		**Total flow $\times$ 10^{-5} (m^2 s^{-1})**	
B	**A**	**FE**	**BE**	$\bar{x}_{\mathbf{flow}}$	$\sigma_{\mathbf{flow}}$
170	170	11.5	11.5	5.4	0.09
170	340	11.0	11.0	5.2	0.06
170	510	10.6	10.6	5.1	0.06
170	850	10.1	10.1	4.9	0.05
170	1,700	9.7	9.7	4.3	0.1

A summary table, showing the effect of increasing the viscosity of A in the MMD, is displayed in Table 5.4. As mentioned previously, the clear edge width decreases and spreading to the film edges increases upon increasing the viscosity of A. Symmetric final films were obtained with the MMD which were not produced using the injector block and end fed die approach. The total flow standard deviation and hence film thickness uniformity (calculated between 19.5 and 390.5 mm) improves with wider viscosity ratios up to the 1:5 case. This improvement occurs despite the lack of a taper at the MMD outlet and is attributed to the more viscous layers slowing down the movement of the unified ABA composition through the MMD. Comparing the flow standard deviation results in Table 5.4 with those in Table 5.2, the MMD is better than the injector block and end fed die at handling large secondary layer viscosities. The standard deviation increases for the 1:10 simulation because the effect of the thick edges spreads further into the film and within the boundary of the calculation made. For this 1:10 viscosity ratio, the standard deviation is equal to 4.4×10^{-7} m^2 s^{-1} between 40 and 370 mm.

5.3.2 The effect of increasing the primary layer viscosity

Compared with the conditions in Table 5.1, the viscosity of the primary B layer was increased to two, three, five and ten times that of A in the MMD.

Figure 5.21 shows the outlet volume fraction of B for a 10:1 B:A viscosity ratio, taken at the same three locations in Figure 5.16. At this wider viscosity ratio, the clear edge width has *increased* from 11.5 to 16.0 and 14.7 mm at the FE and BE respectively. This shows that the A layers have spread less to the film edges despite being significantly less viscous than B. The MMD geometry is believed to cause this effect, with the more viscous B layer forcing the secondary A layers towards the middle of the film upon initial contact. It appears that this effect is more pronounced at the FE, causing a slightly non-symmetric structure. For a 5:1 B:A viscosity ratio, full encapsulation of A around B was observed at the end fed die outlet and clear edges were not produced (Figure 5.12). The edge solutions in Figure 5.21 again shows the MMD to be the better coextrusion option at producing clear edges with wide melt viscosity differences.

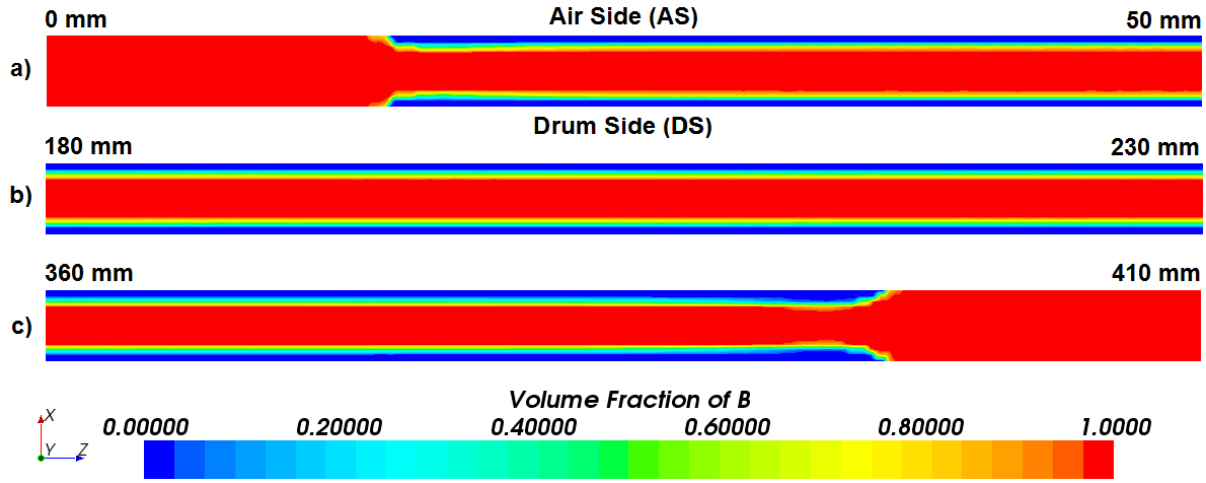

Figure 5.21: The volume fraction of B (shown in red) at the MMD outlet showing: (a) the 0 mm edge, (b) the middle and (c) the 410 mm edge for a 10:1 B:A viscosity ratio. The volume fraction of A is shown in blue.

Figure 5.22 shows how increasing the primary layer viscosity affects the MMD film structure, where Figure 5.22a shows the total flow and Figure 5.22b displays the Polymer A flow. The thin film edges at increasing viscosity ratios (Figure 5.22a) are found because of the sole presence of the more viscous B layer here. These edges would be improved during production using die bolt heaters to manage operational difficulties. The overall flow uniformity *worsens* with increasing B viscosity. For the 10:1 ratio, there is a flow decrease of 12.8 % between the solutions at 19.5 and 390.5 mm. This decrease in thickness uniformity in the MMD is attributed to the less viscous, fast moving A layers causing a sharp total thickness increase near the FE when they first enter the geometry. Neither the MMD outlet nor the secondary channels are tapered which promotes more flow towards the FE. It appears that for the MMD, the film thickness is governed by the skin layer shear viscosity. This is consistent with literature findings in [43, 91, 92] for unified structures.

Between 19.5 and 390.5 mm, the mean total flow increases with increasing primary layer viscosity, see Table 5.5. This is because of the thin film edges found for wide melt viscosity ratios. The total flow standard deviation also increases with widening viscosity ratios. This is caused by the lack of a taper at the MMD outlet and could be easily ameliorated. Comparing the standard deviation results in Table 5.5 with the equivalent

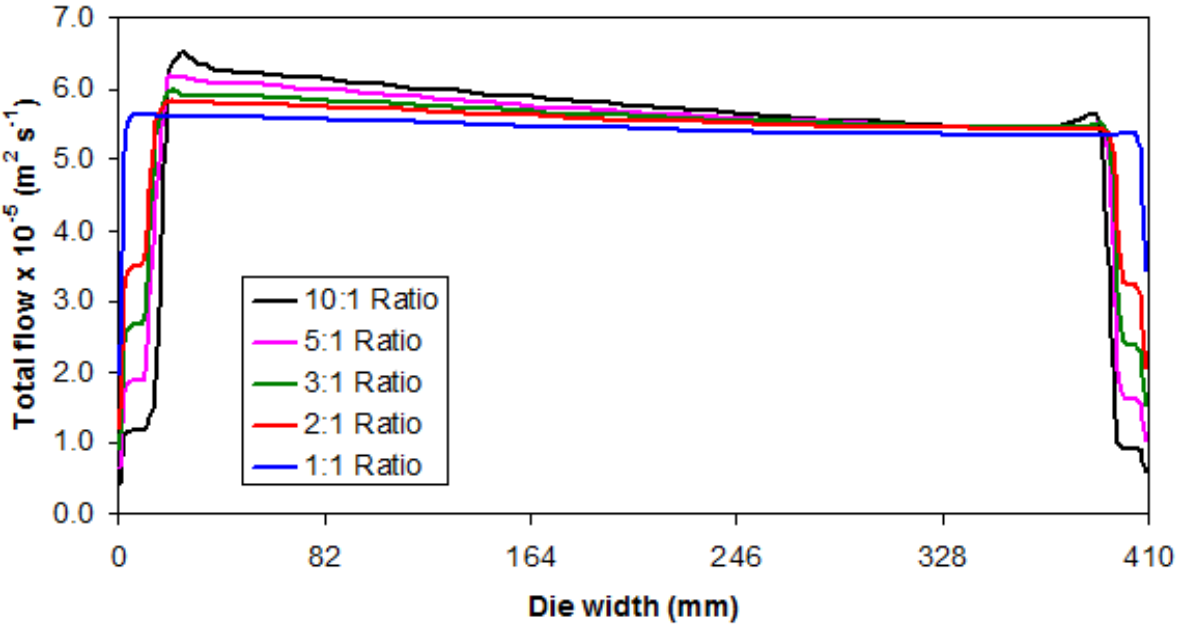

(a)

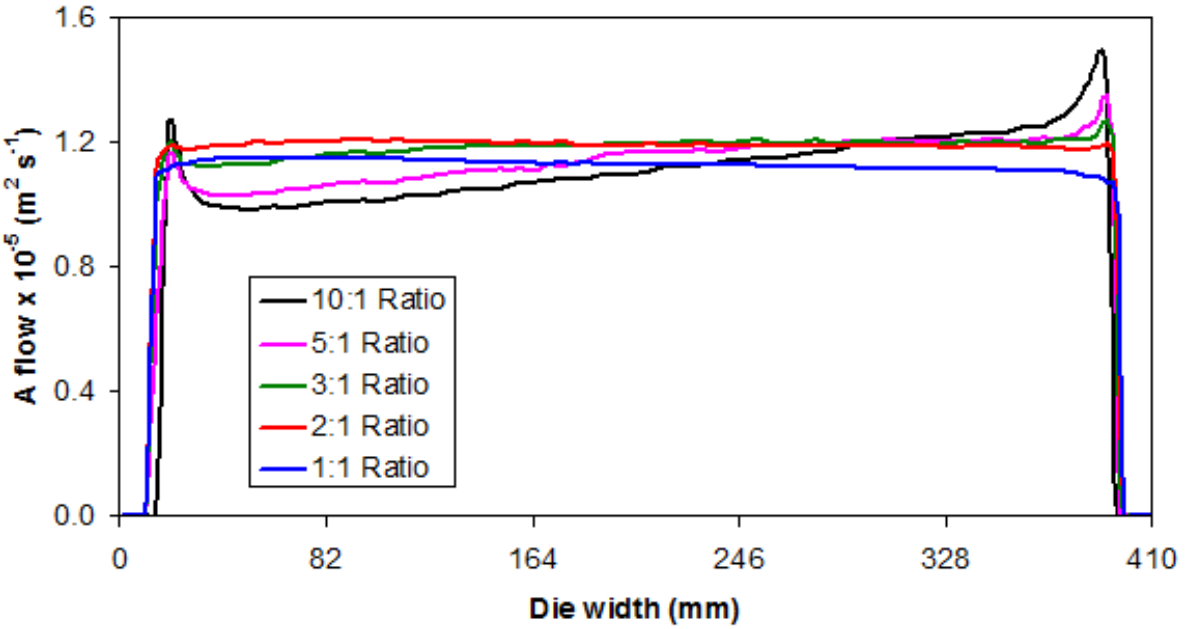

(b)

Figure 5.22: The MMD outlet flow curves for the five primary:secondary melt viscosity ratios modelled, where (a) shows the total flow curves and (b) shows the Polymer A flow curves.

end fed die ones in Table 5.3, there is less noise in the MMD final films despite no tapering of the MMD. These results and others in this Chapter have shown the MMD to be better than the injector block and end fed die at handling increasingly wide viscosity ratios.

The Polymer A flow curves in Figure 5.22b show reduced spreading of the secondary layers when increasing the primary layer viscosity, *i.e.* a wider length of Polymer B at the edges. For the 3:1 viscosity ratios and above, the thickness of Polymer A increases from 45 to 389 mm. This is accompanied by an increase in the velocity of A after spreading in the secondary channels and coming into contact with the very viscous B layer. There are large increases in the Polymer A thickness when the low viscosity layers first enter the MMD. In the die width range from 19.5 to 390.5 mm, the amount of A as a proportion of the total film thickness *decreases* from 20.7 to 19.6 % for the 1:1 and 10:1 viscosity ratios respectively. This is caused by both thinner A layers and a thicker total film across the majority of the film width for this very viscous B layer. For the 5:1 viscosity ratio, the Polymer A flow standard deviation is 6.9×10^{-7} m^2 s^{-1}.

Table 5.5: Summary results for the five modelled viscosity ratios using the MMD.

Viscosity (Pa s)		**Clear edge width (mm)**		**Total flow $\times$ 10^{-5} (m^2 s^{-1})**	
B	**A**	**FE**	**BE**	$\bar{x}_{\mathbf{flow}}$	$\sigma_{\mathbf{flow}}$
170	170	11.5	11.5	5.4	0.09
340	170	12.4	12.4	5.6	0.1
510	170	13.0	12.7	5.6	0.2
850	170	13.9	13.3	5.7	0.2
1,700	170	16.0	14.7	5.8	0.3

5.4 Chapter conclusions

In this Chapter, the comparative ability of an injector block linked to an end fed die and an MMD at handling wide viscosity ratios was analysed using CFD. The modelled

geometries are typical of DTF's pilot scale facilities.

The MMD was found to be the better coextrusion option at producing clear edges, obtaining a smooth polymer-polymer interface and maintaining a symmetric MLF across the film width. Numerical results also showed that the MMD is the better option when producing films with increasingly wide melt viscosity ratios. With DTF's MLF products increasing in complexity, it is likely that the MMD will be used more frequently. The results obtained in this Chapter are consistent with the literature [8, 9, 11, 15, 16, 76]. The MMD was also more numerically efficient than the injector block and end fed die, with less mesh cells and a shorter convergence time required.

Chapter 6

Experimental validations

6.1 Introduction

In this Chapter, experimental analysis of MLFs was conducted to validate the equivalent CFD modelling results. A trial geometry was selected for a series of experimental studies and was also modelled in CFD to enable validation based comparisons to be made.

In Section 6.2, numerical results and experimental analysis of layer proportions within unstretched cast films via light microscopy of MLFs used for reflector film applications is shown. Section 6.3 shows interpretation of MLFs used for heat seal purposes, where temperature and hence melt viscosity effects are scrutinised. The experimental results in Section 6.3.2 show analysis of the layer distribution within frozen die plugs, layer thickness results of chloroform washing data of both cast and biaxially stretched final film samples and white light interferometry (WLI) data of final film samples. Figure 6.1 shows a schematic of the PET film process, where the main experimental methods used in Section 6.3.2 are displayed. Fluorescence microscopy and reflectometry data is also shown in this Section. In both Sections 6.2 and 6.3, an injector block linked to a 410 mm wide end fed die was used to manufacture the films and this hardware is hence modelled in

[1] Aspects of this Chapter have been published in: J. Champion, M. K. Looney and M. J. H. Simmons, Numerical Modeling of Multilayer Film Coextrusion With Experimental Validation, *Polymer Engineering and Science*, 2014. DOI: 10.1002/pen.24022.

CFD; see Figures 5.1 and 5.2b for the meshed geometries.

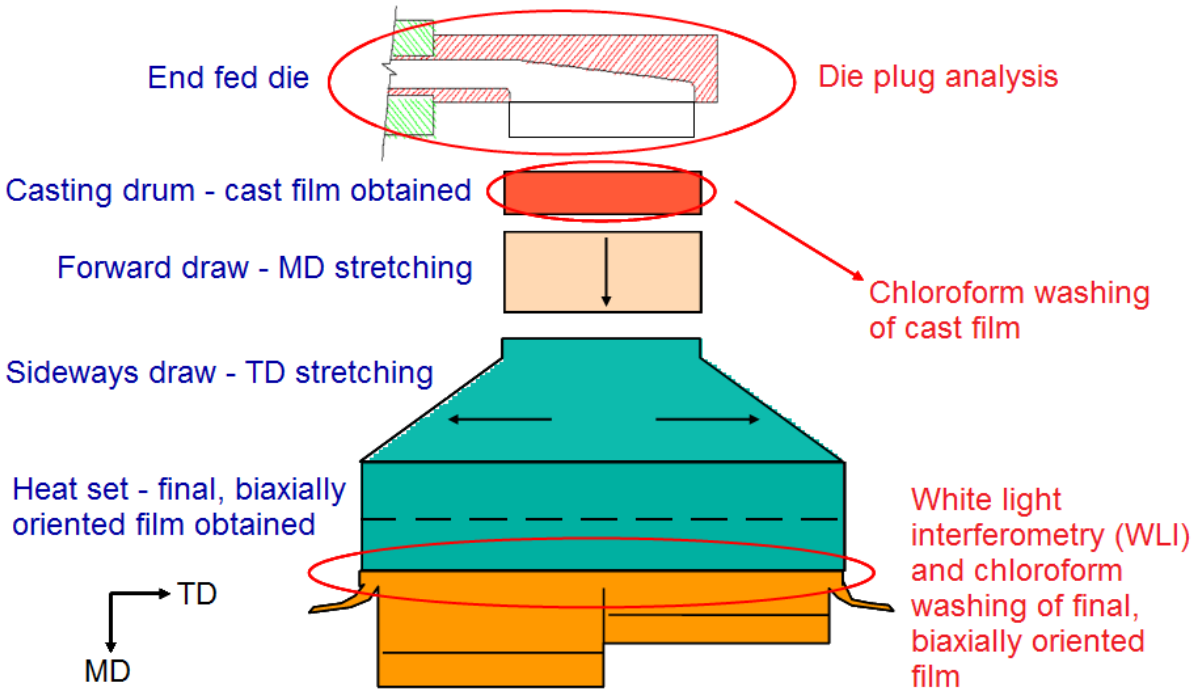

Figure 6.1: The main experimental methods used in Section 6.3.2.

Another aim of this Chapter, alongside experimental validation, is to analyse how both geometry wall and polymer melt temperatures affect the final MLF structures and layer spreading. This is the first occasion where temperature dependent rather than constant viscosities are considered in the models.

6.2 Reflector film trial

ABA structured reflector films were manufactured using DTF pilot scale facilities. The final film thickness was approximately 150 μm with the primary B layer making up around 77 % of this thickness and the A layer split equally into the two secondary injector block inlet pipes. The primary B layer was a heavily filled PET polymer, extruded at 275 °C, and the secondary A layer was a lightly filled PET polymer, extruded at 295 °C. Both B and A were formulated by the blending of several different polymer resins.

The rheology of the polymers making up B and A was measured using a parallel plate rheometer. This rheometry method is described in more detail in Section 2.1.1. Figure 6.2

shows the predicted rheology of each melt layer based on their individual polymer blends between 265 and 300 °C at a constant shear rate of 100 s^{-1}, assuming Newtonian behaviour. The viscosity-temperature relationships (see Table 6.1) used in CFD to fit these two data sets is also shown. At the same temperature, the secondary A layer is more viscous than B and the viscosity ratio exceeds 1:1.5. However, at their individual extrusion temperatures, the melt viscosities of B and A are 127 and 138 Pa s respectively. These almost equal viscosity values are therefore expected to achieve a symmetrical MLF with an even layer distribution.

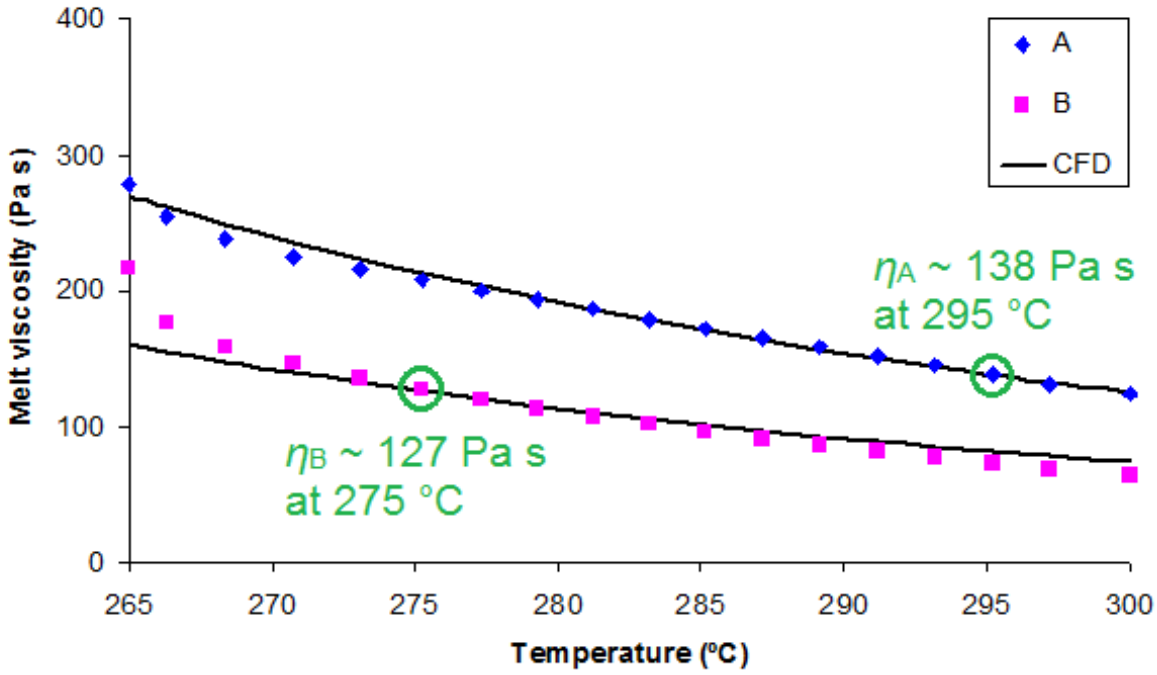

Figure 6.2: Predicted rheology of the two polymer layers used for the reflector film trial at an applied shear rate of 100 s^{-1}. Experimental rheometry performed by David Stocks, Intertek.

For CFD purposes, the melt viscosity-temperature relationships for B and A were approximated using the polymer IVs, $[\eta]$, and the O'Dell model in Equation 2.8. Based on their individual compositions, $[\eta_B] \approx 0.54$ and $[\eta_A] \approx 0.6$. From Figure 6.2, there is good agreement between the shear viscosity data and the CFD functions. Table 6.1 shows the fluid properties assigned to B and A within STAR-CCM+, where density and

thermal conductivity differences are caused by differing quantities of the filler particle. The injector block and 410 mm wide end fed die had a constant wall temperature of 275 °C. The melt viscosity of A is approximately 208 Pa s at 275 °C (slightly overestimated in CFD, see Figure 6.2), meaning there will be viscous wall effects in this system.

Table 6.1: The modelled reflector film fluid properties for B and A.

	B	**A**
Temperature (T)	275 °C	295 °C
Density (ρ)	1,952 kg m^{-3}	1,313 kg m^{-3}
Viscosity (η), Pa s	$10^{\{(2{,}953/(T+273))-3.29\}}$	$10^{\{(2{,}953/(T+273))-3.06\}}$
Thermal conductivity (κ)	0.33 W m^{-1} $°C^{-1}$	0.22 W m^{-1} $°C^{-1}$
Mass flow rate ($\dot{m}$)	110 kg hr^{-1}	33 kg hr^{-1}
Final volume fraction	77 %	23 %

6.2.1 Computational Fluid Dynamics results

CFD was conducted using the properties in Table 6.1. Figure 6.3 shows the progressive viscosity through the 410 mm wide end fed die geometry, where the flow direction is from left to right. The viscosity of the bulk of each fluid is almost identical, which is expected from the viscosity-temperature relationships modelled. The most viscous region (213.4 Pa s) is observed for A at the geometry walls. This is because A enters the die at 295 °C and is cooled by the die walls which have a constant temperature of 275 °C. Although confined to the walls, the higher maximum viscosity will be prominent at the thin outlet exit gap and the ratio between the maximum and bulk viscosity values may have an effect on the final film structure.

The outlet volume fraction plot of B, representing the CFD predicted final film solution, is shown in Figure 6.4, where Figure 6.4a shows the section from the 0 mm edge (feed edge, FE) to 30 mm, Figure 6.4b shows the middle, from 190 to 220 mm, Figure 6.4c

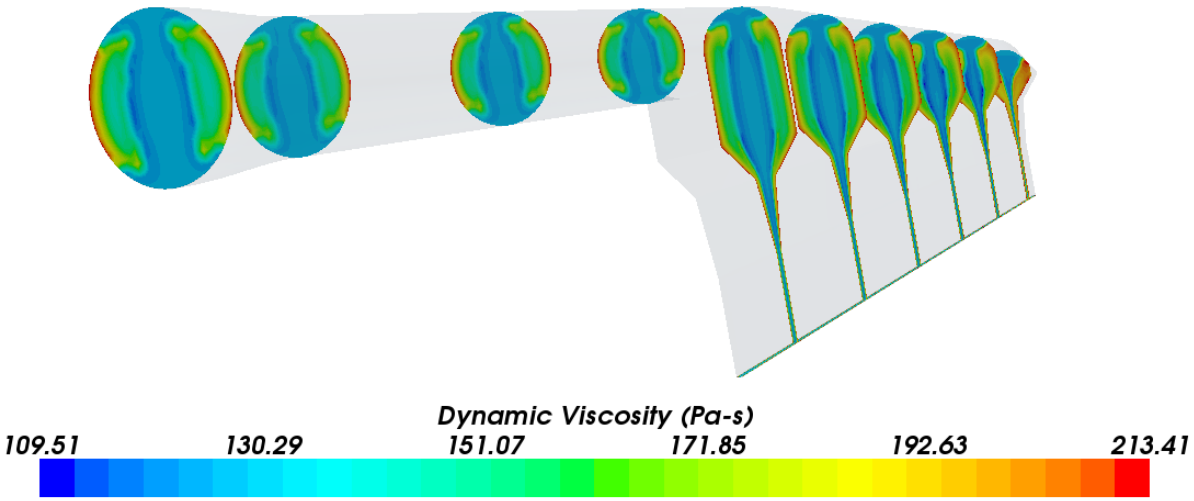

Figure 6.3: The progressive viscosity through the 410 mm wide end fed die for the reflector film. Flow direction is from left to right.

displays from 340 mm to 370 mm and Figure 6.4d shows from 380 mm to the blank edge (BE) at 410 mm. In this plot, B is shown in red with A in blue and the air side (AS) and drum side (DS) are labelled according to the side of the melt curtain touching the casting drum.

From Figures 6.4a and d, clear edges are not attained numerically at either the FE or the BE, with A present at both the AS and DS at the two edges. The lack of numerical clear edges at the BE implies that A is predicted to spread to this far edge despite being the more viscous polymer, which is the opposite to what one would expect. From Figures 6.4c and d, there is more A present towards the far 410 mm edge of the die compared with the other two locations. This spreading and increase in thickness of A towards the BE is attributed to the lower density of A compared with B; the heavier B layer "falls" out of the die quicker, leaving an increasing proportion of A in the film as one moves to the BE. It is believed that the modelled density difference is sufficiently wide to be the dominant factor rather than viscosity for this reflector film case. The phenomenon of the heavier B layer falling out of the die faster than A within the die body is an inertial effect, see the term on the right hand side of Equation 2.25.

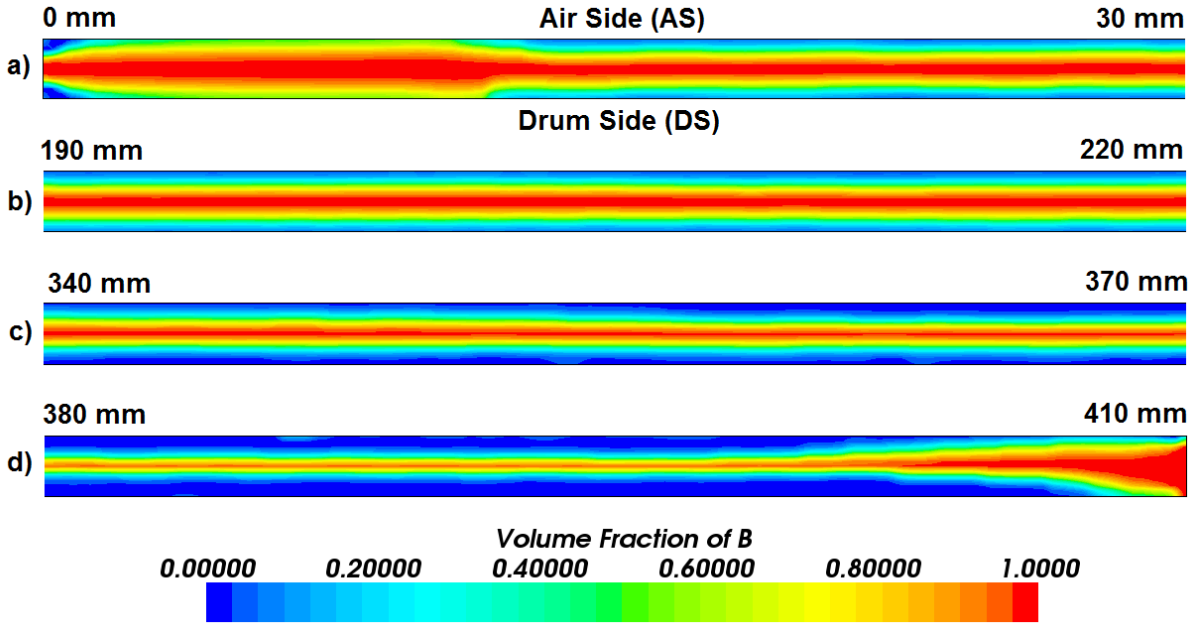

Figure 6.4: The volume fraction of B (shown in red) at the die outlet showing: (a) the 0 mm edge, (b) the middle, (c) between 340 and 370 mm and (d) the 410 mm edge. The volume fraction of A is shown in blue.

Figure 6.5 shows the total, B and both the DS and AS A flow curves across the 410 mm die width. These curves correspond to the CFD predicted total and individual layer thickness profiles, with the derivation methods described in Chapter 4.

A uniformly thin final film is predicted numerically, apart from a sharp thickness increase at the FE and BE. This thickness deviation is caused by less A present at each edge. The wall temperature has caused A to be more viscous at the walls (see Figure 6.3) and less A present results in a decrease in the overall melt viscosity and hence thickness increase. This shows that despite A and B having similar melt viscosity values at their respective extrusion temperatures, the final film structure is also governed by the wall temperature. The two A layers increase in thickness and are well matched when moving from 0 to 410 mm, as also shown in Figure 6.4. Any noise in the individual layer thickness curves is caused by numerical predictions of the interfacial location, see Chapter 4. For the purpose of experimental validation, it is the *trend* in the individual layer thickness curves rather than the noise which is significant.

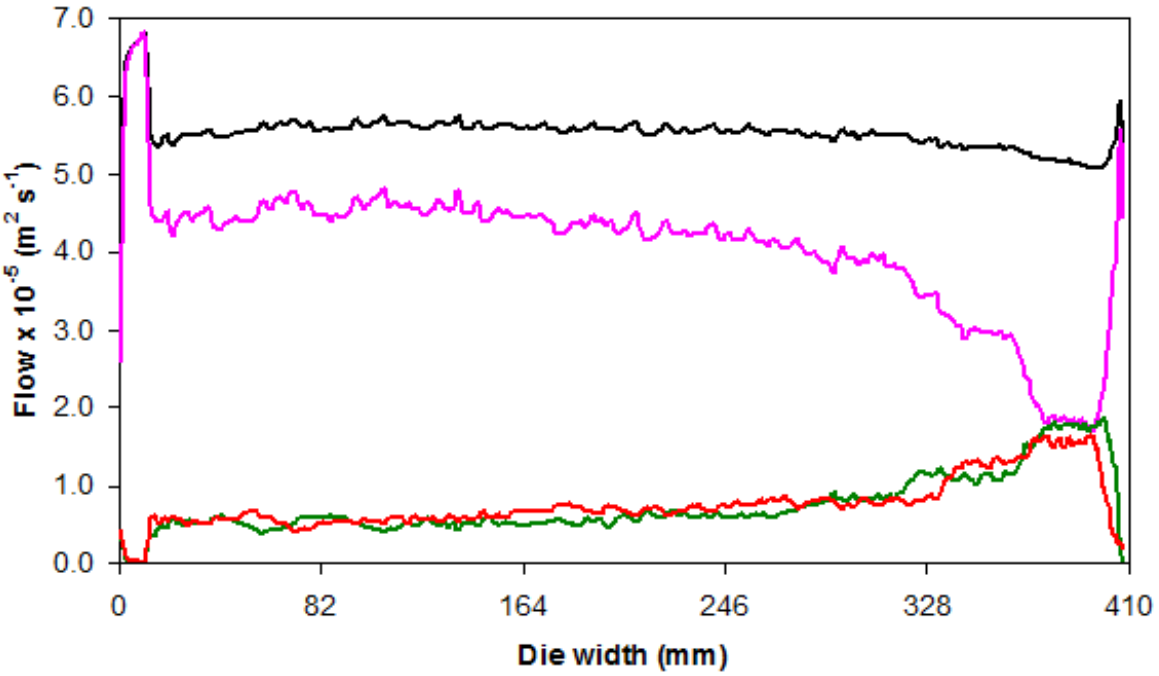

Figure 6.5: The total (shown in black), B (shown in pink), A drum side (shown in green) and A air side (shown in red) flow curves across the die outlet width.

6.2.2 Light microscopy results and comparisons

Light microscopy, as described in Section 3.2.2.1, was conducted across seven locations spanning the reflector cast film width. The film was manufactured using DTF pilot scale facilities. The light microscopy measurement locations were 18, 46, 121, 198, 256, 309 and 355 mm across the cast film of width 395 mm.

The cast film is narrower than the 410 mm end fed die width because of a phenomenon known as *neck-in* [162,163]. When the melt curtain exits the die, it is stretched by a factor of approximately five by the casting drum. The melt curtain edges are unsupported and are not stretched as much so the melt curtain narrows. A cast film width of 395 mm implies a neck-in of 7.5 mm from both die edges.

Figure 6.6 shows light microscopy applied to the cast film, where Figure 6.6a shows the 256 mm measurement and Figure 6.6b shows 309 mm. The cast film sample was sliced in its cross section and set in resin prior to microscopy, with the resin visible either side of the cast film. Both the cast film and the DS A layer thicknesses remain relatively

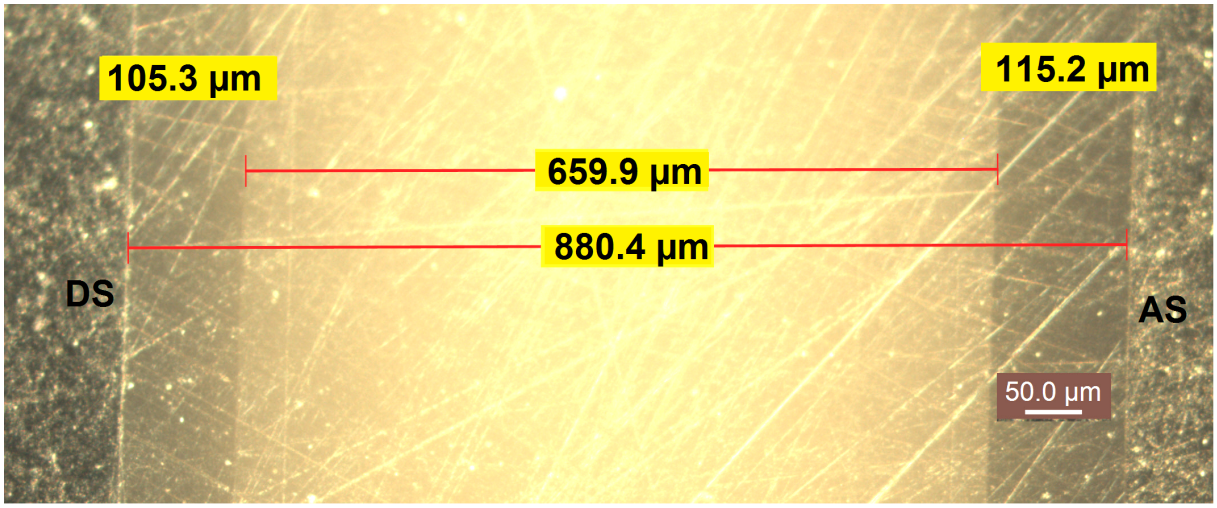

(a)

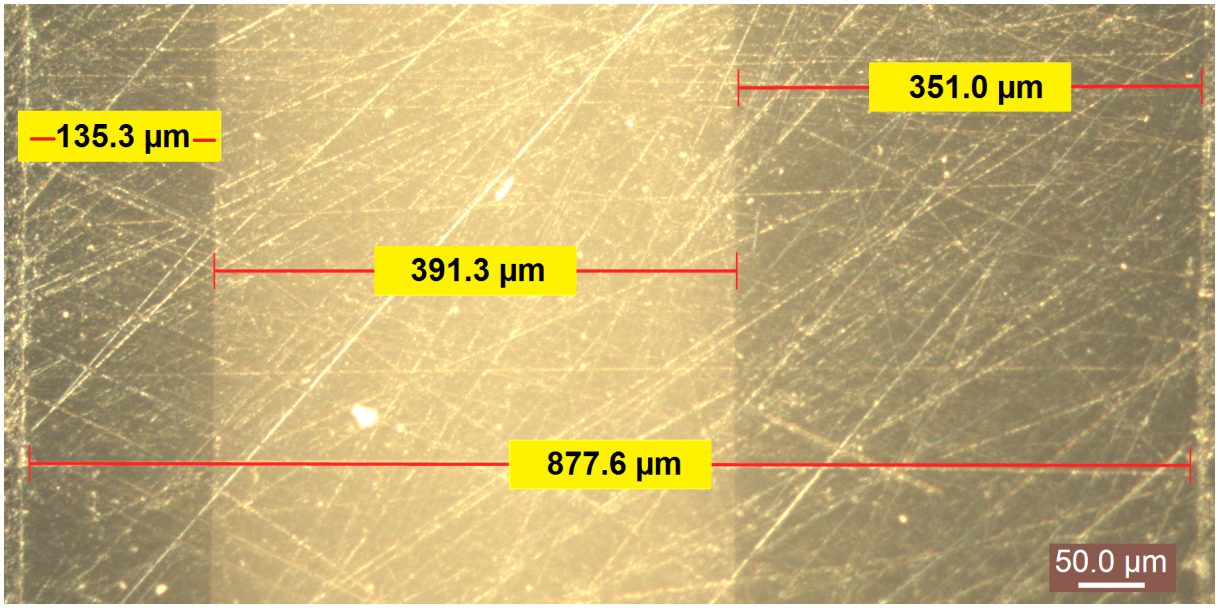

(b)

Figure 6.6: Light microscopy (objective magnification 10X) applied to the cast reflector film in two locations across the film width: (a) 256 mm and (b) 309 mm. Microscopy performed by Jessica Chappell, DuPont Teijin Films.

constant in each location. However, the AS A layer increases in thickness by over 200 µm between the two positions. This is a large increase in the AS A thickness given the small distance between the two microscopy images. The increase in the AS A layer thickness may be caused by a hotspot in the die land at this wall location during the pilot scale

trial, hence reducing the viscosity here.

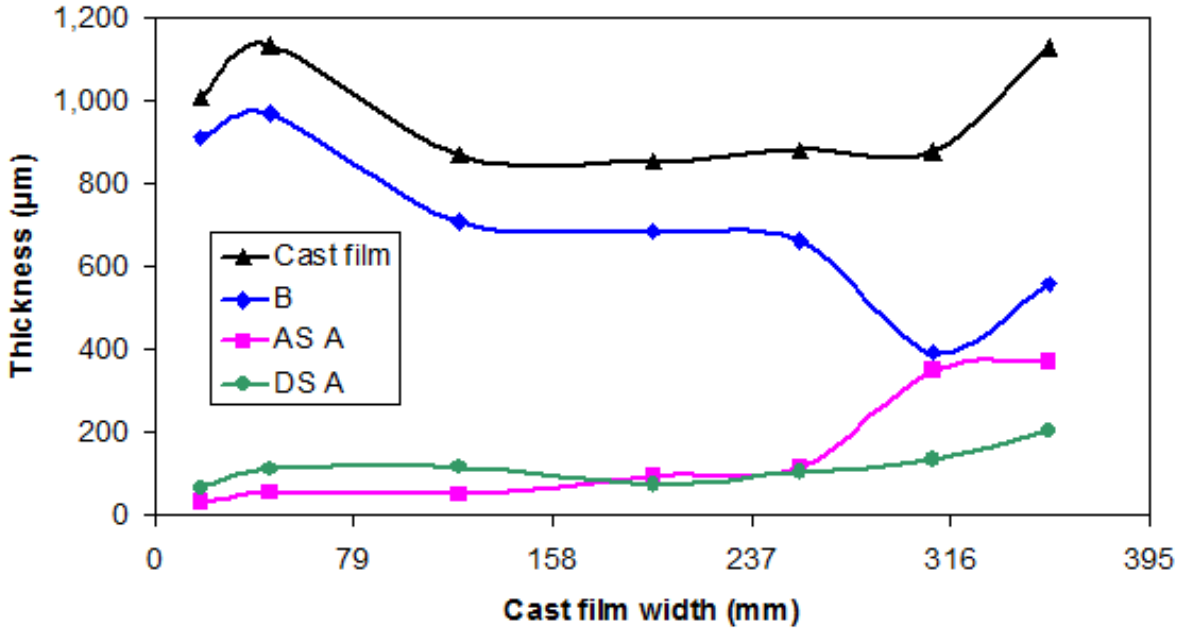

Figure 6.7: The cast film and individual layer thickness values in seven locations. Light microscopy is used to obtain these results.

For the seven light microscopy measurements taken, Figure 6.7 shows the cast film, B, AS A and DS A thickness values. The cast film edges at 18, 46 and 355 mm are thicker than the middle of the film, caused by neck-in. In the middle four locations between 121 and 309 mm, a relatively constant cast film thickness is observed. This is desirable from a commercial perspective and implies a sufficient tapering of the die and a good profile control system to retain this thickness. The B layer also has a constant thickness apart from a sharp decrease at 309 mm (see Figure 6.6). The net thickness increase of both A layers is believed to be caused by A being less dense than B and the injector block slightly favouring flow towards the BE.

The thickness values in Figure 6.7 were converted to a volumetric flow rate per unit width across the die width using both the casting drum speed and the cast film density (corrected for the ambient to PET melt temperature ratio). These flow results allow for direct comparison with the CFD flow curves in Figure 6.5, as shown in Figure 6.8, where Figure 6.8a shows the *total* and Figure 6.8b displays the *AS* and *DS A* flow curves.

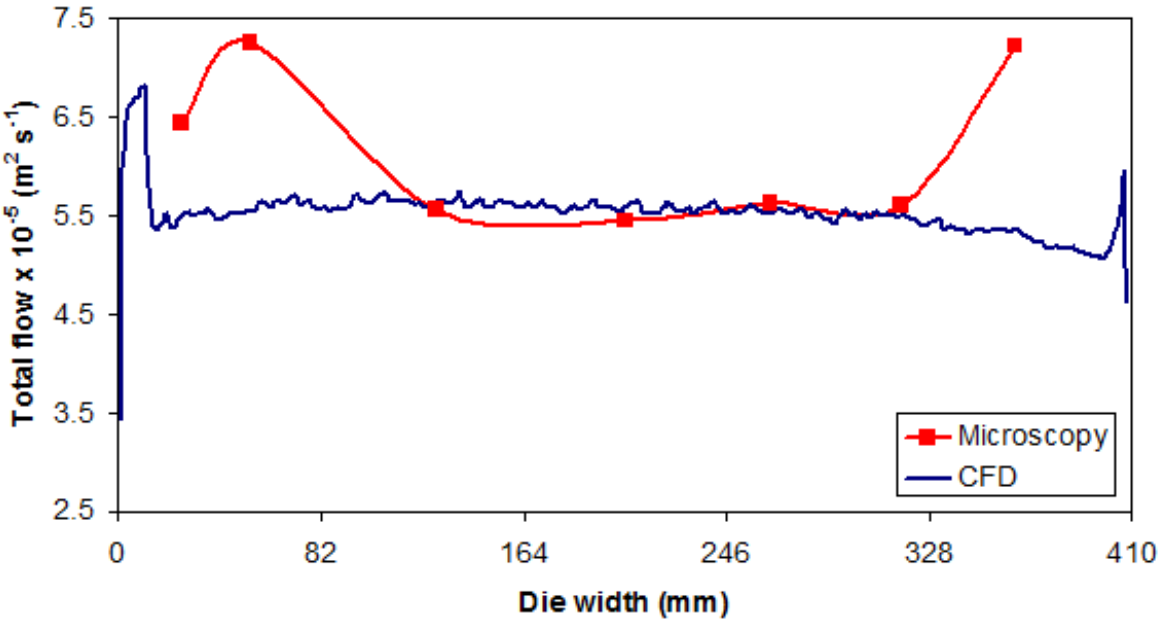

(a)

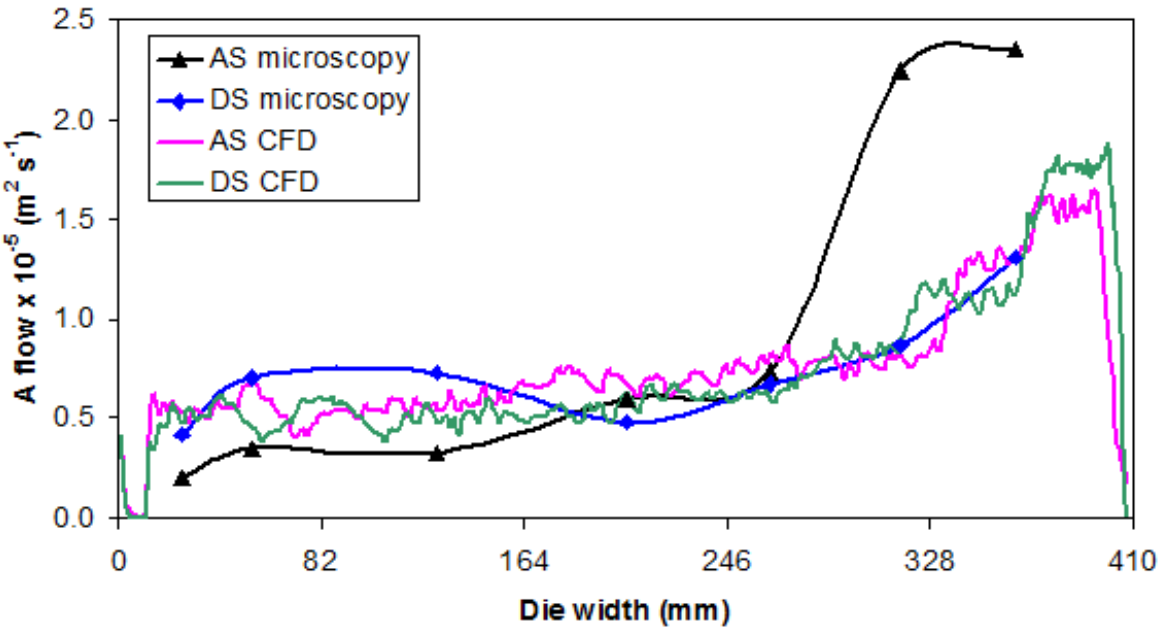

(b)

Figure 6.8: Light microscopy and CFD flow curves across the die outlet width showing: (a) the total flow and (b) the AS A and DS A flow.

For the total flow curves in Figure 6.8a, there is a good agreement found between light microscopy and CFD in the middle of the film. Neck-in is not modelled with CFD and this is the reason for the thicker cast film edges observed with microscopy. Integrating both total flow curves and subsequently multiplying this by either the cast or melt density gives a value of 27 g s^{-1} for microscopy and 28 g s^{-1} for CFD. The percentage difference between the microscopy and CFD mass balance values was 3.72 %. This confirms a conservation of mass within a 5 % error in the measurement and a good agreement despite neck-in.

The secondary A flow curves in Figure 6.8b show generally a good agreement between microscopy and CFD at the DS. However, for the AS flow curves, the light microscopy results are too low for the first three measurements and too high for the final two measurements compared with CFD. These discrepancies in the final two AS results are attributed to a hotspot in the die at this wall location during the pilot scale trial, hence reducing the viscosity here and causing a sharp increase in the thickness of Polymer A. Here, CFD assumes a *constant* wall temperature of 275 °C with thermal non-uniformity not considered. Performing a similar mass balance on both AS A flow curves yields 4 g s^{-1} to the nearest gram for both microscopy and CFD. The percentage difference between the two values is 3.39 %, again confirming an excellent agreement here despite differences in the flow results. For the DS A flow curves, there is a 12.43 % difference between the mass balance values. Although this value is outside the 5 % difference range, there is generally a good agreement found between experimental and numerical results.

6.3 Heat seal film trial

For further experimental validation of CFD results, AB structured MLFs of thickness between 20 and 25 μm were manufactured. These films are generally used for heat seal applications. The primary B layer was a lightly filled PET polymer and the secondary A layer, making up around 25 % of the overall film thickness, a PET co-polymer. Three film samples were manufactured, with the third sample having a secondary A layer made up of 93 % co-PET and 7 % red dyed, high viscosity PET (red-PET). This red-PET was

added for layer visualisation purposes.

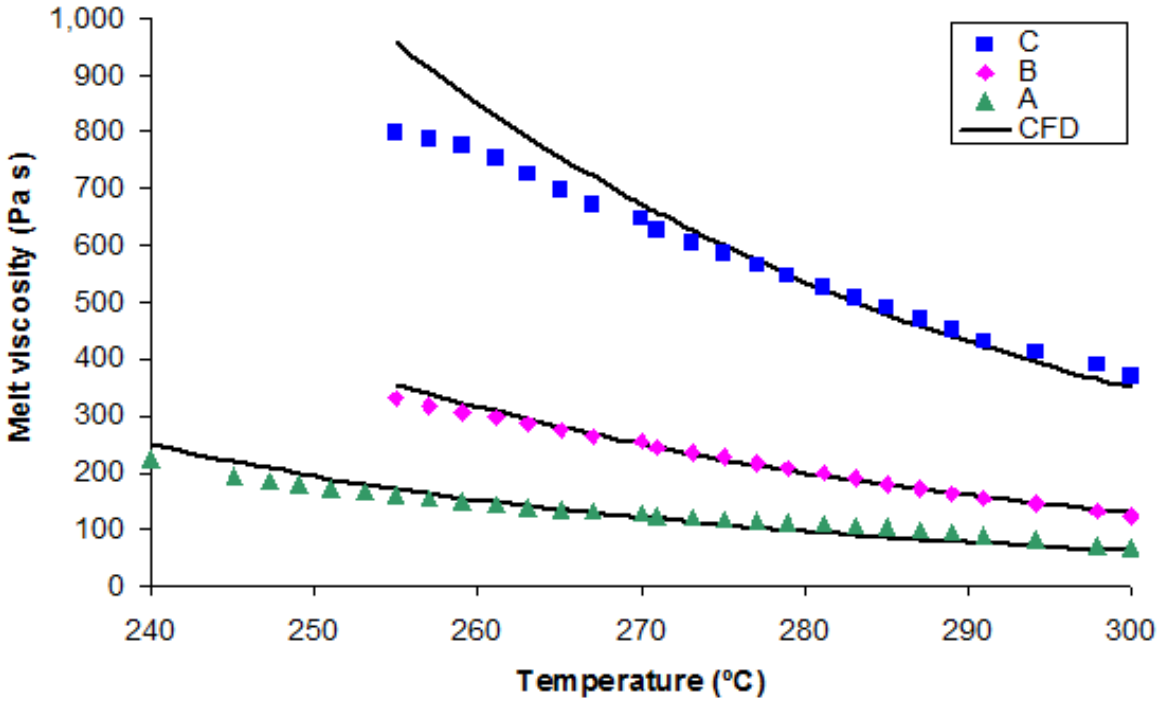

Figure 6.9: Rheology of the primary PET (B), secondary co-PET (A) and red-PET (C) resins used for the heat seal film trial at an applied shear rate of 100 s^{-1}. Experimental rheometry performed by David Stocks, Intertek.

The rheology of the three polymers was measured using a parallel plate rheometer, also used in Section 6.2. Figure 6.9 shows the rheology of the PET (denoted B), co-PET (A) and red-PET (C) resins between 255 and 300 °C for PET and red-PET and between 240 and 300 °C for co-PET at a constant shear rate of 100 s^{-1}, where Newtonian behaviour was assumed. The viscosity-temperature relationships (see Table 6.3) implented in CFD to fit to these three data sets is also shown.

At identical temperatures the primary PET polymer is more viscous than the co-PET resin, but the red-PET resin, as used in the final film sample, is the most viscous. Differential scanning calorimetry was used to determine that the melting temperatures of PET and red-PET was 255 °C and that of co-PET was 220 °C. Furthermore, the glass transition temperature of PET and red-PET was found to be 78 °C and that of co-PET 76 °C.

The three film samples were produced at different extrusion temperatures. At these varying temperatures, the viscosity difference between PET and co-PET is wider for Sample 1 compared with Sample 2. Therefore, one would expect there to be more spreading of the thinner, less viscous co-PET layer to the film edges for Sample 1 [9]. The constant wall temperature of the injector block and die modelled was 280 °C for all three samples. An aim of this work is to investigate the impact of temperature changes upon the secondary layer spreading and the final MLF structures.

Table 6.2: The three MLF samples manufactured for experimental analysis.

Sample	**Primary extruder**	**Secondary extruder**	**PET viscosity**	**co-PET viscosity**
1	$T_{\text{PET}} = 280$ °C	$T_{\text{co-PET}} = 280$ °C	199 Pa s	109 Pa s
2	$T_{\text{PET}} = 290$ °C	$T_{\text{co-PET}} = 265$ °C	146 Pa s	135 Pa s
3	$T_{\text{PET}} = 290$ °C	$T_{\text{co-PET \& red-PET}} = 265$ °C	146 Pa s	≈ 175 Pa s

Table 6.2 shows the processing conditions used for Samples 1-3. For Sample 1, both the PET and co-PET extrusion hardware was set at equal temperature $T = 280$ °C, leading to a higher viscosity for the PET phase. For Sample 2, $T_{\text{PET}} = 290$ °C and $T_{\text{co-PET}} = 265$ °C, which lead to improved viscosity matching as shown in Table 6.2. Sample 3 was identical to Sample 2 except for a small (7 %) amount of red-PET placed within the co-PET polymer for layer visualisation purposes. The secondary co-PET viscosity for Sample 3 was approximated using the co-PET and red-PET viscosity values at 265 °C. Unlike the other two samples, the co-PET layer is *more* viscous than the PET layer for Sample 3. It is therefore expected that for Sample 3, the co-PET layer will not spread as much to the film edges and will be thicker in the middle of the film compared with Samples 1 and 2.

To represent the PET and co-PET melt layers in the coextrusion domain, fluid properties were assigned to both B and A in STAR-CCM+. Table 6.3 shows the physical properties assigned to each melt where Table 6.3a shows the Sample 1 conditions and Table 6.3b

Table 6.3: The modelled heat seal film fluid properties for B and A where: (a) shows Sample 1 and (b) shows Sample 3.

(a)

	B (PET)	**A (co-PET)**
Temperature (T)	280 °C	280 °C
Density (ρ)	1,250 kg m^{-3}	1,250 kg m^{-3}
Viscosity (η), Pa s	$10^{\{(2{,}953/(T+273))-3.04\}}$	$10^{\{(2{,}953/(T+273))-3.36\}}$
Thermal conductivity (κ)	0.2 W m^{-1} °C^{-1}	0.2 W m^{-1} °C^{-1}
Mass flow rate ($\dot{m}$)	47.5 kg hr^{-1}	15.83 kg hr^{-1}
Final volume fraction	75 %	25 %

(b)

	B (PET)	**A (co-PET & red-PET)**
Temperature (T)	290 °C	265 °C
Density (ρ)	1,250 kg m^{-3}	1,250 kg m^{-3}
Viscosity (η), Pa s	$10^{\{(2{,}953/(T+273))-3.04\}}$	$10^{\{(2{,}953/(T+273))-3.25\}}$
Thermal conductivity (κ)	0.2 W m^{-1} °C^{-1}	0.2 W m^{-1} °C^{-1}
Mass flow rate ($\dot{m}$)	47.5 kg hr^{-1}	15.83 kg hr^{-1}
Final volume fraction	75 %	25 %

shows Sample 3, assuming standard PET melt properties. The viscosity-temperature functions used are based on the well established O'Dell model (Equation 2.8) and fit the rheology data as shown in Figure 6.9. The secondary A or co-PET layer was modelled to make up 25 % of the overall flow rate. The CFD simulations were set up to mimic the conditions of Samples 1-3 as described in Table 6.2.

6.3.1 Computational Fluid Dynamics results

CFD was used to model the conditions required to produce Samples 1-3. The coextrusion geometries used were an injector block linked to a 410 mm wide end fed die.

A volume fraction plot of B at the die outlet is shown in Figure 6.10 for Sample 1 in three 30 mm sections. Figure 6.10a shows the section from the 0 mm edge to 30 mm, Figure 6.10b shows the middle, from 190 to 220 mm and Figure 6.10c displays from 380 mm to the far edge at 410 mm.

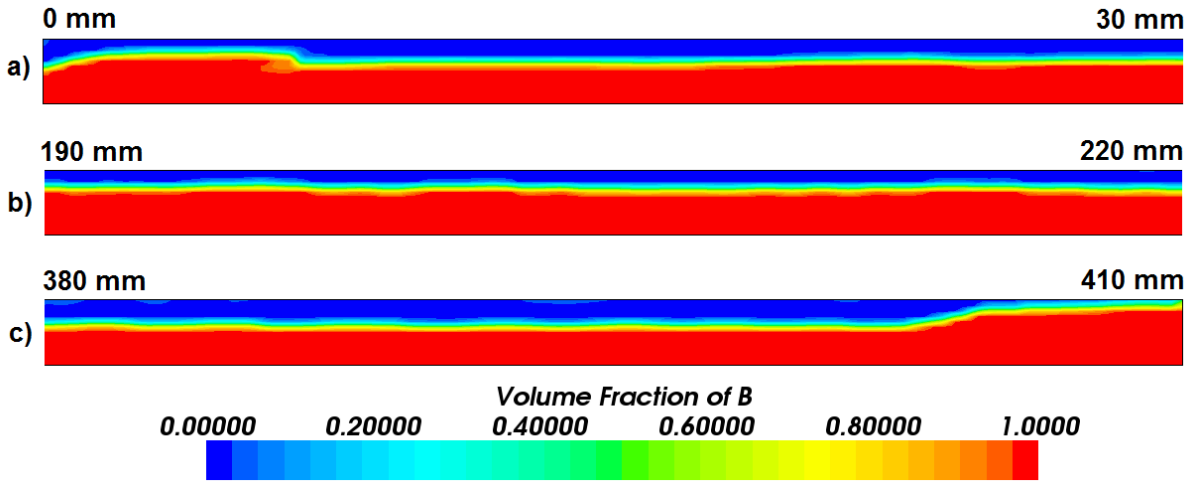

Figure 6.10: The volume fraction of B (shown in red) at the die outlet for Sample 1 showing: (a) the 0 mm edge, (b) the middle and (c) the 410 mm edge. The volume fraction of A is shown in blue.

Figures 6.10a and c show that CFD does not predict the formation of clear edges of the Sample 1 final film, with the blue A layer present at each edge. The lack of numerical clear edges is attributed to the high degree of spreading of the lower viscosity A to the film edges (see Table 6.2, Sample 1). Also, as mentioned in Chapters 4 and 5, the lack of numerical clear edges and more Polymer A at the FE is assumed to be an acceptable numerical error. In the context of this work, apart from the excess amount of A at the 0 mm edge, the final film structure in Figure 6.10 is similar to what was obtained experimentally.

Figure 6.11 shows the volumetric flow rate per unit width across the die width for

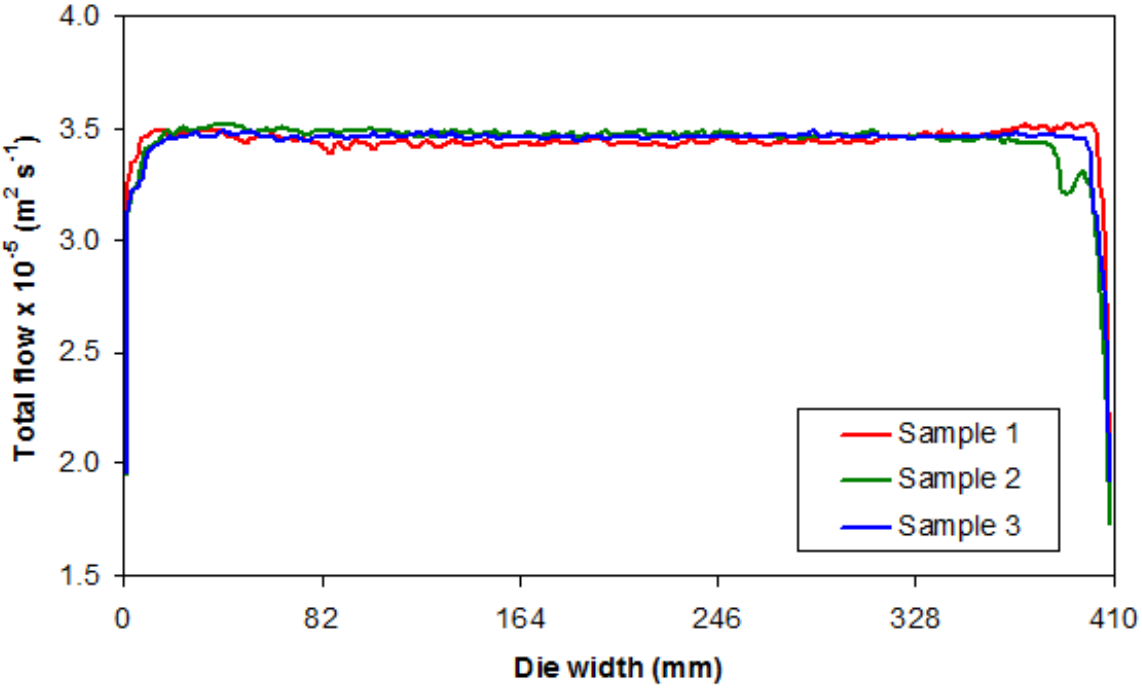

(a)

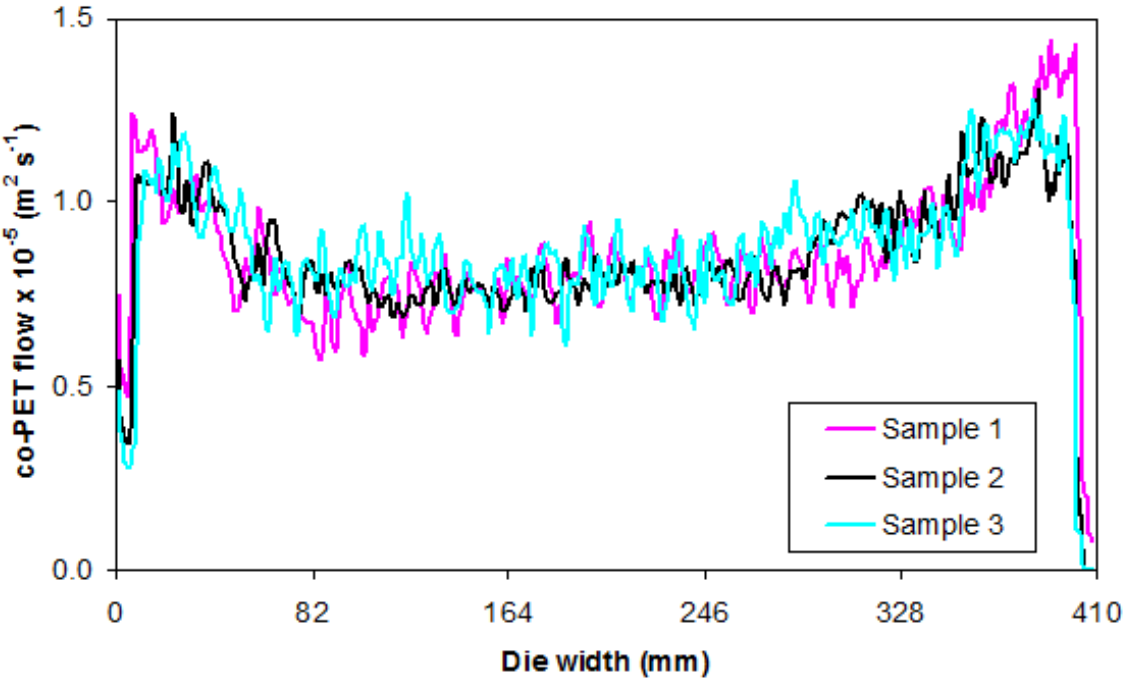

(b)

Figure 6.11: The CFD predicted die outlet flow plots for Samples 1-3, where (a) is the total flow and (b) is the secondary co-PET flow.

Samples 1-3, where Figure 6.11a shows the comparative total flow curves and Figure 6.11b shows the co-PET flows. Comparing the *total* flow curves, a similar profile is observed in each case, with the flow falling to zero at each end of the film as expected due to the no-slip condition. A uniformly thin final film is obtained for the three samples, which is desirable from a commercial perspective. The CFD obtained edges were thickest for Sample 1, particularly at the 410 mm edge. This is believed to be due to a greater spreading of the co-PET layer to the extreme edges in Sample 1. Since the viscosity difference is wider in Sample 1 (Table 6.2), the co-PET layer spreads more. For Sample 3, co-PET is more viscous than PET, with co-PET therefore not spreading as much as in Sample 1.

Analysis of the *co-PET* flow curves in Figure 6.11b again shows that there is more of the less viscous co-PET at the extreme edges for Sample 1 than Samples 2 and 3. This is again due to the greater viscosity difference in Sample 1. Sample 3 has the most co-PET present in the middle of the film, caused by the co-PET layer remaining confined to the centre since it is more viscous than PET. The flow differences in Figure 6.11 are noticeable, but the film structures have not changed significantly despite temperature and hence melt viscosity differences. This suggests that from a CFD perspective, the rheology difference for Sample 1 does not have a negative impact on the final film thickness and is within the limits of DTF's pilot scale facilities. This is what one would expect given that the viscosity ratio is less than 2:1 [8, 16]. Improved control and measurement of the melt temperature of both streams may increase understanding of the solutions.

There is significantly more noise in the co-PET flow data than the total flow data. This is because the flow calculations to obtain Figure 6.11b are based on numerical approximations of the exact interfacial location, as mentioned in more detail in Chapter 4.

6.3.2 Experimental results and comparisons

This experimental results Section is split up into two subsections. Section 6.3.2.1 shows overall flow validation, where die plug analysis and both chloroform washing and fluorescence microscopy of cast film samples are presented. Secondary layer thickness validations, using WLI, chloroform washing and reflectometry applied to final, biaxially oriented film

samples, are shown in Section 6.3.2.2. Comparison with the numerical results are made throughout.

6.3.2.1 Overall flow validation

At the Sample 3 conditions, a die plug was obtained showing the individual layer configuration between the PET and co-PET layers. Such die plug analysis is demonstrated in [8,46,58,89]. The die plug was obtained after rapid cooling of the die and was sectioned in ten points across the inlet pipe and die width. A small amount of red-PET present in the co-PET layer allowed for determination of both layers in these ten locations. The die plug layer structures were then compared with the CFD predicted Sample 3 configurations at the equivalent sections in the pipe or die.

At 125 mm into the inlet pipe, Figure 6.12 shows the PET-co-PET individual layer configuration, where Figure 6.12a shows the die plug structure and Figure 6.12b shows the CFD predicted structure. In Figure 6.12a, PET is in white and co-PET is in pink and in Figure 6.12b, PET is in red with co-PET in blue. In general there is good agreement between the two plots, with the overall flow shape and degree of interfacial curvature observed experimentally validating the numerical result. A section of the die plug is missing at the bottom of Figure 6.12a and this shows a break in the die plug upon extraction from the end fed die geometry. This highlights the difficulties associated with removal of the die plug from such a narrow end fed die.

Further differences between Figures 6.12a and b are based on both the diameter of the whole structure and the co-PET layer width. The diameter of the experimentally obtained die plug is 20.0 mm, compared with 22.25 mm for CFD. This difference is due to the density increase in PET during the transition from a melt to a solid structure so the die plug shrunk when cooled. Furthermore, the co-PET layer is wider in the die plug. This is because of the lower melting point of co-PET compared with PET and the molten co-PET spreading further towards the centre of the pipe when cooled. Despite these differences there is generally a good agreement between the die plug and CFD individual layer results.

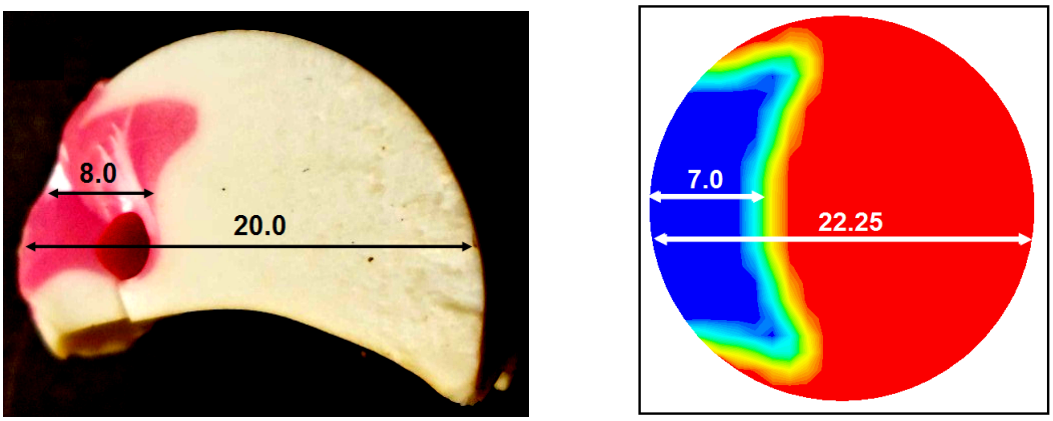

(a) (b)

Figure 6.12: The flow configurations 125 mm into the inlet pipe for Sample 3 where (a) shows the die plug structure and (b) shows the CFD structure. All dimensions shown are in millimetres.

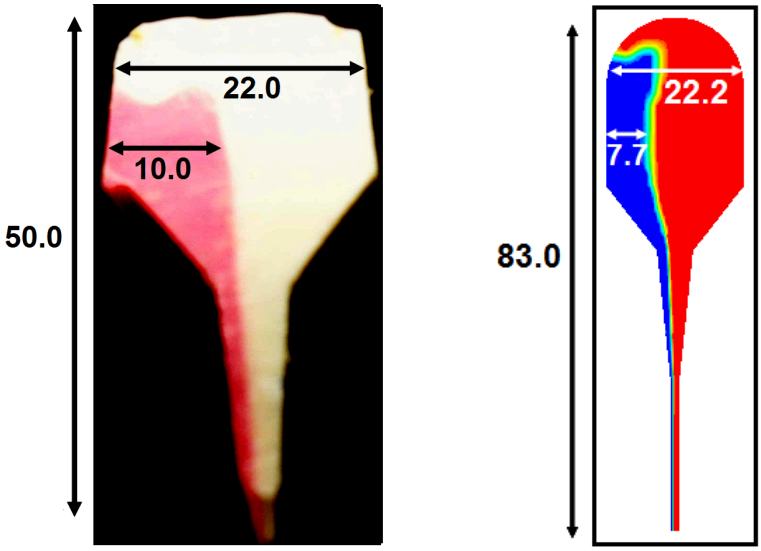

(a) (b)

Figure 6.13: The flow configurations 228 mm into the die body for Sample 3 where (a) shows the die plug structure and (b) shows the CFD structure. All dimensions shown are in millimetres.

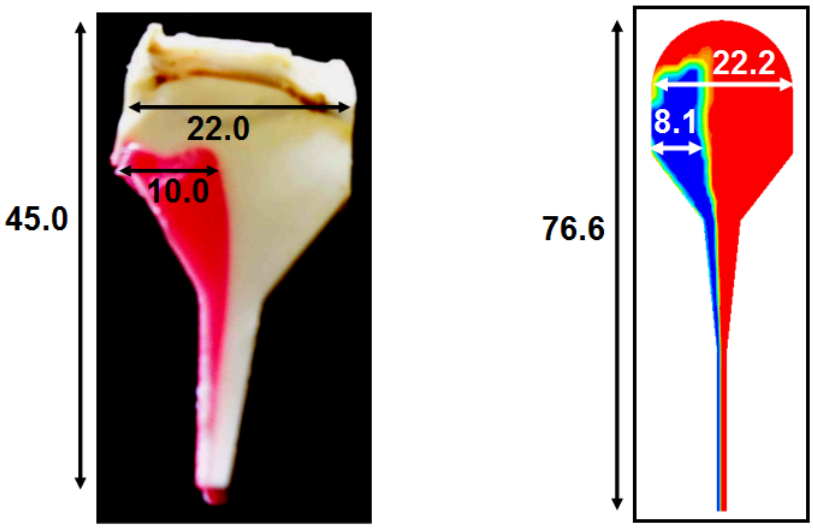

(a) (b)

Figure 6.14: The flow configurations 335 mm into the die body for Sample 3 where (a) shows the die plug structure and (b) shows the CFD structure. All dimensions shown are in millimetres.

Repeating the comparisons 228 and 335 mm into the die (see Figures 6.13 and 6.14 respectively) again shows that the die plug (Figures 6.13a and 6.14a) has validated the CFD flow profile (Figures 6.13b and 6.14b). There is a good match between the co-PET structures in each case. The main differences between the die plug and CFD plots in Figures 6.13 and 6.14 are the overall die plug height and the secondary co-PET layer width and height. Differences in the die plug height and co-PET width are attributed to the breaking of the die plug upon removal from the end fed die and individual polymer layer melting temperature differences respectively.

In Figures 6.13 and 6.14, the co-PET height in CFD form is greater than those found for the equivalent die plug structures. Differences in these two figures based on the co-PET layer height are attributed to both individual polymer layer melting temperature differences, and the no-slip wall velocity condition used in STAR-CCM+. For the no-slip condition, the fluid velocity is zero at the geometry walls. It is therefore hypothesised that the experimental secondary layer velocities near the wall exceed the equivalent numerical

ones, with the co-PET layer within the die plug moving further down the geometry, whilst mass is still conserved. In Figure 6.13, the approximate cross sectional areas of co-PET are 171 and 302 mm^2 for the die plug and CFD structures respectively. This reduces to 153 and 213 mm^2 in Figure 6.14. As alluded to, differences in these area values are believed to be caused by the higher wall velocity of the co-PET layer experimentally compared with numerically. Despite these differences, an adequate agreement between die plug analysis and CFD is observed. Similar agreement was observed for the seven other die plug sections in either the inlet pipe or the die body (not shown). A good agreement between die plug structures and numerically predicted phase distributions is also shown in [8, 59, 60].

To complement the Sample 3 die plug analysis, chloroform washing was performed on Samples 1 and 2 as cast film. Chloroform was applied across the film widths, producing thickness profiles for the total film and secondary co-PET layer. These thickness values were then converted to a volumetric flow rate per unit width across the die width using both the casting drum speed and the cast film density. These flow results allow for direct comparison with the CFD flow curves in Figure 6.11, as shown in Figure 6.15, where Sample 1 and Sample 2 results are presented in Figure 6.15a and Figure 6.15b respectively. Each figure shows the chloroform washing and CFD obtained flow curves. Each chloroform washing flow data point in Figure 6.15 is based on an average of three thickness measurements. For co-PET, the average chloroform washing Sample 1 *standard error* is 5.5×10^{-7} m^2 s^{-1}. This increases to 6.9×10^{-7} m^2 s^{-1} for Sample 2. The average standard error of the *total* chloroform washing flow data is 2.7×10^{-7} m^2 s^{-1} for Samples 1 and 2. The standard error at each measurement location is shown via error bars in Figure 6.15.

Observation of the total flow curves in Figure 6.15 shows a large increase at the edges, caused by neck-in. The Sample 1 and Sample 2 cast film width is 370 mm, implying a neck-in of 20 mm from each edge based on a 410 mm wide end fed die. Integrating the Sample 1 and Sample 2 chloroform washing and CFD total flow curves and subsequently multiplying this by either the cast or melt density gives a value of 18 g s^{-1} to the nearest

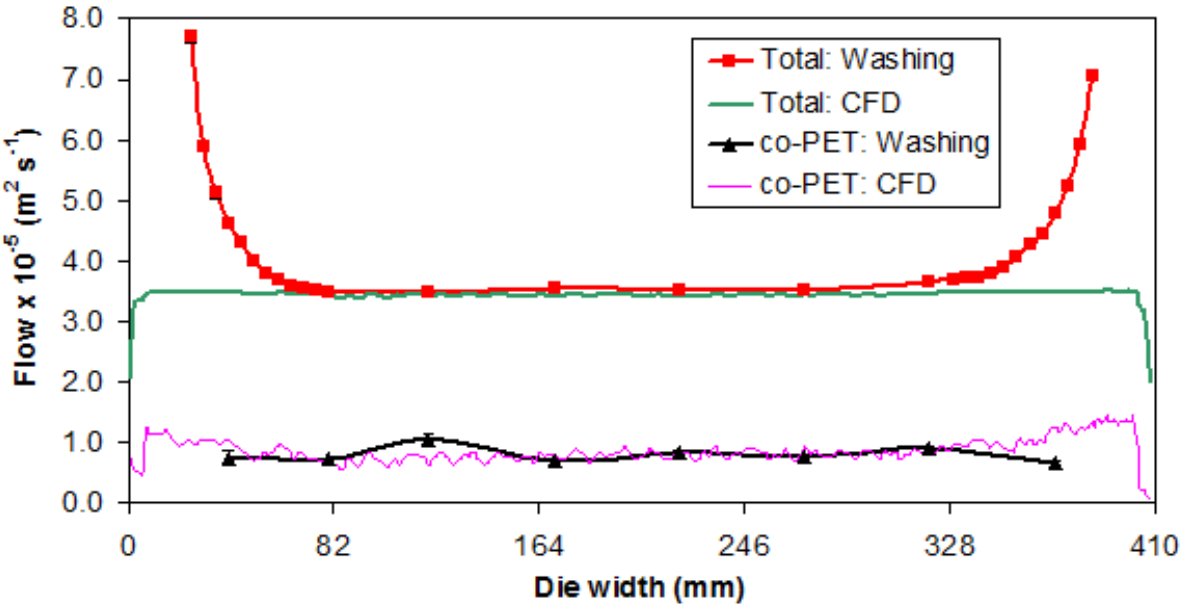

(a)

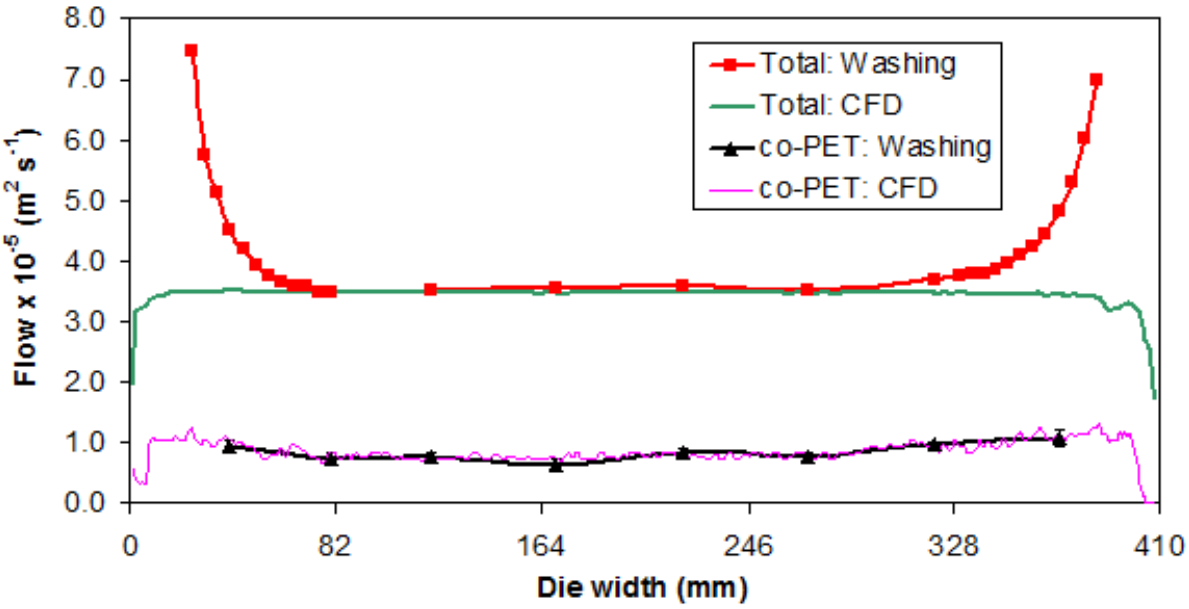

(b)

Figure 6.15: The total and co-PET flow curves across the die outlet width for both chloroform washing and CFD where (a) shows Sample 1 and (b) shows Sample 2. Where they are not visible, the chloroform washing error bars are within the range of the symbol height.

gram for all curves. The percentage difference between the CFD and chloroform washing mass balance values was 3.16 % for Sample 1 and 3.52 % for Sample 2. This confirms a conservation of mass within a 5 % error despite the neck-in in the experimental samples.

There is generally a good agreement between the chloroform washing and CFD flow results for Sample 1 (Figure 6.15a). The main part of the total chloroform washing flow curve matches its CFD equivalent well. There is also a good correlation between the two co-PET flow curves except for two ambiguous chloroform washing results at 100 and 350 mm across the cast film width (plotted at 120 and 370 mm across the die width to correct for the 20 mm neck-in). These outliers are believed to be due to human error when performing chloroform washing, with either the primary PET being partially dissolved or excess co-PET remaining on the film surface at 100 and 350 mm respectively.

An even better agreement between CFD and chloroform washing is found for Sample 2 (Figure 6.15b), with an excellent match between experimental and numerical flow curves. Chloroform washing of cast film samples has validated the CFD outlet flow predictions at the range where data was obtained.

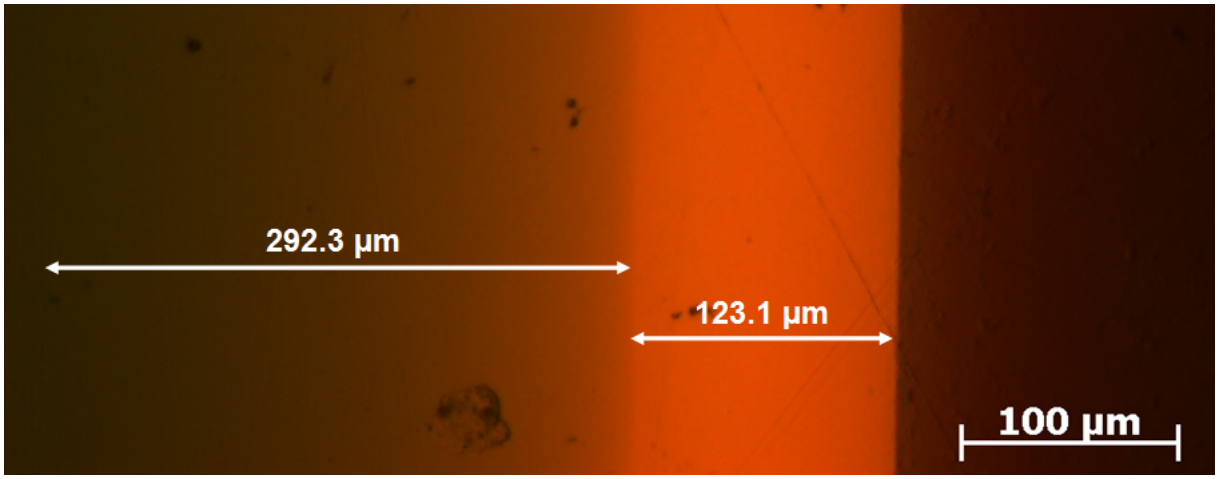

Figure 6.16: Fluorescence microscopy (objective magnification 10X) applied to the Sample 1 cast film at 345 mm. Microscopy performed by Jonathan Whitehead, Intertek.

Fluorescence microscopy was performed on seven locations across the Sample 1 cast film width: 11, 75, 125, 182, 295, 345 and 359 mm. Figure 6.16 shows fluorescence microscopy conducted at 345 mm. Here, co-PET makes up 29.6 % of the cast film thickness.

For the seven measurements, the average co-PET thickness is 23.2 % of the cast film thickness.

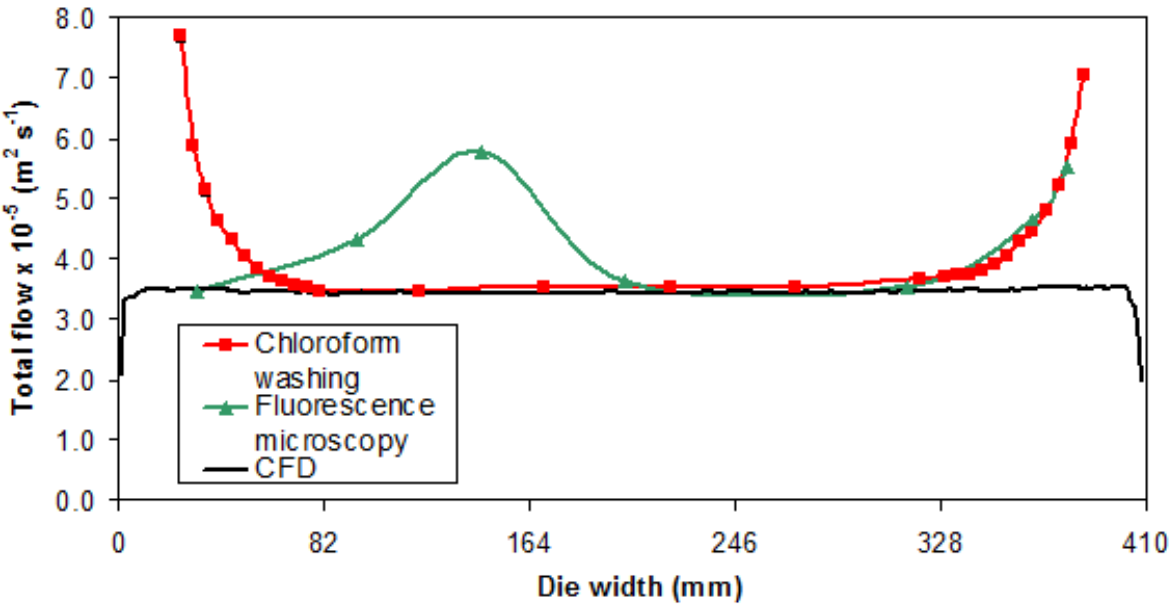

Figure 6.17: The chloroform washing, fluorescence microscopy and CFD total flow curves for Sample 1. Where they are not visible, the chloroform washing error bars are within the limits of the symbol height.

The Sample 1 cast film thickness values calculated from fluorescence microscopy were converted into a volumetric flow rate per unit width across the die width. This allows for direct comparison between the fluorescence microscopy, chloroform washing and CFD flow curves and is shown graphically in Figure 6.17. From this plot, a good agreement is found between CFD and fluorescence microscopy. The thicker fluorescence microscopy results at 75 and 125 mm (plotted at 95 and 145 mm to correct for the 20 mm neck-in) are attributed to a *die streak* [7]. When a melt curtain exits a die, either land temperature changes or build up of polymer degrade can cause a localised film thickness increase which is not modelled with CFD. The die streak was not detected with the thickness gauge when using chloroform washing. This is because the cast film was analysed in the same transverse direction (TD) position, but a different machine direction (MD) position and the streak was not present in the cast film position used for the chloroform washing

analysis, showing the streak to be temporary since the samples were related. Apart from this die streak, fluorescence microscopy has also validated the CFD flow results in the measurement locations taken for Sample 1.

6.3.2.2 Secondary layer thickness validation

For final, biaxially oriented film Samples 1-3, both white light interferometry (WLI) and chloroform washing were applied. This was to calculate the secondary co-PET thickness profile across the final film width of 800 mm. Comparisons between WLI, chloroform washing and CFD for co-PET thickness measurements are shown in this Section. Reference is also made to reflectometry results for Sample 1.

Figure 6.18 shows an example screenshot taken from WLI applied to the middle of Sample 2. For all WLI measurements, a primary topography plot showing the film surface (see Figure 6.18a) was obtained. The interferometric objective then moved vertically downwards, generating a secondary interfacial topography plot (see Figure 6.18b). The z-scale colour bars to the right of Figures 6.18a and b show the height information in micrometers for each plot. The software then calculated the vertical distance between the two topography plots at each point, and hence generated a co-PET layer thickness plot (see Figure 6.18c). The size of the three images in Figure 6.18 is 2.5×1.9 mm, or 640×480 pixels. The co-PET layer thickness in Figure 6.18c is therefore calculated from 307,200 measurement points.

The *average* co-PET layer thickness is calculated from the plot in Figure 6.18c. For the calculation in Figure 6.18, the average co-PET thickness is found to be 6.51 μm, but the thickness range is from 2.08 to 10.48 μm. WLI is a high resolution point by point measurement technique and can detect surface roughness accurately. The large thickness range in Figure 6.18 implies either a film surface or interfacial roughness that one must be aware of when further analysing WLI results. For Samples 1-3, WLI as shown in Figure 6.18 was performed three times at five locations with average co-PET thickness values taken.

Figure 6.19 shows the WLI calculated average total film and individual layer thickness

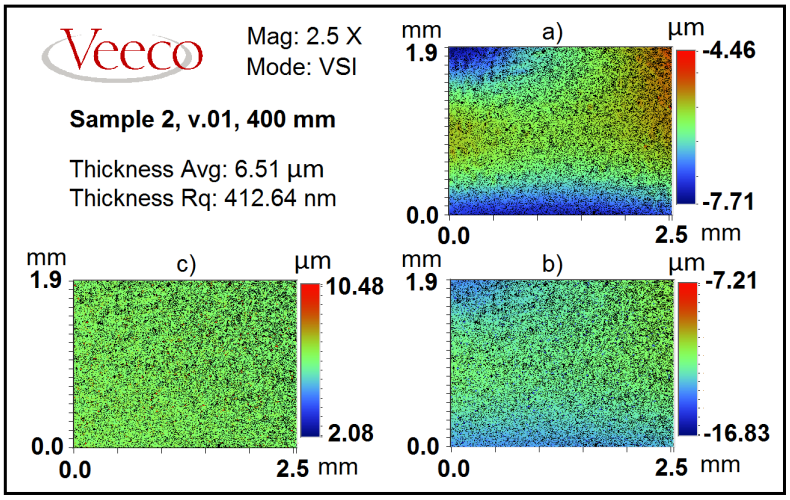

Figure 6.18: A WLI screenshot of Sample 2 400 mm into the film, where (a) shows the primary surface topography plot, (b) shows the secondary interfacial topography plot and (c) shows the co-PET thickness topography plot. The average co-PET thickness is calculated as 6.51 µm.

profiles, where Figures 6.19a and 6.19b show results for Samples 1 and 2 respectively. Measurements were taken at locations 50, 200, 400, 600 and 750 mm across the film width. The data points in Figure 6.19 are based on an average of three measurements. At each of the five measurement locations, there was very little difference between the three thickness values obtained. This shows sample consistency for WLI and a low *sample variance* or a high repeatability with WLI between the three measurements at each point across the film. For the five measurement locations, the average WLI standard error or sample variance of the three values is 75 nm for Sample 1 and 29 nm for Sample 2.

There is however a relatively high *method variance* associated with these WLI results. For any co-PET thickness measurement, the Veeco software quoted the value subject to a roughness value or measurement error R_q (see Figure 6.18). The average co-PET thickness for Samples 1 and 2 is 6.4 µm, using the five data points in Figure 6.19. The values taken across the film width to obtain these averages are typically subject to an R_q of 400-600 nm, or an error of ± 6-9 %. This method variance is caused by smooth surface undulations in the co-PET layer, as films containing this polymer require a degree of surface roughness to provide the heat seal. Another factor causing a high method variance is the low signal

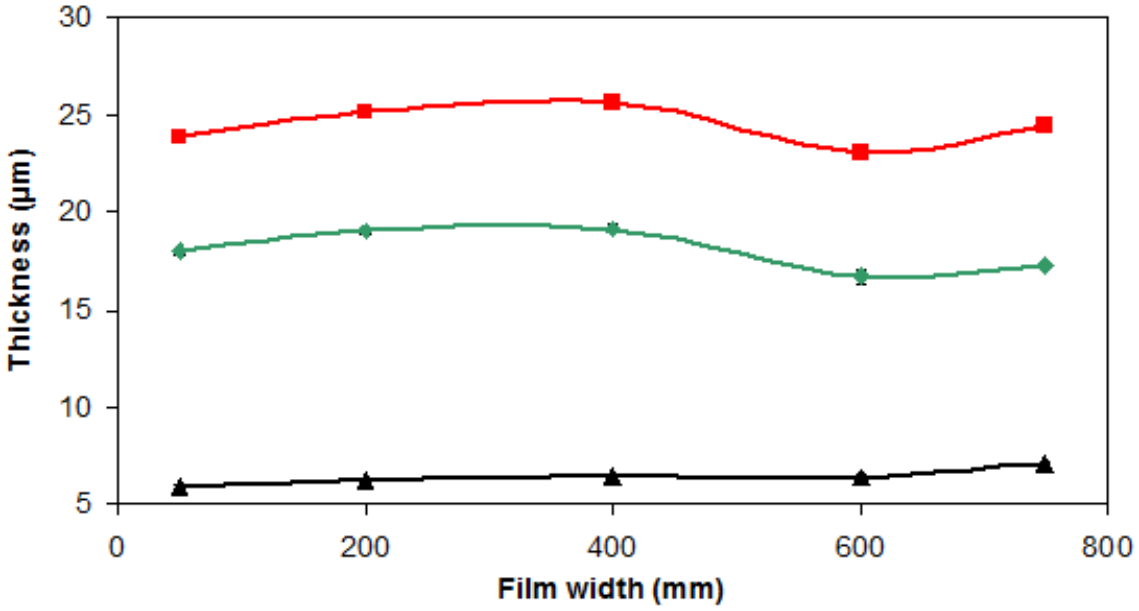

(a)

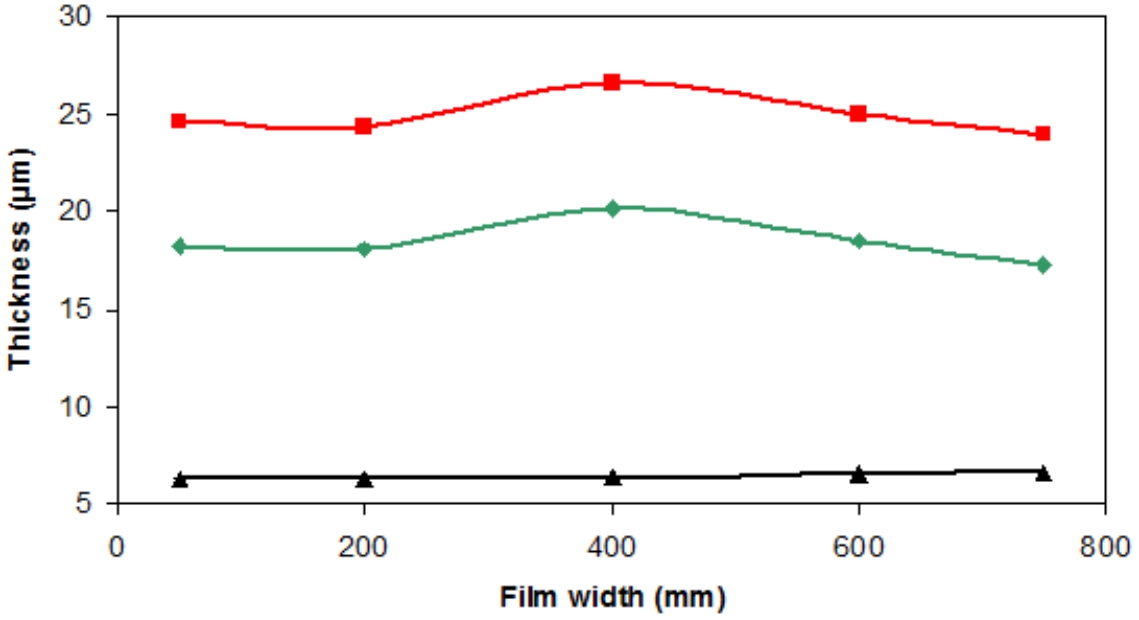

(b)

Figure 6.19: The WLI measured average total film (shown in red), PET (shown in green) and co-PET thickness (shown in black) for (a) Sample 1 and (b) Sample 2. The error bars are within the range of the symbol height.

to noise ratio when measuring the interfacial location through the film surface.

From Figure 6.19, the total Sample 1 and Sample 2 film thickness is highest in the middle of each film. The maximum co-PET thickness is at the far 750 mm edge, again for both samples. At this edge, a thicker co-PET layer is found for Sample 1 (7.1 $\pm$ 0.06 μm; a standard error of 60 nm) compared with Sample 2 (6.6 μm; no sample variance found). This is as expected given the lower viscosity of co-PET compared with PET in Sample 1. At the 50 mm edge measurement, the quantity of co-PET is found to be greater in Sample 2 than Sample 1. This is opposite to what was expected but is within the method variance range.

The equivalent chloroform washing results for the average total film and individual layer thickness profiles are shown in Figure 6.20, where Figure 6.20a shows Sample 1 and Figure 6.20b shows Sample 2 results. The data points in Figure 6.20 are again based on an average of three measurements at five different locations across the film width. Compared with the WLI results, there was a far greater difference between the three thickness measurements taken at each location for chloroform washing results (see the error bars in Figure 6.21). This shows poor repeatability of the chloroform washing results or a high sample variance. Chloroform washing is not as rigorous as WLI, and this alongside measurement error of the digital thickness gauge is believed to cause the sample variance. The average co-PET thickness when using chloroform washing is 5.1 $\pm$ 0.25 μm for Sample 1 and 5.4 $\pm$ 0.26 μm for Sample 2.

Figure 6.21 shows a combination of Figures 6.19 and 6.20, where the average co-PET thickness profiles of Samples 1 and 2 are plotted using both WLI and chloroform washing. At this smaller y-axis range, the high chloroform washing sample variance is detectable via the significantly higher error bars compared with WLI. The general trend in the four thickness profiles shows an increase in the co-PET thickness when moving from 50 to 750 mm. This may be due to an injector block secondary layer inlet port geometry or temperature differences slightly favouring flow towards the far edge of the film when manufacturing the three film samples. At the 750 mm edge, the amount of co-PET is higher for Sample 1 than Sample 2 with WLI as expected. The reverse is found for the

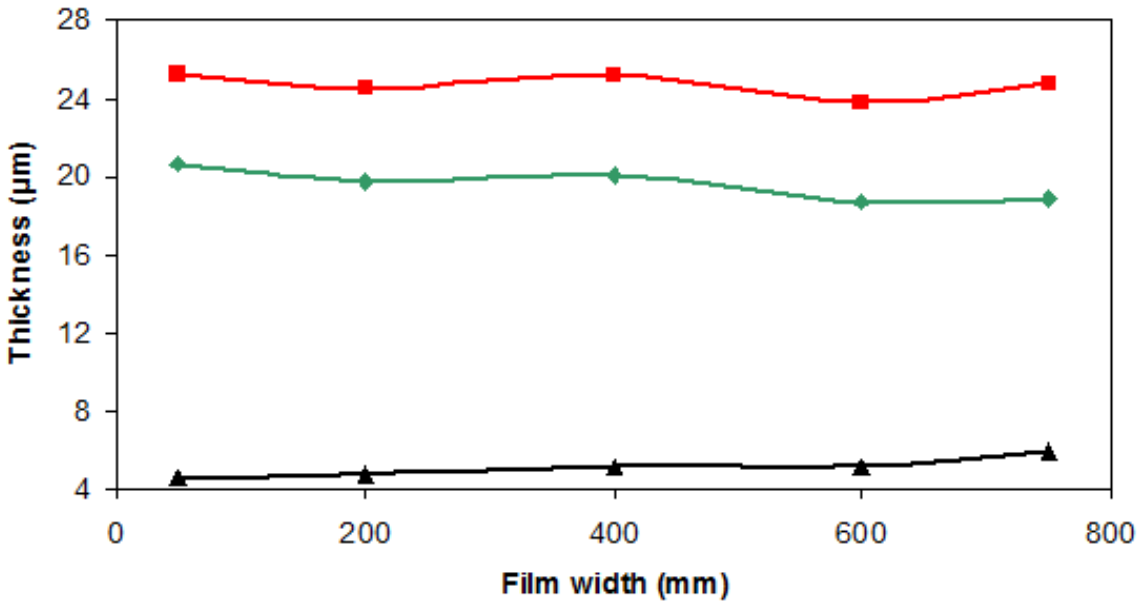

(a)

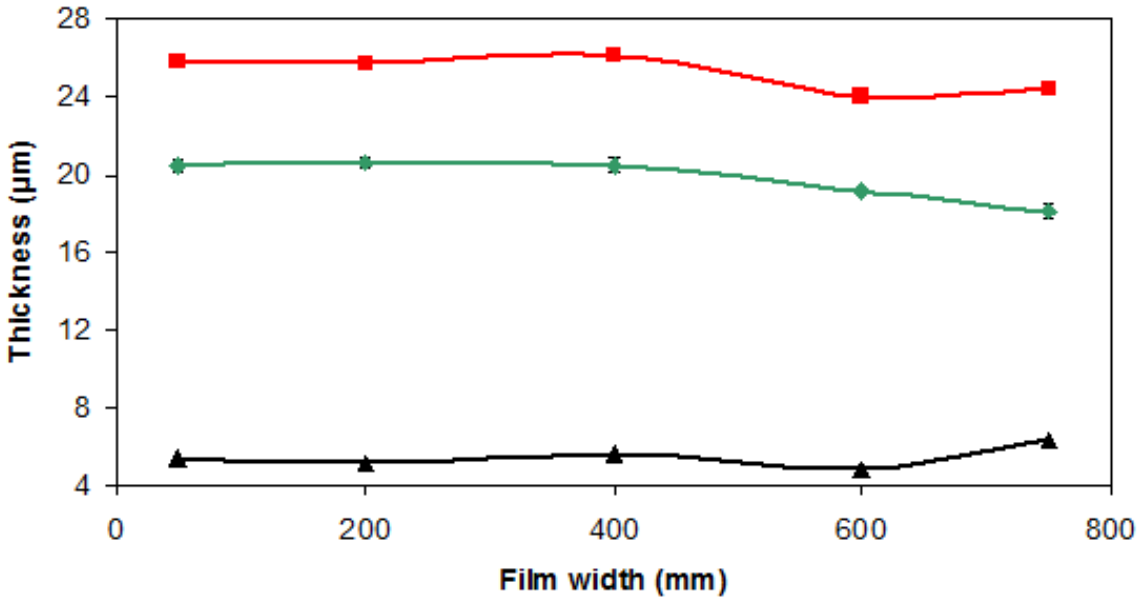

(b)

Figure 6.20: The chloroform washing measured average total film (shown in red), PET (shown in green) and co-PET thickness (shown in black) for (a) Sample 1 and (b) Sample 2. Where they are not visible, the error bars are within the range of the symbol height.

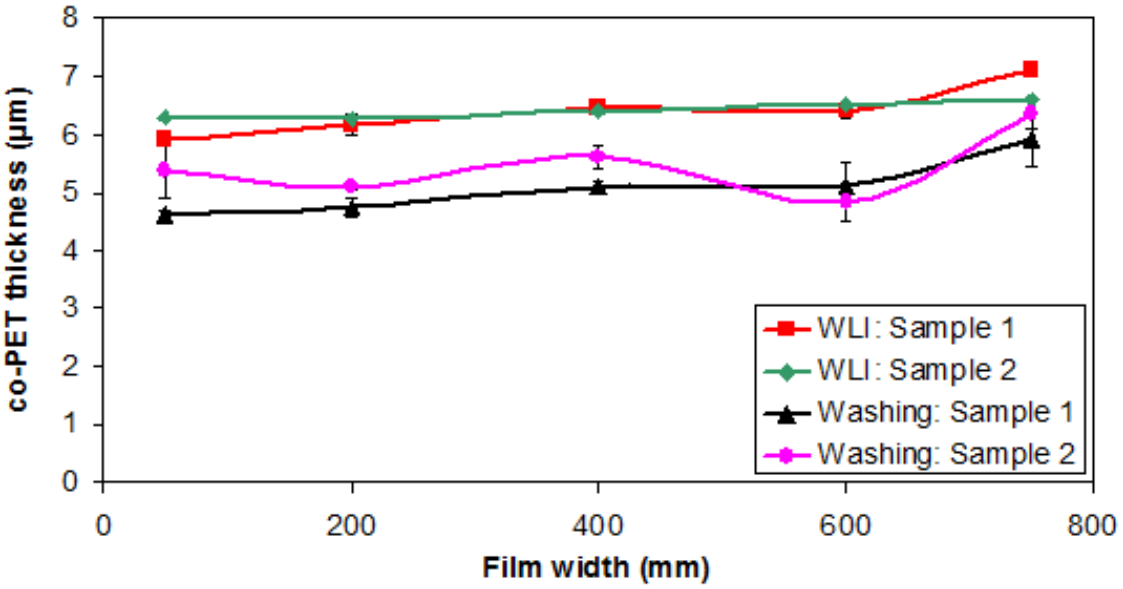

Figure 6.21: The average Sample 1 and Sample 2 co-PET thickness profiles using both WLI and chloroform washing. Where they are not visible, the error bars are within the range of the symbol height.

chloroform washing results, but these thickness differences are within the range of the error bars or sample variance.

For the five data points in Figure 6.21, there is a thickness difference between both measurement techniques, with WLI consistently measuring 1 µm thicker co-PET layer for identical MLF samples. The inconsistency of the two methods is attributed to both WLI method variance and chloroform washing sample variance. Despite differences between the measurement techniques, the Sample 1 and Sample 2 results are fairly consistent. This suggests that the temperature and hence polymer melt viscosity differences were not wide enough to significantly change the co-PET spreading. This was also found numerically and future work will need to repeat the analysis presented in this Chapter on more rheologically different polymer melts.

Table 6.4 shows the average co-PET layer thickness as a percentage of the total film thickness for Samples 1-3 using WLI, chloroform washing and CFD. The percentage thickness values in Table 6.4 are based on an average of the thickness data obtained at the five

measurement locations across the film width for WLI and chloroform washing. The CFD thickness values are based on an average of the co-PET flow calculations as a percentage of the total flow calculations at the equivalent five measurement locations across the die width.

Table 6.4: The percentage co-PET thickness of the total film thickness using both experimental and numerical methods for Samples 1-3.

Sample	**WLI (%)**	**Chloroform washing (%)**	**CFD (%)**
1	26.2	20.6	24.9
2	25.8	21.6	24.6
3	27.1	22.6	26.6

WLI shows a significantly better agreement with CFD than chloroform washing. The WLI results are slightly higher than the CFD equivalent, but these thickness differences are within the measurement error or method variance range for this technique. For validating CFD results, WLI is shown to be more accurate than chloroform washing. A reason for this is that unlike chloroform washing, WLI is non-intrusive to the film surface and the secondary co-PET layer is not disturbed or damaged. Also WLI is better than chloroform washing at capturing fine surface or interfacial detail. WLI is the more accurate and robust measurement technique and is less susceptible than chloroform washing to human or experimental error.

From Table 6.4, the chloroform washing data for final film samples is too low compared with CFD and does not fully validate the numerical results. Comparing Table 6.4 with Figure 6.15 implies that the chloroform washing data is inconsistent between cast and equivalent final film samples of the same film. It appears that more co-PET was retained on the final film than the cast film upon chloroform application.

A suggested reason for this is partial crystallisation of the co-PET layer at the PET-co-PET interface when stretching and heating the film. A white light based reflectometry technique also yielded too low co-PET thickness values when applied to Sample 1. Fig-

ure 6.22 shows the average co-PET thickness profile for Sample 1 using WLI, chloroform washing and reflectometry. The reflectometry thicknesses are much lower than those obtained with either WLI or chloroform washing. This further justifies the partial crystallisation theory since previous DTF work has found that reflectometry layer thickness measurement errors can arise upon crystallisation of one of the polymer layers.

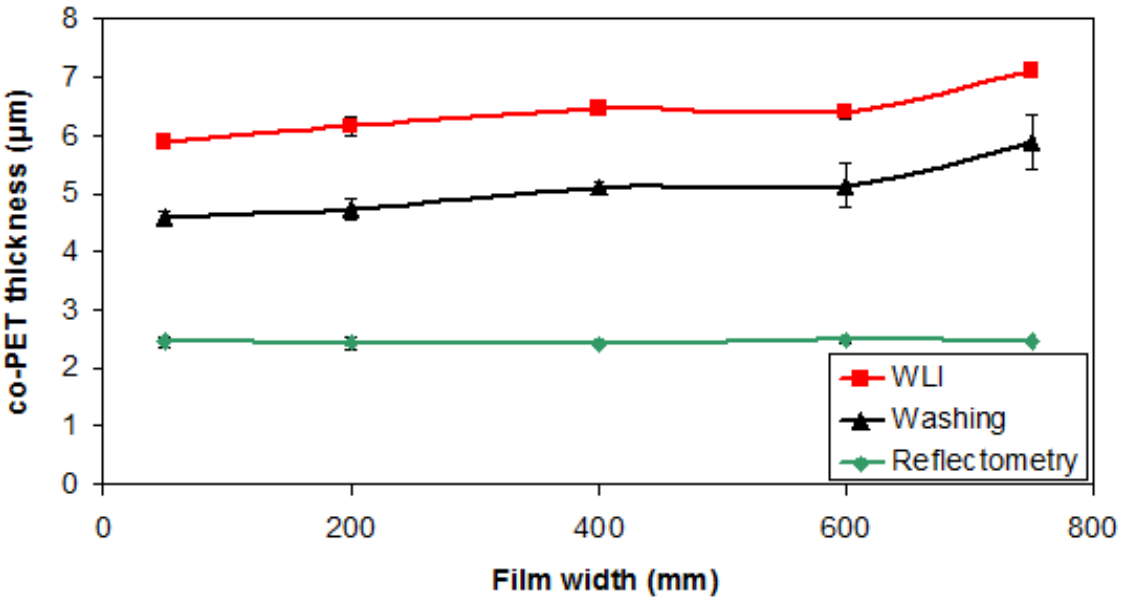

Figure 6.22: The average Sample 1 co-PET thickness profile using WLI, chloroform washing and reflectometry. Where they are not visible, the error bars are within the range of the symbol height.

A second method used to test the partial crystallisation theory was Time-of-Flight Secondary Ion Mass Spectrometry (ToF-SIMS) surface analysis applied to Sample 1, see Section 3.2.2.6. ToF-SIMS, using a Bi_3^{2+} ion source, was applied to three different Sample 1 surfaces: the untreated PET and co-PET sides and the co-PET side *after* applying chloroform (the PET-co-PET interface). If the co-PET had been fully dissolved by the chloroform, one would expect the washed co-PET spectrum to exactly match the unwashed PET one. However, the three spectra observed (see Figure 6.23) shows that the washed co-PET spectrum (Figure 6.23c) instead matches the unwashed co-PET result (Figure 6.23b). This confirms that there is still some co-PET present on the film af-

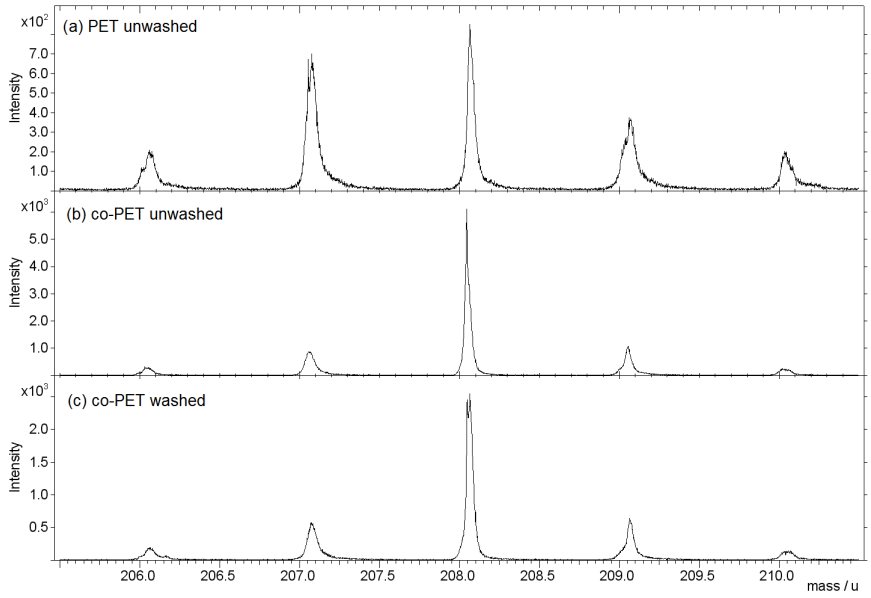

Figure 6.23: ToF-SIMS positive ion spectra showing: (a) unwashed PET, (b) unwashed co-PET and (c) chloroform washed co-PET surfaces for Sample 1. ToF-SIMS performed by Ian Fletcher, Intertek.

ter chloroform application, hence the low chloroform washing co-PET thickness results. The suggested, logical reason for these ambiguous results is partial crystallisation of the co-PET layer at the interface.

When manufacturing this heat seal film, the temperature during the transverse draw process exceeds 220 °C, the co-PET melting temperature. Upon rapid cooling of the film, this should produce a fully amorphous co-PET layer. It is believed that inefficient surface heating of the film melted the secondary co-PET polymer, *except* deep into this layer (the PET-co-PET interface). Thus, a thin crystalline layer of co-PET was observed at the interface. Another factor attributed to the partial crystallisation theory is strain induced crystallisation during the transverse draw process. In [164], it is stated that strain induced crystallisation of PET increases with increasing levels of co-polymer, and as one gets further into the polymer layer. This, coupled with inefficient heating of the co-PET layer, explains the crystallisation of this polymer at the interface.

Partial crystallisation of the amorphous co-PET polymer would have resulted in a thin crystalline region that was insoluble in chloroform. This crystalline region therefore

remains on the film at the PET-co-PET interface upon chloroform application, and the co-PET thickness is measured to be lower than its actual value for final film samples.

The thickest co-PET layer is found both experimentally and numerically in Sample 3. This suggests that the addition of the red-PET *increased* the co-PET shear viscosity, with less spreading to the edges in Sample 3 compared with Samples 1 and 2. This reduced co-PET spreading for Sample 3 is what one would expect given the data shown in Figure 6.9 and Table 6.2 [8, 9, 11, 22, 23, 37, 62, 94].

6.4 Chapter conclusions

In this Chapter, CFD was used to model the production of two commercial MLF samples, with experimental validations also shown.

A reflector film was scrutinised using both numerical tools and light microscopy in Section 6.2. There was generally a good agreement found between CFD and light microscopy, with differences in results attributed to the modelling of a constant rather than varying wall temperature profile in CFD. A better understanding of the wall and in particular die land temperature variation would have improved the CFD results. In Chapter 7, varying land temperature profiles representing a full set of die bolt heaters are modelled.

In Section 6.3, die plug analysis, chloroform washing, fluorescence microscopy and WLI were used to validate CFD modelling of a film used for heat seal purposes. There was a good agreement found between CFD and die plug structures. For cast film analysis, excellent agreement was shown between chloroform washing, fluorescence microscopy and CFD when comparing flow curves. When investigating final films, the WLI obtained secondary co-PET thickness values validated CFD within the bounds of experimental error. However, the chloroform washing results for final films were found to be too low compared with both CFD and cast film results. This is attributed to partial crystallisation of the co-PET layer upon orienting the cast film, justified using reflectometry and ToF-SIMS. In this Section, the temperature and hence polymer melt viscosity differences investigated were shown to be within the range of DTF's pilot scale facilities.

There was generally a very good agreement between numerical and experimental results and CFD modelling of polyester coextrusion has been validated in this Chapter at the data points analysed.

Chapter 7

Thermoviscous control in polyester coextrusion

7.1 Introduction

In this Chapter, the effect of changing the hardware temperature and hence melt viscosity on the CFD predicted final film thickness and structure is investigated.

DTF use die bolt heaters across the land width to locally alter the melt viscosity and hence final film thickness. Varying land temperature profiles, representing a full set of die bolt heaters, are modelled in Sections 7.2-7.4. Section 7.2 shows a narrow template geometry, Section 7.3 shows a 410 mm wide MMD and a production scale MMD is modelled in Section 7.4. For further information on die bolt heaters and background work showing the derivation of land temperature curves, the reader is referred to Appendix A.

For an injector block linked to a 410 mm wide end fed die, the effect of thermal non-uniformity of the geometry walls is investigated in Section 7.5.

7.2 Template geometry

To provide a foundation for work in Sections 7.3 and 7.4 showing land heater profiles across wider geometries, a template geometry was created in STAR-CCM+. This 135

mm wide structure is representative of the middle segment of the 410 mm wide MMD modelled in Sections 5.3 and 7.3.

The meshed template geometry is shown in Figure 7.1. ABA structured MLFs were modelled with the primary B layer entering via the top inlet and the secondary A layers entering in the two thin secondary inlets of width 0.5 mm. The outlet die gap is constant at 3 mm from 0 to 135 mm, and the land length is 15 mm. Symmetry planes were set at both 0 and 135 mm, meaning that the solution is the same either side of these planes [105].

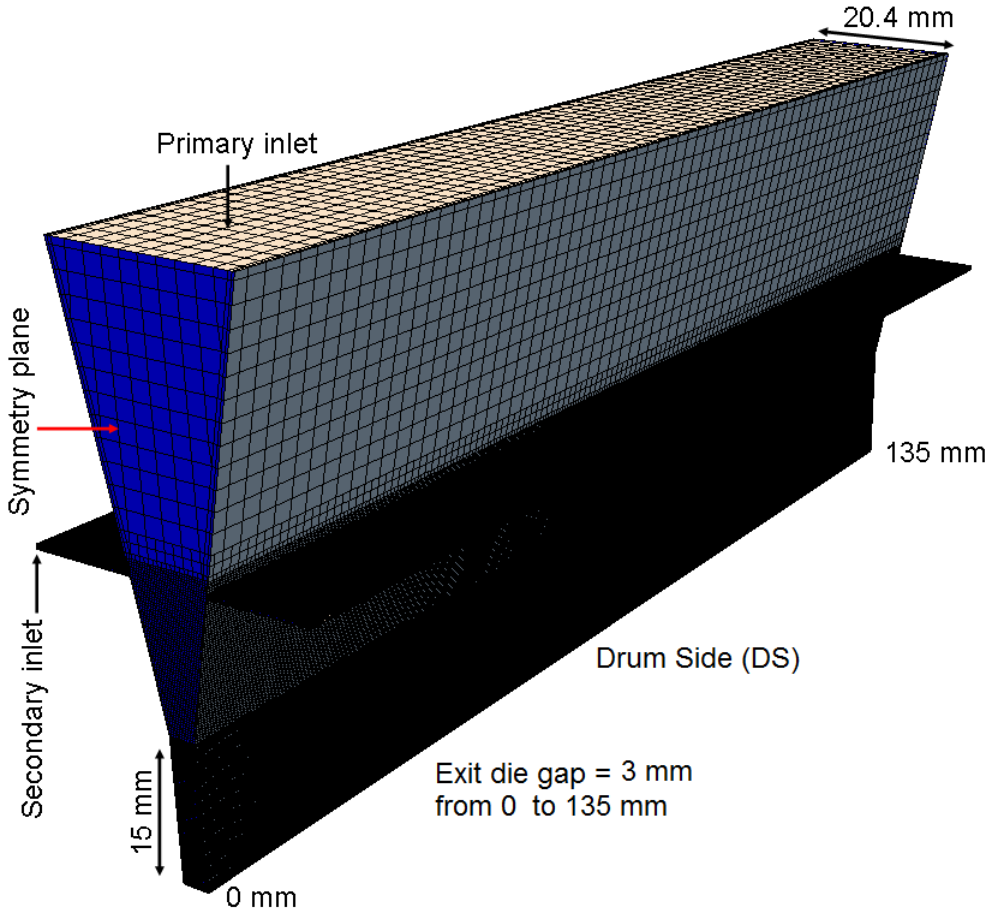

Figure 7.1: The meshed template geometry. Geometry created by Richard Maltby, DuPont Teijin Films Placement Student, 2012-13. Flow direction is from top to bottom.

Approximately 4.5 million mesh cells were required to discretise the template geometry. A base mesh cell size of 2.0 mm was used alongside a minimum of 0.15 mm. Finer mesh regions were selected once the different fluids are in contact and across the land width.

Table 7.1 shows the CFD modelled fluid properties assigned to B and A. For this

base case geometry, identical fluids with standard PET melt properties are assumed. The viscosity of B and A is approximately 200 Pa s at 285 °C. The specific heat capacity (c_p) modelled, typical of PET melts, is used to calculate the heat flux Q_h (see Appendix A) and has units J kg^{-1} °C^{-1}. The mass flow rates used for B and A are scaled from 94.5 and 8.9 kg hr^{-1} respectively, through the 410 mm wide MMD. Uniform flow across the width enters all three channels. Excluding the varying land temperature values, the template geometry has a constant wall temperature of 285 °C.

Table 7.1: The modelled fluid properties for B and A.

	B	**A**
Temperature (T)	285 °C	285 °C
Density (ρ)	1,250 kg m^{-3}	1,250 kg m^{-3}
Viscosity (η), Pa s	$10^{\{(2{,}953/(T+273))-2.99\}}$	$10^{\{(2{,}953/(T+273))-2.99\}}$
Thermal conductivity (κ)	0.2 W m^{-1} °C^{-1}	0.2 W m^{-1} °C^{-1}
Specific heat capacity (c_p)	$1,060 + 1.72(T + 273)$	$1,060 + 1.72(T + 273)$
Mass flow rate ($\dot{m}$)	31.1 kg hr^{-1}	3.1 kg hr^{-1}
Final volume fraction	90.9 %	9.1 %

For this template geometry, heaters were set at 0, 45, 90 and 135 mm across the AS land and at 22.5, 67.5 and 112.5 mm for the DS. This is assumed to be six heaters in total since the effect of the individual heater curves are halved for the 0 and 135 mm heaters. For the properties in Table 7.1, a flow factor (FF) of 1 and every heater set to 40 % power, a CFD simulation was generated. The resulting DS land temperature profile for this simulation is shown in Figure 7.2. Using the evaluated velocity and temperature line integrals, the total heat transferred to the melt was calculated as: $Q_\mathrm{h} = 764.6$ W. Comparing this with the assumed Q'_h of 360 W, $FF = 0.4708$ (see Appendix A), which is used throughout this Section and reduces the DS land temperature by around 50 °C as demonstrated in Figure 7.2.

Using this new FF, a CFD case was ran with all heaters at 40 % operating power.

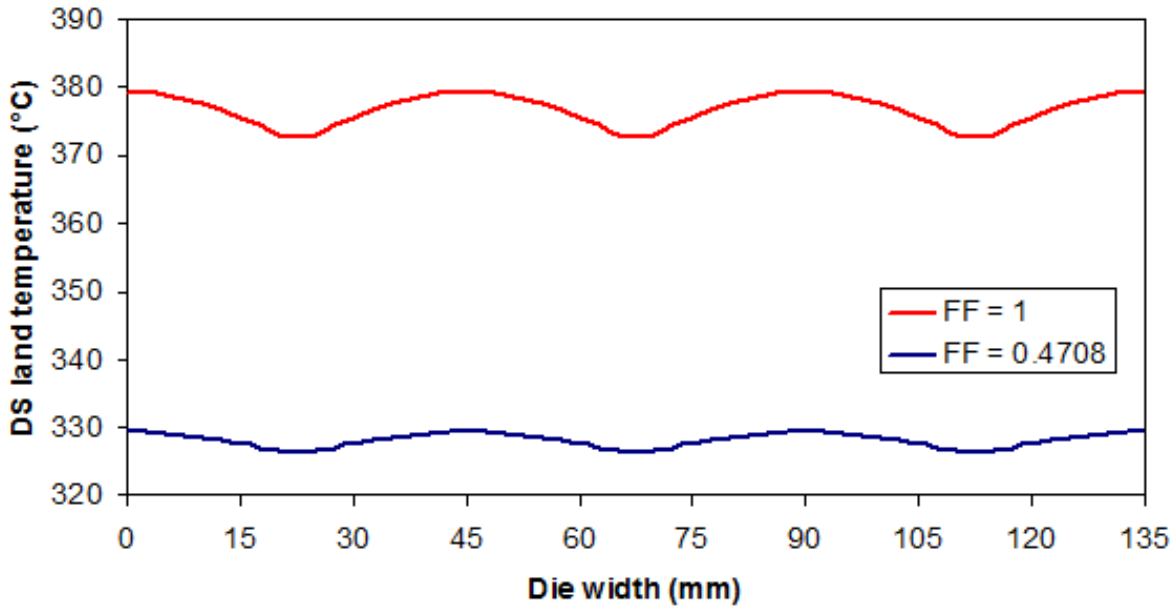

Figure 7.2: The DS land temperature profile for both the original and calculated flow factors.

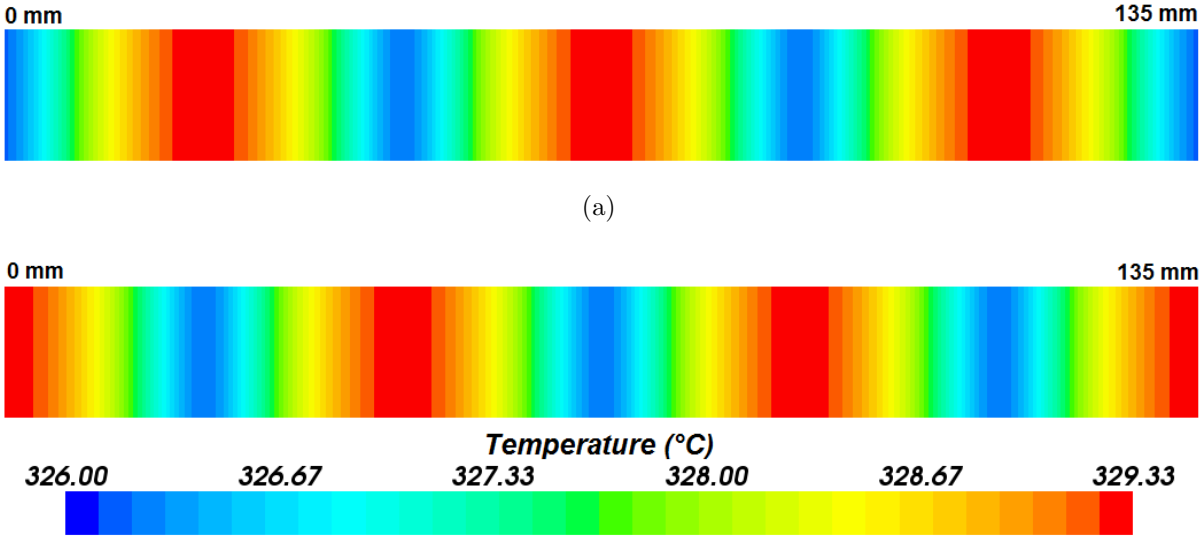

(a)

(b)

Figure 7.3: The land temperature profiles when each heater is set to 40 % operating power for (a) the AS and (b) the DS.

Figure 7.3 shows the resulting land temperature profiles for (a) the AS and (b) the DS. Here, the regions of *minimum* temperature show the heater locations, with the maximum

temperature observed *between* two heaters. This is due to the 96 mm span of each heater curve, and every heater having identical power. Because the same amount of power is applied to each heater, there is only a 3.3 °C difference between the maximum and minimum land temperatures on both the AS and DS. One would therefore expect this set of heaters to have a minimal effect on the final film thickness.

Figure 7.4 shows the volume fraction of B across the template die outlet, where Figure 7.4a shows from 0 to 45 mm, Figure 7.4b shows from 45 to 90 mm and Figure 7.4c displays from 90 to 135 mm. A smooth, linear and well defined interface is maintained across the die width. This is desirable from a commercial perspective and occurs because the two fluids are in contact for a short period of time, and a sufficiently fine mesh is used.

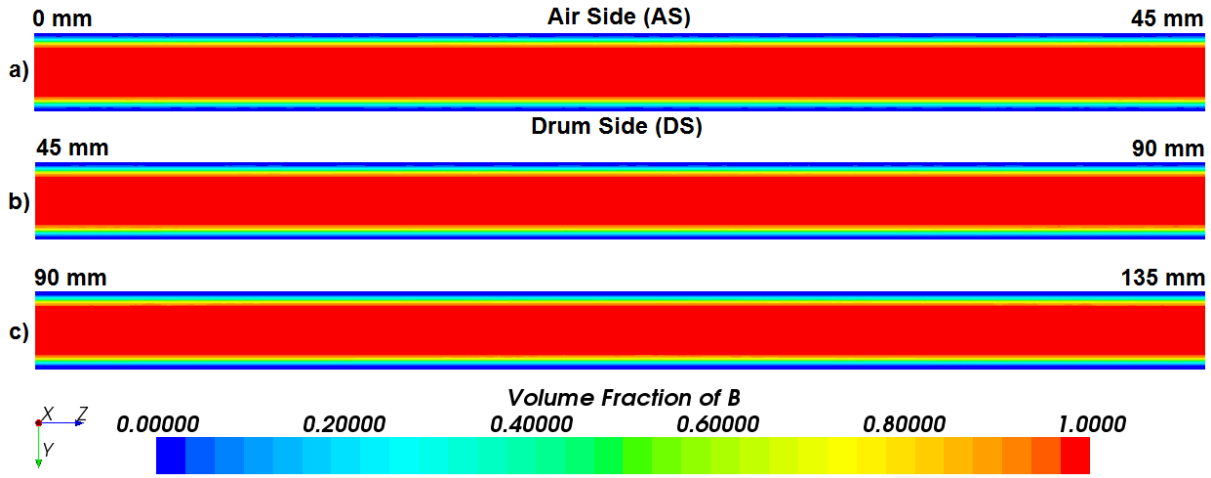

Figure 7.4: The volume fraction of B (shown in red) at the template die outlet when all heaters are set to 40 % operating power showing (a) the 0 mm edge, (b) the middle (c) the 135 mm edge. The volume fraction of A is shown in blue.

The outlet flow was calculated from 0 to 135 mm. At each increment, the percentage variation with respect to the minimum flow value was evaluated. Figure 7.5 shows this flow variation graphically. There is a maximum thickness difference of only 0.47 %, showing that when all heaters are set to 40 % power, this has very little effect on the final film profile. Regions of maximum thickness occur between two heater locations. This is again due to the concept of summing 96 mm wide heater curves, where the *average* temperature

of the AS and DS land temperature profiles (see Figure 7.3) is a maximum between rather than at heater locations.

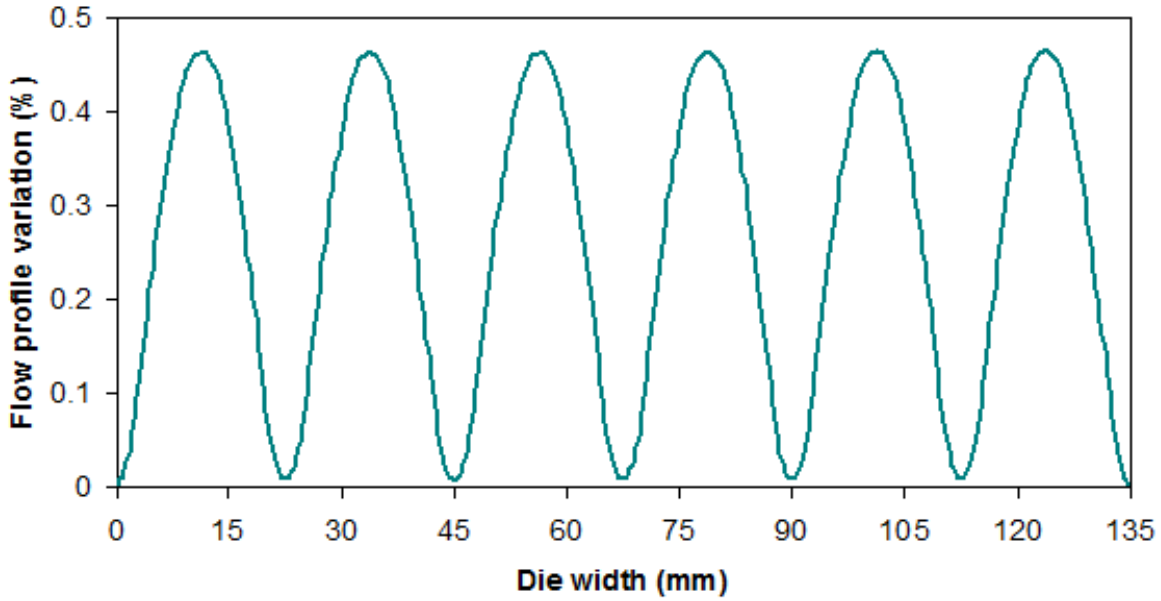

Figure 7.5: The flow profile variation across the template die width when all heaters are set to 40 % operating power.

7.2.1 The effect of increasing one heater to 80 % operating power

The heater located at 67.5 mm was increased from 40 to 80 % power to observe the effect on the final film. Every other heater remained at 40 % power. Figure 7.6 shows the resulting land temperature profiles for both the AS and DS. For the DS, there is a maximum land temperature of 363.2 °C at 67.5 mm. Here, there is a temperature range of 36.6 °C, with the minimum temperature values located at the two remaining heater positions. The AS land profile is unchanged from that in Figure 7.3a.

Figure 7.7 shows the CFD predicted interfacial variation at the outlet across the 135 mm wide template die, where Figure 7.7a shows the AS interface and Figure 7.7b displays the DS interface. The AS interface remains relatively linear from 0 to 135 mm because of the presence of equal powered heaters here. At 67.5 mm on the DS, there is significant

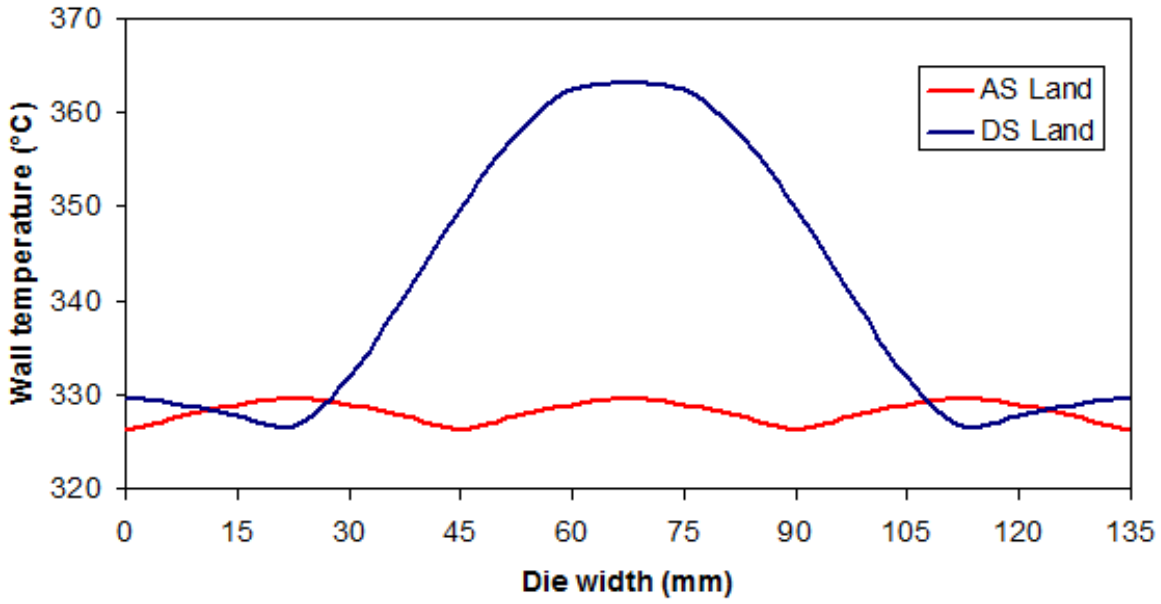

Figure 7.6: The land temperature profiles for both the AS and DS when one heater is set to 80 % operating power and the other heaters are set to 40 % power.

thinning of the A layer, and the interface is more confined to the wall. This occurs because the A layer becomes hotter than B due to the presence of the 80 % powered heater at 67.5 mm. The DS A layer therefore flows faster than B due to a localised reduction in viscosity. The fast flowing A layer needs less space to flow and draws the B layer towards the wall in its place. This interfacial thinning is also observed at regions of maximum AS land temperature in Figure 7.7a, but to a much less extent than the DS plot in Figure 7.7b.

The flow profile variation with respect to the minimum flow value is shown in Figure 7.8. There is a maximum thickness difference of 13.2 % at the 80 % heater location of 67.5 mm, caused by a localised decrease in viscosity. The thickness increase exceeds DTF's rule of thumb which assumes an 8 % increase in thickness for a 40 % increase in power. This result shows that the rule of thumb is not fully applicable on a pilot scale and it is recommended that lower powered heaters be used here. Based on this work, pilot scale film trials have been conducted with the heater powers halved. Significant improvements in the profile control for the line have been observed; there is tighter control and more measured response to disturbances at this reduced power.

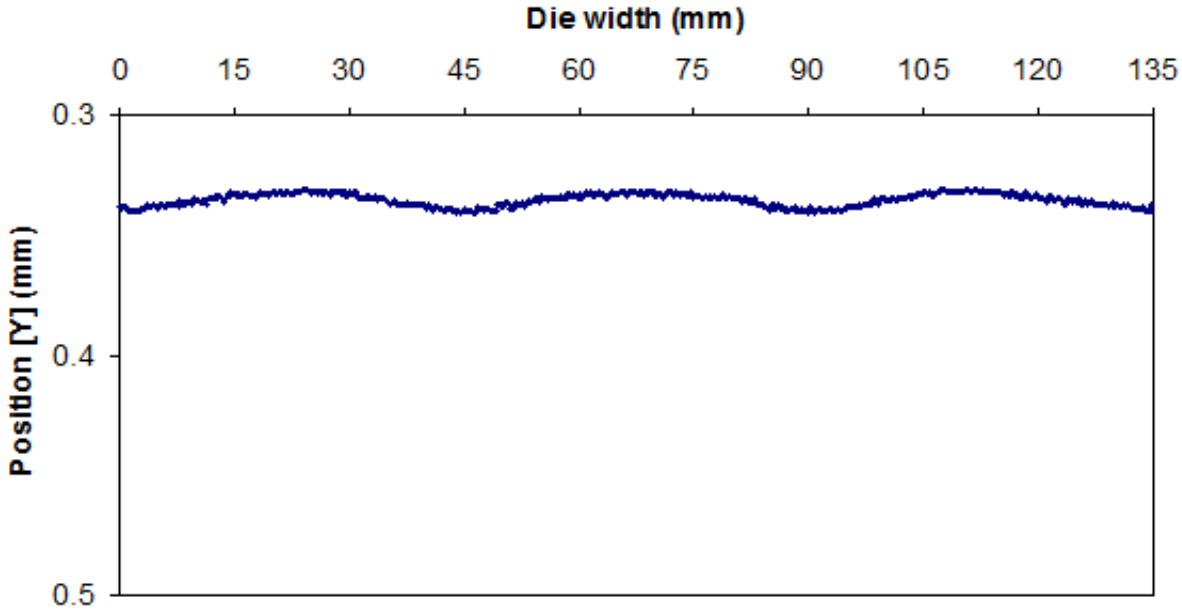

(a)

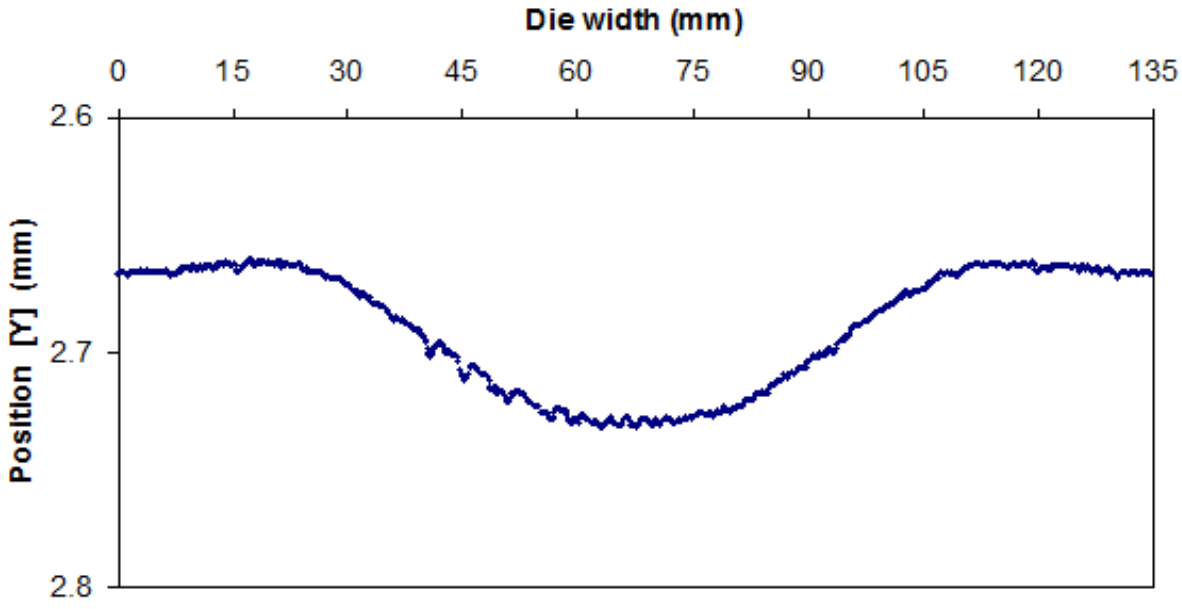

(b)

Figure 7.7: The interfacial outlet plot across the template die width for (a) the AS and (b) the DS.

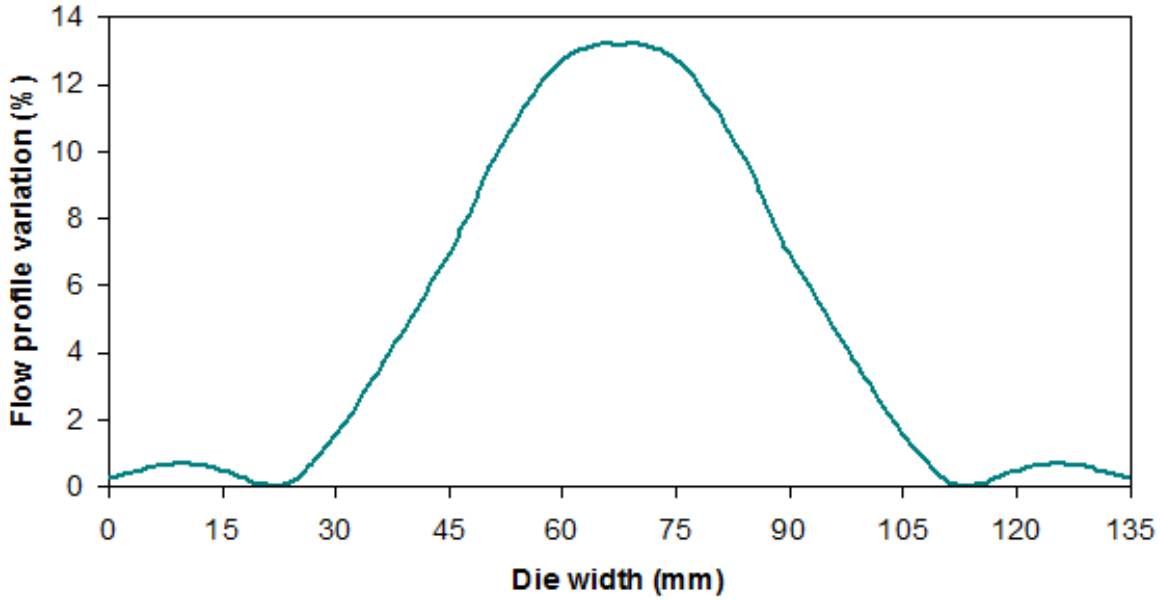

Figure 7.8: The flow profile variation across the template die width when one heater is set to 80 % power.

7.3 410 mm wide multi-manifold die

In this Section, a 410 mm wide MMD with a full set of die bolt heaters is modelled. This meshed MMD geometry is shown in Figure 5.14b. The heaters in this Section are set to try improving the thick or thin film edges caused by melt viscosity differences and the MMD guaranteeing clear edges.

Curves were created to represent the full set of die bolt heaters used for this pilot scale geometry. There are a total of 17 heaters used for this MMD in its standard format, with nine on the AS and eight across the DS. For the AS land, the first heater is attached 31.5 mm from the FE. The second heater is placed 70 mm from the FE. There is then a spacing of 45 mm between adjacent heaters from 70 to 340 mm, before a final heater at 378.5 mm. On the DS, the first heater is set at 47.5 mm (see Figure 7.9). There is a 45 mm spacing between adjacent heaters, with the final heater placed at 362.5 mm.

The edge heaters on both the AS and DS are beyond the projected clear edge width of 13 mm. Work in this Section evaluates whether the edge heaters are placed too far into the geometry to significantly improve the film profile here. The same *FF* as used in

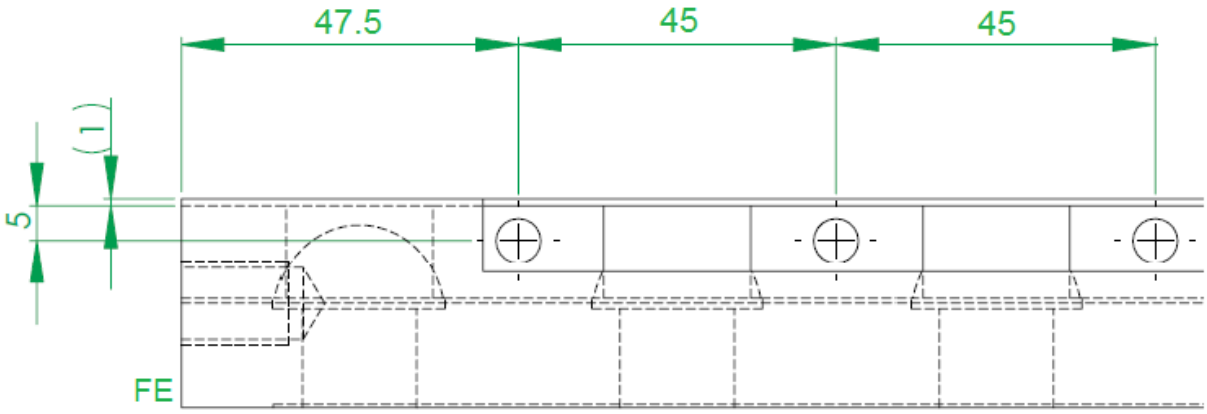

Figure 7.9: The first three heaters across the DS land for the 410 mm wide MMD. All dimensions shown are in millimetres. Diagram obtained from the DTF database.

Section 7.2 is applied. A base CFD simulation justified this assumption as the flow rates and polymer properties remained similar.

7.3.1 The effect of low powered edge heaters

ABA structured MLFs were produced using CFD, with the primary B layer making up 80 % of the overall flow rate. Table 7.2 shows the modelled properties assigned to B and A. The MMD wall temperature, excluding the land, was set to 285 °C.

Table 7.2: The modelled fluid properties for B and A.

	B	**A**
Temperature (T)	285 °C	285 °C
Density (ρ)	1,250 kg m^{-3}	1,250 kg m^{-3}
Viscosity (η), Pa s	$10^{\{(2{,}953/(T+273))-3.06\}}$	$10^{\{(2{,}953/(T+273))-2.76\}}$
Thermal conductivity (κ)	0.2 W m^{-1} °C^{-1}	0.2 W m^{-1} °C^{-1}
Specific heat capacity (c_p)	$1,060 + 1.72(T + 273)$	$1,060 + 1.72(T + 273)$
Mass flow rate ($\dot{m}$)	80 kg hr^{-1}	20 kg hr^{-1}
Final volume fraction	80 %	20 %

At the melt temperature of 285 °C, $\eta_B \approx 170$ Pa s and $\eta_A \approx 340$ Pa s. At this 1:2 viscosity ratio, thick edges are predicted because of clear edges produced using the MMD and consisting solely of the less viscous B layer, see Section 5.3.1. To attempt to improve these film edges, the land edge heaters were set to have a lower power than the remaining ones. The heaters at 31.5 and 378.5 mm have a power of 10 %, with 20 % used for the 47.5 and 362.5 mm heaters. The remaining middle heaters have a 40 % operating power.

Figure 7.10 shows the resulting land temperature profiles for the 410 mm wide MMD. At the DS edge, the temperature approaches the base of 285 °C because the 47.5 mm heater position is almost identical to half of the 96 mm heater curve span. This lower temperature is set to attempt to increase the viscosity of the B layer and improve the thicker edges caused by viscosity differences. On the AS land, the maximum temperature range is 41.7 °C, which increases to 44.5 °C for the DS.

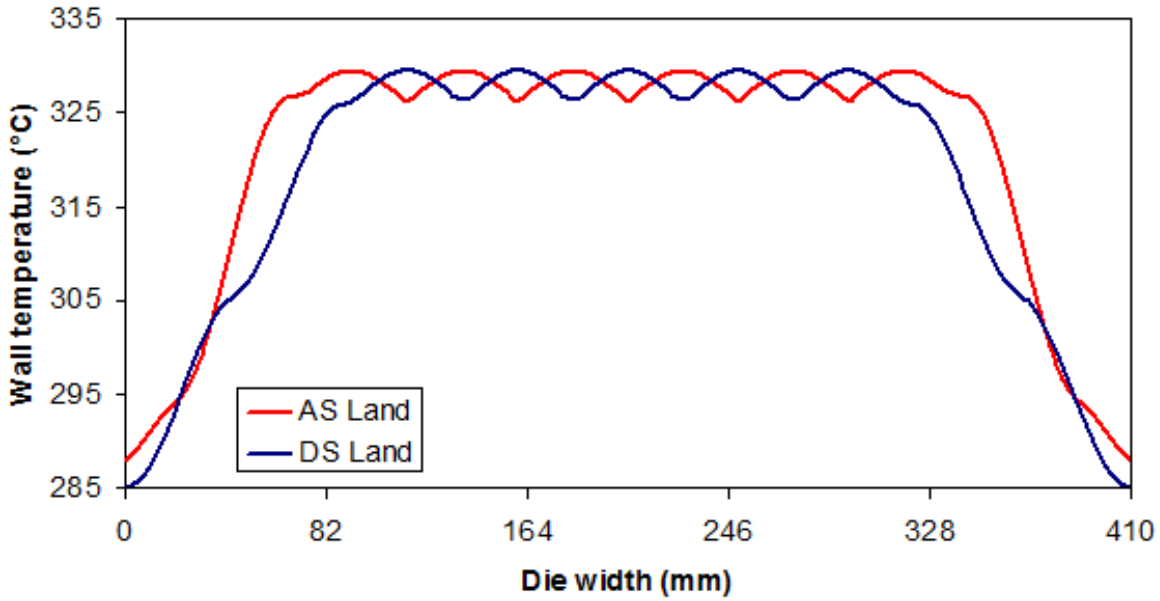

Figure 7.10: The land temperature profiles for both the AS and DS for low powered edge heaters.

Figure 7.11 shows the CFD predicted interfacial variation at the outlet across the MMD width. At the low powered heater positions, there is a thickening of the A layers and the interface moves away from the walls. This is because the A layers become colder

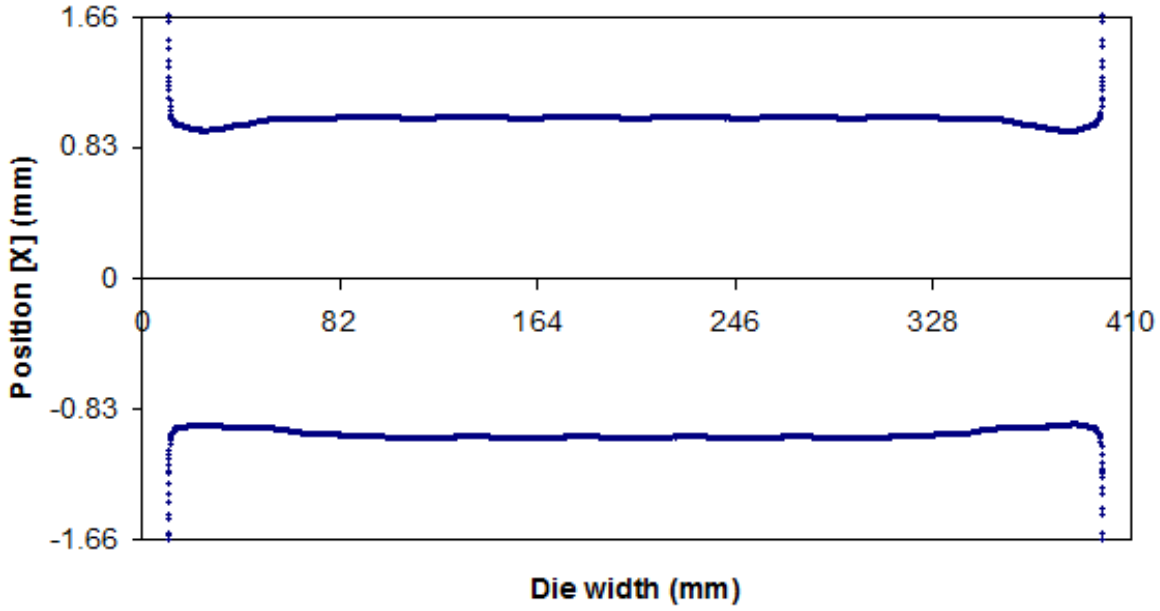

Figure 7.11: The interfacial outlet plot across the 410 mm wide MMD.

since less heat is applied. These secondary layers therefore move slower than B and need more space, forcing the primary B layer towards the middle of the outlet.

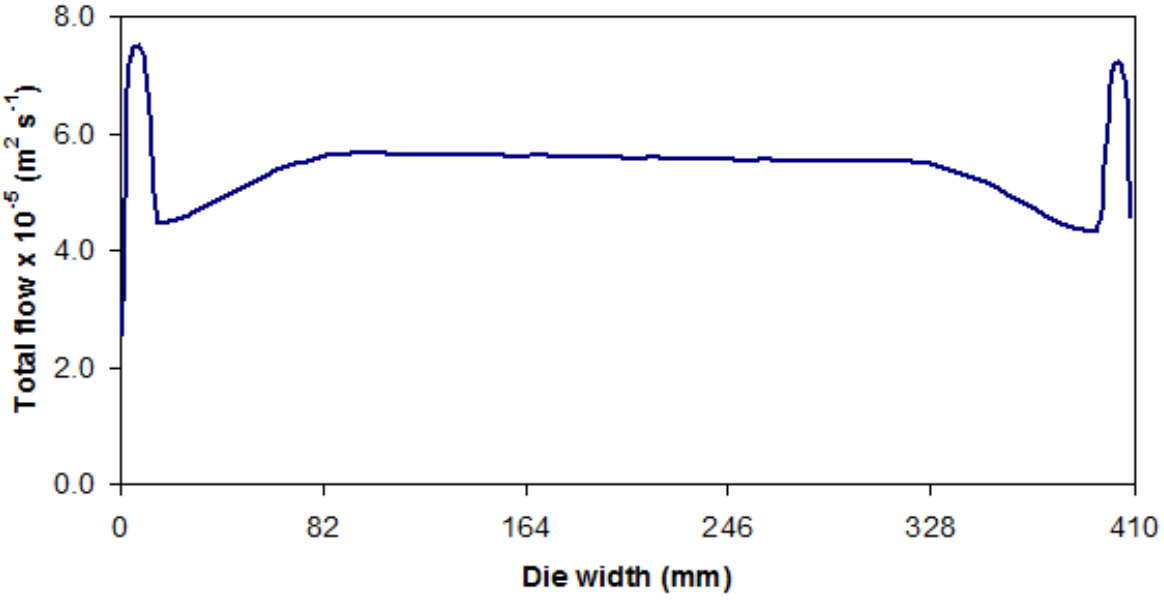

Figure 7.12: The total outlet flow across the 410 mm wide MMD.

For low powered edge heaters and the fluid properties in Table 7.2, the total outlet

flow plot in Figure 7.12 shows the CFD predicted film thickness profile. Thick edges are obtained despite the presence of low powered edge heaters. This implies that for the 410 mm wide MMD, the initial heaters are too far into the die to significantly ameliorate the edges. There is a decrease in the film thickness between the thick edges and the middle of the film. This is caused by the low powered edge heaters and again demonstrates that they are too far into the die. The graph in Figure 7.12 shows undesirable viscous and thermal effects simultaneously.

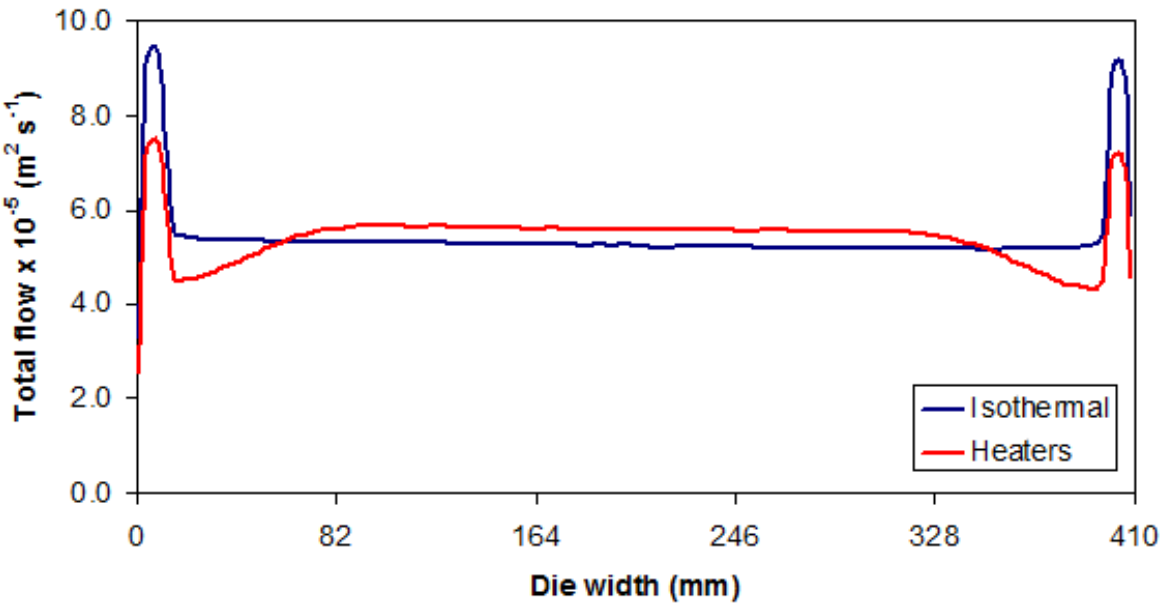

Figure 7.13: The total outlet flow across the 410 mm wide MMD for both a constant land temperature and low powered edge heaters. The primary:secondary melt viscosity ratio is 1:2.

Figure 7.13 shows a comparison between the flow result in Figure 7.12 and the equivalent result from Section 5.3.1 for a 1:2 viscosity ratio and an isothermal case. The low powered edge heaters have caused a 21 % thickness reduction in the edges, but the film is still thicker here compared with the middle. Furthermore, the position of the low powered edge heaters has caused a reduction in the film thickness at their location. This is another process issue that is undesirable. Figure 7.13 confirms that the edge heaters are positioned too far into the MMD to completely improve the edges. If the die bolt heater

system was redesigned, it is suggested that the edge heaters be placed within 13 mm from both the FE and BE.

7.3.2 The effect of high powered edge heaters

Using the fluid properties in Table 7.2, a CFD simulation was generated upon reversing the viscosities of B and A. The primary B layer is now twice as viscous as A. From Section 5.3.2, such a viscosity ratio causes thin film edges for an isothermal case. To try improving such edges, the MMD heaters at 31.5 and 378.5 mm were set to 80 % power, with 60 % used for the heaters at 47.5 and 362.5 mm. A heater power of 40 % is maintained for the middle heaters.

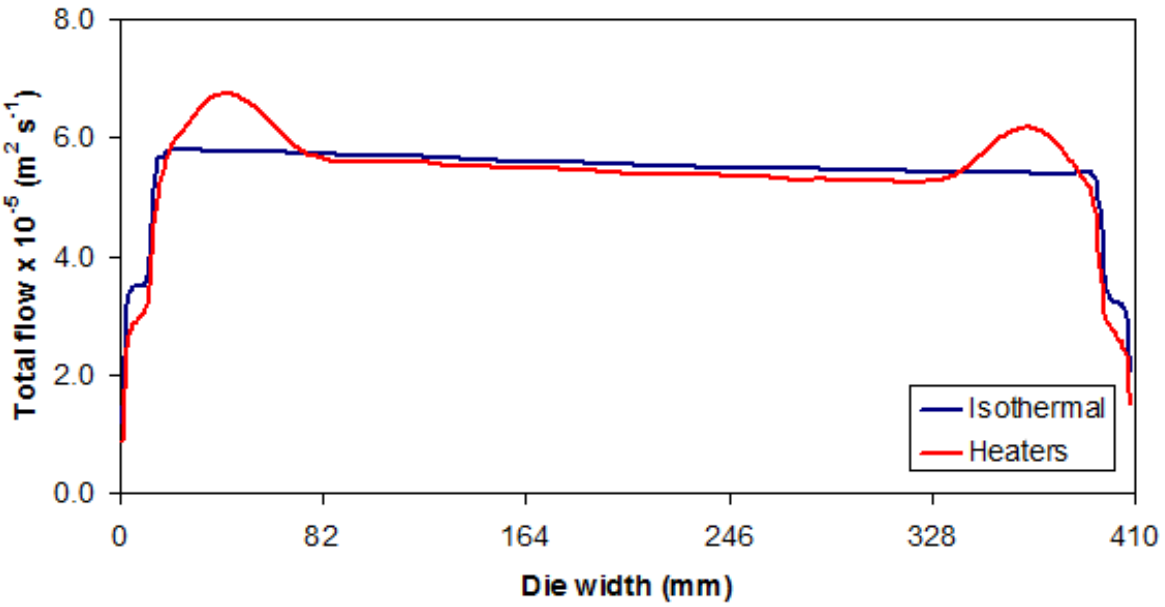

Figure 7.14: The total outlet flow across the 410 mm wide MMD for both a constant land temperature and high powered edge heaters. The primary:secondary melt viscosity ratio is 2:1.

For this 2:1 viscosity ratio, Figure 7.14 shows the outlet flow results for both high powered edge heaters and the isothermal case from Section 5.3.2. It is again clear from this graph that the edge heaters are too far into the MMD geometry. The high powered heaters here have caused an undesirable thickness increase away from the extreme film

edges. The thin film edges are still problematic and simultaneous viscous and thermal effects occur.

7.4 1,285 mm wide multi-manifold die

In this Section, a 1,285 mm wide production scale MMD is modelled. Polymer properties and heater power settings based on a film production trial are presented. The MMD design has been extrapolated from the pilot scale design shown in Figure 5.14. AB structured MLFs were manufactured, with the A layer entering via the AS. The width of the secondary channels are 1,140 mm, giving a projected clear edge width of 72.5 mm on both the FE and BE. The exit die gap increases linearly from 4 to 4.25 mm from the FE to the BE at 1,285 mm and the land length is 25 mm.

Approximately 11 million mesh cells were required for the MMD. A base mesh cell size of 8.0 mm was used alongside a minimum mesh cell size of 0.45 mm. Finer mesh regions are used once the different fluids are in contact with each other and across the MMD outlet width to try maintaining as smooth an interface as possible.

The modelled fluid properties for B and A are displayed in Table 7.3. B is a highly filled PET polymer and A is a filled PET co-polymer, making up 10 % of the overall flow rate. The viscosity-temperature relationships used are based on the O'Dell model (Equation 2.8) and IV estimations for both polymers. It was found that $[\eta_B] \approx 0.685$ and $[\eta_A] \approx 0.667$, where $[\eta]$ is the IV. At their respective melt temperatures, $\eta_B = 241.9$ Pa s and $\eta_A = 362.0$ Pa s. This yields a primary:secondary melt viscosity ratio of approximately 1:1.5. One would therefore expect the final film produced to have thick edges compared with the middle without the use of heaters. Apart from the varying land temperature profiles, the MMD has a constant wall temperature of 275 °C.

The MMD was modelled here with all its land heaters on both the DS and AS. On the DS, the first heater is positioned 36.5 mm from the FE. Unlike the pilot scale MMD modelled in Section 7.3, the edge heaters on the production scale geometry are within the projected clear edge width on both the DS and AS. It is therefore expected that the

Table 7.3: The modelled fluid properties for B and A.

	B	**A**
Temperature (T)	300 °C	275 °C
Density (ρ)	1,250 kg m^{-3}	1,050 kg m^{-3}
Viscosity (η), Pa s	$10^{\{(2{,}953/(T+273))-2.77\}}$	$10^{\{(2{,}953/(T+273))-2.83\}}$
Thermal conductivity (κ)	0.2 W m^{-1} °C^{-1}	0.2 W m^{-1} °C^{-1}
Specific heat capacity (c_p)	$1,060 + 1.72(T + 273)$	$1,060 + 1.72(T + 273)$
Mass flow rate ($\dot{m}$)	1,620 kg hr^{-1}	180 kg hr^{-1}
Final volume fraction	90 %	10 %

heaters used for this production scale MMD will be capable of improving the final film edge profiles.

To calculate FF, a base case CFD simulation was generated. This simulation used the properties in Table 7.3, all heaters set to 40 % power and an initial FF of 1. Upon convergence, a spreadsheet based calculation found $FF = Q'_\mathrm{h}/Q_\mathrm{h} = 0.3865$. This value of FF is used throughout this Section.

7.4.1 Production scale trial considerations

7.4.1.1 Initial heater settings

In the production trial, a maximum heater power of 70.8 % was observed for a single heater, with a minimum power of 19.6 % used close by. An operating mean of 40 % power is maintained. Figure 7.15 shows the DS and AS land temperature profiles. There is a maximum wall temperature of 341.5 °C at a location of 137.5 mm.

Using the land temperature profiles in Figure 7.15 and polymer properties in Table 7.3, Figure 7.16 shows the outlet volume fraction of B across the 1,285 mm wide MMD for: (a) the FE to 90 mm, (b) 300 to 390 mm, (c) 900 to 990 mm and (d) 1,195 mm to the BE. A smooth, linear and well defined interface is maintained throughout. This is desirable

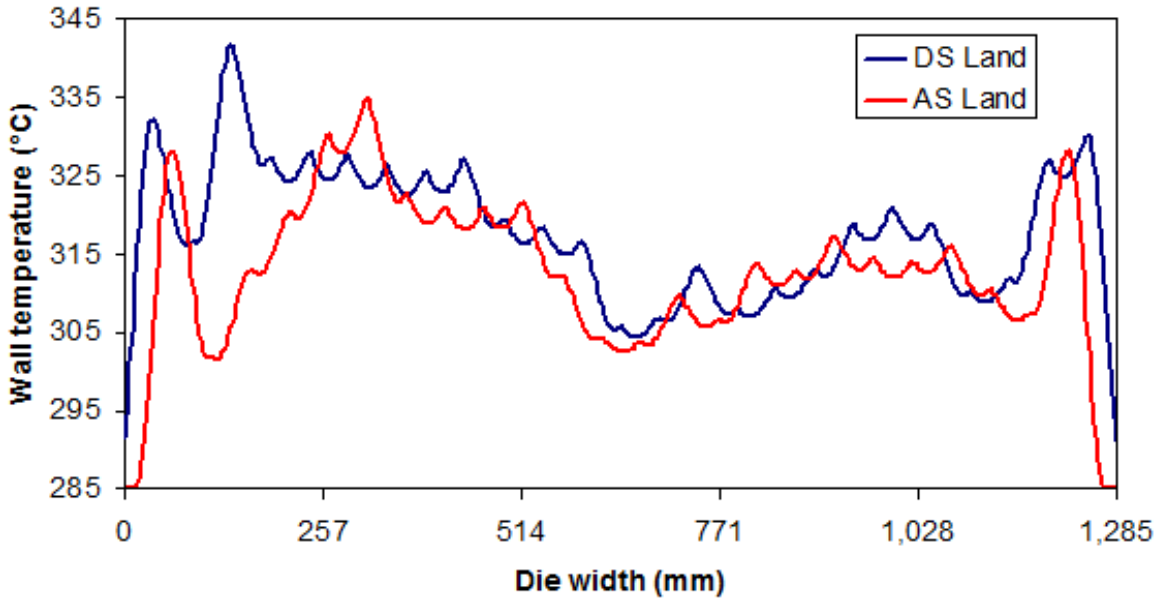

Figure 7.15: The land temperature profiles for both the DS and AS.

and implies that a sufficiently fine mesh is selected across the MMD outlet width. Clear edges of width 72.2 mm are obtained at both the FE and BE, which is another desirable product feature.

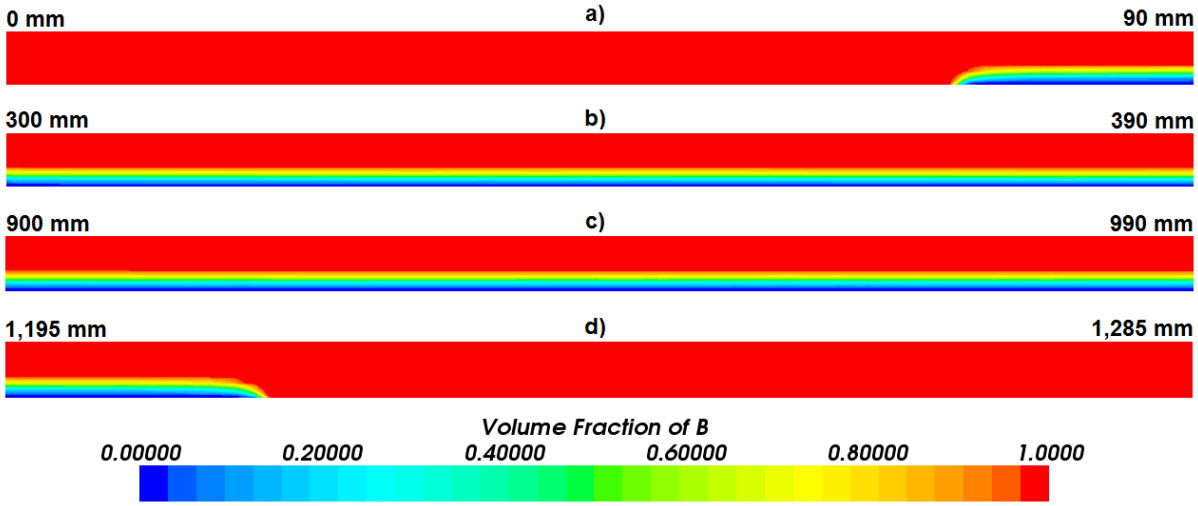

Figure 7.16: The volume fraction of B (shown in red) at the MMD outlet showing: (a) the 0 mm edge, (b) from 300 to 390 mm, (c) from 900 to 990 mm and (d) the 1,285 mm edge. The volume fraction of A is shown in blue.

The total, B and A outlet flow curves for this simulation are shown in Figure 7.17.

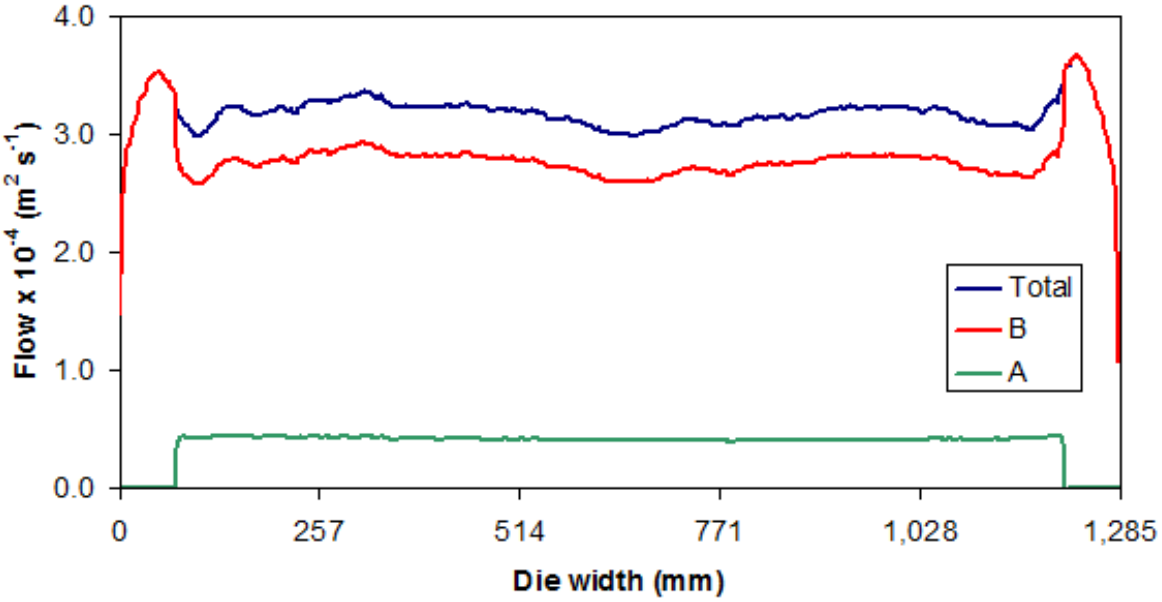

Figure 7.17: The total, B and A flow curves across the MMD outlet width.

From the total flow curve, the edges are thicker than the middle of the film. This is caused by Polymer A being more viscous than B and implies that the edge heaters are too powerful in their current setting for any improvement. Away from the edges, the film thickness is governed by the heater settings and consequent land temperature values. Thick total film regions occur where the heaters in this vicinity have a high average power setting. The total film thickness drops towards zero at both the FE and BE due to the no-slip condition imposed at the walls. The thickness of B is well matched to the total thickness, whereas A remains uniformly thin. Where it is present (neglecting the clear edges), the average thickness of A is 13.1 % of the total film thickness.

For the total thickness in Figure 7.17, Figure 7.18 shows the flow profile variation with respect to the *average* value. This graph confirms that the edges are too thick compared with the middle of the film. The FE and BE edges are 11.4 and 15.7 % thicker than the average respectively.

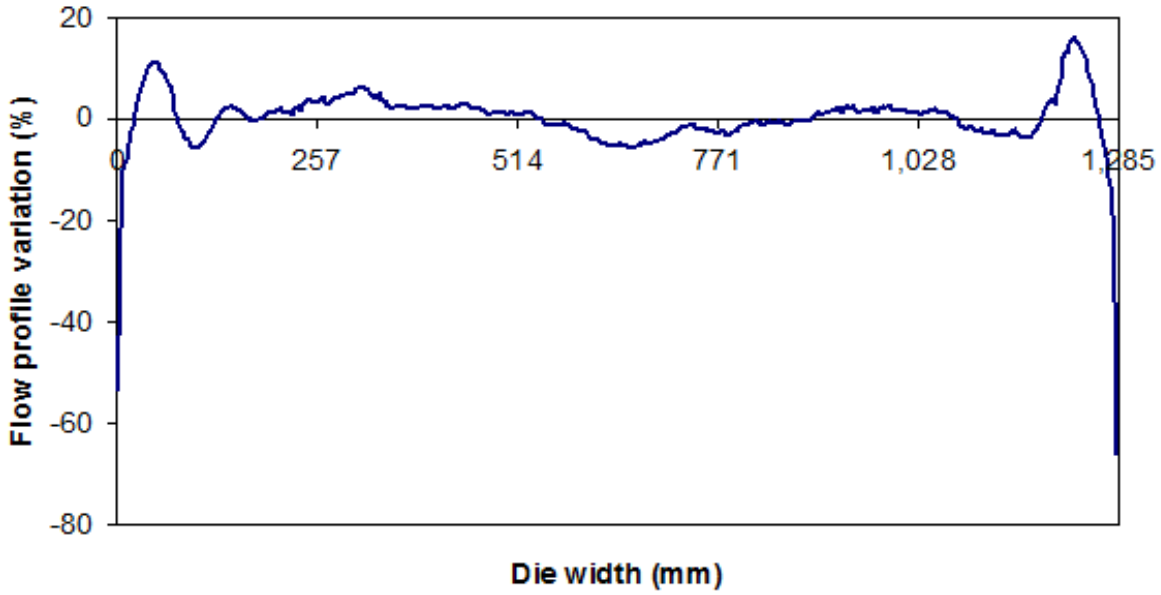

Figure 7.18: The flow profile variation across the 1,285 mm wide MMD.

7.4.1.2 Lower powered edge heaters

To attempt to ameliorate the thick edges shown in Figure 7.18, the initial edge heater settings were reduced. For Heaters 1-3, the power was reduced to 20, 22 and 20 % respectively. For the three BE heaters, 24.8, 26 and 27.2 % power was applied. The remaining heaters maintain the same land temperature from Figure 7.15.

For the low powered edge heaters and fluid properties in Table 7.3, Figure 7.19 shows the AS and DS land temperature profiles and resulting total flow curve. The localised film thickness is governed by the AS and DS heater settings in the vicinity and resulting land temperature values. Compared with Figure 7.17, the film edges have reduced in thickness, and a more uniform flow is observed, caused by a reduction in the edge heater power settings.

The flow profile variation with respect to the average value (see Figure 7.20) confirms that the edge profiles have improved significantly upon reducing the heater power here. The FE and BE edges are now 0.5 and 6.8 % thicker than the average respectively, which are more acceptable values. This reduction in edge thickness demonstrates that the film thickness profile on a production scale can be improved by optimising temperature

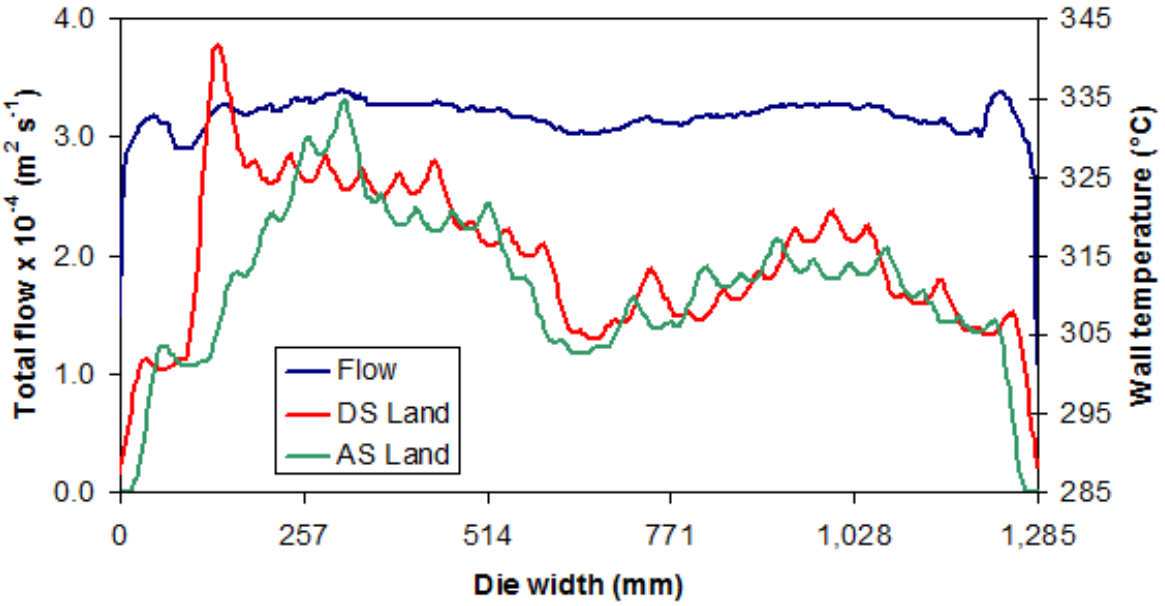

Figure 7.19: The total outlet flow and land temperature profiles for low edge heater powers.

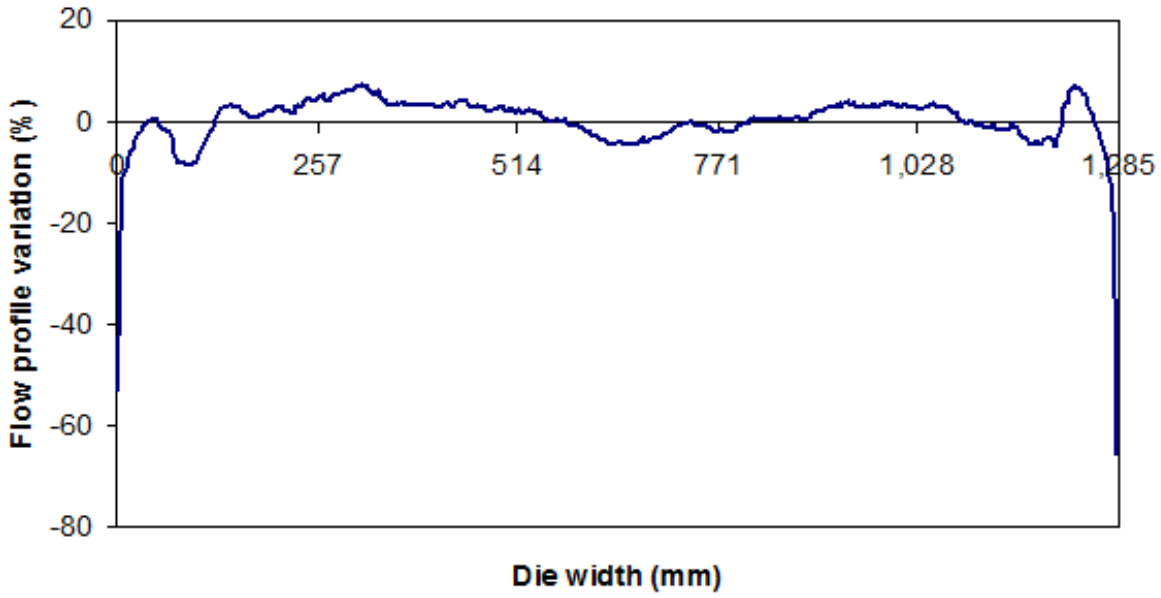

Figure 7.20: The flow profile variation across the MMD width for low powered edge heaters.

control. Additionally, it shows that for the 1,285 mm wide MMD, the edge heaters are placed in a position that allows for thickness improvements to be made here.

The edge thickness improvement was also observed experimentally. During the production scale trial, two *forward drawn* film samples were obtained at both heater settings. The edge thicknesses were measured in 10 mm increments from the FE at 0 mm up to 110 mm, and then converted into thickness profile variation values with respect to the mean thickness. This is shown in Figure 7.21, where the extreme edge thickness has approximately halved upon reducing the heater power, which is a desirable improvement. For the low powered edge heater settings, the increase in film thickness is caused by the initial presence of the secondary layer. DTF use both tapering of the die outlet and die bolt heaters to improve the final film thickness profile.

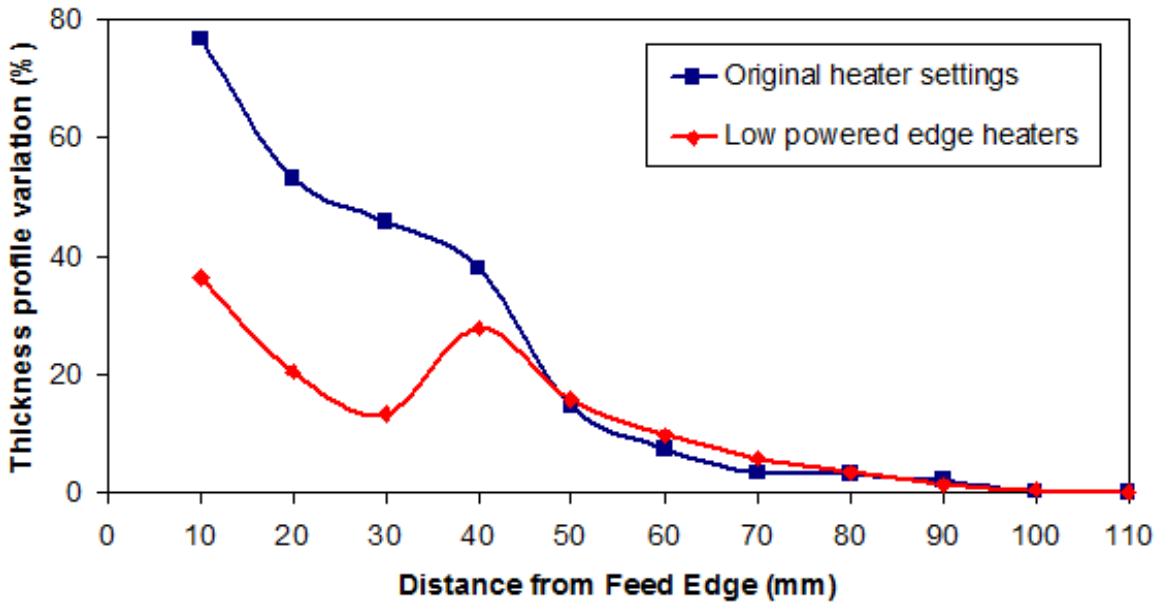

Figure 7.21: The forward drawn film edge thickness variation for both the original and low edge heater settings.

7.5 Injector block linked to a 410 mm wide end fed die

In this Section, thermal non-uniformity across DTF coextrusion apparatus is investigated numerically. The geometry modelled is an injector block linked to a 410 mm wide end fed die (see Figures 5.1 and 5.2) and ABA films are produced. Die bolt heaters are *not* modelled, but varying wall temperatures are. Such thermal non-uniformity is undesirable for the final film product, but it is important to be aware of the consequences.

7.5.1 Hot spot in a pipe

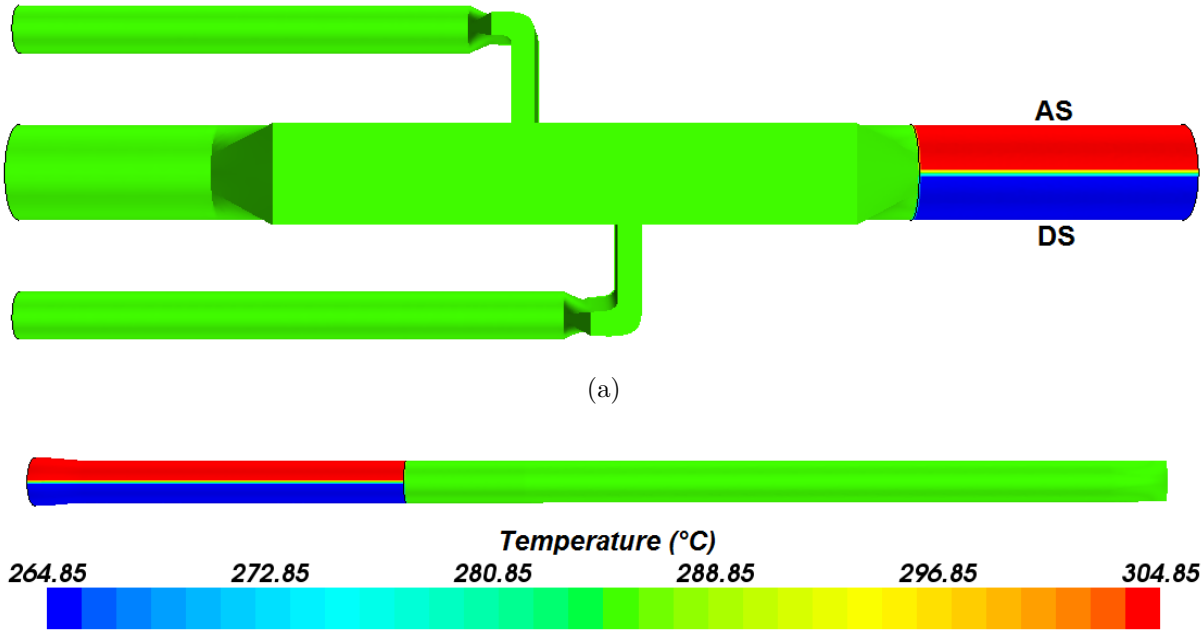

(a)

(b)

Figure 7.22: The wall temperature profiles from an aerial perspective for (a) the injector block and (b) the end fed die. Flow direction is from left to right.

The melt pipe temperature will sometimes be non-constant during the film production process. In particular, the AS temperature may vary compared with the DS. To model this, both the injector block outlet pipe and the die inlet pipe were set to have non-constant

wall temperatures on the AS and DS halves. The AS pipe temperature was set to 264.85 °C, with the DS prescribed to 304.85 °C. The remaining wall temperature is constant at 285 °C. Figure 7.22 shows the wall temperature profiles viewed aerially for both (a) the injector block and (b) the end fed die. The wall temperature gradient is exaggerated numerically compared with what is observed in reality, but the aim of this investigation is to analyse whether the pipe temperature or the die body temperature governs the final film structure and the spreading of the individual A layers. The fluid properties for this hot spot in a pipe problem are shown in Table 7.1, but with the mass flow rate of B and A increased to 80 and 20 kg hr^{-1} respectively. Also, the viscosity-temperature functions were set to give a viscosity of 170 Pa s rather than 200 Pa s at 285 °C for both B and A.

For the hot spot in a pipe, Figure 7.23 shows the outlet volume fraction of B, where Figure 7.23a shows the first 30 mm, Figure 7.23b shows the middle, from 190 to 220 mm and Figure 7.23c displays from 380 mm to the BE at 410 mm. The interface appears smooth and linear throughout, which is desirable. Figure 7.23 implies that there is very little difference in the AS and DS A layer thickness profiles. This is despite the melt viscosity difference of each layer in the injector block and die melt pipes. Therefore, the core die body temperature rather than the inlet pipe temperature is believed to govern the final film structure. There is an AS clear edge width of 3.7 mm at the BE, which increases to 8.1 mm for the DS. Differences here are caused by the injector block geometry rather than the pipe temperature, see Section 5.2.

Figure 7.24 shows the total, B, A AS and A DS outlet flow curves. The A AS and DS flow curves are generally well matched, again implying that the inlet pipe temperature has very little effect on the layer spreading within the final film structure. Polymer A is thicker at the FE on the AS compared with the DS. This is due to the increased wall temperature and hence reduced melt viscosity of A here. Polymer A is also slightly thicker on the AS compared with the DS at the BE. This is caused by the injector block geometry rather than pipe temperature differences. For the total flow curve, a uniformly thin film is obtained. This is a result of using equal viscosity polymers and sufficient tapering of the die outlet.

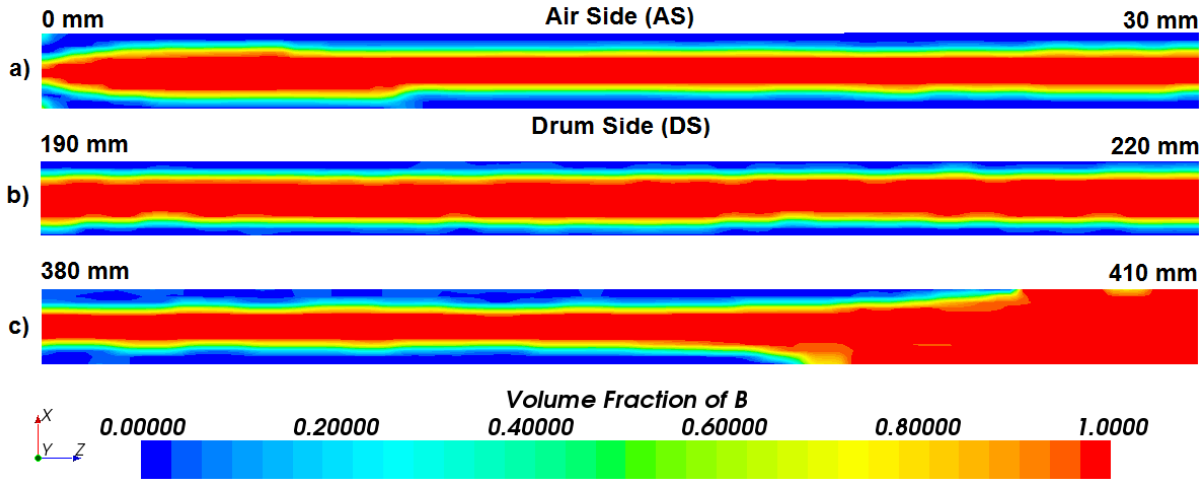

Figure 7.23: The volume fraction of B (shown in red) at the end fed die outlet showing: (a) the FE, (b) the middle and (c) the BE. The volume fraction of A is shown in blue.

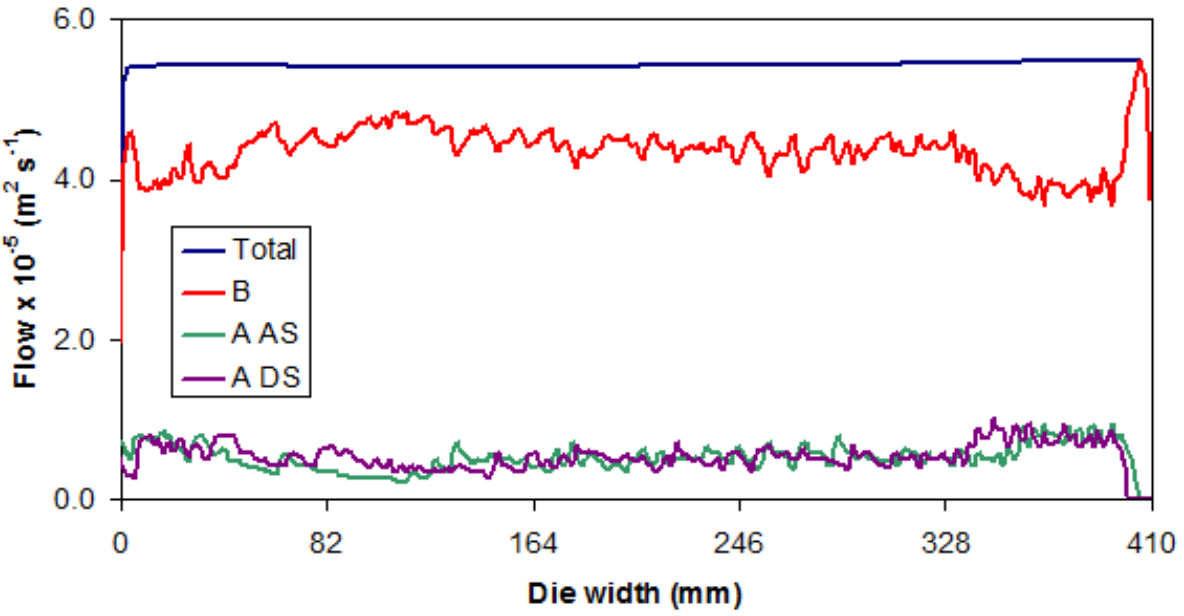

Figure 7.24: The total, B, A AS and A DS outlet flow curves.

Comparing the *total* flow curve in Figure 7.24 with that obtained for an equivalent isothermal case from Section 5.2 (see Figure 7.25) shows that there is very little difference in thickness across the die width. For the two thickness curves, there is an average absolute percentage difference of 0.2 %. This implies that it is the die body rather than pipe temperature that governs the final film thickness and a hotspot in a pipe would only

cause negligible changes for a 1:1 primary:secondary melt viscosity ratio.

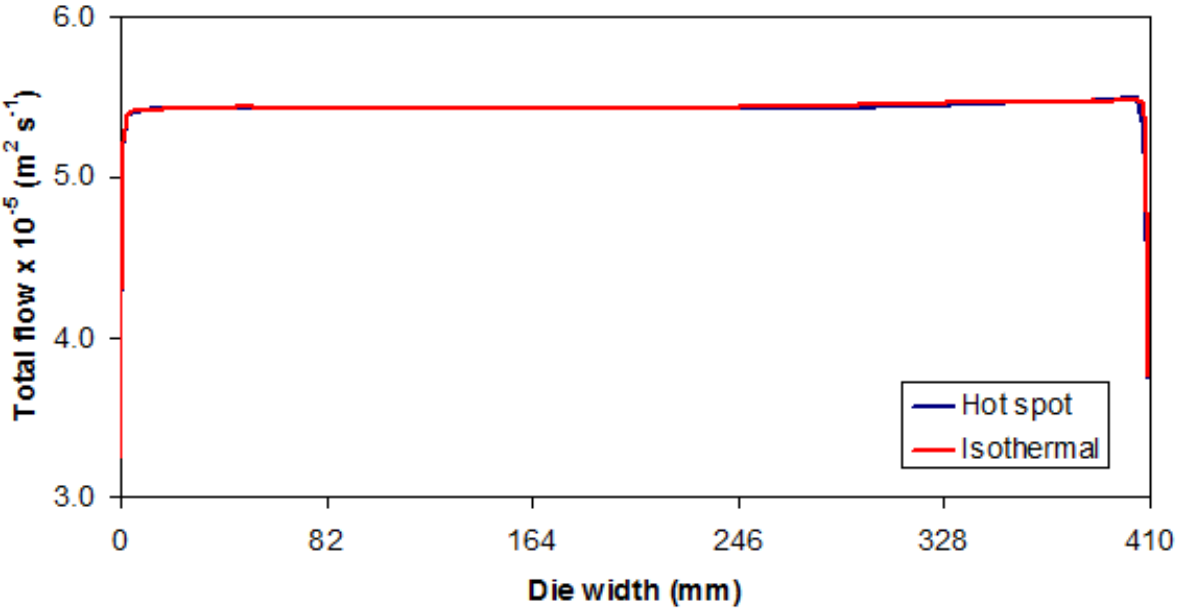

Figure 7.25: The total flow curves for a hot spot in a pipe and an isothermal case. The primary:secondary melt viscosity ratio is 1:1.

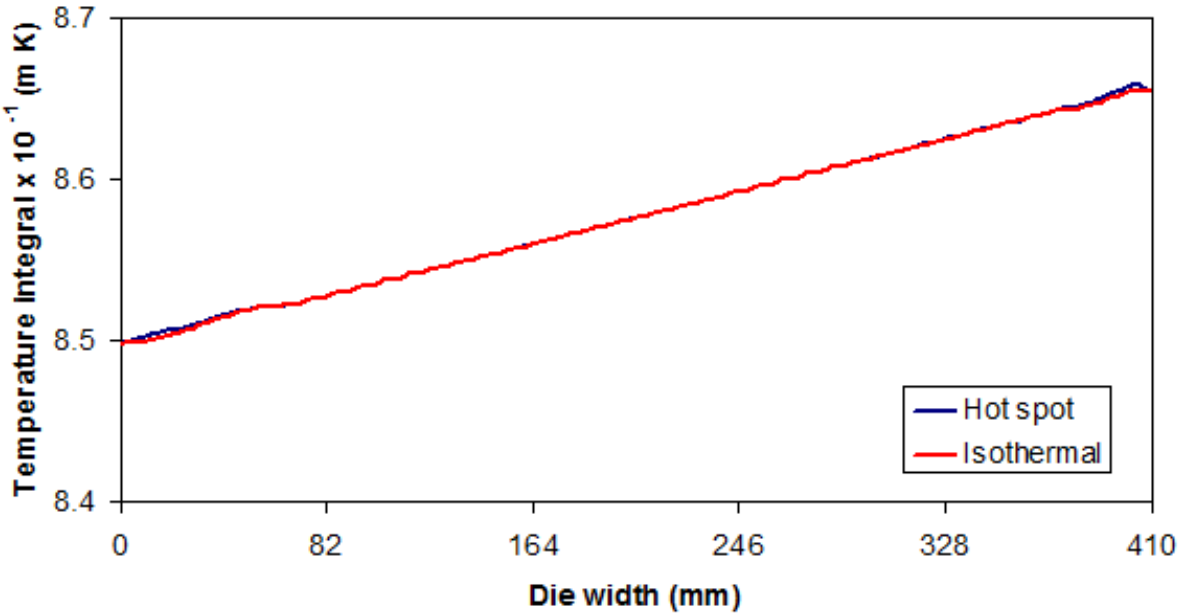

Figure 7.26: The outlet temperature integral curves for a hot spot in a pipe and an isothermal case. The primary:secondary melt viscosity ratio is 1:1.

To test the thermal variation across the film for both the pipe hot spot and isothermal simulations, the temperature was integrated across plane sections spanning the die outlet width. Figure 7.26 shows this temperature integral (measured in m K) for both models. There is very little difference between the two cases; an average absolute discrepancy of 0.0076 %. It is predicted using CFD that the non-uniform pipe temperature will not significantly alter the outlet thermal profile compared with an isothermal model. This leads to almost identical film structures as shown in Figure 7.25.

7.5.2 Temperature changes across the die body

Another problematic feature that may arise during film production is temperature changes across a die body, where thermal uniformity is desirable. In this Section, the effect of both cooling and heating the die on the final MLF structure and thickness is investigated. The fluid properties used in this Section are shown in Table 7.2; A is twice as viscous as B at 285 °C.

7.5.2.1 Cooling of the die

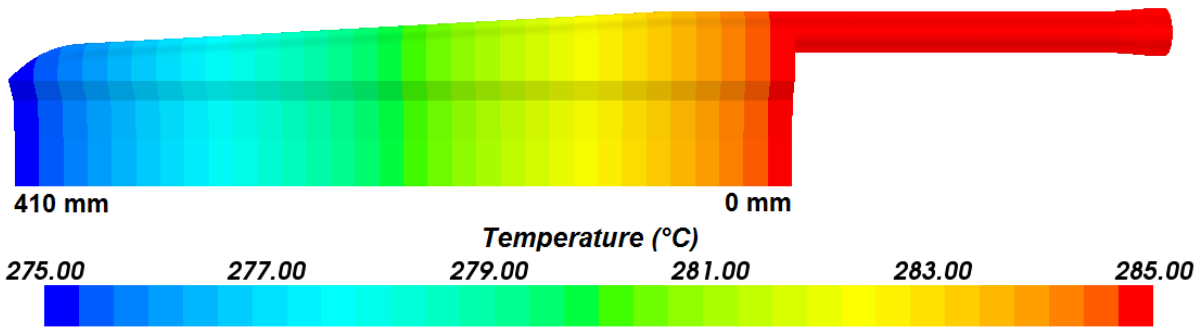

Figure 7.27: The wall temperature profile across the die body. Flow direction is from right to left.

Using the fluid properties in Table 7.2, a CFD simulation was generated where the die body cools linearly from 285 to 275 °C (see Figure 7.27). The die inlet pipe and injector block both have a constant wall temperature of 285 °C. The cooling of the die causes an increase in the viscosity of the A layers at the wall to 425 Pa s. It is therefore expected

there to be *less* spreading of the A layers for this case compared with an equivalent isothermal simulation.

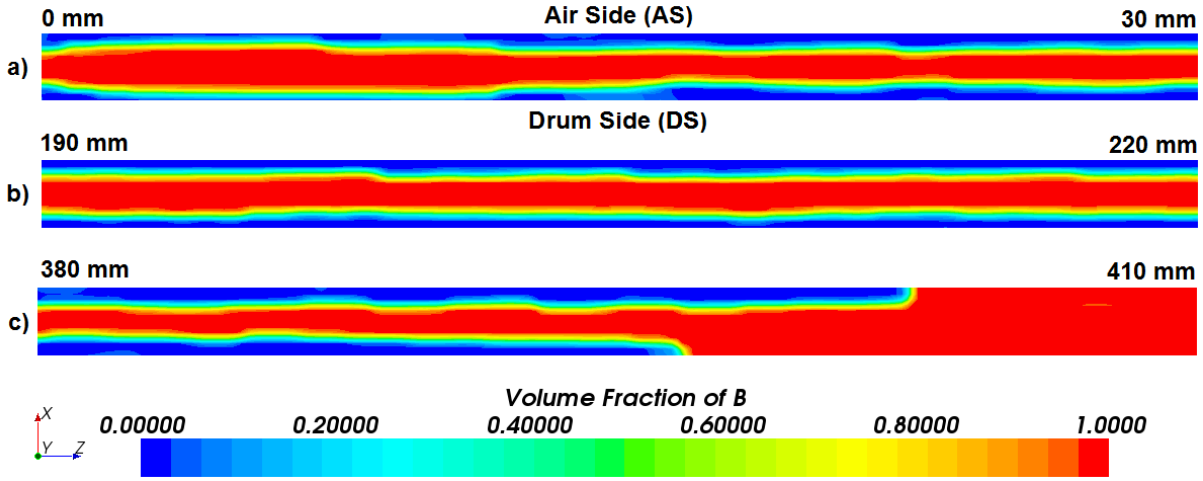

Figure 7.28: The volume fraction of B (shown in red) at the end fed die outlet showing: (a) the FE, (b) the middle and (c) the BE. The volume fraction of A is shown in blue.

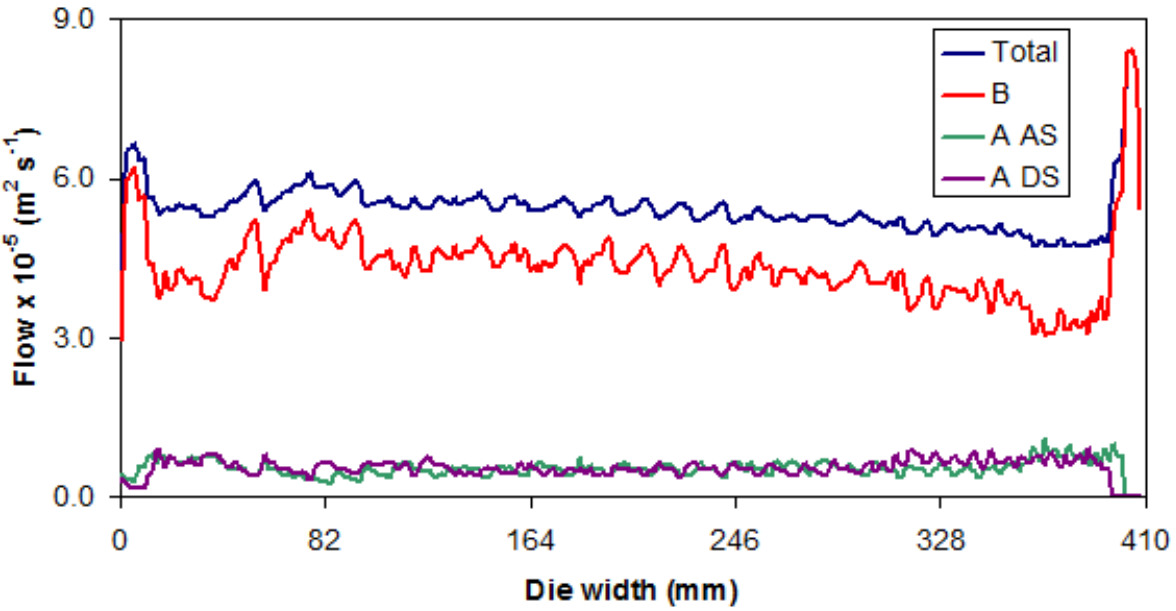

Figure 7.29: The total, B, A AS and A DS outlet flow curves.

Figure 7.28 shows the outlet volume fraction of B at the same three locations as in Figure 7.23. The AS BE clear edge width is 7.6 mm and is 12.8 mm for the DS. Comparing these values with the equivalent results for an isothermal case and a 1:2 melt viscosity

ratio (see Table 5.2), the spreading of A has reduced with cooling of the die body as expected. This is caused by the increased viscosity of A from FE to BE.

For the cooled die, Figure 7.29 displays the total, B, A AS and A DS outlet flow curves. The thickness of B is similar to the total thickness, where the increase in thickness near the BE is caused by individual melt viscosity differences. Both A layers have a relatively constant thickness across the die body and are well matched. The noisy individual layer thickness curves are caused by numerical approximations of the exact interfacial location, see Chapter 4 for more detail.

7.5.2.2 Heating of the die

Another CFD simulation was generated, modelling *heating* of the die body from 285 to 295 °C from FE to BE. At this increased temperature, η_A reduces from 340 to 275 Pa s. It is therefore expected that the A layers will spread further towards the BE compared with the isothermal case. After convergence, the clear edge width was found to be 5.7 and 6.1 mm for the AS and DS respectively. These values are lower than the equivalent isothermal case, confirming that the spreading of the A layers has increased.

Figure 7.30 shows the total outlet flow curves for an isothermal case and both heating and cooling of the die body. Near the FE, the film is thickest when the die is quenched. Around the BE, heating the die yields the thickest film. This phenomenon is caused by increased spreading of the unified structure upon increasing the die temperature. The film thickness for the isothermal case generally remains between the two other results. For the two simulations showing thermal non-uniformity, the average absolute thickness difference is 7.09 %. This is an acceptable value and could be ameliorated using die bolt heaters.

The thickness curves in Figures 7.25 and 7.30 show that the thermal non-uniformity investigated here has only small effects on the final film thickness. This implies that for the two cases of non-constant hardware temperature modelled, these will not have a significant detrimental effect on the final product.

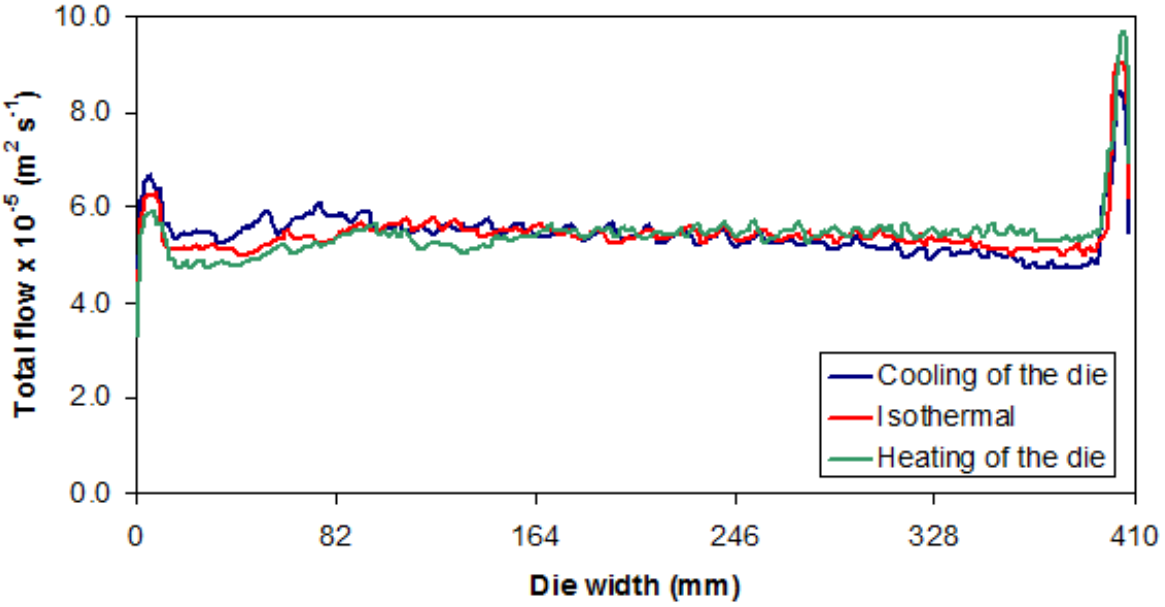

Figure 7.30: The total outlet flow curves showing an isothermal simulation and both cooling and heating of the die body. The primary:secondary melt viscosity ratio is 1:2.

7.6 Chapter conclusions

In this Chapter, the effect of changing the hardware temperature and hence melt viscosity was investigated numerically.

Varying land temperature profiles, representing a full set of die bolt heaters, were assigned to a template geometry and both pilot and production scale DTF MMDs. It was shown that the edge heaters are too far into the pilot scale geometry to improve the film thickness profile here. For the production scale MMD, the edge heaters are placed in a position that allows for significant improvement. It was demonstrated in this Chapter that heat can be applied to give a more uniformly thin final film.

Thermal non-uniformity in polyester coextrusion was also investigated via a hot spot in a pipe and non-uniform die body temperatures. In each case, the CFD predicted final film thickness does not change significantly compared with the equivalent isothermal result.

Chapter 8

Conclusions and future work

The primary aim of this thesis was to use CFD modelling to improve the layer thickness control of polyester based MLFs. The work was based on the following objectives:

- Assessment of the ability of STAR-CCM+ CFD software to accurately model DTF's pilot and production scale coextrusion apparatus. This includes both mesh and timestep independence studies alongside analysis of the suitability of the VOF method for polymer-polymer interface tracking;
- Performing suitable experimental validation methods to test the accuracy of the numerical results;
- Comparing the ability of the injector block and MMD in handling increasingly wide melt viscosity ratios;
- Investigating the use of heat to improve the film thickness profile (thermoviscous control).

8.1 Conclusions

The CFD modelling shown throughout this thesis is believed to be sufficiently accurate and representative of reality. Prior to both pilot and production scale trials, CFD has been used to successfully predict the compatibility of different polymer melt flows involved

in a potential new product. This has saved DTF time and money and the main aim of this thesis has been met. If potential new DTF MLFs were suggested for development, CFD would be used to test the product suitability. Both pilot and production scale MMDs were modelled in this thesis, with the same level of accuracy maintained. This shows that STAR-CCM+ is capable of handling industrial scale-up which is beneficial to DTF.

The main numerical limitations were observed when modelling the injector block and end fed die approach. These are: clear edges *not* predicted at the near edge of the die outlet and noisy secondary layer thickness curves. The former limitation is attributed to numerical diffusion errors at the sharp transition region from horizontal to vertical flow in the die. Clear edges were still not obtained despite modifying both the injector block and die geometries, and refining the end fed die mesh. Apart from the solution at this near edge, the numerical results are sufficiently accurate and representative of reality. The noise in the secondary layer flow curves is due to numerical approximations of the exact interfacial location and this improved with a finer mesh. However, using such a large number of mesh cells for every simulation is not feasible and noisy secondary layer flow curves were therefore observed. It is the trend rather than the noise of individual layer thickness curves that is important for the purpose of this work.

A mesh independence investigation showed that the numerically predicted film thickness profile remains constant despite the implementation of a significantly finer mesh. This demonstrates a mesh independent solution. Such mesh refinement studies were performed on all the geometries modelled and mesh independence was found. The meshes used to discretise the geometries are therefore believed to be sufficiently accurate. The film thickness also did not change at different timesteps, showing a timestep independent solution. In regions where a sufficiently fine mesh was implemented, the VOF method was found to be an excellent interfacial capturing technique, yielding a smooth and well defined interface when the different polymer melt layers were in contact.

Experimental validation methods, via light microscopy, die plug analysis, chloroform washing, fluorescence microscopy and WLI, were used to test how well the CFD results represent reality. There was generally an excellent match between numerical and exper-

imental data. This successful experimental validation shows that the results obtained from STAR-CCM+ are both sufficiently accurate and representative of reality, which is desirable.

A full numerical investigation showed that the MMD was better than the injector block approach at handling increasingly wide melt viscosity ratios. This is consistent with the findings in [8, 9, 11, 15, 16, 76]. With MLFs increasing in complexity and the melt viscosity ratios getting wider, it is envisaged that the MMD system will be used more by DTF in the future.

Further work modelling die bolt heaters demonstrated that heat can be used to improve the film thickness profile. This is because of localised changes in the melt viscosity. A full set of die bolt heaters, spanning a production scale MMD was shown to be capable of improving the film thickness edge profiles, which was confirmed experimentally. It was also found that unwanted thermal non-uniformity in polyester coextrusion does *not* cause a detrimental effect on the final film thickness.

8.2 Future work

Based on the work in this thesis, it is recommended that the following areas be studied in the future:

- **Addressing the lack of clear edges predicted numerically for end fed die geometries**

For all end fed die geometries modelled in this thesis, the secondary layer(s) were present at the near edge of the outlet solution, and clear edges were not attained. This is despite experimental evidence suggesting that clear edges should be observed, and was attributed to numerical diffusion errors when moving from horizontal to vertical flow within end fed dies. Although factored into the interpretation and taken to be an acceptable numerical error, the lack of clear edges should be addressed and ameliorated in the future. Any future work should attempt to reduce the numerical diffusion errors observed. This study should involve using the VOF method alongside QUICK and other high-order accurate in-

terpolation schemes, and implementing automatic mesh refinement of problematic regions based on preliminary solution gradients [105, 110, 132].

- **Alternative interfacial capturing schemes**

The VOF method was used throughout this thesis to capture and track the polymer-polymer interface. Alternative interfacial capturing and tracking techniques have been used to previously to model polymer coextrusion. Such methods include: the level set approach [28, 90, 129], the mapping method [8, 59] and mesh partitioning [49, 50, 98]. If these three approaches were applied to the geometries and polymers modelled here, this would allow for a direct comparison with the VOF method. It could also be tested whether these interfacial capturing methods yield clear edges. Another option for future study would be to investigate a combination of VOF and Youngs' PLIC approach [120] and compare with the VOF based results in this thesis.

- **Improving the CFD convergence times**

For the numerical simulations presented in this thesis, convergence times were often very long; a runtime of around seven days was required for certain cases. These long simulation times were mainly due to the "flushing out" of the primary polymer melt from the geometry walls with the secondary polymer, both melt flows having a high viscosity. Methods to improve convergence times could be explored. In particular, a set of initial conditions which would position the correct polymer (primary and secondary layers) on each wall to improve the flushing out and hence convergence times should be attempted.

- **Novel technology**

Work in this thesis has focussed on using CFD to produce AB and ABA PET based MLFs via both the injector block and MMD approaches. Developing this study on melt flows to model more complex MLFs is suggested. This would allow DTF to further test the capabilities of STAR-CCM+. Potential areas of study include: combining the injector block and MMD geometries to produce ABCBA MLFs, modelling PEN rheology and

MLFs and simulating the layer multiplication approach (first patented by Tollar in [69]) to produce MLFs with hundreds of sub-micron thin layers.

- **Further film process studies**

CFD was used to model polymer melt flows within the MLF production process. This represents only a small part of the polyester film production process and work could be done to model further aspects. Potential areas of the process to investigate with CFD include: polymer extrusion, film coating and air flow during both casting and stretching of the film.

- **Extending the work on thermoviscous control**

Curves were derived to represent a full set of die bolt heaters spanning both pilot and production scale MMDs. There is scope to extend this work and model both pilot and production scale end fed die geometries. If heater curves were assigned to every DTF coextrusion geometry, the company could use CFD to predict the final film thickness and layer compatibility for different polymer melts and heater settings before attempting a trial. This work would also benefit from the solution of the conductive heating of the metal die lip from the cartridge pencil heaters used (see Figure A.1).

8.3 Business impact

Work in this thesis has significantly improved DTF's understanding of MLF processing. The predictive numerical models developed here have been used to successfully predict the outcome of both pilot and production scale trials. An example of this is shown in Section 7.4, where the CFD data obtained was used to improve the final film edge profiles and maintain a sustainable process via thermoviscous control. On a pilot scale, DTF's die bolt heaters have been reduced in power based on numerical interpretation of a template geometry (see Section 7.2), greatly improving the profile control of this line. Prior to commencing this project, WLI had never been used at DTF to measure individual

layer thicknesses of an MLF. Since its successful implementation for this purpose (Section 6.3.2.2), WLI has been utilised for MLF characterisation and this will continue in the future.

With MLFs increasing in complexity, the models developed here will be used to predict the compatibility of different melt layers in potential new products. This will reduce the need for film trials, hence saving DTF considerable time and money. CFD will be used to design new and more complex coextrusion geometries such as wider injector blocks and MMDs with five inlet channels. DTF have retained their STAR-CCM+ licence for further use, and it is envisaged that this will be used to model the full film process in greater detail, see Section 8.2. Work on this is ongoing and STAR-CCM+ has been used to redesign a production scale coating head geometry.

Appendix A

Modelling die bolt heaters using Computational Fluid Dynamics

This Chapter outlines the background theory and methods when using CFD to model a full set of die bolt heaters in Chapter 7.

A.1 Die bolt heaters

DTF use die bolt heaters to improve the film thickness uniformity. Such heaters are used on both pilot and production scale dies and are bolted to the internal metalwork of the die land (see Figure 2.12). Die bolt heaters span the land width from FE to BE on both the air side (AS) and drum side (DS). On a die, the heaters are offset rather than opposite each other on both sides. For each side of the land on a standard die, there is typically 45-50 mm space between individual heaters, where this is reduced to 25-30 mm for high-resolution dies.

Die bolt heaters can operate in manual, automatic or a combination of both. Heaters are commonly used to ameliorate the film edges, where thick or thin edges are caused by wide melt viscosity differences (see Figure 5.20a for example). Increasing the power and hence temperature of a single heater causes a localised film thickness increase, due to a reduction in melt viscosity here. A general rule of thumb applied at DTF is that a 10 %

increase in heater power causes a 2 % film thickness increase here. Typically each heater has a power of 150 W and for all heaters across a die, an operating mean of 40 % power is maintained. This means that when the power of a single heater is increased, other heaters decrease in power to give this 40 % average.

Figure A.1 shows a CFD approximation of the temperature variation around a single die bolt heater for a given polymer flow rate down the lip. The region marked *die lip* is the section that heats the die walls in contact with the polymer melt. Here, a maximum temperature of 337 °C is observed at the land. The die lip can reach temperatures up to 400 °C when higher powered heaters are used or the flow rate is reduced.

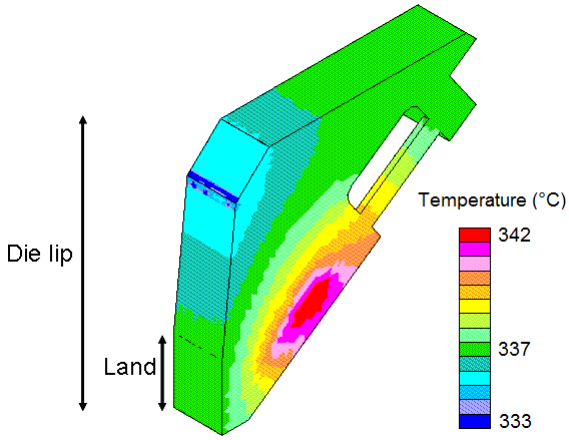

Figure A.1: A CFD approximation of the temperature of a die bolt heater. Diagram obtained from the DTF database.

A.2 Computational Fluid Dynamics modelling of die bolt heaters

This Section outlines how CFD is used to accurately represent a full set of die bolt heaters spanning the land width on both the AS and DS. The aim of this work is to prescribe varying land temperature boundary conditions that represent a complete set of die bolt heaters. These land temperature profiles will be a function of flow rate. *The background work shown here was conducted with the assistance of Richard Maltby, DTF Placement*

Student, 2012-13.

To gauge how to represent a single die bolt heater numerically, experimental results were considered. For a pilot scale high-resolution die, Figure A.2 shows the impact of increasing the power of Heater 11 by 20 %. This power increase causes a maximum profile variation of 10 %, significantly higher than the rule of thumb. Production scale dies are much closer to the rule of thumb because they have a greater flow per unit width and thus the local temperature rise for a given heater power is smaller.

From Figure A.2, increasing the power of a single heater causes a film thickness increase across three heater positions either side of Heater 11. For this particular die, the distance between two heaters is 16 mm (or 32 mm when considering heaters on the same side of the land). The curve for Heater 11 spans a distance of 96 mm. It is therefore assumed throughout that the width of a single heater curve is 96 mm.

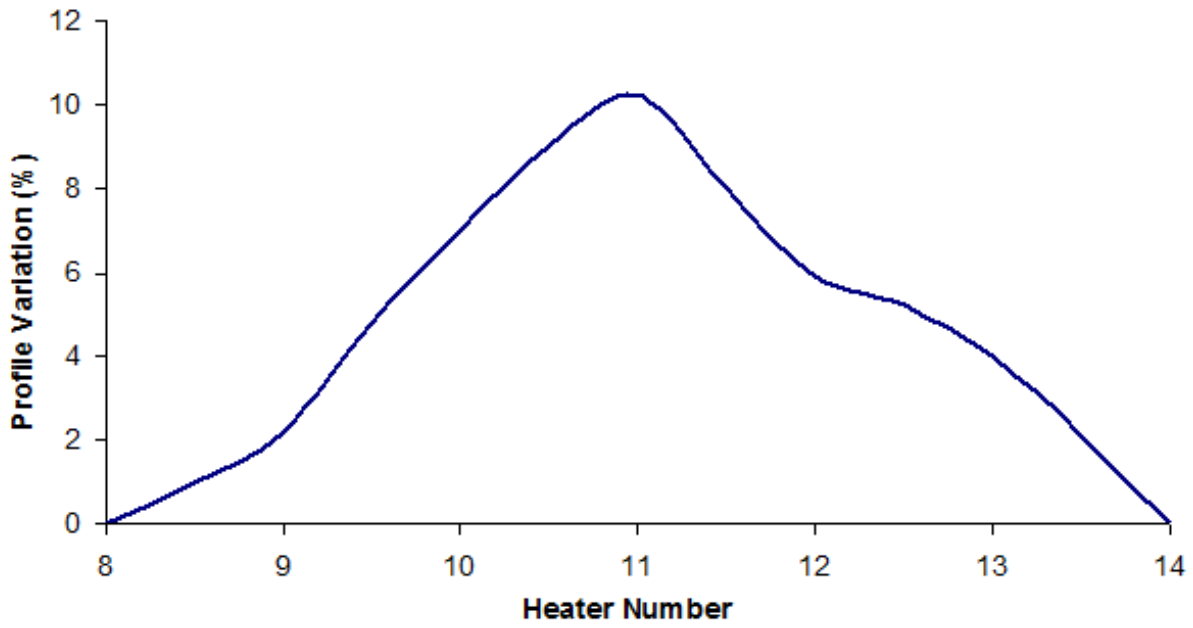

Figure A.2: The effect of increasing the power of Heater 11 by 20 %. Experimental work conducted by Ian Alexander, DuPont Teijin Films.

To represent an individual heater curve in CFD, a sinusoidal curve was derived to fit the curve showing a 20 % increase in power in Figure A.2. This curve is displayed in Figure A.3, where the skewed fit to the right of Heater 11 is attributed to experimental

error and is ignored here. The graph in Figure A.3 was converted into a wall temperature-position curve for 100 % heater power, see Figure A.4. There is a maximum land wall temperature of 508.1 °C at the heater location (in this case 48 mm across the land width). This value of 508.1 °C is found from coupling the result in Figure A.2 with numerical and experimental work conducted by Simon Hill (DTF Placement Student, 2002-03), who predicted this temperature at 100 % heater power. A minimum temperature of 285 °C is found ± 48 mm from the heater. This assumption is maintained throughout; the minimum land temperature when modelling die bolt heaters in CFD is 285 °C.

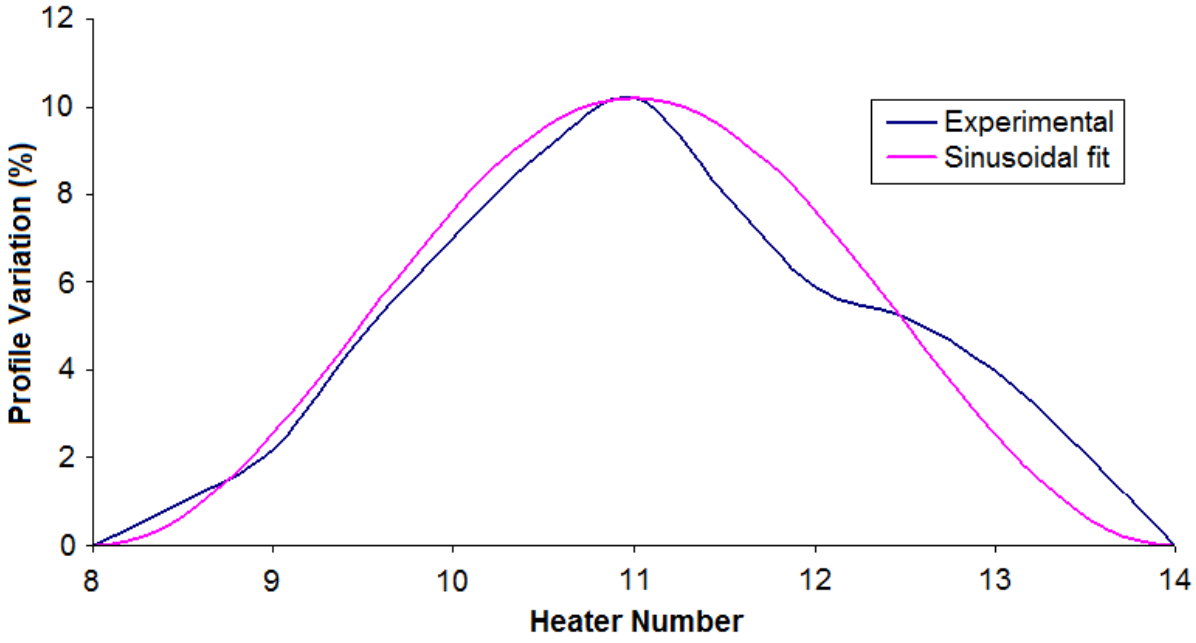

Figure A.3: The sinusoidal fit to the experimental heater curve.

Generalising the curve in Figure A.4 for any position across the land, the wall temperature equation for a heater operating at 100 % power is:

$$T_{\mathrm{w,\ 100\ \%}} = 111.55 \cos\left[\frac{2\pi}{0.096}\left(z - z_{\mathrm{h}}\right)\right] + 396.55, \tag{A.1}$$

where $T_{\mathrm{w,\ 100\ \%}}$ is the land wall temperature for 100 % heater power, z is any position across the land width (measured in m) and z_{h} is the position of an individual die bolt heater. To maintain the assumed 96 mm span for an individual heater, Equation A.1 is only valid for z within 48 mm either side of a heater position, or $z_{\mathrm{h}} - 0.048 \leqslant z \leqslant z_{\mathrm{h}} + 0.048$.

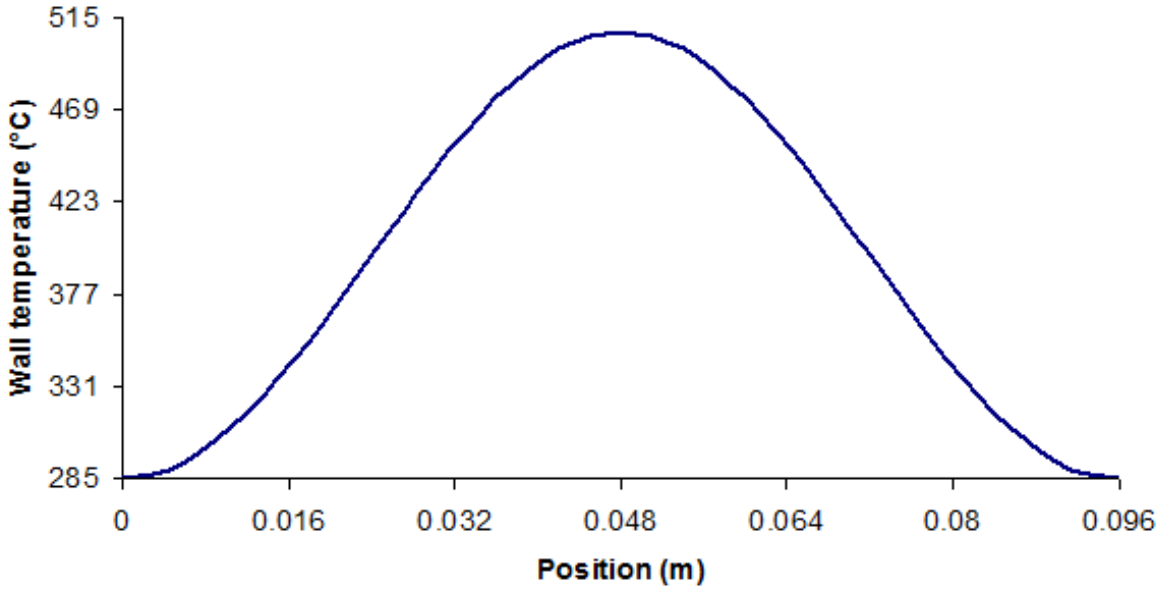

Figure A.4: A 100 % heater curve.

The term in square brackets is in radians and the constants 111.55 and 396.55 were found from trial and error, with the latter constant ensuring a minimum land temperature of 285 °C.

Die bolt heaters never operate at their maximum power and scaling of Equation A.1 is required. Previous CFD and experimental work by Simon Hill has shown that there is a non-linear relationship between wall temperature and heater power. Therefore, to obtain a 50 % heater curve, it does not suffice to halve Equation A.1. The *multiplication factor* (*MF*) is introduced because of this non-linear relationship. The dimensionless *MF* is defined as the ratio between the wall temperature at a desired heater power and the maximum temperature at 100 % power, or:

$$MF = \frac{T_{\mathrm{w},\,P\,\%} - 285}{T_{\mathrm{w},\,\mathrm{max}} - 285}, \tag{A.2}$$

subtracting the base temperature of 285 °C from both the numerator and denominator.

Using the relationship in Equation A.2, *MF* is plotted against percentage heater power P in Figure A.5, based on 2D CFD work and experimental validation by Simon Hill. Hill used a model geometry to represent a DTF production scale die and predicted the non-linear relationship between wall temperature and heater power, evident in Figure A.5.

The equation of the curve in Figure A.5 is:

$$MF = \text{-}0.000012P^2 + 0.0111977P, \tag{A.3}$$

which is used throughout. Using Equation A.3, a 50 % heater power requires an MF of 0.53, and this coefficient would be used.

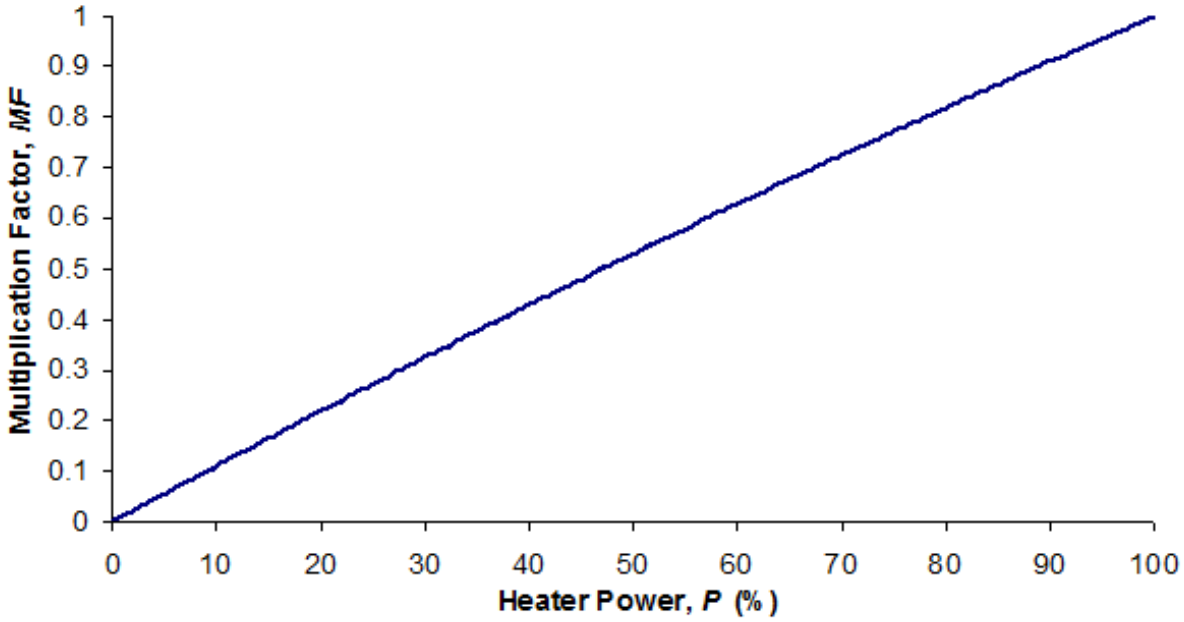

Figure A.5: How the multiplication factor changes with increasing heater power. This correlation is based on CFD work by Simon Hill, DuPont Teijin Films Placement Student, 2002-03.

It is assumed that Equation A.1 is the 100 % heater curve equation for both pilot and production scale dies. However, the work used to calculate MF in Equation A.3 was based on a DTF production die at prescribed inlet conditions; Hill modelled a single polymer with IV = 0.6 and a melt temperature of 285 °C, flowing through a model geometry with a 20 mm land length at 3,200 kg hr^{-1} (scaled down accordingly). The rate of heat transfer, Q_{h}, from the die land to the polymer is given as [165]:

$$Q_{\mathrm{h}} = hA\Delta T, \tag{A.4}$$

where h is the heat transfer coefficient and A is the area available for heat transfer. Since $h \propto v^{\mathrm{n}}$ (flow rate variation [166]), any change in $\dot{m}$ from the original conditions used

to obtain MF will skew the results, using Equation A.4. Furthermore, the heat transfer curves span the land width and are the temperature conditions used to heat the incoming polymer melt flows. A depends on the land length, die width and die bolt heater spacings and any geometrical modifications will also alter the MF results.

A *flow factor* (FF) is introduced which allows any polymer properties and die geometries to be modelled whilst retaining the original MF correlation in Equation A.3. The FF incorporates both h and A into Equation A.4, and once calculated $Q_{\mathrm{h}} \propto \Delta T$ (thermal variation). Once obtained, the FF only holds for the particular mass flow rate and die geometry used in the calculation. Any changes in either requires re-calculation of FF.

For any die geometry and desired polymer properties, the procedure for calculating FF is as follows:

- Select $FF = 1$;
- Have every heater within the die to be 100 % efficient and operating at 40 % power. Import the resulting summed heater curves (see later) as land temperature conditions for both the AS and DS;
- Using the desired polymer properties and conditions, run a "base case" CFD simulation;
- Once the simulation has fully converged, generate both velocity and temperature line integral outlet plots across the die width;
- Use the outlet plots and a spreadsheet to calculate the total heat transferred to the melt, Q_{h}. This calculation is based on [165]:

$$Q_{\mathrm{h}} = \dot{m} c_{\mathrm{p}} \Delta T, \tag{A.5}$$

  where c_{p} is the specific heat capacity (units are J kg^{-1} $^{\circ}$C^{-1}). For PET melt flows, $c_{\mathrm{p}} = 1,060 + 1.72(T + 273)$;

- Calculate the total theoretical power supplied to the heaters within the die, Q'_{h}:

$$Q'_{\mathrm{h}} = 150 \times 0.4 \times N = 60N, \tag{A.6}$$

assuming N 150 W heaters, all operating at 40 % power;

- Compare Q_{h} with Q'_{h} to calculate the new FF:

$$FF = \frac{Q'_{\mathrm{h}}}{Q_{\mathrm{h}}}. \tag{A.7}$$

At a desired heater power, the equation for an individual wall temperature (T_{w}) curve is given as:

$$T_{\mathrm{w}} = [0.9 \times FF \times MF \times (T_{\mathrm{w,\ 100\ \%}} - 285)] + 285, \tag{A.8}$$

guaranteeing a minimum land temperature of 285 °C. In Equation A.8, FF is calculated from Equation A.7, MF from Equation A.3 and $T_{\mathrm{w,\ 100\ \%}}$ from Equation A.1. The 0.9 coefficient in Equation A.8 represents a 90 % heater efficiency, with 10 % of heater power assumed to be lost to the surroundings. The heater efficiency can be changed by altering the 0.9 value, but the 90 % assumption is maintained throughout this thesis. Equation A.8 allows the calculation of a single heater curve for any percentage power.

To model a full set of die bolt heaters on a DTF die, a curve for each heater at a prescribed power, based on Equation A.8, is required. The curves span the land width on both the AS and DS from FE to BE, with peaks at the heater location. As mentioned in Section A.1, the space between two land heaters is around 45 mm on a standard die. Since each curve spans 96 mm, there is an overlap of heater curves across the land width (see Figure A.6), and at certain locations, several heater curves may be present.

To consider this overlap, the contributing temperature resulting from each curve (shown in square brackets in Equation A.8) across one side of the land is summed from FE to BE in increments of 1 mm. After adding each summed value to the base temperature of 285 °C, this yields a total temperature profile across the land width. This procedure is then repeated on the other side of the land, with a second temperature profile obtained. The resulting profiles are then imported into STAR-CCM+ and used as land temperature conditions for both the AS and DS.

For a modelled 135 mm wide template die geometry (see Section 7.2), heaters were set at 0, 45, 90 and 135 mm across the AS land, and at 22.5, 67.5 and 112.5 mm across the DS. Figure A.6 shows the individual heater curves and the resulting summed land

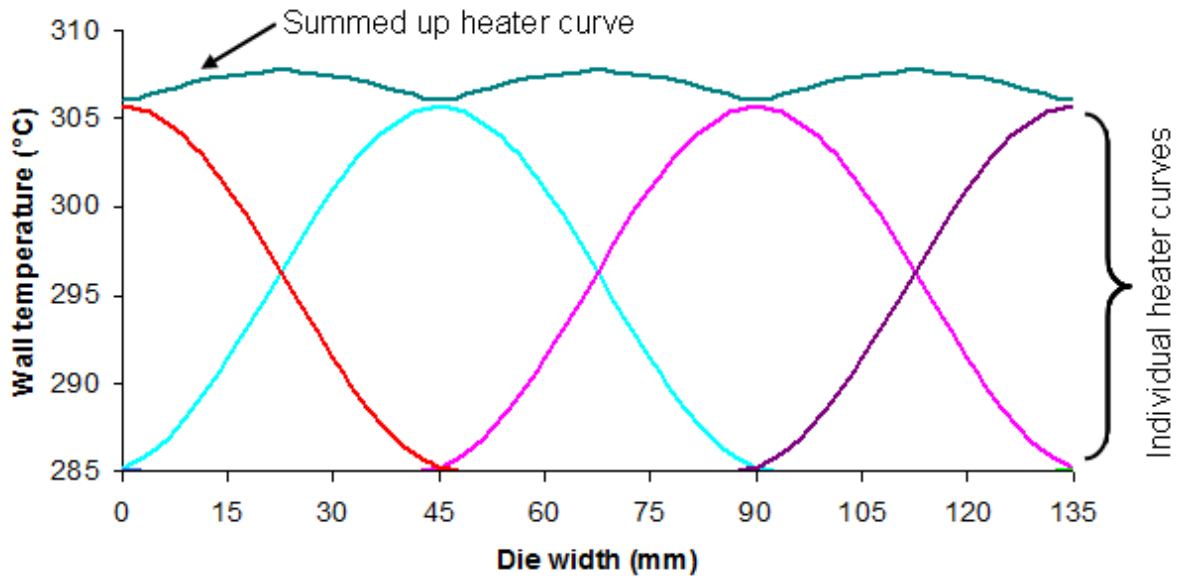

(a)

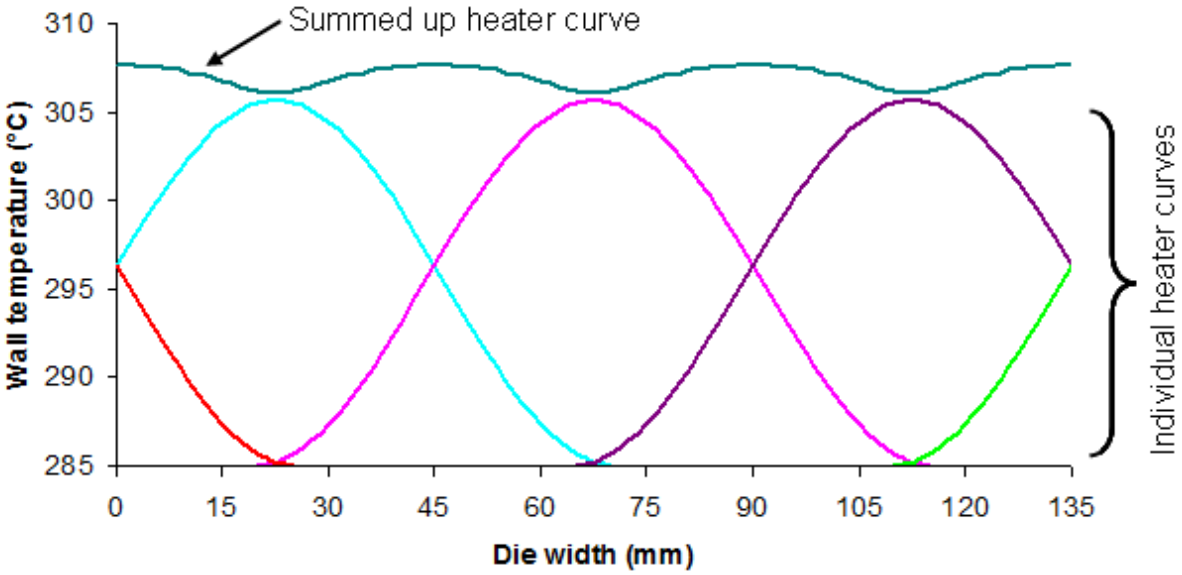

(b)

Figure A.6: The concept of summing up land heater curves on a 135 mm wide template geometry for (a) the air side (AS) and (b) the drum side (DS).

temperature profiles for both the AS (Figure A.6a) and DS (Figure A.6b). Here, every heater is set to 40 % operating power and $FF = 0.24$. This geometry is designed to be a fraction of a pilot scale MMD, with the effect of heaters outside the 135 mm domain also

considered due to the predicted 96 mm span.

The resulting summed heater curves from Figure A.6 are then set as land temperature conditions for both the AS and DS, representing a full set of die bolt heaters. For the die walls except at the land, the temperature is taken to be *constant* and independent of the final land temperature profiles. For this 135 mm wide geometry, the maximum land temperature on both sides is between two heaters rather than at a heater location. This is due to the summing of heaters spanning 96 mm, but placed 45 mm apart. For the 100 % heater curve (see Figure A.4), the maximum temperature is 508.1 °C. When summed with another curve, this increases to 529.9 °C, assuming a land heater spacing of 45 mm.

It is assumed that the heaters on one side do not effect heaters on the other side of the land. Such heater curves shown in Figure A.6 can be extended to wider geometries and varying heater powers, demonstrated in Chapter 7. When modelling geometries wider than 135 mm, more curves are required to represent the greater quantity of heaters.

References

[1] `www.dupontteijinfilms.com`. Page viewed: 27 June 2013.

[2] *Introduction to DuPont Teijin Films' Business Market and Products*. DuPont Teijin Films, 2014.

[3] `www.dupont.com`. Page viewed: 20 June 2013.

[4] `www.teijin.co.jp`. Page viewed: 22 July 2014.

[5] *DuPont Teijin Films: Formulating Success Together*. DuPont Teijin Films, 2014.

[6] `http://europe.dupontteijinfilms.com/markets-and-applications.aspx`. Page viewed: 22 July 2014.

[7] D. W. Brooks and G. A. Giles, *PET Packaging Technology*. Sheffield Academic Press, 2002. ISBN 0-84127-222-1.

[8] J. Dooley, *Viscoelastic Flow Effects in Multilayer Polymer Coextrusion*. PhD thesis, Technische Universiteit Eindhoven, 2002.

[9] D. Djordjevic, "Coextrusion," *Rapra Review Reports*, vol. 6, no. 2, pp. 1–150, 1992. ISBN 0-9023448-71-X.

[10] M. T. Martyn, R. Spares, P. D. Coates, and M. Zatloukal, "Imaging and analysis of wave type interfacial instability in the coextrusion of low-density polyethylene melts," *Journal of Non-Newtonian Fluid Mechanics*, vol. 156, pp. 150–164, 2009.

[11] C. Rauwendaal, *Polymer Extrusion*. Hanser Gardner Publications; 4$^{\text{th}}$ edition, 2001. ISBN 978-1569903216.

[12] C. W. Hirt and B. D. Nichols, "Volume of Fluid (VOF) Method for the Dynamics of Free Boundaries," *Journal of Computational Physics*, vol. 39, pp. 201–225, 1981.

[13] J. Dooley and K. Hughes, "Coextrusion Layer Thickness Variation - Effect of Polymer Viscoelasticity on Layer Uniformity," *Polymers, Laminations & Coatings Conference*, pp. 85–90, 1995.

[14] C. D. Han, *Rheology and Processing of Polymeric Materials, Volume 2: Polymer Processing*. Oxford University Press, 2007. ISBN 978-0-19-518782-3.

[15] C. D. Han and R. Shetty, "Studies on Multilayer Film Coextrusion I. The Rheology of Flat Film Coextrusion," *Polymer Engineering and Science*, vol. 16, no. 10, pp. 697–705, 1976.

[16] R. S. Lenk, *Polymer Rheology*. Applied Science Publishers Ltd, 1978. ISBN 0-85334-765-4.

[17] M. Zatloukal, J. Perdikoulias, C. Tzoganakis, and P. Sáha, "The Influence of Die Design and Extensional Rheology On the Onset of 'Wave' Interfacial Instabilities in Coextrusion flows," *TAPPI PLACE Conference*, 2001.

[18] M. Zatloukal, J. Vlček, C. Tzoganakis, and P. Sáha, "Viscoelastic Stress Calculation in Multi-Layer Coextrusion Dies: Die Design and Extensional Viscosity Effects On the Onset of 'Wave' Interfacial Instabilities," *Polymer Engineering and Science*, vol. 42, no. 7, pp. 1520–1533, 2002.

[19] R. H. Beck, *Extrusion apparatus and processes of extruding*. US Patent, May 1955. Patent number 2,901,770.

[20] D. Chisholm and W. J. Schrenk, *Method of Extruding Laminates*. US Patent, January 1971. Patent number 3,557,265.

[21] `www.dow.com`. Page viewed: 20 June 2013.

[22] J. H. Southern and R. L. Ballman, "Stratified Bicomponent Flow of Polymer Melts in a Tube," *Applied Polymer Science*, no. 20, pp. 175–189, 1973.

[23] J. H. Southern and R. L. Ballman, "Additional Observations on Stratified Bicomponent Flow of Polymer Melts in a Tube," *Journal of Polymer Science*, vol. 13, pp. 863–869, 1975.

[24] C. D. Han, "A Study of Bicomponent Coextrusion of Molten Polymers," *Journal of Polymer Science*, vol. 17, pp. 1289–1303, 1973.

[25] B.-L. Lee and J. L. White, "An Experimental Study of Rheological Properties of Polymer Melts in Laminar Shear Flow and of Interface Deformation and Its Mechanisms in Two-Phase Stratified Flow," *Transactions of The Society of Rheology*, vol. 18, no. 3, pp. 467–492, 1974.

[26] C. D. Han and R. Shetty, "Studies on Multilayer Film Coextrusion II. Interfacial Instability in Flat Film Coextrusion," *Polymer Engineering and Science*, vol. 18, no. 3, pp. 180–186, 1978.

[27] W. J. Schrenk, N. L. Bradley, T. Alfrey, Jr, and H. Maack, "Interfacial Flow Instability in Multilayer Coextrusion," *Polymer Engineering and Science*, vol. 18, no. 8, pp. 620–623, 1978.

[28] P. Yue, C. Zhou, J. Dooley, and J. J. Feng, "Elastic encapsulation in bicomponent stratified flow of viscoelastic fluids," *Journal of Rheology*, vol. 52, no. 4, pp. 1027–1042, 2008.

[29] G. Oliver, "Coextrusion Short Course," *TAPPI*, 2010. Website: `www.tappi.org/content/events/10EXTRU/papers/3.3.pdf`. Page viewed: 12 September 2013.

[30] T. I. Butler, "Effects of flow instability in coextruded films," *TAPPI JOURNAL*, vol. 9, pp. 205–211, 1992.

[31] H. Helmy, "Recent Developments in Flat Film and Sheet Dies," *Journal of Plastic Film and Sheeting*, vol. 4, pp. 193–213, 1987.

[32] www.cd-adapco.com. Page viewed: 11 November 2013.

[33] J. Champion, M. K. Looney, and M. J. H. Simmons, "Using Computational Fluid Dynamics (CFD) to analyse the limits of the secondary layer thickness in multi-layered polyester film processes," *TAPPI PLACE Europe Conference*, 2013.

[34] E. A. Grulke, *Polymer Process Engineering*. Prentice Hall, 1994. ISBN 0-13-015397-4.

[35] J. Vlachopoulos and D. Strutt, "The Role of Rheology in Polymer Extrusion," website: www.polydynamics.com/Rheology.pdf. Page viewed: 13 September 2013.

[36] R. Greenwood, *Lecture notes on Colloidal Chemistry and Rheology*. University of Birmingham, October 2012.

[37] R. M. M. Mallens and C. J. Waringa, "Investigation of Layer Thickness Distribution During Co-Extrusion with Generalized Newtonian and Visco-Elastic Flow Models," *TAPPI PLACE Division Conference*, pp. 32–49, 2004.

[38] O. Mahdaoui, P. Laure, and J.-F. Agassant, "Numerical investigations of polyester coextrusion instabilities," *Journal of Non-Newtonian Fluid Mechanics*, vol. 195, pp. 67–76, 2013.

[39] L. C. Mendes, P. S. C. Pereira, and V. D. Ramos, "Effectiveness of the Transesterification Catalyst on the Thermal, Dynamic-Mechanical and Rheological Properties of PET/PC Reactive Melting Blends," *Macromolecular Symposia*, vol. 299/300, pp. 183–189, 2011.

[40] V. Tanrattanakul, A. Hiltner, E. Baer, W. G. Perkins, F. L. Massey, and A. Moet, "Effect of elastomer functionality on toughened PET," *Polymer*, vol. 38, no. 16, pp. 4117–4125, 1997.

[41] G. Fortunato, A. Tenniche, L. Gottardo, and R. Hufenus, "Development of poly-(ethylene terephthalate) masterbatches incorporating highly dispersed TiO_2

nanoparticles: Investigation of morphologies by optical and rheological procedures," *European Polymer Journal*, vol. 57, pp. 75–82, 2014.

[42] `www.intertek.com`. Page viewed: 8 July 2013.

[43] J. Dooley, "Determining the Processability of Multilayer Coextruded Structures," *TAPPI PLACE Conference*, 2007.

[44] O. Prakash, "Defects in multilayer plastic films I: Interface defects in extrusion," *Computational Materials Science*, vol. 37, pp. 7–11, 2006.

[45] `www.metal.ntua.gr/uploads/3798/1032/D10_v2.pdf`. Page viewed: 10 July 2013.

[46] J. Dooley, H. Kim, P. C. Lee, and R. Wrisley, "The Effect of Coathanger Die Manifold Symmetry on Layer Uniformity in Multilayer Coextrusion," *ANTEC*, vol. 59, pp. 994–1000, 2013.

[47] Y. Huang, C. R. Gentle, and J. B. Hull, "A Comprehensive 3-D Analysis of Polymer Melt Flow in Slit Extrusion Dies," *Advances in Polymer Technology*, vol. 23, no. 2, pp. 111–124, 2004.

[48] A. Rincon, J. Ulcej, and D. Pitsch, "Analysis of Polymer Flow in a 3-Layer Coextrusion Feed Block with an Adjustable Geometry," *TAPPI PLACE Conference*, 2002.

[49] M. Gupta, "Three Dimensional Simulation of Coextrusion in a Complex Profile Die," *ANTEC*, vol. 56, pp. 2030–2036, 2010.

[50] M. Gupta, "Effect of Polymer Viscosity on Post-Die Extrudate Shape Change in Coextruded Profiles," *ANTEC*, vol. 58, 2012.

[51] R. B. Bird, W. E. Stewart, and E. N. Lightfoot, *Transport Phenomena*. Wiley, 1960.

[52] `http://composite.about.com/library/glossary/v/bldef-v5954.htm`. Page viewed: 18 July 2013.

[53] Davenport, "Melt Viscometer User Manual," 1998.

[54] O. Catherine, "Advances in shear rheology and flow simulation for high performance extrusion die design," *TAPPI PLACE Europe Conference*, 2013.

[55] J. Bowen, *Lecture notes on Colloidal Chemistry and Rheology*. University of Birmingham, October 2012.

[56] G. Oliver, "An Introduction to Coextrusion Systems," *TAPPI PLACE Conference*, 2002.

[57] M. T. Martyn, *Lecture notes on Flow Behaviour of Polymer Melts*. University of Bradford, May 2013.

[58] A. Karagiannis, A. N. Hrymak, and J. Vlachopoulos, "Three-dimensional studies on bicomponent extrusion," *Rheologica Acta*, vol. 29, pp. 71–87, 1990.

[59] P. D. Anderson, J. Dooley, and H. E. H. Meijer, "Viscoelastic Effects in Multilayer Polymer Extrusion," *Applied Rheology*, vol. 16, pp. 198–205, 2006.

[60] B. Debbaut, T. Avalosse, J. Dooley, and K. Hughes, "On the development of secondary motions in straight channels induced by the second normal stress difference: experiments and simulations," *Journal of Non-Newtonian Fluid Mechanics*, vol. 69, pp. 255–271, 1997.

[61] K. Matsunaga, T. Kajiwara, and K. Funatsu, "Numerical Simulation of Multi-Layer Flow for Polymer Melts - A Study of the Effect of Viscoelasticity on Interface Shape of Polymers Within Dies," *Polymer Engineering and Science*, vol. 38, no. 7, pp. 1099–1111, 1998.

[62] K. B. Sunwoo, S. J. Park, S. J. Lee, K. H. Ahn, and S. J. Lee, "Three-dimensional numerical simulation of nonisothermal coextrusion process with generalized Newtonian fluids," *Korea-Australia Rheology Journal*, vol. 12, no. 3/4, pp. 165–173, 2000.

[63] K. B. Sunwoo, S. J. Park, S. J. Lee, K. H. Ahn, and S. J. Lee, "Numerical simulation of three-dimensional viscoelastic flow using the open boundary condition method in coextrusion process," *Journal of Non-Newtonian Fluid Mechanics*, vol. 99, pp. 125–144, 2001.

[64] S. J. Park, K. H. Ahn, and S. J. Lee, "Numerical simulation of coextrusion process of viscoelastic fluids using the open boundary condition method," *Korea-Australia Rheology Journal*, vol. 13, no. 1, pp. 37–45, 2001.

[65] `www.extrusiondies.com`. Page viewed: 12 September 2013.

[66] `www.cloeren.com`. Page viewed: 12 September 2013.

[67] A. Blin and J. Miethlinger, "Raw Material Selection for Coextrusion - Practical Experience of the Machinery Supplier," *TAPPI PLACE Conference*, 2003.

[68] G. D. Oliver, "Micro-layer Coextrusion Methods and Applications," *TAPPI PLACE Conference*, 2012.

[69] J. E. Tollar, *Interfacial Surface Generator*. US Patent, March 1966. Patent number 3,239,197.

[70] T. Oya, M. Ono, and T. Yoshida, *Uniaxially stretched multilayer laminate film and uniaxially stretched multilayer laminate film laminate comprising the same*. Japanese Patent, May 2012. Patent number JP2012088613A.

[71] T. Oya, M. Ono, and Y. Tetsuo, *Uniaxially stretched multilayer laminated film*. Japanese Patent, December 2012. Patent number JP2012237853A.

[72] T. Oya, M. Ono, and T. Yoshida, *Uniaxially oriented multi-layer laminate film*. Japanese Patent, April 2013. Patent number WO2013057845A1.

[73] H. Helmy, "Aspects of the Design of Coathanger Dies for Cast Film and Sheet Applications," *Advances in Polymer Technology*, vol. 7, no. 1, pp. 59–69, 1987.

[74] M. L. Clifford, "The Design of Melinex dies." An internal, unpublished Imperial Chemical Industries document, November 1989.

[75] J. Vlcek, G. N. Mailvaganam, J. Vlachopoulos, and J. Perdikoulias, "Computer Simulation and Experiments of Flow Distribution in Flat Sheet Dies," *Advances in Polymer Technology*, vol. 10, no. 4, pp. 309–322, 1990.

[76] M. M. Kostic and L. G. Reifschneider, "Design of Extrusion Dies," *Enyclopedia of Chemical Processing*, pp. 633–649, 2006.

[77] L. G. Reifschneider, M. M. Kostic, and S. R. Vaddiraju, "Computational Design of a U-Profile Die and Calibrator," *ANTEC*, pp. 246–250, 2004.

[78] P. C. Lee, L. Dietsche, J. Dooley, and S. Parashar, "Improving Film Die Flow Uniformity Using Optimization Methods Coupled with Finite Element CFD Analysis," 2011. Website: `http://www.esteco.it/modefrontier/improving-film-die-flow-uniformity-using-optimization-methods`. Page viewed: 19 September 2013.

[79] N. G. McCrum, C. P. Buckley, and C. B. Bucknall, *Principles of Polymer Engineering*. Oxford Science Publications; 2nd edition, 1997. ISBN 0-19-856526-7.

[80] J. H. Kim and M. Y. Lyu, "Predictions of Flow Behaviors and Entrance Pressure Drop Characteristics of a Rubber Compound in a Capillary Die Using Various Rheological Models," *Polymer Engineering and Science*, vol. 54, no. 10, pp. 2441–2448, 2014.

[81] W. A. Gifford, "Compensating for Die Swell in the Design of Profile Dies," *Polymer Engineering and Science*, vol. 43, no. 10, pp. 1657–1665, 2003.

[82] W. A. Gifford, "The Effect of Wall Slip on the Performance of Flat Extrusion Dies," *Polymer Engineering and Science*, vol. 41, no. 11, pp. 1886–1892, 2001.

[83] W. A. Gifford, "The Effect of Surface Tension on Extrudate Swell From Square and Rectangular Channels," *Polymer Engineering and Science*, vol. 38, no. 7, pp. 1167–1173, 1998.

[84] W. A. Gifford, "A Three-Dimensional Finite Element Analysis of the Effect of Reynolds Number on Extrudate Swell of Newtonian Liquids from Square Dies," *The Canadian Journal of Chemical Engineering*, vol. 71, pp. 161–167, 1993.

[85] N. Minagawa and J. L. White, "Co-Extrusion of Unfilled and TiO_2-Filled Polyethylene: Influence of Viscosity and Die Cross-Section on Interface Shape," *Polymer Engineering and Science*, vol. 15, no. 12, pp. 825–830, 1975.

[86] D. L. MacLean, "A Theoretical Analysis of Bicomponent Flow and the Problem of Interface Shape," *Transactions of the Society of Rheology*, vol. 17, no. 3, pp. 385–399, 1973.

[87] A. E. Everage, Jr, "Theory of Stratified Bicomponent Flow of Polymer Melts. I. Equilibrium Newtonian Tube Flow," *Transactions of the Society of Rheology*, vol. 17, no. 4, pp. 629–646, 1973.

[88] M. C. Williams, "Migration of Two Liquid Phases in Capillary Extrusion: An Energy Interpretation," *American Institute of Chemical Engineering*, vol. 21, no. 6, pp. 1204–1207, 1975.

[89] J. Dooley and L. Rudolph, "Viscous and Elastic Effects in Polymer Coextrusion," *TAPPI PLACE Conference*, 2002.

[90] D. Borzacchiello, E. Leriche, B. Blottière, and J. Guillet, "On the mechanism of viscoelastic encapsulation of fluid layers in polymer coextrusion," *Journal of Rheology*, vol. 58, no. 2, pp. 493–512, 2014.

[91] J. Dooley, "The Effect of Multilayer Rheology on Coextrusion Die Design," *TAPPI PLACE Conference*, 2004.

[92] J. Dooley, C. Costeux, R. Wrisley, and A. Schlader, "Multilayer Rheology Effects In Coextruded Structure Design," *TAPPI PLACE Conference*, 2008.

[93] G. Sornberger, B. Vergnes, and J. F. Agassant, "Two Directional Coextrusion Flow of Two Molten Polymer in Flat Dies," *Polymer Engineering and Science*, vol. 26, no. 7, pp. 455–461, 1986.

[94] A. Karagiannis, H. Mavridis, A. N. Hrymak, and J. Vlachopoulos, "Interface Determination in Bicomponent Extrusion," *Polymer Engineering and Science*, vol. 28, no. 15, pp. 982–988, 1988.

[95] W. A. Gifford, "A Three-Dimensional Analysis of Coextrusion," *Polymer Engineering and Science*, vol. 37, no. 2, pp. 315–320, 1997.

[96] H. Mavridis, A. N. Hrymak, and J. Vlachopoulos, "Finite-Element Simulation of Stratified Multiphase Flows," *American Institute of Chemical Engineering*, vol. 33, no. 3, pp. 410–422, 1987.

[97] A. Torres, A. N. Hrymak, J. Vlachopoulos, J. Dooley, and B. T. Hilton, "Boundary conditions for contact lines in coextrusion flows," *Rheological Acta*, vol. 32, no. 6, pp. 513–525, 1993.

[98] M. Gupta, "Viscoelastic Simulation of Bi-layer Coextrusion in a Square Die: An Analysis of Viscous Encapsulation," *ANTEC*, vol. 59, pp. 1227–1231, 2013.

[99] B. G. M. Rijksen, B. A. Fehr, and K. Zuercher, "Coex Optimization with Rheology in Flat Die Extrusion," *TAPPI PLACE Europe Conference*, 2013.

[100] M. Zatloukal, W. Kopytko, A. Lengálová, and J. Vlček, "Theoretical and Experimental Analysis of Interfacial Instabilities in Coextrusion Flows," *Journal of Applied Polymer Science*, vol. 98, pp. 153–162, 2005.

[101] M. Zatloukal, M. Martyn, P. Coates, and J. Perdikoulias, "Theoretical and Experimental Investigation of Wave Interfacial Instabilities at Coextrusion in Flat Dies," *TAPPI PLACE Conference*, 2003.

[102] Y. Sun, M. Gupta, J. Dooley, K. A. Koppi, and M. A. Spalding, "Experimental and Numerical Investigation of the Elongational Viscosity Effects in a Coat-hanger Die," *ANTEC*, pp. 81–85, 2005.

[103] M. Zatloukal, A. Xue, and M. Amon, "Theoretical and Experimental Investigation of Interfacial Instabilities in Coextrusion Feed-block Dies," *ANTEC*, pp. 2023–2029, 2010.

[104] `http://www.leica-microsystems.com/products/light-microscopes/`. Page viewed: 4 December 2013.

[105] J. H. Ferziger and M. Perić, *Computational Methods for Fluid Dynamics*. Springer-Verlag; 3rd edition, 2002. ISBN 3-540-42074-6.

[106] R. Bhaskaran and L. Collins, "Introduction to CFD Basics," website: `http://dragonfly.tam.cornell.edu/teaching/mae5230-cfd-intro-notes.pdf`. Page viewed: 20 June 2011.

[107] CD-adapco, "STAR-CCM+ Training guide Version 01/11," handed out during a three day training course, June 2011.

[108] CD-adapco, "STAR-CCM+ inbuilt online support," page viewed: 16 December 2013.

[109] P. Wesseling, *Principles of Computational Fluid Dynamics*. Springer-Verlag; 3rd edition, 2001. ISBN 978-3642051456.

[110] A. Bakker, *Lecture notes on Computational Fluid Dynamics*. Dartmouth College, 2006. Website: `http://www.bakker.org/dartmouth06/engs150/`. Page viewed: 23 June 2011.

[111] M. Rudman, "Volume-Tracking Methods for Interfacial Flow Calculations," *International Journal for Numerical Methods in Fluids*, vol. 24, pp. 671–691, 1997.

[112] J. M. Hyman, "Numerical Methods for Tracking Interfaces," *Physica D*, vol. 12, pp. 396–407, 1984.

[113] M. Marek, W. Aniszewski, and A. Boguslawski, "Simplified Volume of Fluid (SVOF) for two-phase flows," *Task Quarterly*, vol. 12, no. 3, pp. 255–265, 2008.

[114] F. H. Harlow and J. E. Welch, "Numerical Calculation of Time-Dependent Viscous Incompressible Flow of Fluid with Free Surface," *The Physics of Fluids*, vol. 8, no. 12, pp. 2182–2189, 1965.

[115] S. McKee, M. F. Tomé, V. G. Ferreira, J. A. Cuminato, A. Castelo, F. S. Sousa, and N. Mangiavacchi, "The MAC method," *Computers and Fluids*, vol. 37, pp. 907–930, 2008.

[116] W. F. Noh and P. Woodward, "SLIC (Simple Linear Interface Calculation)," *Lecture notes in Physics*, vol. 59, pp. 330–340, 1976.

[117] J. C. Anderson, C. Garth, M. A. Duchaineau, and K. I. Joy, "Smooth, Volume-Accurate Material Interface Reconstruction," *Transactions on Visualisations and Computer Graphics*. Website: `www.idav.ucdavis.edu/~garth/pdfs/tvcg10a.pdf`. Page viewed: 16 December 2013.

[118] A. J. Chorin, "Flame Advection and Propagation Algorithms," *Journal of Computational Physics*, vol. 35, pp. 1–11, 1980.

[119] P. K. Barr and W. T. Ashurst, "An Interface Scheme for Turbulent Flame Propagation," *Sandia National Laboratories report SAND82-8773*, 1982.

[120] D. L. Youngs, "Time-dependent multi-material flow with large fluid distortion," *Numerical Methods for Fluid Dynamics, editors K. W. Morton and M. J. Baines*, pp. 273–285, 1982.

[121] X. Lv, Q. Zou, Y. Zhao, and D. Reeve, "A novel coupled level set and volume of fluid method for sharp interface capturing on 3D tetrahedral grids," *Journal of Computational Physics*, vol. 229, pp. 2573–2604, 2010.

[122] J. López, J. Hernández, P. Gómez, and F. Faura, "An improved PLIC-VOF method for tracking thin fluid structures in incompressible two-phase flows," *Journal of Computational Physics*, vol. 208, pp. 51–74, 2005.

[123] J. E. Pilliod, Jr and E. G. Puckett, "Second-order accurate volume-of-fluid algorithms for tracking material interfaces," *Journal of Computational Physics*, vol. 199, no. 2, pp. 465–502, 2004.

[124] V. Dyadechko and M. Shashkov, "Reconstruction of multi-material interfaces from moment data," *Journal of Computational Physics*, vol. 227, no. 11, pp. 5361–5384, 2008.

[125] S. P. Schofield, R. V. Garimella, M. M. Francois, and R. Loubère, "Material order-independent interface reconstruction using power diagrams," *International Journal for Numerical Methods in Fluids*, vol. 56, pp. 643–659, 2008.

[126] S. Osher and J. A. Sethian, "Fronts Propagating with Curvature Dependent Speed: Algorithms Based on Hamilton-Jacobi Formulations," *Journal of Computational Physics*, vol. 79, pp. 12–49, 1988.

[127] `http://math.berkeley.edu/~sethian/2006/Explanations/level_set_explain.html`. Page viewed: 18 December 2013.

[128] M. Gupta, "Comparison of Mesh Partitioning Technique with Level-Set Method for Coextrusion Simulation," *ANTEC*, vol. 60, pp. 1013–1020, 2014.

[129] Y. Zhang, Q. Zou, and D. Greaves, "Numerical simulation of free-surface flow using the level-set method with global mass correction," *International Journal for Numerical Methods in Fluids*, vol. 63, no. 6, pp. 651–680, 2010.

[130] P. Kruijt, *Analysis and optimization of laminar mixing: design, development and application of the mapping method*. PhD thesis, Technische Universiteit Eindhoven, 2000.

[131] O. S. Galaktionov, P. D. Anderson, G. W. M. Peters, and C. L. Tucker III, "A global, multi-scale simulation of laminar fluid mixing: the extended mapping method," *International Journal of Multiphase Flow*, vol. 28, no. 3, pp. 497–523, 2002.

[132] D. Apsley, *Lecture notes on Computational Hydraulics*. The University of Manchester, 2013. Website: `http://personalpages.manchester.ac.uk/staff/david.d.apsley/lectures/comphydr/index.htm`. Page viewed: 20 June 2013.

[133] S. V. Patankar and D. B. Spalding, "A calculation procedure for heat, mass and momentum transfer in three-dimensional parabolic flows," *International Journal of Heat and Mass Transfer*, vol. 15, no. 10, pp. 1787–1806, 1972.

[134] R. I. Issa, "Solution of the implicitly discretized fluid flow equations by operator-splitting," *Journal of Computational Physics*, vol. 62, no. 1, pp. 40–65, 1986.

[135] `http://www.phy.syr.edu/courses/PHY600.10Fall/Presentations/jorge.pdf`. Page viewed: 02 January 2014.

[136] `http://projects.exeter.ac.uk/fluidflow/Courses/ComputationalEng3213-4/slidesCFD/lecture3-slides.pdf`. Page viewed: 02 January 2014.

[137] S. D. Housley, Y. Khandhia, and U. Mullane, "The Application of the Computational Fluid Dynamics Code FIDAP to Melinex Coextrusion Lines 17, 24 and 46." An internal, unpublished Imperial Chemical Industries document, 1994.

[138] `http://science.howstuffworks.com/light-microscope1.htm`. Page viewed: 06 January 2014.

[139] Leica, "Leica DMR instructions manual," 1999.

[140] `http://www.nobelprize.org/educational/physics/microscopes/fluorescence/`. Page viewed: 07 January 2014.

[141] http://micro.magnet.fsu.edu/primer/techniques/fluorescence/fluorhome.html. Page viewed: 07 January 2014.

[142] https://www.sigmaaldrich.com/sigma-aldrich/home.html. Page viewed: 28 August 2014.

[143] http://cmi.epfl.ch/metrology/files/Wyko/Interferometery_Basics.pdf. Page viewed: 07 January 2014.

[144] Veeco, "WYKO Surface Profilers, Technical Reference Manual," September 1999.

[145] Veeco, "Introduction to the NT9080," April 2010.

[146] J. Wyant, "White Light Interferometry," website: http://optics.arizona.edu/jcwyant. Page viewed: 07 January 2014.

[147] H. A. Macleod, *Thin-Film Optical Filters*. Adam Hilger Ltd, 1969. ISBN 0-85274-091-3.

[148] O. S. Heavens, *Thin Film Physics*. Methuen & Co Ltd, 1970. ISBN 0-416-07650-5.

[149] O. S. Heavens, *Optical Properties of Thin Solid Films*. Dover Publications Inc, 1991. ISBN 0-486-66924-6.

[150] http://pages.cs.wisc.edu/~dyer/ah336/papers/01_reflection-refraction.pdf. Page viewed: 13 January 2014.

[151] https://www.phi.com/surface-analysis-techniques/tof-sims.html. Page viewed: 27 May 2014.

[152] J. C. Vickerman and D. Briggs, *TOF-SIMS: Material Analysis by Mass Spectrometry*. IM Publications LLP and Surface Spectra Limited; 2nd edition, 2013. ISBN 978-1-906715-17-5.

[153] http://www.ceac.ethz.ch/Nanoanalysis/PR_Benninghoven.ppt#269,37,Slide37. Page viewed: 28 August 2014.

[154] http://www.aps.org/units/fiap/meetings/presentations/upload/tompkins.pdf. Page viewed: 30 April 2015.

[155] http://www.eng.utah.edu/~lzang/images/Lecture_10_AFM.pdf. Page viewed: 30 April 2015.

[156] http://www.np.ph.bham.ac.uk/pic/. Page viewed: 30 April 2015.

[157] http://ocw.nthu.edu.tw/ocw/upload/2/111/Viscous%20Flow%20in%20Pipes.pdf. Page viewed: 30 April 2015.

[158] http://www.engr.uconn.edu/~wchiu/ME3250FluidDynamicsI/lecture%20notes/ch08.pdf. Page viewed: 20 May 2014.

[159] http://peltiertech.com/WordPress/loess-utility-awesome-update/. Page viewed: 21 May 2014.

[160] W. S. Cleveland, "Robust Locally Weighted Regression and Smoothing Scatterplots," *Journal of the American Statistical Association*, vol. 74, no. 368, pp. 829–836, 1979.

[161] W. S. Cleveland and S. J. Devlin, "Locally Weighted Regression: An Approach to Regression Analysis by Local Fitting," *Journal of the American Statistical Association*, vol. 83, no. 403, pp. 596–610, 1988.

[162] D. Silagy, Y. Demay, and J. F. Agassant, "Numerical simulation of the film casting process," *International Journal for Numerical Methods in Fluids*, vol. 30, no. 1, pp. 1–18, 1999.

[163] C. Sollogoub, Y. Demay, and J. F. Agassant, "Cast Film Problem: A Non Isothermal Investigation," *International Polymer Processing*, vol. 18, no. 1, pp. 80–86, 2003.

[164] E. Harkin-Jones, L. Figiel, P. Spencer, R. Abu-Zurayk, W. Al-Shabib, V. Chan, R. Rajeev, K. Soon, P. Buckley, J. Sweeney, G. Menary, C. Armstrong, H. Assender, P. Coates, F. Dunne, T. McNally, and P. Martin, "Performance enhancement of

polymer nanocomposites via multiscale modelling of processing and properties," *Plastics, Rubber and Composites*, vol. 37, no. 2, pp. 113–123, 2008.

[165] G. Leeke, *Lecture notes on Process Engineering Fundamentals*. University of Birmingham, October 2011.

[166] J. M. Coulson and J. F. Richardson, *Chemical Engineering Volume 1: Fluid Flow, Heat Transfer and Mass Transfer*. Butterworth Heinemann; 6$^{\text{th}}$ edition, 1999. ISBN 0-7506-4444-3.

Numerical Modeling of Multilayer Film Coextrusion With Experimental Validation

James Champion,[1,2] M. Kieran Looney,[1] Mark J.H. Simmons[2]
[1] *DuPont Teijin Films U.K. Limited, The Wilton Centre, Redcar, TS10 4RF, UK*
[2] *School of Chemical Engineering, University of Birmingham, Edgbaston, B15 2TT, UK*

Computational fluid dynamics (CFD) using a finite volume technique and the volume of fluid method of interface tracking is used to model the production of polyester-based multilayered films via coextrusion. Experimental methods encompass both overall flow validation and secondary layer thickness validation. The interpretation of frozen die plugs and layer thickness measurements of unstretched cast films using chloroform washing are used for overall flow validation. For secondary layer thickness validation, layer thickness measurements via both white light interferometry and chloroform washing of stretched final film samples are presented. Good agreement between CFD results and both die plug structures and layer thicknesses from chloroform washing of cast film is observed. When investigating final film samples, there is a good agreement between CFD and white light interferometry, based on individual layer thickness calculations. However, the layer thicknesses from chloroform washing of final films are lower than those obtained from both CFD and white light interferometry. This is attributed to partial crystallization of the thinner polymer at the interface after stretching and heating the film. **POLYM. ENG. SCI., 00:000–000, 2014.** **© 2014 The Authors. Polymer Engineering & Science published by Wiley Periodicals, Inc. on behalf of Society of Plastics Engineers**

INTRODUCTION

Multilayer polymer film coextrusion is defined as two or more separately extruded polymer melt streams coming together to form a single stratified structure with multiple layers [1–4]. In the coextrusion process, the different melt layers must remain distinct but well bonded (or compatible) when in contact [5, 6]. Assuming that a desirable final coextrusion structure is obtained, coextrusion can combine the properties of different polymers into a single structure with improved features [1–4, 7]. There are many aspects that one must consider to obtain a successful coextruded product. These include both the flow properties of the polymer melts involved and details of the coextrusion hardware used [8].

DuPont Teijin Films (DTF) uses coextrusion to produce biaxially oriented polyester-based multilayered films on a commercial scale. The individual layers of a DTF multilayered film are based on either polyethylene terephthalate (PET) or polyethylene naphthalate (PEN). The main market areas for such multilayered films include flexible electronics, photovoltaics, cards, and food packaging. Typical DTF multilayered films are shown in cross-section in Fig. 1, where A (blue), B (pink), and C (yellow) represent different polymer layers. The multilayered films increase in complexity when moving from Fig. 1a–e. Figure 1a depicts an AB structured film, as investigated numerically and experimentally in this article.

The multilayered films in Fig. 1 are produced when different polymers are extruded, producing separate polymer melt streams. These streams then come together for the first time in either an injector (or feed) block linked to a die or a multimanifold die [1, 4, 5, 8–15]. A thin, unified melt curtain sheet exits the die, which is then rapidly cooled by a casting drum before being stretched in both the machine and transverse directions, producing a biaxially oriented *final film* [5]. Any film sample that has been cooled but not stretched is referred to as cast film. It is often desirable to produce a film with clear edges (Fig. 1a and b). This is when the thinner secondary layers are not present at the edges of the film. The main advantage of attaining clear edges is that trimming of these film edges during production leads to single-component recycling of the main primary polymer.

The multilayered films in Fig. 1 are idealized; there is tight individual layer thickness control across the film widths and there is a linear interface between the different layers. This is not always obtainable and certain coextrusion issues can have a negative impact on the final product performance [3]. Both viscous and elastic melt property differences can lead to an unwanted nonlinear interface, which would have deleterious effects upon the optical, physical, and mechanical film properties [15, 16]. Such interfacial irregularity can be either spatial (caused by viscous effects) or temporal (elastic effects). At the shear rates in the film production process ($\dot{\gamma} < 150\ s^{-1}$ for the hardware and polymers used in this study), polyester melt flows are considered Newtonian and inelastic [17–20]. The analysis presented in this article therefore considers only viscous effects in polymer coextrusion and ignores elastic effects. Further justification of the Newtonian, inelastic assumption made for the PET polymers is shown in the materials section.

When the polymer melts are flowing as a unified structure, the lower viscosity polymer moves to the geometry walls and flows round the higher viscosity polymer(s), producing a curved final interface [1, 8, 10, 21, 22]. This phenomenon is known as interfacial curvature and occurs because the higher viscosity material seeks the area of lowest resistance away from the geometry walls, which is energetically more favorable. The more viscous fluid tends to push into the less viscous one to minimize viscous dissipation [21, 23, 24]. Interfacial curvature

This is an open access article under the terms of the Creative Commons Attribution License, which permits use, distribution and reproduction in any medium, provided the original work is properly cited.
Correspondence to: James Champion; e-mail: james.champion@gbr.dupont.com
Contract grant sponsors: Engineering and Physical Sciences Research Council (EPSRC) and DuPont Teijin Films in the Industrial Doctoral Centre in Formulation Engineering, School of Chemical Engineering, University of Birmingham (Engineering Doctorate Studentship to J.C.).
DOI 10.1002/pen.24022
Published online in Wiley Online Library (wileyonlinelibrary.com).
© 2014 The Authors. Polymer Engineering & Science published by Wiley Periodicals, Inc. on behalf of Society of Plastics Engineers

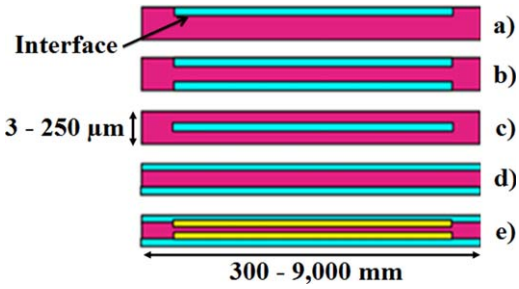

FIG. 1. Typical DTF multilayered film cross-sectional structures: (a) AB with clear edges, (b) ABA with clear edges, (c) BAB encapsulated core, (d) ABA without clear edges, and (e) ACBCA with C clear of edges. Diagram obtained from the internal DTF database. [Color figure can be viewed in the online issue, which is available at wileyonlinelibrary.com.]

can lead to full encapsulation of the lower viscosity polymer around the higher viscosity one(s) for wide geometries or large viscosity ratios. Everage [25] and to a lesser extent Williams [26] showed theoretically that full encapsulation is the most energetically preferred interfacial configuration as it has the lowest energy loss overall.

Work on viscous effects in polymer coextrusion has been ongoing since the 1970s. This early work focused on experimental and theoretical analysis of injector block rather than multimanifold die coextrusion. In the injector block approach, as modeled in this article, the separate polymer melt streams come together to form a unified melt structure. This melt composition then enters a die, where it is spread across the die width and then converted into a uniformly thin melt curtain [1, 8, 10]. In the more controlled, but less flexible multi-manifold die configuration, both layers are spread independently before merging to form the melt curtain [12, 13].

Some of the early fundamental publications on viscous effects include those by Han [27], Southern and Ballman [28, 29], and Lee and White [30]. Han [27] demonstrated via experiment full encapsulation of low density polyethylene (LDPE) around polystyrene (PS) at high LDPE flow rates. Southern and Ballman [28, 29] experimentally demonstrated a reversal of the direction of interfacial curvature for two PS resins at a critical wall shear rate value ($\dot{\gamma}_w$) of 14.9 s^{-1}. LDPE and PS melt flows exhibit a degree of shear thinning and work in Refs. [27–30] demonstrates the effect of shear rate on the interfacial configuration. Shear effects on viscosity are not considered in this article due to the Newtonian nature of polyester melt flows but they are important when studying polymer coextrusion as a whole. A detailed summary of the important early findings in polymer coextrusion is given by Han [31].

More recent publications have been on experimental measurement and numerical modeling of polymer coextrusion. Recent experimental studies further investigated viscous encapsulation. The degree of interfacial curvature, which leads to encapsulation, increases with both increasing viscosity ratios and wider geometries [1, 21]. It is stated in [23] that under standard conditions, encapsulation occurs after 100D, where D is the pipe diameter. Differences in the elasticity of the melt layers can also affect the coextruded structure and lead to elastic-based layer deformation and encapsulation [1, 8, 9, 14, 22, 23, 32, 33]. In elastic encapsulation, the more elastic fluid tends to push into the less elastic one [14, 30]. For further information on elastic effects in polymer coextrusion (not described in this study), the reader is directed toward Refs. [1, 3, 13, 14, 21, 23], and [32–37]. It is stated in Ref. [23] that the viscous rather than elastic contrast between different polymer melt layers is the more dominant factor regarding encapsulation.

Dooley [1] and Dooley and Rudolph [38] showed encapsulation of a lower viscosity PS resin around a higher viscosity PS resin in a laboratory scale injector block and die. In these works, the thicker primary polymer was dyed using carbon black, allowing for easy visualization of the two layers when the die was cooled and the consequent die plug extracted. A similar die plug analysis on a DTF die is demonstrated in the experimental section of this article.

Dooley [39, 40] and Dooley et al. [41] used a novel experimental method to measure the rheology of coextruded structures based on either PE or LDPE. An experiment was designed, allowing for the rheology of fully encapsulated melt structures to be measured. This multilayer rheology was then compared with the individual melt phases making up the structure, based on their shear thinning behavior. A main finding in Refs. [39–41] was that the rheology of the fully encapsulated form was similar to the skin layer rheology and this did not change even in four layered structures. This observation occurs because in fully encapsulated form only the secondary layer is at the walls and the shear rate is highest here. This explains why changing the secondary layer thickness does not alter either the pressure drop or the edge thickness profile during extrusion.

With the increase in computer power and software packages available, numerical methods have been used since the 1980s to study the viscous effects of polymer coextrusion. The majority of numerical coextrusion investigations use a finite element computational fluid dynamics (CFD) technique. A common theme, as shown by Mavridis et al. [42], Karagiannis et al. [43], Gifford [44], and Gupta [45, 46] is that the degree of numerically predicted interfacial curvature is less than that predicted experimentally using similar conditions in publications such as Refs. [28] and [29]. This disagreement is attributed to the wall conditions set in the CFD models. Full encapsulation has never before been modeled in a full three dimensional (3D) simulation.

Sornberger et al. [47] used a simplified iterative finite difference approach to model polymer coextrusion. Two 2D die geometries were modeled after linking to an injector block: A centre fed die and a slight variant of this. The authors show that viscosity-based interfacial curvature occurs and is mainly apparent in the die body rather than the lips. The authors also demonstrate good agreement between numerical and experimental work. However, the model is of a simplified nature and is unable to represent full encapsulation.

Unidirectional, 2D coextrusion was modeled by Karagiannis et al. [48]. A finite element, evolving mesh was used. As expected, it was found that interfacial curvature increases with increasing viscosity and (less viscous : more viscous fluid) flow rate ratios. Full encapsulation was shown numerically for large viscosity ratios. In Ref. [48], such encapsulation is attributed to the minimum viscous dissipation principle as shown in Refs. [25] and [26]. Three dimensional studies investigating the viscosity and flow rate ratios were conducted by Gifford [44]. Similar results to those in Ref. [48] were found, although full encapsulation was not predicted.

A problem with finite element-based CFD modeling is in the discontinuity of the viscous stress and pressure at the interface

 DOI 10.1002/pen

[39]. This problem was investigated in Refs. [42] and [43] by having nodes either side of the interface that the pressure and velocity are solved on, known as the double node method. Both publications apply 3D finite element modeling to simplified injector block geometries. In each case, there is good qualitative but poor quantitative agreements with the experimental results in Refs. [28] and [29]. In particular, the degree of interfacial curvature predicted numerically was less than that observed experimentally. Mitsoulis and Heng [24] also used the double node technique to simulate inelastic polymer coextrusion. Pressure gradient discrepancies were found to exist between the numerical results in Ref. [24] and the experimental data presented by Han [49].

One of the suggested reasons in Ref. [43] for the slightly ambiguous numerical and experimental correlation is the numerical treatment of contact lines. A fluid/fluid/solid contact line is defined as a region between the interface and the wall [43, 50]. In finite element simulations a no-slip condition (zero wall velocity) can give an unrealistic multivalued velocity. Also, there is infinite pressure at the three phase contact point since the no-slip condition cannot hold if this contact point is moving. In Ref. [43], a slight variant of the no-slip contact line was used. Torres et al. [50] extended this to introduce a slip condition for the contact line. Although it showed an improvement on the predicted interfacial curvature compared with the no-slip condition there was still not exact agreement with the results in Refs. [28] and [29].

In more recent publications, Gupta [45, 46] used a mesh partitioning technique to represent the interface between different polymer melt layers. In Refs. [45] and [46], a 3D tetrahedral mesh was used to discretize the full die geometry. The polymer–polymer interface was then captured by a separate surface mesh of linear triangular elements. The interface was allowed to pass through the core part of the die geometry, and new mesh shapes were created upon such intersection. Interfacial curvature was again produced numerically, but less than that predicted experimentally and without encapsulation. The lack of full, 3D encapsulation predicted numerically in the literature may be due to the wall conditions used and a lack of mesh refinement at the contact lines. Having movable meshes may lead to full encapsulation to be observed. Finite volume modeling, as used in this article, should not have the problematic contact line and pressure issues. This is because mass is conserved at every mesh cell including interfacial ones.

Interfacial curvature can have a detrimental effect on the final film properties [3]. To reduce this and produce a desired linear interface (see Fig. 1) either the different polymer melt viscosities should be similar or modifications to existing geometries can be made [8, 12, 13, 51, 52]. A method of viscosity matching of polymer melts is to change the temperature of one of the melts to get similar viscosities at the shear rates of interest, as shown in this study. It is also advisable to coextrude non-Newtonian polymers with similar viscosity–shear rate gradients so that viscosity matching is possible in all regions of the coextrusion hardware [53, 54].

Most previous publications on viscous effects in polymer coextrusion have investigated shear thinning polymer melts at a constant temperature. Since DTF's polyester melt viscosities are independent of shear rate but dependent on temperature, this approach is of limited relevance to this work. Karagiannis et al. [55] used a finite element code to demonstrate that nonisothermal effects in mono-component extrusion can lead to phenomena such as extrudate swell. When investigating polymer coextrusion, Sunwoo et al. [56] and Mallens and Waringa [17] implemented temperature effects into their finite element simulations. In Refs. [17] and [56] it was shown that changing the fluid temperature (and hence viscosity) can lead to an improved final structure and interfacial configuration based on viscosity matching. Temperature effects are relevant to this work and are analyzed both numerically and experimentally in this article.

Typically within DTF the polyester melt viscosity differences between resins are such that interfacial curvature rather than full encapsulation occurs. If the outer or secondary layer viscosity is sufficiently lower than the core or primary layer viscosity, the less viscous, thinner polymer will spread out to the film edges meaning that clear edges are not obtained. In this work, finite volume-based CFD is used to model an AB structured film produced using a DTF pilot scale injector block linked to a 410 mm wide die. The main advantages of the finite volume method compared with the finite element approach is that mass conservation is rigorously enforced and it offers greater efficiency when solving for complex geometries.

The temperature of each melt layer is varied, hence altering the viscosity ratio. One of the aims of this work, is to investigate the impact of temperature changes upon the secondary layer spreading and the final film structures. Both thermal and viscous effects are modeled, which leads to increased understanding since previous publications on polymer coextrusion have focused on viscosity as a function of shear rate and rarely temperature.

Another aim of this work, is to validate experimentally the CFD data. Die plug analysis, as demonstrated in Refs. [1, 11], and [38], allows for direct visualization of the flow behavior within the die and for comparison with the CFD predicted flow behavior. Chloroform washing of the outer soluble copolymer was applied to both cast and final, biaxially oriented film samples. This yielded individual A and B layer thickness data and subsequent comparisons with CFD and white light interferometry results. White light interferometry was applied to final film samples to also give individual layer thickness values. Neither chloroform washing nor white light interferometry have been used before to validate CFD analysis of multilayered films or polymer coextrusion. Interferometry was applied to multilayered sheets in Refs. [57] and [58] but this was to characterize the surface roughness rather than individual layer thickness values. A good agreement between numerical and experimental results is demonstrated in this article.

MATERIALS AND METHODS

Materials

The modeling was performed using the finite volume-based CFD software STAR-CCM+ Version 8.02.008 (CD-adapco) installed on a 32 GB Dell Precision T7500 Westmere workstation. The polymer properties and geometries modeled were representative of a pilot scale trial used to produce the AB structured film samples. Two different polymer melts were modeled for this purpose.

The film samples manufactured for experimental analysis were AB structures (Fig. 1a) of thickness between 20 and 25 μm. These samples were produced using an injector block linked to a 410 mm wide end fed die, which was replicated for

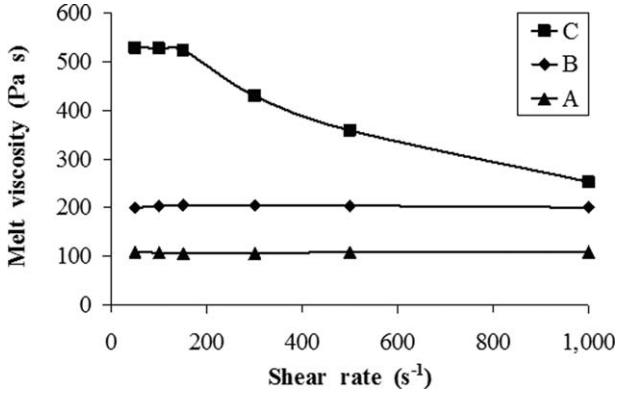

FIG. 2. Viscosity–shear rate curves for the primary PET (B), secondary co-PET (A), and red-PET (C) resins at a temperature of 280°C.

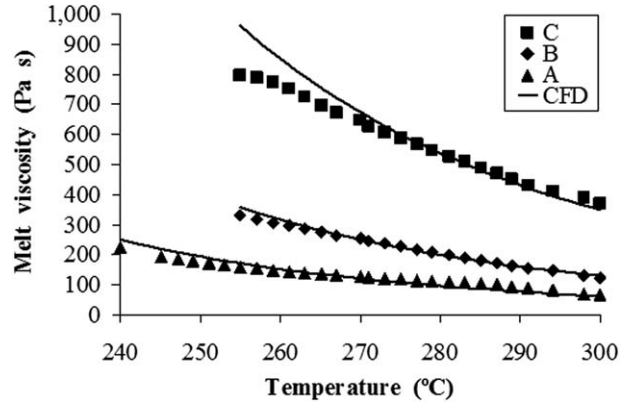

FIG. 4. Rheology of the primary PET (B), secondary co-PET (A), and red-PET (C) resins at an applied shear rate of 100 s^{-1}.

the CFD simulations. The primary B layer was a lightly filled PET polymer and the secondary A layer was a PET copolymer, making up around 25% of the overall final film thickness. For the final film sample obtained, the secondary A layer was made up of 93% co-PET and 7% red dyed, high viscosity PET (red-PET). This red-PET was added to the co-PET polymer for layer visualization purposes.

The three polymers used in this study are denoted PET (B), co-PET (A), and red-PET (C). Figure 2 shows how the melt viscosity of B, A, and C vary with shear rate ($\dot{\gamma} \leq 1000$ s^{-1}), measured using a rheometrics parallel plate rheometer. Newtonian behavior is exhibited by B and A up to 1000 s^{-1}. The high viscosity C resin shear thins at high shear rates but is Newtonian up to 150 s^{-1}, the maximum shear rate for the hardware and polymers used in this study. Therefore, a Newtonian assumption for PET is made throughout this article. The decrease in the viscosity of C observed at the higher shear rates is likely to be an artifact of the test; such high molecular weight PET is known to breakdown under these conditions.

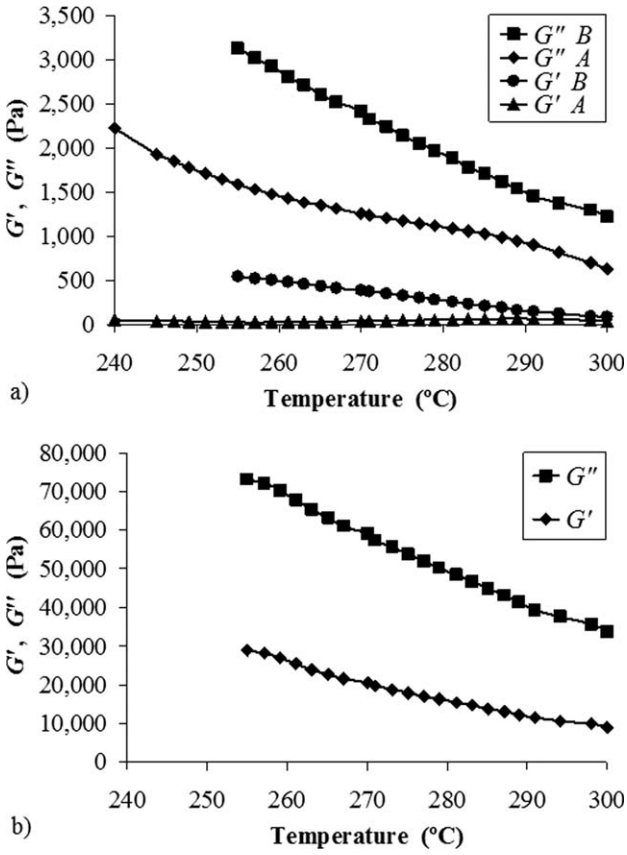

FIG. 3. The storage (G') and loss (G'') modulus at an applied shear rate of 100 s^{-1} for the three resins where: (a) shows the primary PET (B) and the secondary co-PET (A) polymers and (b) shows red-PET (C).

Figure 3 shows how the storage (G') and loss (G'') modulus of the three PET polymers vary with temperature at an applied shear rate of 100 s^{-1}, where Fig. 3a shows B and A and Fig. 3b displays C. This was also measured using a rheometrics parallel plate rheometer. Within the temperature range shown, $G'' > G'$ for all three resins. At the core processing temperature of 280°C, $\tan\delta$ is equal to 7.1, 21.9, and 3.1 for B, A, and C, respectively, where $\tan\delta = G''/G'$ [9]. This implies that viscous effects dominate over elastic ones for the three polymers used in this study and therefore elastic effects are not considered. Both the primary (N_1) and secondary (N_2) normal stress difference values are also used to ascertain the elasticity of a fluid [16, 59]. For the three PET polymers investigated in this study, Newtonian behavior is exhibited within the shear rates of interest (Fig. 2) and therefore $N_1 = N_2 = 0$ for B, A, and C [59]. This further justifies the inelastic assumption for PET used throughout this article.

Figure 4 shows the rheology of the PET (denoted B), co-PET (A), and red-PET (C) resins between 255 and 300°C for PET and red-PET and between 240 and 300°C for co-PET at a constant shear rate of 100 s^{-1}, where Newtonian behavior was assumed. The viscosity–temperature relationships (see Tables 2 and 3 in the next section) implemented in CFD to fit to these three datasets is also shown. At identical temperatures the primary PET polymer is more viscous than the co-PET resin, but the red-PET resin, as used in the final film sample, is the most viscous. It is common practice within DTF to process PET at

TABLE 1. The three film samples manufactured for experimental analysis.

Sample	Primary extruder	Secondary extruder	PET viscosity	co-PET viscosity
1	$T_{PET} = 280°C$	$T_{co\text{-}PET} = 280°C$	199 Pa s	109 Pa s
2	$T_{PET} = 290°C$	$T_{co\text{-}PET} = 265°C$	146 Pa s	135 Pa s
3	$T_{PET} = 290°C$	$T_{co\text{-}PET\ \&\ red\text{-}PET} = 265°C$	146 Pa s	≈175 Pa s

DOI 10.1002/pen

temperatures approaching 300°C. Within the total melt system residence time of 127 s for the polymers and hardware used in this study, thermal degradation is only observed at temperatures exceeding 300°C [60]. Differential scanning calorimetry was used to determine that the melting temperatures of PET and red-PET was 255°C and that of co-PET 220°C. Furthermore, the glass transition temperature of PET and red-PET was found to be 78°C and that of co-PET 76°C.

Three film samples at different processing conditions (temperatures) were manufactured. At the different extrusion temperatures, the viscosity difference between PET and co-PET is wider for Sample 1 compared with Sample 2. Therefore one would expect there to be more spreading of the thinner, less viscous co-PET layer to the film edges for Sample 1 [1, 8, 28, 45, 48]. The constant wall temperature of the injector block and die modeled was 280°C for all three samples.

Table 1 shows the processing conditions used for Samples 1–3. For Sample 1, both the PET and co-PET extrusion hardware were set at equal temperature $T = 280°C$, leading to a higher viscosity for the PET phase. For Sample 2, $T_{PET} = 290°C$ and $T_{co\text{-}PET} = 265°C$, which lead to improved viscosity matching as shown in Table 1. Sample 3 was identical to Sample 2 except for a small (7%) amount of red-PET placed within the co-PET polymer for layer visualization purposes. The secondary co-PET viscosity for Sample 3 was approximated using the co-PET and red-PET viscosity values at 265°C. Unlike the other two samples, the co-PET layer is more viscous than the PET layer for Sample 3. It is therefore expected that for Sample 3, the co-PET layer will not spread as much to the film edges and will be thicker in the middle of the film compared with Samples 1 and 2 [1, 4, 8, 17, 56].

Methods

Numerical Methods. CFD modeling of the two polymer melts flowing through DTF pilot scale coextrusion geometries was accomplished. Within the CFD domain, B was used to denote the primary PET melt flow and A the secondary co-PET melt. Full 3D CFD simulations were solved based on the assumption of incompressible, steady state and low Reynolds number flow with no body forces. The governing numerical equations for this nonisothermal, inelastic problem are shown in Refs. [11] and [56]:

$$\nabla . \underline{u}_k = 0, \tag{1}$$

$$\rho_k \underline{u}_k . \nabla \underline{u}_k = -\nabla p_k + \nabla . \underline{\underline{\tau}}_k, \tag{2}$$

$$(\rho c_p)_k \underline{u}_k . \nabla T_k = \kappa_k \nabla^2 T_k + \underline{\underline{\tau}}_k : \nabla \underline{u}_k, \tag{3}$$

which represent the mass continuity, momentum, and energy equations, respectively. In *Eqs. 1–3*, the subscript k is used to denote an individual melt phase within the coextrusion system; $k=1$ is B or PET and $k=2$ is A or co-PET. The symbols $\underline{u}$, ρ, p, $\underline{\underline{\tau}}$, c_p, and κ are the 3D velocity field, density, pressure, viscous stress tensor, specific heat capacity, and thermal conductivity, respectively, applying to individual melt phases. A no-slip condition (zero velocity at the geometry walls) was implemented throughout.

Two common dimensionless numbers used to quantify the viscous effects of polymer melts in coextrusion are the Reynolds number, *Re*, and the capillary number, *Ca*. *Re* is the ratio between inertial and viscous forces [23]:

$$Re = \frac{\rho u D}{\eta}, \tag{4}$$

and *Ca* is the ratio between viscous and surface (or interfacial) tension forces:

$$Ca = \frac{\eta u}{\sigma}, \tag{5}$$

where D is a length scale, η is the polymer melt viscosity, and σ is the surface (or interfacial) tension between the two fluids.

Approximations by Yue et al. [23] showed that for a typical polymer melt flow $Re \approx 10^{-4} \ll 1$, implying that inertial effects are negligible during coextrusion, and justifying the creeping flow assumption made in Ref. [23]. Again, for typical polymer melt flows (assuming $\sigma \approx 0.01$ N m^{-1}), Yue et al. [23] found $Ca \approx 10^3$, suggesting that the influence of interfacial tension between the two melt flows is negligible when they are in contact and thus it is not usually considered for numerical purposes [43, 61, 62]. For the polymers used in this study, $Ca \approx 2,000$. Thus, interfacial tension is not modeled in this article but inertial terms are included. Inertial terms are embedded within STAR-CCM+ and solving for these allows this work to not rely exclusively on the assumptions made in Ref. [23].

Discretized versions of *Eqs. 1–3* were solved for every mesh cell covering the CFD geometries at every iteration. The volume of fluid (VOF) method was used to numerically capture and track the interface between B and A. First published by Hirt and Nichols [63], the approach of the VOF method is to assign a volume fraction function, F, to every mesh cell, where $F=1$ corresponds to a cell full of B and $F=0$ implies a cell empty of B or full of A. Any cell such that $0 < F < 1$ is an interfacial cell, and $F=0.5$ is treated as the actual interface location.

Once the interface has been obtained at an initial time step, the interfacial evolution must be tracked at every subsequent iteration to interpret how this changes as the solution progresses. The evolution of F at time t is governed by the equation [63]:

$$\frac{DF}{Dt} \equiv \frac{\partial F}{\partial t} + \underline{u} . \nabla F = 0, \tag{6}$$

which alongside *Eqs. 1–3* provides a closed system of governing equations for the CFD simulations. Because of the unsteady nature of *Eq. 6*, implicit unsteady physics with a time step of 0.05 seconds per iteration was implemented into the model. The numerical methods used in this study are not as complex as those in (for example) Refs. [1, 23, 37, 43, 45, 46], and [50]. However, the simpler numerical approach is justified due to the Newtonian, inelastic nature of the PET melts modeled and readily enables the 3D complexity to be accounted for. The excellent agreement observed in this article between the numerical and experimental data gives further vindication of the numerical approach used.

To replicate the coextrusion hardware used to produce Samples 1–3, an injector block and a 410 mm wide end fed die were modeled. Figure 5 shows the meshed geometries created in STAR-CCM+, where Fig. 5a shows the injector block and Fig. 5b shows the end fed die. The flow direction in Fig. 5 is from right to left. The inlet duct diameter to the die is 23.75 mm, which then reduces to 22.5 mm for the remainder of the pipe as shown in Fig. 5b. The exit die gap increases when moving from

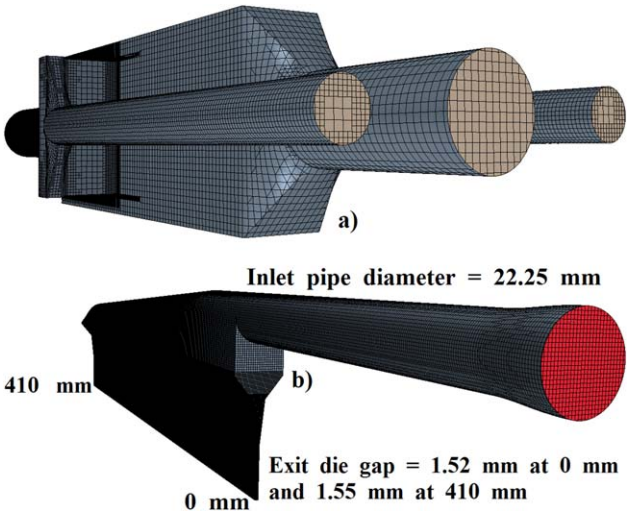

FIG. 5. The meshed CFD geometries used, where: (a) is the injector block and (b) is the 410 mm wide end fed die. The flow direction is from right to left. [Color figure can be viewed in the online issue, which is available at wileyonlinelibrary.com.]

0 to 410 mm edges to ensure a uniform exit flow across the die outlet width. The inlet pipe leading into the die is 196 mm long.

In the injector block geometry, there are two thinner secondary inlet channels and one primary inlet channel. To produce an AB structured film, the secondary A layer entered the block in the left side secondary channel. B entered the block in both the primary channel and right side secondary channel. A unified AB structure was produced at the injector block outlet. The injector block outlet solution was taken as an inlet condition into the end fed die. In the die, the unified melt structure is converted from a circular inlet into a thin rectangular outlet plot representative of the final film solution.

Around 1.5 million mesh cells were used to discretize the injector block with 14.5 million cells required for the end fed die. A trimmer mesh with hexahedral template cells was used for both geometries. Particularly fine mesh regions were selected when the melt flows were in contact with each other, with the aim of achieving a smooth, well defined interface between the different melt layers. A fine mesh (12 mesh cells across a gap of approximately 1.5 mm) was selected across the thin rectangular end fed die outlet due to the high aspect ratio in this study. For any CFD simulation, increasing the number of mesh cells leads to increased accuracy but there are limitations since a finer mesh will lead to longer convergence times and will require larger amounts of computer memory.

To represent the PET and co-PET melt layers in the coextrusion domain, fluid properties were assigned to both B and A in STAR-CCM+. Tables 2 and 3 shows the physical characteristics assigned to each melt where Table 2 shows the Sample 1 conditions and Table 3 shows Sample 3, assuming standard PET melt properties. The viscosity–temperature functions used are based on well established relationships within DTF and fit the rheology data as shown in Fig. 4. Melt viscosity is a function of molecular weight as well as temperature in these relationships.

TABLE 2. The modeled fluid properties for B and A for Sample 1.

	B (PET)	A (co-PET)
Temperature (T)	280°C	280°C
Density (ρ)	1250 kg m^{-3}	1250 kg m^{-3}
Viscosity (η), Pa s	$10^{\{(2{,}953/(T+273))-3.04\}}$	$10^{\{(2{,}953/(T+273))-3.36\}}$
Thermal conductivity (κ)	0.2 W $m^{-1}°C^{-1}$	0.2 W $m^{-1}°C^{-1}$
Mass flow rate ($\dot{m}$)	47.5 kg hr^{-1}	15.83 kg hr^{-1}
Final volume fraction	75%	25%

TABLE 3. The modeled fluid properties for B and A for Sample 3.

	B (PET)	A (co-PET & red-PET)
Temperature (T)	290°C	265°C
Density (ρ)	1250 kg m^{-3}	1250 kg m^{-3}
Viscosity (η), Pa s	$10^{\{(2{,}953/(T+273))-3.04\}}$	$10^{\{(2{,}953/(T+273))-3.25\}}$
Thermal conductivity (κ)	0.2 W $m^{-1}°C^{-1}$	0.2 W $m^{-1}°C^{-1}$
Mass flow rate ($\dot{m}$)	47.5 kg hr^{-1}	15.83 kg hr^{-1}
Final volume fraction	75%	25%

The secondary A or co-PET layer was modeled to make up 25% of the overall flow rate. The CFD simulations were set up to mimic the conditions of Samples 1–3 as described in Table 1. It was assumed that uniform flow from each extruder was delivered to the injector block inlet ports. Any interfacial smudging between A and B is a numerical artifact and is a function of the mesh cell size at a particular region.

Experimental Methods. Die plug analysis, chloroform washing of the co-PET layer and white light interferometry were used for experimental validation of CFD results. Die plug analysis was performed to analyze the flow within the 410 mm wide end fed die at the end of the pilot scale trial. Chloroform washing was applied to Samples 1–3 for both cast and biaxially oriented films to derive the secondary layer thickness profile across the whole film width. White light interferometry was conducted on final film samples to also give a secondary layer thickness profile. White light interferometry was not applied to cast film samples because the co-PET cast thickness is beyond the measurable limits for white light interferometry.

For die plug analysis, the end fed die was rapidly cooled at the end of the trial and a solid phase frozen polymer heel was produced. This polymer heel or die plug was carefully extracted from the end fed die. Since red dye was present in the secondary co-PET layer (see Sample 3 in Table 1), individual layer visualization was possible. The die plug was sectioned at different points across the die width. These sections were then scrutinized and compared directly with the CFD predicted layer configuration in the die when modeling Sample 3.

Chloroform washing was applied to both cast and final film samples, providing co-PET thickness profiles across the film width. The solvent chloroform (obtained from Sigma-Aldrich and used as received) was applied to the film surface in 2.5 mm spots across the film width, dissolving the thinner co-PET layer at each point. The film thickness was measured at each spot before and after chloroform application using a Sylvac D100S digital thickness gauge, calibrated using feeler gauges. The calibration performed internally implied a thickness gauge accuracy of 500 nm. This procedure was conducted three times across every film sample measured with averages taken, allowing for the total film and individual layer thicknesses to be obtained.

DOI 10.1002/pen

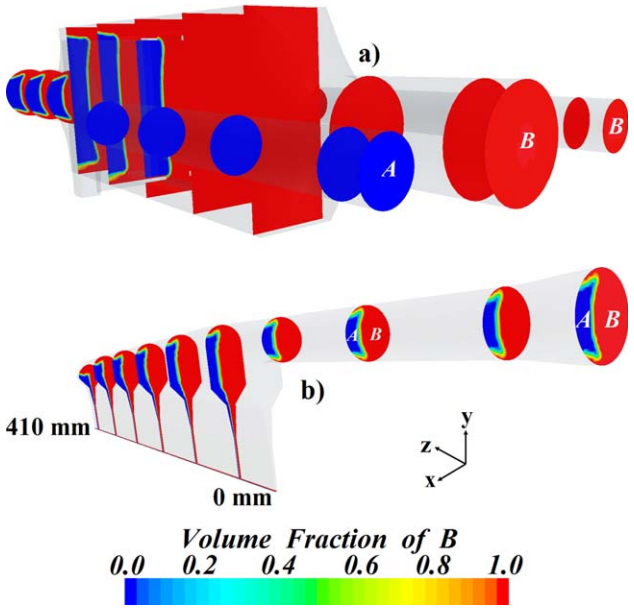

FIG. 6. The progressive volume fraction of B (shown in red) for Sample 1 through: (a) the injector block, where B enters through the two right inlet ports and (b) the end fed die, where B is on the right side of the unified structure. The flow direction is from right to left. The volume fraction of A is shown in blue and both B and A are labeled. [Color figure can be viewed in the online issue, which is available at wileyonlinelibrary.com.]

The thickness values derived for cast film analysis were converted, knowing the casting speed, and cast film density, to a volumetric flow rate per unit width across the die width, allowing for direct comparison with the CFD equivalent. For final film interpretation, the co-PET thickness values were compared with both the white light interferometry thickness values and the CFD co-PET flow values.

White light interferometry was used to obtain co-PET thicknesses for final film samples. A Veeco NT9800 interferometer, operating in vertical scanning interferometry (VSI) mode, was used. Small sections of the film samples were mounted onto a clear glass slide, ensuring as flat a field of view as possible. Once the film surface was in focus, a primary interferogram representative of the film surface was observed. The interferometric objective moved vertically downwards and a secondary interferogram, representative of the PET-co-PET interface was observed.

For the section of film measured, the Veeco software calculated the vertical distance between both interferograms and consequently an average co-PET thickness value. This is an average thickness value since the white light interferometry field of view is relatively wide containing a number of small pixels and the quoted thickness value is based on a point by point average difference. For the three film samples, white light interferometry was conducted three times in five different regions across the film width, with average co-PET thickness values generated. The total film thickness was measured at the points of white light interferometry application, generating the total and individual layer thickness profiles. The minimum vertical resolution of the Veeco NT9800 when operating in VSI is 3 nm.

When applying chloroform washing to final film samples, the secondary co-PET layer thickness was found to be too low compared with the equivalent white light interferometry and CFD results. A suggested reason for this is partial crystallization of the co-PET layer at the PET-co-PET interface when stretching and heating the film. Partial crystallization of the amorphous co-PET polymer would have resulted in a thin crystalline region that was insoluble in chloroform.

A method used to test the partial crystallization theory was time-of-flight secondary ion mass spectrometry (ToF-SIMS) surface analysis applied to Sample 1. The general operating principle of ToF-SIMS is as follows [64]: A primary positive ion source is directed toward a surface of interest. This causes charged secondary ions of varying size characteristic of the surface to be emitted. These secondary ions are detected by a time-of-flight detector and hence converted into a positive ion spectrum. The resulting spectrum can distinguish between different sized molecules because of their difference in mass and is then analyzed to determine the overall surface composition. ToF-SIMS, using a Bi_3^{2+} ion source, was applied to three different Sample 1 surfaces: The untreated PET and co-PET sides and the co-PET side after applying chloroform (the PET–co-PET interface). The spectrum for the chloroform treated co-PET side was then compared with the PET and co-PET spectra to determine whether any co-PET was present at the interface.

RESULTS AND DISCUSSION

Numerical Simulations

Figure 6 shows the CFD predicted volume fraction of B through both the injector block (Fig. 6a) and the end fed die (Fig. 6b) for Sample 1 (Table 1). In Fig. 6, B is in red, A in blue, and the flow direction is from right to left.

Polymer B is shown to enter the injector block through the main primary inlet channel and the right secondary inlet channel, with A entering through the left secondary inlet. The melt layers then come together within the block to form a unified AB structure with A making up 25% of the overall composition. There is a smooth, well defined interface throughout between the two melt flows within the injector block and end fed die, implying a sufficiently fine mesh within the domain once the fluids are in contact.

The volume fraction and other results at the injector block outlet were taken as initial conditions into the end fed die. In the die, the circular melt structure is converted into a uniformly thin rectangular melt curtain at the outlet upon entering the main die body from the inlet pipe. The direction of flow within the die changes from horizontal (z) to both horizontal and vertical ($-y$) when moving from the pipe into the main part of the die. A volume fraction plot of B at the die outlet is what defines the CFD predicted final film structure. This is shown for Sample 1 in three 45 mm sections at the die outlet in Fig. 7, where Fig. 7a shows the section from the 0 mm edge to 45 mm, Fig. 7b shows the middle, from 180 to 225 mm, and Fig. 7c displays from 365 mm to the far edge at 410 mm.

Figure 7a and c show that CFD does not predict the formation of clear edges at either edge of the Sample 1 final film structure with the blue A layer present at each edge. This is despite clear edges being attainable for actual multilayered films produced using the injector block and end fed die system. The lack of numerical clear edges is attributed to the high degree of spreading of the lower viscosity A to the film edges (see Table

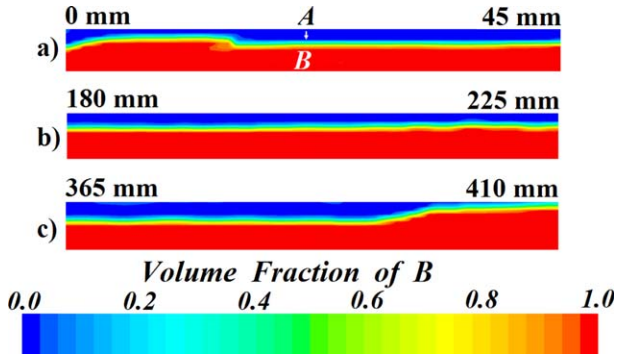

FIG. 7. The volume fraction of B (shown in red, the bottom layer) at the die outlet for Sample 1 showing: (a) the 0 mm edge, (b) the middle, and (c) the 410 mm edge. The volume fraction of A is shown in blue and is the top layer. [Color figure can be viewed in the online issue, which is available at wileyonlinelibrary.com.]

1, Sample 1). Also, numerical diffusion errors exacerbate this, particularly at the 0 mm edge where the flow goes through a sharp 90° transition on entering the die body [65]. In the context of this work, the numerical diffusion is not significant and the CFD results are shown experimentally to accurately represent the die plug and both cast and final film solutions in all but the extreme edges.

There is more A present at the 0 mm edge compared with the 410 mm edge. This greater bias of spreading towards the 0 mm edge is observed in reality but is exaggerated numerically. As mentioned in the previous paragraph, the flow is not properly resolved at the sharp transition point from the horizontal to vertical flow direction in the end fed die. The 0 mm edge profile at the outlet may have improved with the input of a finer mesh at this region but this would have increased the total convergence time. The number of mesh cells possible is a limitation of this study, however apart from the excess amount of A at the 0 mm edge the final film structure in Fig. 7 is similar to what was obtained experimentally.

The volumetric flow rate per unit width across the whole die outlet width was derived for the total and co-PET flows, with flow curves plotted in each case. These flow curves correspond to the CFD predicted total film and co-PET thickness profiles across the die width. To derive the total flow curves, lines were created in the CFD domain across the exit die gap from 0 to 410 mm in increments of 1 mm. The outlet velocity magnitude was then integrated across each line using the CFD software, yielding the total volumetric flow rate per unit width (measured in $m^2\ s^{-1}$) for every line. For the co-PET flow curves, the same procedure was performed on lines spanning the co-PET outlet location from the top outlet wall (see Fig. 7) to the $F=0.5$ interfacial location, where F is the volume fraction function.

These flow curves are shown graphically in Fig. 8 for Samples 1–3, where Fig. 8a shows the comparative total flows and Fig. 8b shows the secondary co-PET flows. Comparing the total flow curves, a similar profile is observed in each case, with the flow falling to zero at each end of the film as expected due to the no-slip condition. A uniformly thin final film is obtained for the three samples, which is desirable from a commercial perspective. The CFD obtained edges were thickest for Sample 1, particularly at the 410 mm edge. This is believed to be due to a greater spreading of the co-PET layer to the extreme edges in Sample 1. For Samples 1 and 2, co-PET is less viscous than PET. Since the viscosity difference is wider in Sample 1 (Table 1), the co-PET layer spreads more. For Sample 3, co-PET is more viscous than PET, with co-PET therefore not spreading as much as in Sample 1.

Analysis of the co-PET CFD flow curves in Fig. 8b again shows that there is more of the less viscous co-PET at the extreme edges for Sample 1 than Samples 2 and 3. This is again due to the greater viscosity difference in Sample 1. Sample 3 has the most co-PET present in the middle of the film, caused by the co-PET layer remaining confined to the center since it is more viscous than PET. The flow differences in Fig. 8 are noticeable but the film structures have not changed significantly despite temperature and hence melt viscosity differences. This suggests that from a CFD perspective, the rheology difference for Sample 1 does not have a negative impact on the final film thickness and is within the limits of DTF pilot scale facilities. Improved control and measurement of the melt temperature of both streams may increase understanding of the solutions.

There is significantly more noise in the co-PET flow data than the total flow data. This is because the flow calculations to obtain Fig. 8b are based on numerical approximations of the exact interfacial location. At the die outlet, the $F=0.5$ interfacial contour changes position within a mesh cell when moving from 0 to 410 mm across the die. The outlet mesh is coarse with respect to the $F=0.5$ contour so the exact $F=0.5$ interfacial location cannot be determined. To amend for this, STAR-CCM+ uses a smoothing function (linear in the flow direction) to estimate the $F=0.5$ position in every interfacial mesh cell.

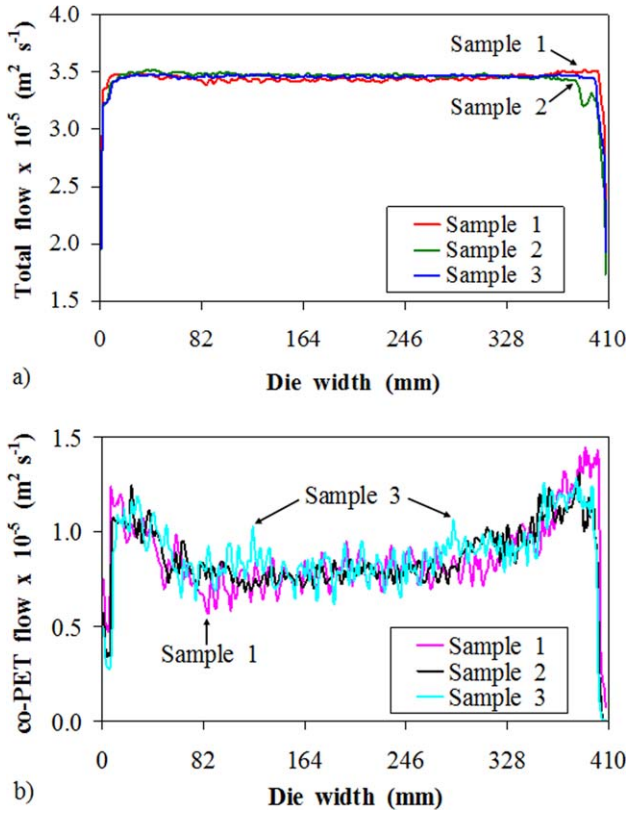

FIG. 8. The CFD predicted die outlet flow plots for Samples 1–3, where (a) is the total flow and (b) is the secondary co-PET flow. [Color figure can be viewed in the online issue, which is available at wileyonlinelibrary.com.]

DOI 10.1002/pen

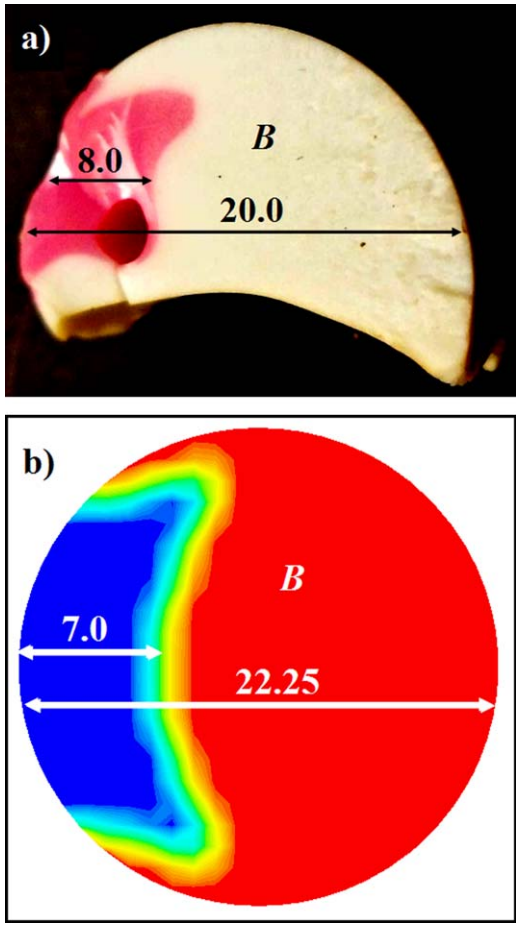

FIG. 9. The flow configurations 125 mm into the inlet pipe for Sample 3 where (a) shows the die plug structure and (b) shows the CFD structure. The primary polymer B is labeled in each figure. All dimensions shown are in millimeters. [Color figure can be viewed in the online issue, which is available at wileyonlinelibrary.com.]

This leads to noisy data which would be ameliorated with a finer mesh or smoothing the data in the axial direction along the die body, again showing numerical limitations of this work. For the purpose of this work, the overall co-PET flow trend rather than the noise is important. As shown in the next section, there is an excellent agreement between CFD and chloroform washing of cast film samples based on the co-PET flow trend.

Experimental Findings

The experimental results are split into two sections: Overall flow validation and secondary layer thickness validation. Die plug analysis and thickness measurements via chloroform washing of cast film samples are shown in the overall flow validation section. The secondary layer thickness validation section shows both white light interferometry and chloroform washing applied to final, biaxially oriented film samples with the secondary layer thickness calculated. Comparison with the numerical results are made throughout.

Overall Flow Validation

At the Sample 3 conditions, a die plug was obtained showing the individual layer configuration between the PET and co-PET layers through the die. The die plug was obtained after rapid cooling of the die and was sectioned in ten points across the inlet pipe and die width. A small amount of red-PET present in the co-PET layer allowed for determination of both layers. The die plug layer structures were then compared with the CFD predicted Sample 3 configurations at the equivalent sections in the pipe or die.

At 125 mm into the inlet pipe, Fig. 9 shows the PET-co-PET individual layer configuration, where Fig. 9a shows the die plug structure and Fig. 9b shows the CFD predicted structure. In Fig. 9a, PET is in white and co-PET in pink and in Fig. 9b, PET is in red with co-PET in blue. In general there is good agreement between the two plots, with the overall flow shape and degree of interfacial curvature observed experimentally validating the numerical result. A section of the die plug is missing at the bottom of Fig. 9a and this shows a break in the die plug upon extraction from the end fed die geometry. This highlights the difficulties associated with removal of the die plug from such a narrow end fed die.

Further differences between Fig. 9a and b are based on both the diameter of the whole structure and the co-PET layer width. The diameter of the experimentally obtained die plug is 20.0 mm, compared with 22.25 mm for CFD. This difference is due to the density increase in PET during the transition from a melt to a solid structure so the die plug shrunk when cooled. Furthermore, the co-PET layer is wider in the die plug. This is because of the lower melting point of co-PET compared with PET and the molten co-PET spreading further toward the center of the pipe when cooled. Despite these differences there is generally a good agreement between the die plug and CFD individual layer results.

Repeating the comparisons 335 mm into the die (see Fig. 10) again shows that the die plug (Fig. 10a) has validated the CFD flow profile (Fig. 10b). There is an excellent match between the co-PET structures in each case. The main differences between Fig. 10a and b are the overall die plug height and secondary co-PET layer width. These differences are attributed to the breaking of the die plug upon removal and different polymer layer melting temperature differences respectively. Similar agreement was observed for the eight other die plug sections in either the inlet pipe or the die body (not shown). An excellent agreement

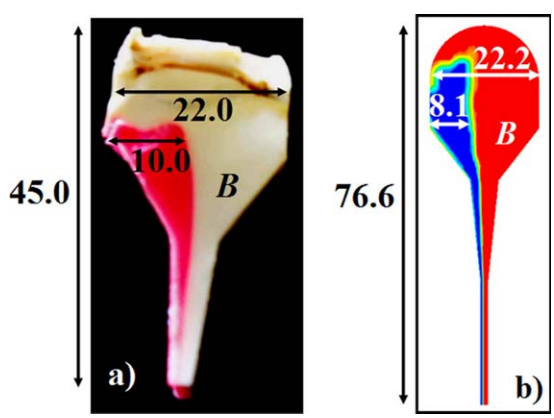

FIG. 10. The flow configurations 335 mm into the die body for Sample 3 where (a) shows the die plug structure and (b) shows the CFD structure. The primary polymer B is labeled in each figure. All dimensions shown are in millimeters. [Color figure can be viewed in the online issue, which is available at wileyonlinelibrary.com.]

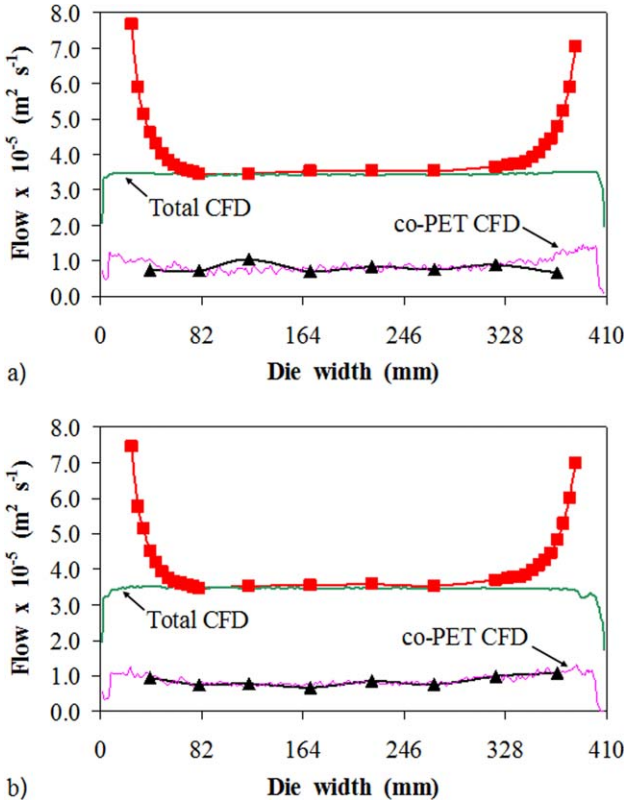

FIG. 11. The total and co-PET flow curves across the die outlet width for both chloroform washing and CFD where (a) shows Sample 1 and (b) shows Sample 2. For the curves in both figures, the total chloroform washing flow is in red (■), the total CFD flow is in green, the co-PET chloroform washing flow is in black (▲), and the co-PET CFD flow is in pink. [Color figure can be viewed in the online issue, which is available at wileyonlinelibrary.com.]

between die plug structures and numerically predicted phase distributions is also shown in Refs. [1, 22, 37], and [66].

To complement the Sample 3 die plug analysis, chloroform washing was performed on Samples 1 and 2 as cast (unstretched) film. Chloroform was applied across the film widths, producing thickness profiles for the total film and the secondary co-PET layer. These thickness values were then converted to a volumetric flow rate per unit width across the film width using both the casting drum speed and the cast film density (corrected for the ambient to PET melt temperature ratio). These flow results allow for direct comparison with the CFD flow curves in Fig. 8, as shown in Fig. 11, where Sample 1 and Sample 2 results are presented in Fig. 11a and b, respectively. Each figure shows the chloroform washing and CFD obtained total and co-PET flow curves.

Observation of the total flow curves in Fig. 11 shows a large increase at the edges for chloroform washing compared with CFD. This is due to a phenomenon known as neck-in of the cast film [67, 68]. When a melt curtain exits a polymer die, it is stretched by a factor of around five by the casting drum. Since its edges are unsupported during this stretching, the edges are not stretched as much, and the melt curtain and hence cast film width narrows. The phenomenon of neck-in was not modeled with CFD, with the solution obtained for the die outlet being taken as representative of the final film.

The Sample 1 and Sample 2 cast film width is 370 mm, implying a neck-in of 20 mm from each edge based on a 410 mm wide end fed die. The measurement range of the total chloroform washing flow data in Fig. 11 is from 5 to 365 mm across the 370 mm cast film width. This is plotted from 25 to 385 mm across the 410 mm die width to correct for the 20 mm neck-in and allow for a direct comparison with the CFD flow data. The co-PET chloroform washing flow curves in Fig. 11 are based on thickness measurements between 20 and 350 mm across the cast film width. These are plotted from 40 to 370 mm across the die width to again account for neck-in.

Integrating the Sample 1 and Sample 2 chloroform washing and CFD total flow curves and subsequently multiplying this by either the cast or melt density gives a value of 0.018 kg s^{-1} to three decimal places for all curves. The percentage difference between the CFD and chloroform washing mass balance values was 3.16% for Sample 1 and 3.52% for Sample 2. This confirms a conservation of mass within a 5% error despite neck-in not being modeled with CFD.

There is generally a good agreement between the chloroform washing and CFD flow results for Sample 1 (Fig. 11a). The main part of the total chloroform washing flow curve matches its CFD equivalent well. There is also a good correlation between the two co-PET flow curves except for two ambiguous chloroform washing results at 100 and 350 mm across the cast film width (plotted at 120 and 370 mm to correct for the 20 mm neck-in). These outliers are believed to be due to human error when performing chloroform washing, with either the primary PET layer being partially dissolved or excess co-PET remaining on the film surface at 100 and 350 mm, respectively.

An even better agreement between CFD and chloroform washing is found for Sample 2 (Fig. 11b), with an excellent match between experimental and numerical flow curves. Chloroform washing of cast film samples has validated the CFD outlet flow predictions at the range where data was obtained. These results alongside the die plug analysis confirm the successful validation of CFD flow results.

Secondary Layer Thickness Validation

For final, biaxially oriented film Samples 1–3, both white light interferometry and chloroform washing were applied. This was to calculate the secondary co-PET thickness profile across the final film width of 800 mm. Comparisons between white light interferometry, chloroform washing, and CFD for co-PET thickness measurements are shown in this section.

Figure 12 shows an example screenshot taken from white light interferometry applied to the middle of Sample 2. For all white light interferometry measurements, a primary topography plot showing the film surface (see Fig. 12a) was obtained. The interferometric objective then moved vertically downwards, generating a secondary interfacial topography plot (see Fig. 12b). The *z*-scale color bars to the right of Fig. 12a and b show the height information in micrometers for each plot. The software then calculated the vertical distance between the two topography plots at each point, and hence generated a co-PET layer thickness plot (see Fig. 12c). The size of the three images in Fig. 12 is 2.5 × 1.9 mm, or 640 × 480 pixels. The co-PET layer thickness plot in Fig. 12c is therefore calculated from 307,200 measurement points.

DOI 10.1002/pen

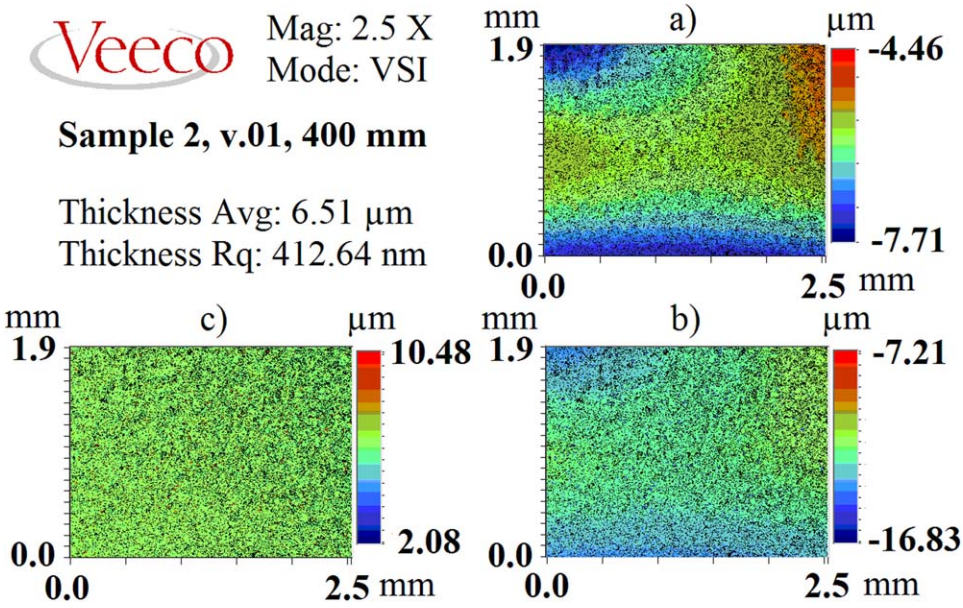

FIG. 12. A white light interferometry screenshot showing analysis of Sample 2 400 mm into the film, where (a) shows the primary surface topography plot, (b) shows the secondary interfacial topography plot, and (c) shows the co-PET thickness topography plot. The average co-PET thickness is calculated as 6.51 µm. [Color figure can be viewed in the online issue, which is available at wileyonlinelibrary.com.]

The average co-PET layer thickness is calculated from the plot in Fig. 12c. For the calculation in Fig. 12, the average co-PET thickness is found to be 6.51 µm, but the thickness range is from 2.08 to 10.48 µm. White light interferometry is a high resolution point by point measurement technique and can detect surface roughness accurately. The large thickness range in Fig. 12 implies either a film surface or interfacial roughness that one must be aware of when further analyzing white light interferometry results. For Samples 1–3, white light interferometry as shown in Fig. 12 was performed three times at five locations across the film width with average co-PET thickness values taken.

Figure 13 shows the white light interferometry calculated average total film and individual layer thickness profiles, where Fig. 13a and b show results for Samples 1 and 2, respectively. Measurements were taken at locations 50, 200, 400, 600, and 750 mm across the film width. The data points in Fig. 13 are based on an average of three measurements. At each of the five measurement locations, there was little difference between the three thickness values obtained. This shows sample consistency for white light interferometry and a low sample variance or a high repeatability with white light interferometry between the three measurements at each point across the film.

There is however a relatively high method variance associated with these white light interferometry results. For any co-PET thickness measurement, the Veeco software quoted the value subject to a roughness value or measurement error R_q (see Fig. 12) for the white light interferometry measurement technique. The average co-PET thickness for Samples 1 and 2 is 6.4 µm, using the five data points in Fig. 13. The values taken across the film width to obtain these averages are typically subject to an R_q of 400–600 nm, or an error of ±6–9%. This method variance is caused by smooth surface undulations in the

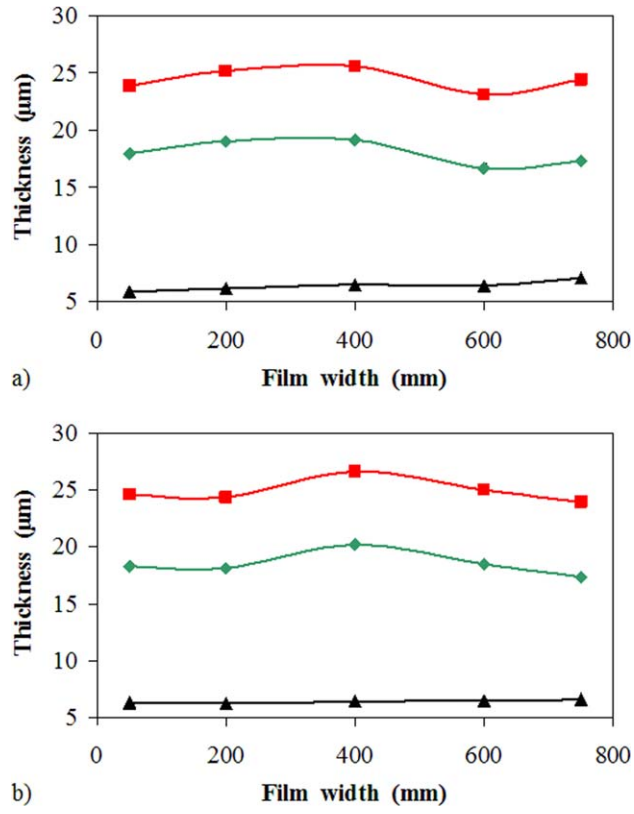

FIG. 13. The white light interferometry measured average total film, PET and co-PET thickness for (a) Sample 1 and (b) Sample 2. For the curves in both figures, the total film thickness is shown in red (■), the primary PET thickness is in green (◆), and the secondary co-PET thickness is in black (▲). The error bars are within the range of the symbol height. [Color figure can be viewed in the online issue, which is available at wileyonlinelibrary.com.]

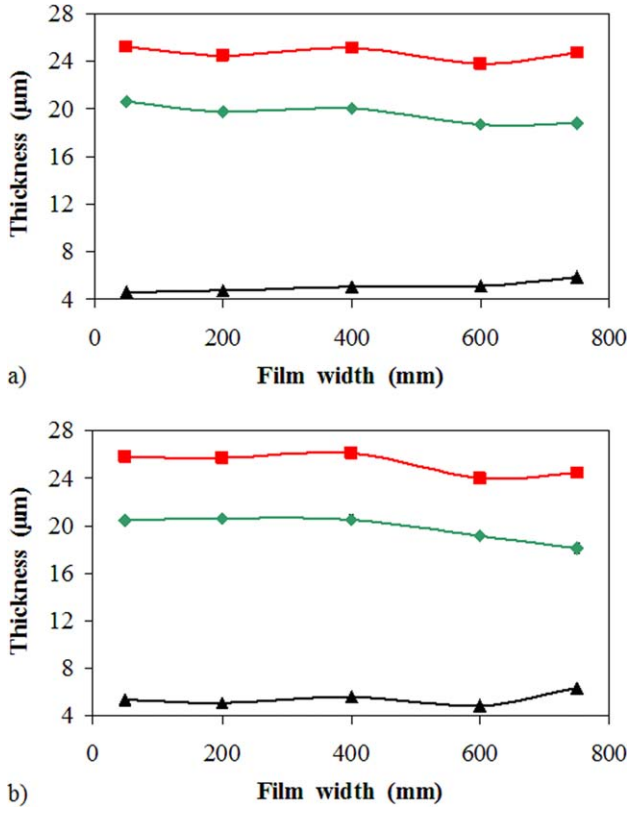

FIG. 14. The chloroform washing measured average total film, PET, and co-PET thickness for (a) Sample 1 and (b) Sample 2. For the curves in both figures, the total film thickness is shown in red (■), the primary PET thickness is in green (◆), and the secondary co-PET thickness is in black (▲). The error bars are within the range of the symbol height. [Color figure can be viewed in the online issue, which is available at wileyonlinelibrary.com.]

co-PET surface layer, as films containing this polymer require a degree of surface roughness. Another factor causing a high method variance is the low signal to noise ratio when measuring the interfacial location through the film surface.

From Fig. 13, the total Sample 1 and Sample 2 film thickness is highest in the middle of each film. The maximum co-PET thickness is at the far 750 mm edge, again for both samples. At this edge, a thicker co-PET layer is found for Sample 1 (7.1 μm) compared with Sample 2 (6.6 μm). This is as expected given the lower viscosity of co-PET compared with PET in Sample 1 [1, 4, 8, 10, 48]. At the 50 mm edge measurement, the quantity of co-PET is found to be greater in Sample 2 than Sample 1. This is opposite to what was expected but is within the method variance range.

The equivalent chloroform washing results for the average total film and individual layer thickness profiles are shown in Fig. 14, where Fig. 14a shows Sample 1 and Fig. 14b shows Sample 2 results. The data points in Fig. 14 are again based on an average of three measurements at five locations across the film width. Compared with the white light interferometry results, there was a far greater difference between the three thickness measurements taken at each location for chloroform washing results (see the error bars in Fig. 15). This shows poor repeatability of the chloroform washing results or a high sample variance. Chloroform washing is not as rigorous as white light interferometry, and this alongside measurement error of the digital thickness gauge is believed to cause the sample variance. The average co-PET thickness when using chloroform washing is 5.1 μm for Sample 1 and 5.5 μm for Sample 2.

Figure 15 shows a combination of Figs. 13 and 14, where the average co-PET thickness profiles of Samples 1 and 2 are plotted using both white light interferometry and chloroform washing. At this smaller *y*-axis range, the high chloroform washing sample variance is detectable via the significantly higher error bars compared with white light interferometry. The general trend in the four thickness profiles shows an increase in the co-PET thickness when moving from 50 to 750 mm. This may be due to an injector block secondary layer inlet port geometry or temperature differences slightly favoring flow toward the far edge of the film when manufacturing the three film samples. At the 750 mm edge, the amount of co-PET is higher for Sample 1 than Sample 2 with white light interferometry as expected. The reverse is found for the chloroform washing results but these thickness differences are within the range of the error bars or sample variance.

For the five data points in Fig. 15, there is a thickness difference between both measurement techniques, with white light interferometry consistently measuring a 1 μm thicker co-PET layer for identical film samples. The inconsistency of the two methods is attributed to both white light interferometry method variance and chloroform washing sample variance. Despite differences between the measurement techniques, the Sample 1 and Sample 2 results are fairly consistent. This suggests that the temperature and hence polymer melt viscosity differences were not wide enough to significantly change the co-PET spreading. This was also found numerically and future work will need to repeat the analysis in this article on more rheologically different polymer melts.

For the three biaxially oriented final film samples, Table 4 shows the average co-PET layer thickness as a percentage of the total film thickness for white light interferometry, chloroform washing, and CFD. The percentage thickness values in Table 4 are based on an average of the thickness data obtained at the five measurement locations across the film width for white light

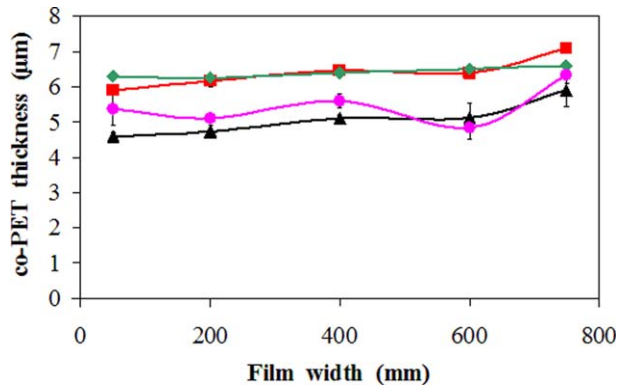

FIG. 15. The average Sample 1 and Sample 2 co-PET thickness profiles using both white light interferometry and chloroform washing. In this study, white light interferometry analysis of Sample 1 is in red (■), white light interferometry analysis of Sample 2 is in green (◆), chloroform washing analysis of Sample 1 is in black (▲), and chloroform washing analysis of Sample 2 is in pink (●). The white light interferometry error bars are within the range of the symbol height. [Color figure can be viewed in the online issue, which is available at wileyonlinelibrary.com.]

DOI 10.1002/pen

TABLE 4. The percentage co-PET thickness of the total film thickness using both experimental and numerical methods for all three film samples.

Sample	White light interferometry (%)	Chloroform washing (%)	CFD (%)
1	26.2	20.6	24.9
2	25.8	21.6	24.6
3	27.1	22.6	26.6

interferometry and chloroform washing. The CFD thickness values are based on an average of the co-PET flow calculations as a percentage of the total flow calculations at the equivalent five measurement locations across the die width.

White light interferometry shows a significantly better agreement with CFD than chloroform washing. The white light interferometry results are slightly higher than the CFD equivalent but these thickness differences are within the measurement error or method variance range for this technique. For validating CFD results, white light interferometry is shown to be more accurate than chloroform washing. A reason for this is that unlike chloroform washing, white light interferometry is non-intrusive to the film surface and the secondary co-PET layer is not disturbed or damaged. White light interferometry is also better than chloroform washing at capturing fine surface or interfacial detail. White light interferometry is the more accurate and robust measurement technique and is less susceptible than chloroform washing to human or experimental error.

From Table 4, the chloroform washing data for final film samples is too low compared with CFD and does not fully validate the numerical results. Comparing Table 4 with Fig. 11 implies that the chloroform washing data is inconsistent between cast and equivalent final film samples of the same film. It appears that more co-PET was retained on the final film than the cast film upon chloroform application.

A suggested reason for this is partial crystallization of the co-PET layer at the PET–co-PET interface when stretching and heating the film. A white light based reflectometry technique (not shown) also yielded too low co-PET thickness values, further justifying the partial crystallization theory. Partial crystallization of the amorphous co-PET polymer would have resulted in a thin crystalline region that was insoluble in chloroform. This crystalline region therefore remains on the film at the PET-co-PET interface upon chloroform application, and the co-PET thickness is measured to be lower than its actual value for final film samples.

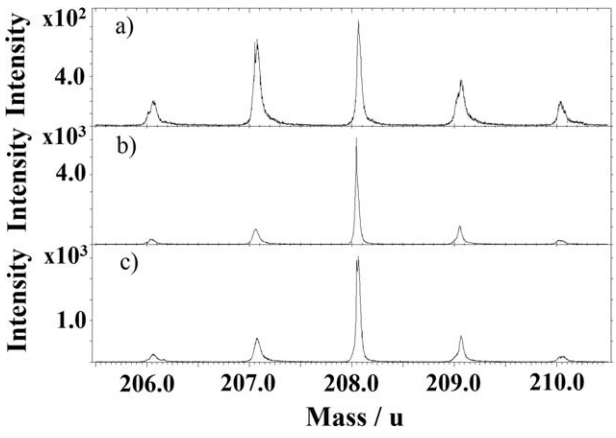

FIG. 16. ToF-SIMS positive ion spectra showing: (a) unwashed PET, (b) unwashed co-PET, and (c) chloroform washed co-PET surfaces for Sample 1.

A second method used to test the partial crystallization theory was ToF-SIMS surface analysis applied to Sample 1. ToF-SIMS, using a Bi_3^{2+} ion source, was applied to three different surfaces: the untreated PET and co-PET sides and the co-PET side after applying chloroform (the PET–co-PET interface). If the co-PET had been fully dissolved by the chloroform, one would expect the washed co-PET spectrum to exactly match the unwashed PET one. However, the three spectra observed (see Fig. 16) shows that the washed co-PET spectrum (Fig. 16c) instead matches the unwashed co-PET result (Fig. 16b). This confirms that there is still some co-PET present on the film after chloroform application, hence the low chloroform washing thickness results. The suggested, logical reason for this is partial crystallization of the co-PET layer at the interface.

The thickest co-PET layer is found both experimentally and numerically in Sample 3. This suggests that the addition of the red-PET increased the co-PET rheology, with less spreading to the edges in Sample 3 compared with Samples 1 and 2. This reduced co-PET spreading for Sample 3 is what one would expect given the data shown in Fig. 4 and Table 1 [1, 4, 8, 17, 28, 29, 48, 56].

CONCLUSIONS

Die plug analysis, chloroform washing, and white light interferometry were used to validate CFD modeling of polyester coextrusion. There was a good agreement between die plug structures and CFD results, with a good correlation based on the degree of encapsulation and the overall flow configuration. Both cast and final, biaxially oriented multilayered film samples were manufactured for experimental purposes.

For cast film analysis, excellent agreement was found between chloroform washing and CFD when comparing flow curves. When investigating final films, the white light interferometry obtained secondary co-PET thickness values validated CFD within the bounds of experimental error. However, the chloroform washing results for final films were found to be too low compared with both CFD and cast film results. This is attributed to partial crystallization of the co-PET layer upon orienting the cast film. There was generally a good agreement between numerical and experimental results and CFD modeling of polyester coextrusion was validated in this article at the data points analyzed.

The temperature and hence viscosity differences between the primary PET and secondary co-PET melt layers did not cause significant changes in the final film structures. It is envisaged that more rheologically different polymer melt flows would cause greater changes in the final film systems. Similarly, changing the amount of red-PET present in the co-PET layer would alter the layer composition.

ACKNOWLEDGMENTS

The authors gratefully acknowledge John Francis (DuPont Teijin Films) for providing chloroform washing training, Karl Rakos and David Bell (DuPont Teijin Films) for providing white light interferometry training, David Stocks (Intertek) for the rheological characterization of the polymers involved and Ian Fletcher (Intertek) for ToF-SIMS surface analysis.

REFERENCES

1. J. Dooley, *Viscoelastic Flow Effects in Multilayer Polymer Coextrusion*. PhD Thesis, Technische Universiteit Eindhoven (2002).
2. J. Dooley and K. Hughes, *TAPPI PLACE Conference*, 85 (1995).
3. M.T. Martyn, R. Spares, P.D. Coates, and M. Zatloukal, *J. Non-Newton. Fluid Mech.*, **156**, 150 (2009).
4. C. Rauwendaal, *Polymer Extrusion*, 4th ed., Hanser Gardner Publications, Munich (2001).
5. D.W. Brooks and G.A. Giles, *PET Packaging Technology*, Sheffield Academic Press, London (2002).
6. C.D. Han, *Rheology and Processing of Polymeric Materials, Vol. 2, Polymer Processing*, Oxford University Press (2007).
7. C.D. Han and R. Shetty, *Polym. Eng. Sci.*, **16**, 697 (1976).
8. D. Djordjevic, *Coextrusion*, Vol. 6, Rapra Review Reports, UK, 1 (1992).
9. R.S. Lenk, *Polymer Rheology*, Applied Science Publishers Ltd., London 31 (1978).
10. G. Oliver, *TAPPI* (2010), http://www.tappi.org/content/events/10EXTRU/papers/3.3.pdf.
11. J. Dooley, H. Kim, P.C. Lee, and R. Wrisley, *ANTEC*, **59**, 994 (2013).
12. E. Mitsoulis, *Adv. Polym. Technol.*, **8**, 225 (1988).
13. X.-L. Luo and E. Mitsoulis, *Adv. Polym. Technol.*, **10**, 47 (1990).
14. K. Lamnawar, H. Zhang, and A. Maazouz, "Coextrusion of Multilayer Structures, Interfacial Phenomena," in *Encyclopedia of Polymer Science and Technology*, John Wiley & Sons 1 (2013).
15. H. Zhang, K. Lamnawar, and A. Maazouz, *Polym. Eng. Sci.* (2014). DOI: 10.1002/pen.23945.
16. K. Lamnawar and A. Maazouz, *Polym. Eng. Sci.*, **49**, 727 (2009).
17. R.M.M. Mallens and C.J. Waringa, *TAPPI PLACE Conference*, Indianapolis, USA 32 (2004).
18. O. Mahdaoui, P. Laure, and J.-F. Agassant, *J. Non-Newton. Fluid Mech.*, **195**, 67 (2013).
19. L.C. Mendes, P.S.C. Pereira, and V.D. Ramos, *Macromol. Symp.*, **299**, 183 (2011).
20. V. Tanrattanakul, A. Hiltner, E. Baer, W.G. Perkins, F.L. Massey, and A. Moet, *Polymer*, **38**, 4117 (1997).
21. B. Khomami, *J. Non-Newton. Fluid Mech.*, **37**, 19 (1990).
22. J. Dooley and L. Dietsche, *Plast. Eng.*, **52**, 37 (1996).
23. P. Yue, C. Zhou, J. Dooley, and J.J. Feng, *J. Rheol.*, **52**, 1027 (2008).
24. E. Mitsoulis and F.L. Heng, *J. Appl. Polym. Sci.*, **34**, 1713 (1987).
25. A.E. Everage Jr., *Trans. Soc. Rheol.*, **17**, 629 (1973).
26. M.C. Williams, *AIChE. J.*, **21**, 1204 (1975).
27. C.D. Han, *J. Appl. Polym. Sci.*, **17**, 1289 (1973).
28. J.H. Southern and R.L. Ballman, *J. Appl. Polym. Sci.*, **20**, 175 (1973).
29. J.H. Southern and R.L. Ballman, *J. Polym. Sci.*, **13**, 863 (1975).
30. B.-L. Lee and J.L. White, *Trans. Soc. Rheol.*, **18**, 467 (1974).
31. C.D. Han, *Multiphase Flow in Polymer Processing*, Academic Press, New York (1981).
32. J. Dooley and L. Rudolph, *J. Plast. Film Sheet.*, **19**, 111 (2003).
33. K. Lamnawar, M. Bousmina, and A. Maazzouz, *Macromolecules*, **45**, 441 (2012).
34. G.M. Wilson and B. Khomami, *J. Non-Newton. Fluid Mech.*, **45**, 355 (1992).
35. J. Dooley, K.S. Hyun, and K. Hughes, *Polym. Eng. Sci.*, **38**, 1060 (1998).
36. J.L. White, R.C. Ufford, K.R. Dharod, and R.L. Price, *J. Appl. Polym. Sci.*, **16**, 1313 (1972).
37. B. Debbaut, T. Avalosse, J. Dooley, and K. Hughes, *J. Non-Newton. Fluid Mech.*, **69**, 255 (1997).
38. J. Dooley and L. Rudolph, *TAPPI PLACE Conference* (2002).
39. J. Dooley, *TAPPI PLACE Conference* (2004).
40. J. Dooley, *TAPPI PLACE Conference* (2007).
41. J. Dooley, C. Costeux, R. Wrisley, and A. Schadler, *TAPPI PLACE Conference* (2008).
42. H. Mavridis, A.N. Hrymak, and J. Vlachopoulos, *AIChE. J.*, **33**, 410 (1987).
43. A. Karagiannis, A.N. Hrymak, and J. Vlachopoulos, *Rheol. Acta*, **29**, 71 (1990).
44. W.A. Gifford, *Polym. Eng. Sci.*, **37**, 315 (1997).
45. M. Gupta, *ANTEC*, **56**, 2030 (2010).
46. M. Gupta, *ANTEC*, **58** (2012).
47. G. Sornberger, B. Vergnes, and J.F. Agassant, *Polym. Eng. Sci.*, **26**, 455 (1986).
48. A. Karagiannis, H. Mavridis, A.N. Hrymak, and J. Vlachopoulos, *Polym. Eng. Sci.*, **28**, 982 (1988).
49. C.D. Han, *J. Appl. Polym. Sci.*, **19**, 1875 (1975).
50. A. Torres, A.N. Hrymak, J. Vlachopoulos, J. Dooley, and B.T. Hilton, *Rheol. Acta.*, **32**, 513 (1993).
51. T.I. Butler, *TAPPI* 205 (1992).
52. A. Rincon, J. Ulcej, and D. Pitsch, *TAPPI PLACE Conference* (2002).
53. H. Helmy, *Adv. Polym. Tech.*, **7**, 59 (1987).
54. H. Helmy, *J. Plast. Film Sheet.*, **4**, 193 (1987).
55. A. Karagiannis, A.N. Hrymak, and J. Vlachopoulos, *Rheol. Acta.*, **28**, 121 (1989).
56. K.B. Sunwoo, S.J. Park, S.J. Lee, K.H. Ahn, and S.J. Lee, *Korea-Aust. Rheol. J.*, **12**, 165 (2000).
57. B.K. Carter, R.L. Lucking, J.A. Klein, and S.J. Israel, U.S. Patent 5,759,467 (1998).
58. J.A. Klein, B.K. Carter, S.J. Israel, and R.L. Lucking, U.S. Patent 5,783,283 (1998).
59. E.A. Grulke, *Polymer Process Engineering*, PTR Prentice Hall, New Jersey (1994).
60. S.A. Jabarin and E.A. Lofgren, *Polym. Eng. Sci.*, **24**, 1056 (1984).
61. K.B. Sunwoo, S.J. Park, S.J. Lee, K.H. Ahn, and S.J. Lee, *J. Non-Newton. Fluid Mech.*, **99**, 125 (2001).
62. S.J. Park, K.H. Ahn, and S.J. Lee, *Korea-Aust. Rheol. J.*, **13**, 37 (2001).
63. C.W. Hirt and B.D. Nichols, *J. Comput. Phys.*, 201 (1981).
64. J.C. Vickerman and D. Briggs, *TOF-SIMS: Surface Analysis by Mass Spectrometry*, 2nd ed., IM Publications LLP, London (2013).
65. J. Champion, M.K. Looney, and M.J.H. Simmons, *TAPPI PLACE Conference* (2013).
66. P.D. Anderson, J. Dooley, and H.E.H. Meijer, *Appl. Rheol.*, **16**, 198 (2006).
67. D. Silagy, Y. Demay, and J.F. Agassant, *Int. J. Numer. Meth. Fl.*, **30**, 1 (1999).
68. C. Sollogoub, Y. Demay, and J.F. Agassant, *Int. Polym. Proc.*, **18**, 80 (2003).